ISBN 978-82-326-4112-3 (printed version)
ISBN 978-82-326-4113-0 (electronic version)
ISSN 1503-8181

NTNU
Norwegian University of
Science and Technology

Loup Suja-Thauvin

Doctoral Thesis

Doctoral theses at NTNU, 2019:258

Loup Suja-Thauvin

Response of Monopile Wind Turbines to Higher Order Wave Loads

Doctoral theses at NTNU, 2019:258

NTNU

NTNU
Norwegian University of
Science and Technology
Faculty of Engineering
Department of MarineTechnology

NTNU
Norwegian University of
Science and Technology

Loup Suja-Thauvin

Response of Monopile Wind Turbines to Higher Order Wave Loads

Thesis for the degree of Philosophiae Doctor

Trondheim, October 2019

Norwegian University of Science and Technology
Faculty of Engineering
Department of MarineTechnology

NTNU
Norwegian University of
Science and Technology

NTNU
Norwegian University of Science and Technology

Thesis for the degree of Philosophiae Doctor

Faculty of Engineering
Department of MarineTechnology

ISBN 978-82-326-4112-3 (printed version)
ISBN 978-82-326-4113-0 (electronic version)
ISSN 1503-8181

Doctoral theses at NTNU, 2019:258

Printed by Skipnes Kommunikasjon as

Abstract

Monopile bottom-fixed offshore wind turbines have been in operation for around 30 years, and more are being planned for the next decades. The location and wave conditions of the planned wind farms make them susceptible to encounter steep and /or breaking waves during extreme weather events, typically storms with a return period of 50 years. These waves can produce large dynamic responses that threaten the structural integrity of the turbine. It is therefore necessary to accurately model the loads produced by these steep waves and the responses of the structure during the design stage of offshore wind turbines.

In this thesis, measurements from three experimental campaigns with model-scale wind turbines subjected to extreme sea states are presented. In all three campaigns, the largest responses were measured when a steep and breaking wave was passing through the turbine. The response was a combination of a ringing type of response (i.e. transient excitation of the first eigenmode of the structure) and excitation of the second mode of the structure. Ringing responses were attributed to second and third order hydrodynamic loads, while second mode response was triggered by so-called slamming loads (i.e. impulse loads produced by a wave breaking at the cylinder). The response was decomposed and for extreme events, quasi-static response accounted for 40 to 50% of the total response, the first mode accounted for 30 to 40% and the second mode for up to 20%. Higher modes were not analyzed.

Three design standards typically used for wind turbines in the North Sea were followed in this thesis. Different models suggested in the standards were implemented to simulate the responses measured during the experimental campaigns. Consistently with previous research, it was found that models that did not include non-linear kinematics did not match the measured first mode response, and models that did not include slamming loads did not produce significant second mode response. One of the commonly used models, the Morison equation with stream function wave kinematics and Wienke's slamming load model, was found to have the capability of exciting both the first and second mode of the turbine, but generally missed the balance between the contribution of these two modes.

The model recently developed by Kristiansen and Faltinsen (2017), hereafter referred to as *KF* was implemented for irregular waves, and it was found that this model has the capability to produce ringing responses, but generally overestimates the first mode response for very steep waves. The Rainey model, which in the present implementation only differs from the KF model in their respective point loads, produced responses very similar to those calculated with the KF model. This was shown to be due to the point loads producing similar forces for steep waves.

The original contributions of this work to the offshore wind research community include the quantification of the contributions of different eigenmodes in the response to steep and breaking waves, the assessment of different hydrodynamic load models compared to experimental results, and a suggestion for the implementation of the KF model in irregular waves with fully non-linear kinematics.

Acknowledgments

The first person I would like to thank is my main supervisor Jørgen Krokstad. I am part of the lucky PhD students whose relationship with their supervisor goes beyond a professional one. In addition to all the academic support he has provided, we have shared conference trips, team-building sessions, late-night technical and philosophical discussions and Chartreuse.

I am also extremely grateful to Erin Bachynski, who became my co-supervisor halfway through the PhD. At a point where it was not certain that the project would go ahead, having her join the team, with her amazingly sharp knowledge and constructive feedback was definitely a breath of fresh air. It is absolutely fair to say that she saved this PhD.

I also want to thank my co-supervisor Jørgen Amdhal for fruitful discussions during this PhD and for participating in the review process of the thesis.

The Marine Technology Department of NTNU has provided an inspiring environment that facilitated highly interesting discussion and challenging questions. In particular, I want to express my gratitude to Lene Eliassen, whose positive attitude always made it fun to be at work and to Trygve Kristiansen for his relevant input and advice in the implementation of the KF model that he has contributed to develop.

A number of research organizations have contributed to this PhD, and their support is gratefully acknowledged: Marintek/Sintef Ocean provided the experimental set-up and support for the experiments in the Lilletanken. The WiFi Joint Industry Project provided experimental data and support. The Wave Loads project supplied experimental and numerical data. A paper based on that data was devised during a two-week stay at the Wind Energy Department of DTU, funded by DTU, with the invaluable help of Henrik Bredmose and Fabio Pierella.

I also want to say thanks to Paul, Per-Ivar and Ruben, my friends at Simis. It's hard to work and write a PhD at the same time, but their support and enthusiasm made it possible.

Many friends should be acknowledged here as well, but I don't think I need to cite names for them to know. They provided a safe environment in which it was easy to not forget what the important things are. Together we explored part of the amazing Norwegian nature, and enjoyed these years to the fullest. If it was not for this 'Trondheim/friends' system, I might have finished my PhD a bit earlier, but I certainly would be a less happy person.

Finally, I am extremely grateful for the family that I have, who are always present and whose love I feel despite having been away for many years. Having their constant support and knowing that they are my home gives me a peace of mind that is hard to describe.

And of course, thank you Diana for you. *Ubitchomte Mnogo*.

This thesis was partly funded by Statkraft and the Norwegian Research Council, project number 237192. The other part was mainly funded by a consumption society that throws insane amounts of food every year. Only in Norway, 385 000 tons of edible food were thrown away in 2017, contributing to about 1.3 million tons of CO_2-eq (Stensgård et al. 2018). This enables PhD students to get into dumpsters at night and save lots of perfectly edible veggies, tasty cheeses or luxurious meat. This support is gratefully acknowledged.

Contents

List of Tables

List of Figures

Nomenclature

List of symbols

A	wave amplitude [m]
A_n	wave amplitude of the nth component in irregular waves [m]
a	horizontal wave particle acceleration [m·s^{-2}]
B	damping coefficient [Nm·(rd·s^{-1})$^{-1}$]
B_n	nth Fourier coefficient of the stream function [-]
b_n	modal damping for the nth mode
C_a	added mass coefficient [-]
C_M	inertia coefficient [-]
C_D	drag coefficient [-]
C_S	slamming coefficient [-]
C	stiffness [Nm·rd^{-1}]
c	wave celerity [m·s^{-1}]
c_n	modal stiffness for the nth mode
E	Young's modulus [Pa]
$F^{(1)}$, $F^{(2)}$, $F^{(3)}$	first, second and third order forces due to the linear incident potential in the FNV [N]
f_n	modal excitation for the nth mode
$f^{(n)}$	eigenfrequency of the nth mode [Hz]
F_I	inertia term in the Morison equation [N]
F_{slam}	slamming force [N]
F^{ψ}	point force due to the non-linear potential in the FNV [N]
F^{η}	point force in the Rainey model [N]
g	acceleration due to gravity [m·s^{-2}]
H	wave height [m]
H_S	significant wave height [m]
h	water depth [m]
I	moment of inertia [Nm·(rd·s^{-2})$^{-1}$]
$\vec{i}$, $\vec{j}$, $\vec{k}$	unit vectors of the Cartesian coordinate system [-]
k	wave number [m^{-1}]
k_n	wave number of the nth component in irregular waves [m^{-1}]
l	length of the structure [m]
m_a	added mass in surge [kg·m^{-1}]
M_{exc}	excitation moment [Nm]
m_n	modal mass for the nth mode
N	stream function order [-]
p_{exc}	exceedance probability [-]
R	cylinder radius [m]
S	wave spectrum
s	wave steepness [-]
T	wave period [s]

T_1	first eigenperiod [s]
T_P	spectral peak period [s]
t_d	impulse load duration [s]
U_r	Ursell number [-]
u, v, w	fluid particle velocity in the $x-$, $y-$ and $z-$directions [m·s^{-1}]
x, y, z	coordinates along the $\vec{i}$, $\vec{j}$, $\vec{k}$ axis in the Cartesian coordinate system [m]
$\vec{V}$	fluid particle velocity [m·s^{-1}]
α	angle between the water surface and the axis of the cylinder [rd]
β	auxiliary function in the FNV formulation [-]
γ	peak shape parameter for JONSWAP spectrum [-]
ϵ	perturbation parameter for the FNV theory [-]
ϵ_n	phase of the nth component in irregular waves [rd]
ζ	free surface elevation [m]
$\zeta^{(1)}$	first order free surface elevation [m]
ζ_m	maximum wave elevation for a slamming event [m]
η_n	damping ratio of the nth mode [-]
θ	coordinate of the one degree of freedom system [rd]
λ	wave length [m]
λ_c	curling factor [-]
ξ_n	modal displacement of the nth mode
ρ	water density [kg·m^{-3}]
Φ	velocity potential
$\Phi^{(1)}$	linear velocity potential
$\Phi^{(n)}$	velocity potential of order n
Ψ	stream function
Ψ_1, Ψ_2	spatially varying functions in the FNV formulation [-]
Ψ_d	structural deflection [m]
ψ	non-linear potential in the FNV theory
ψ_n	mode shape of the nth mode [-]
ω	wave circular frequency, also called fundamental frequency [rd·s^{-1}]
ω_n	wave circular frequency of the nth in component irregular waves [rd·s^{-1}]

Abbreviations

DLF: dynamic load factor

FLS: fatigue limit state

FNV: Faltinsen-Newman-Vinje model, as presented in Faltinsen et al. (1995)

GBS: gravity base structure

KF: Kristiansen-Faltinsen model, as presented in Kristiansen and Faltinsen (2017)

MSL: mean sea level

M_SF: Morison equation with stream function wave kinematics

M_SF_W: Morison equation with stream function wave kinematics and Wienke's slamming model

SLC: secondary load cycle

ULS: ultimate limit state

Chapter 1

Introduction

This chapter gives an overview of the motivation, objectives, scope and contribution of this thesis to the research community. The 5 papers that form the basis for this thesis are listed here and appended in appendix A.

1.1 Motivation

Over the last decades, leading scientists have raised concern about how the current use of natural resources poses serious threats to the biodiversity of our planet and the survival of the human species (Hoekstra and Wiedmann 2014). One of these threats is climate change, which leads to higher average temperatures worldwide, more occurrences of extreme weather events and threats to unique ecosystems, to name only a few (Robinson and Shine 2018). Among the solutions suggested by the research community to this sustainability challenge, the Intergovernmental Panel for Climate Change (IPCC) advocates for a technology-oriented option that requires only minor changes in the economic, social and political systems (IPCC 2014). While it has been suggested that technological solutions alone might not be sufficient (Creutzig et al. 2016), science and technological progress can help reduce the CO2 emissions due to human activities, thus contributing to mitigate climate change. The solutions suggested by this school of thought imply, among others, the development of carbon-neutral ways of producing energy.

One of these is wind energy, which emits virtually no CO2 during operation. Within the wind energy industry, bottom-fixed offshore wind represents 10.1% of the installed capacity across Europe (Whiteman et al. 2019). Figure 1.1 shows the main components of a bottom-fixed offshore wind turbine: the Rotor-Nacelle Assembly (RNA) is mounted on top of a tubular tower which is fastened onto a substructure. For monopile substructures (as the one shown in the example), a transition piece connects the tubular tower and the monopile. The substructure transfers the environmental loads experienced by the turbine

to the sea bed.

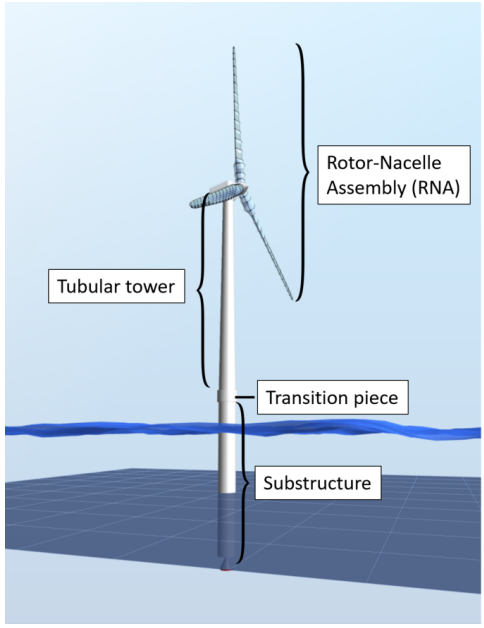

Figure 1.1: Different components of an offshore wind turbine. In this example, a monopile type of substructure is shown

Offshore wind turbines present advantages compared to their land-based counterparts, some of which are listed below:

- More space available offshore than on-land
- Reduced visual impact on the landscape, allowing for larger turbines
- Lower vertical shear in the wind
- No size limitations due to transport by rail or road

These advantages have enabled a reduction in the levelized cost of energy of offshore wind and an increase in the total installed capacity worldwide. Figure 1.2 shows the reported and predicted cumulative bottom-fixed offshore wind power from 2011 to 2030 (data from GWEC 2017). The number of offshore wind farms is foreseen to increase over the next decade.

Figure 1.3 shows the existing and planned bottom-fixed offshore wind farms in Europe (WindEurope 2018). The near future will see several new wind farms being built in water depths up to 50 m. Within these water depths, the monopile type of substructure, which

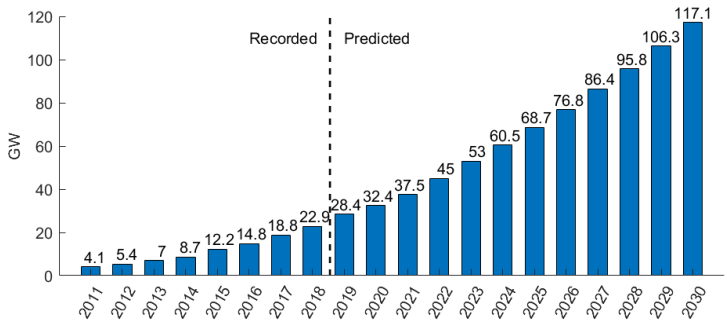

Figure 1.2: Cumulative installations of offshore wind in the world, recorded and predicted, with data from GWEC (2017)

consists of a circular cylinder that is piled into the sea bed and extends above the mean sea level, is preferred. 81.7% of all substructures for offshore wind turbines in Europe (for all depths, including floating) are monopiles (WindEurope 2018).

1.2 Challenges

This section presents some of the challenges that the offshore wind industry is facing with respect to designing monopile substructures in finite water depth.

1.2.1 Loads and load effects

As shown in Figure 1.3, a significant number of offshore wind turbines are planned or being built in finite water depths in terms of hydrodynamics (see Section 2.2), where waves, especially in storm conditions, can be significantly non-linear. These non-linear waves can lead to the so-called *ringing*, *springing* and *slamming* phenomena, which threaten the structural integrity of the turbine. These phenomena are defined hereafter.

Ringing: A ringing event is defined as a sudden transient oscillation of the structure produced by a steep wave whose fundamental frequency is significantly lower than the first eigenfrequency of the structure. It is characterized by a fast build-up (only a few oscillations, Chaplin et al. 1997) and a much slower decay (Natvig and Teigen 1993). Figure 1.4 shows an example of a ringing event, where the bending moment of a vertical cylinder at the sea bed oscillates in its first mode after the passage of a steep wave.

Ringing was first observed in the 1990s on model tests of the Hutton and Heidrun tension leg platforms and then on concrete towers of the Draugen and Troll A platforms (Natvig and Teigen 1993). Shortly after, numerical models were developed by Faltinsen et al. (1995) and Malenica and Molin (1995) to predict ringing responses in infinite water. The model developed by Faltinsen et al. (1995) is analyzed in detail in Section 2.3.2.

Figure 1.3: Average water depth and distance to shore for bottom-fixed offshore wind farms in Europe. The size of the bubble indicates the overall capacity of the site (taken from WindEurope 2018).

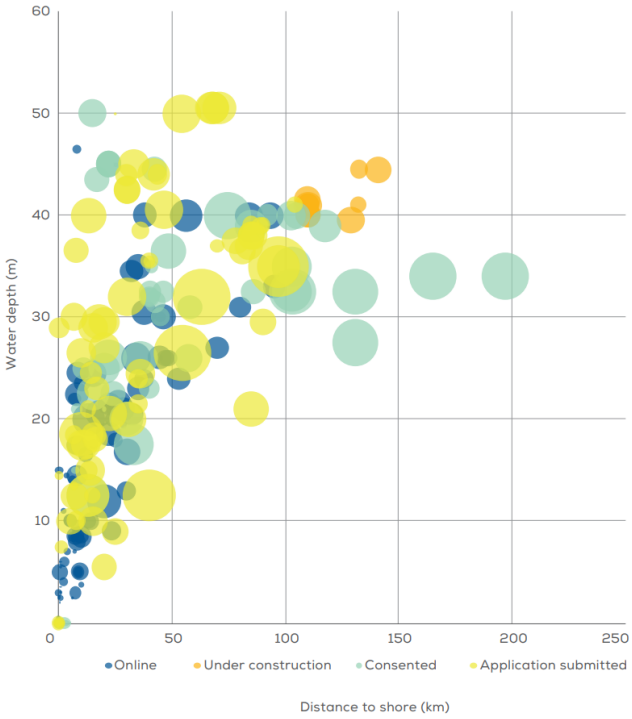

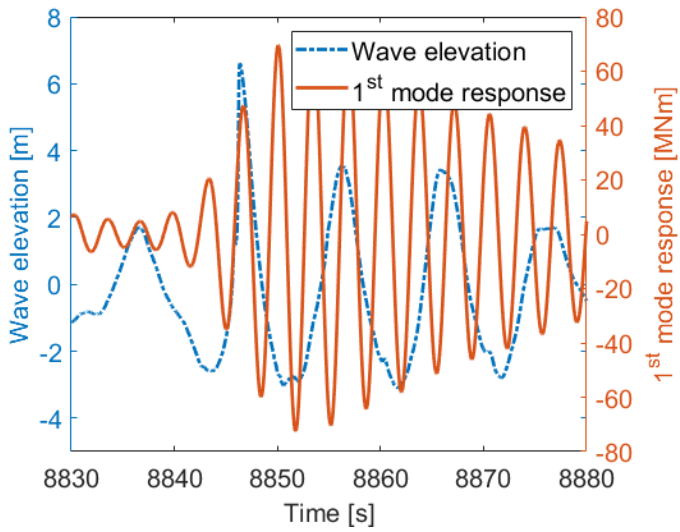

Figure 1.4: Illustration of a ringing event. A surface-piercing vertical cylinder is exposed to a steep wave, and the bending moment is measured at the sea bottom (note that in this picture the bending moment has been filtered around the first eigenfrequency of the structure).

In the same period, many experimental campaigns studying ringing events were carried out (Grue and Huseby 2002, Krokstad and Stansberg 1995, Huseby and Grue 2000, Welch et al. 1999). By analyzing stiff cylinders, it was found that in a significant number of occurrences of steep waves producing ringing, the excitation load experienced a sudden high frequency increase. This phenomenon is called *secondary load cycle* (SLC), also known as *hydraulic jump* and is illustrated in Figure 1.5. The SLC typically occurs about one quarter wave period after the main peak of the excitation force (Grue and Huseby 2002), lasts for about 15% of the wave period (Grue et al. 1993) and has a magnitude of up to 12% of the peak-to-peak excitation force (Riise et al. 2018), i.e. the difference between the maximum and the minimum of the excitation force for the given event.

There is no general scientific consensus on the causality link between SLCs an ringing events. Grue and Huseby (2002) analyzed several experiments on both infinitely stiff and responding surface piercing cylinders and concluded that "The secondary load cycle gives and important contribution to build-up of resonant body responses [...]". Rainey (2007) used high-speed photography from the experimental campaigns of Chaplin et al. (1997) and Rainey and Chaplin (2003) to conclude that "the rapid loading cycle causing the "ringing" vibration is traceable to local wave breaking around the cylinder [...]". However, Paulsen et al. (2014) carried out a numerical investigation of the SLC by solving the two-phase incompressible Navier-Stokes equations and found that "[...] the secondary load cycle is thus an indicator of strongly non-linear flow rather than a direct contributor to the resonant forcing". This is in agreement with the earlier findings of Krokstad and Stansberg (1995), who studied the phasing between the SLC and the ringing response and concluded that "The hydraulic jump has no direct connection with the non-linear behaviour of the

ringing force [...]".

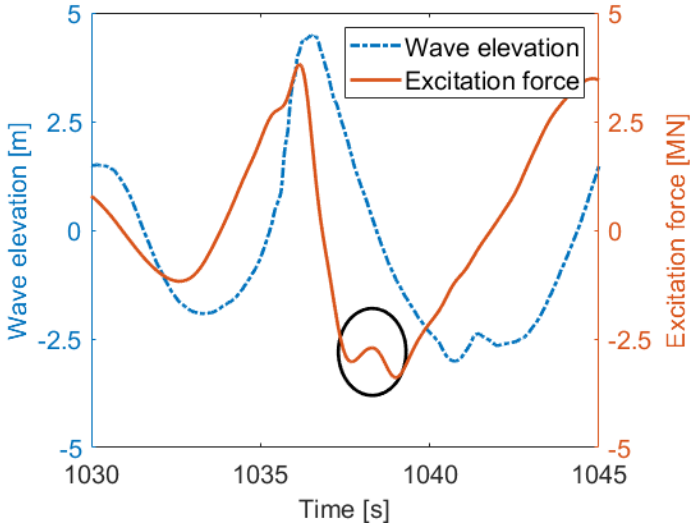

Figure 1.5: Occurrence of secondary load cycle, visible on the excitation force (circled in black)

In the last decade, the increase in the size of bottom-fixed offshore wind turbines has led to an increase of the first eigenperiod of the structures to levels where it can coincide with the third and fourth harmonics of a large wave (Suja-Thauvin et al. 2014). Ringing responses have been observed in model-scale experiments where structures with the characteristics of an idling wind turbine were subjected to steep waves (de Ridder et al. 2011, Bredmose et al. 2013b). In such an experiment, analyzed by Suja-Thauvin et al. (2017), it was found that the contribution of the first mode to the maximum response bending moment at the seabottom during a ringing event was up to 30%. This result will be studied in detail in Section 4.1.

Slamming: Another phenomenon relevant for surface piercing bodies subjected to steep waves is the loads from breaking waves. For very non-linear waves, the velocity of the water particles at the crest become higher than the velocity of the wave itself (also called *wave celerity*, noted c), leading to the wave breaking. When a wave breaks at the structure, the wall of water hitting the cylinder produces a load at the point of impact of very short duration and high amplitude that can be assimilated to an impulse type of load (Faltinsen 1990). These type of events are called *slamming events* and produce the so-called *slamming loads*. Slamming loads have gained relevance for offshore wind turbines because the depths of installation shown in Figure 1.3 increase the probability of occurrence of breaking waves and thus of slamming events. Bunnik et al. (2015) and Hallowell et al. (2015) report breaking waves on full-scale wind turbines, and the model tests performed by de Ridder et al. (2011) and Bredmose et al. (2013b) show that slamming loads can trigger large accelerations of the nacelle.

Slamming loads on monopiles are difficult to predict because of their chaotic nature: small changes in the system such as air entrapment, slightly different times of impact or surface roughness make it very challenging to reproduce slamming loads experimentally. Bachynski et al. (2017) analyzed an experimental campaign where a cylinder was subjected to extreme irregular seas and found variations of up to 10% in the response of the structure when repeating a slamming event. However, some simple models give reasonably accurate predictions of the loads produced by breaking waves. As will be see in Section 2.5, a model commonly used in the industry is the one developed by Wienke and Oumeraci (2005) (referred to hereafter as *Wienke's model*). This model is based on earlier work by Wagner (1932), who assumed potential flow theory to derive the pressure forces around a cylinder entering water. Wienke's model will be described in more details in Section 2.3.2.

Springing: As mentioned in Section 1.1, non-linear waves carry energy at different harmonics of the fundamental wave frequency. When these harmonics are close to the first eigenfrequency of the structure, it will respond in its first mode. This type of response is defined as *springing*. The main difference between springing and ringing is that springing is a continuous response, while ringing is a transient response. In practice, it is not straightforward to distinguish between ringing and springing responses.

1.2.2 Difference between wind turbines and oil and gas platforms

The effects of ringing responses and slamming loads on surface piercing cylinders have been extensively studied in the context of offshore oil and gas platforms. The models that were developed to account for these phenomena are therefore based on the conditions encountered by this type of structures. However, the oil and gas platforms are generally located in deep water depth whereas, as seen in Figure 1.3, bottom-fixed offshore wind turbines can be in finite water depth. This has the following consequences.

More non-linearities in the wave: Waves in finite water depth are more non-linear than in infinite waters (Dalrymple and Dean 1991), which increases the likelihood and the magnitude of phenomena such as ringing and slamming. Kristiansen and Faltinsen (2017) extended the FNV model, initially developed by Faltinsen et al. (1995) for infinite water, to finite water. Both models will be analyzed in detail in Section 2.3.2.

Different point of action of the hydrodynamic loads: The mode shapes of oil and gas platforms mounted on a gravity base structure (GBS) and of bottom-fixed offshore wind turbines have some similarities due to the large mass of the deck or nacelle (see Figure 1.6). For oil and gas platforms, the hydrodynamic loads acting around the mean sea level (MSL) will have an influence closer to the top mass than for wind turbines. Figure 1.6 illustrates this effect by comparing the mode shapes of the Draugen GBS platform (Natvig and Teigen 1993) and a 4 MW wind turbine. For instance, it can be seen that the displacement of the normalized second mode shape of the wind turbine at the MSL is larger for the wind turbine than for the oil and gas platform. This means that slamming loads, which act at the MSL, can produce significant second mode response on wind turbines, as shown for

instance by Peeringa and Hermans (2017).

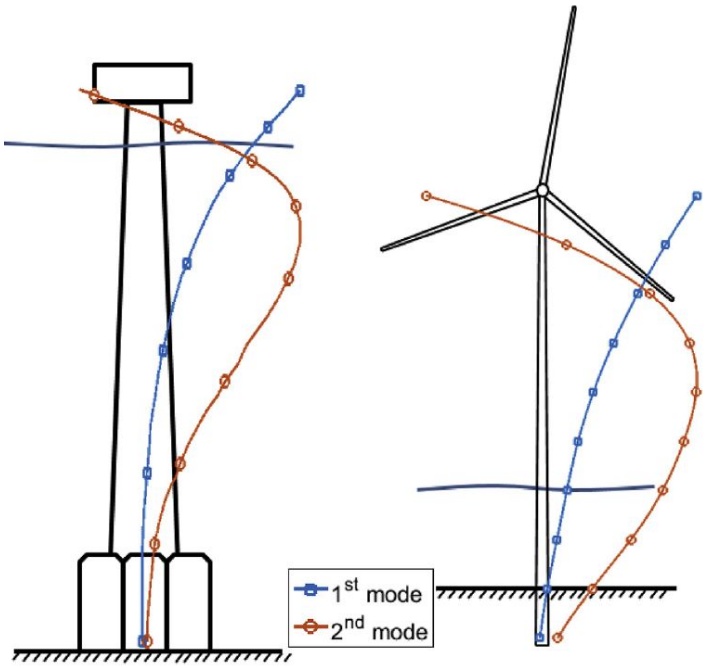

Figure 1.6: Schematic representation of the Draugen platform (Faltinsen and Timokha 2016) and a 4 MW offshore wind turbine (Bunnik et al. 2015). The lines represent the first and second mode shapes normalized against their maximum value. The drawings are not to scale.

Larger influence of the load distribution around the MSL: When evaluating the bending moment at the sea bed, the arm with which the force acts is roughly equal to the water depth. In infinite water, the length of this arm is such that inaccuracies in the point of application of the hydrodynamic loads have a small influence on the bending moment. In finite water, that influence becomes comparatively bigger and an inaccurate description of the distribution of the load around the MSL might introduce a significant error in the estimation of the bending moment at the sea bed.

1.2.3 Simulation of the structure

One challenge inherent to designing physical structures is to obtain data about how the structure will behave once installed. This is not particular to offshore wind but is a central element in this thesis. Three ways to obtain data on offshore wind turbines in finite waters were explored in this work.

Model testing: a small-scale model of the wind turbine is built and placed in a controlled environment that reproduces the most important physical effects of interest, and different measurement devices are used to record the behaviour of the structure and the environ-

mental conditions. In this thesis, data from three experimental campaigns, listed in Section 3, was used. In all three cases, a small-scale model of an idling wind turbine was placed in a wave basin, and wave makers were used to produce the required wave conditions.

Numerical modeling: a numerical representation of the wind turbine is generated on a computer. The equations that determine the behaviour of this model are coded according to a given theory. This requires representing the loads from the environmental conditions, the turbine, and its behaviour numerically. In the present context, a wide number of theoretical models were available to represent the structure and how it responds to external loading. The challenge was therefore to accurately simulate the environmental loads.

Full-scale measurements: it is possible to place measurement devices on and around a full-scale structure, which gives the behaviour of the structure in actual environmental conditions. Full-scale data from a meteorological mast located in the Dogger Bank site off the coast of the UK was analyzed during this thesis, but due to the insufficient quality of the data the project had to be abandoned. No further analysis of full-scale measurement data was carried out in the thesis.

Table 1.1 gives an overview of the advantages and disadvantages of the three methods listed above.

Table 1.1: Comparison of different methods to obtain data on a structure

	Advantages	**Disadvantages**
Model testing	• Quick (days/weeks) and cheap compared to full-scale • Controlled environmental conditions • High degree of repeatability	• Possible scale effects • Limited by experimental set-up & measurement accuracy • Limited by the representation of the stochastic environment
Numerical modelling	• Cheapest and quickest option • Perfectly repeatable, thus enabling parametric studies or different models	• Will miss phenomena not accounted for by the theory • Limited by accuracy of the model
Full-scale measurements	• Provides data from the actual environmental conditions with the actual model	• Most expensive • Time-consuming, typically months/years • Not possible to control the environmental conditions

1.3 Objectives

Currently, it is common in the North Sea to design offshore wind turbine substructures using standards and guidelines that have been adapted from the oil and gas industry. In particular, this thesis analyzes the suggestions from the IEC-61400-3 (2009), the DNV-RP-C205 (2017) and the DNV-OS-J101 (2014) standards. Uncertainties in design analyses are generally accounted for by having large safety factors and therefore producing more expensive designs. The main objective of these thesis is to reduce uncertainties in the hydrodynamic load models commonly used to simulate the wave loads in storm conditions. To achieve this, the following research objectives are explored:

RO1 Importance of different non-linear hydrodynamic phenomena for extreme structural responses

RO2 Relevance and accuracy of the methods suggested in the standards

RO3 Assessment of new models in ULS design of monopiles in finite water

1.4 Scope

To address these research topics, a leitmotif in this thesis work has been to analyze data from experimental campaigns and compare the measured responses with numerical models. The work considers

- Monopiles: single column circular cylinder type of substructure with a diameter of the order of magnitude of the wave amplitude
- Finite water depths: depths varying between 20 and 50 m, where the infinite water approximation is not possible
- Ultimate Limit State (ULS) analysis: idling or parked turbines experiencing wave conditions with a return period higher than 10 years
- Computationally efficient methods: models that enable to simulate thousands of load cases within a time frame that fits the design process of wind turbines for the industry, or that simplify several load cases into one

1.5 List of publications

The following papers form the scope of this thesis:

P1 Loup Suja-Thauvin, Jørgen R. Krokstad, and Joakim Frimann-Dahl. Maximum loads on a one degree of freedom model-scale offshore wind turbine. *Energy Procedia*, 94:329–338, 2016

Relevance to the thesis: This paper presents the results obtained during the NTNU experimental campaign (see Section 3). It compares the response measured on a one degree of freedom model in extreme irregular sea states to numerical simulations using the FNV method (Faltinsen et al. 1995). Based on one extreme response event, it shows that the FNV alone suffices to trigger first mode response, without the need for slamming models.

My contribution: Together with Joakim Frimann-Dahl and as part of his master thesis, we designed and set up the experimental campaign and carried out the experiments. I then post-processed the results, implemented the numerical models and ran the numerical simulations.

P2 Loup Suja-Thauvin and Jørgen Ranum Krokstad. Simplified Bottom Fixed Offshore Wind Turbine in Extreme Sea States. In *The 26th International Ocean and Polar Engineering Conference*, Rhodos (Greece), June 2016. International Society of Offshore and Polar Engineers. ISBN 978-1-880653-88-3. URL https://www.onepetro.org/conference-paper/ISOPE-I-16-468

Relevance to the thesis: This study uses the same experimental data as the previous paper, and its conclusion are extended from one to a large number of events. Combined with the previous paper, the main conclusion of this work is that ringing responses can result from second and third order hydrodynamic loads, and that slamming loads alone cannot produce significant first mode response.

My contribution: I developed a model for linearizing measured wave elevation time series. I implemented the numerical models and carried out all the analysis and the post-processing of the results.

P3 Loup Suja-Thauvin, Jørgen R. Krokstad, Erin E. Bachynski, and Erik-Jan de Ridder. Experimental results of a multimode monopile offshore wind turbine support structure subjected to steep and breaking irregular waves. *Ocean Engineering*, 146: 339–351, December 2017. ISSN 0029-8018. doi: 10.1016/j.oceaneng.2017.09.024. URL http://www.sciencedirect.com/science/article/pii/S0029801817305437

Relevance to this thesis: This paper analyses experimental data from a fully-flexible model of an offshore wind turbine in similar environmental conditions as the previous paper. It describes the physical processes that occur when the model experiences large wave-induced bending moment responses. In particular, it shows that second mode response is significant and is triggered by breaking wave loads. It also quantifies the contribution of ringing responses and responses to breaking waves to the total response.

My contribution: The experimental data was produced by the Maritime Research Institute Netherlands (MARIN) for the WiFi JIP (de Ridder et al. 2017). I post-processed the data and carried out the analysis of the results.

P4 Loup Suja-Thauvin, Jørgen R. Krokstad, and Erin E. Bachynski. Critical assessment of non-linear hydrodynamic load models for a fully flexible monopile offshore

wind turbine. *Ocean Engineering*, 164:87–104, September 2018. ISSN 0029-8018. doi: 10.1016/j.oceaneng.2018.06.027. URL https://www.sciencedirect.com/science/article/pii/S0029801818310515

Relevance to this thesis: This paper compares the experimental data presented in the previous paper with numerical models suggested in the common standards for offshore wind energy. It demonstrates that slamming models are necessary to trigger second mode response in the numerical simulations. The paper also shows that for the most extreme sea states, even if the total bending moment prediction is reasonably accurate, these models do not capture the first and second mode responses accurately.

My contribution: I implemented the numerical models and ran the simulations, carried out the comparisons and analyzed the results.

P5 Loup Suja-Thauvin, Erin Elizabeth Bachynski, Fabio Pierella, Michael Borg, Jørgen Ranum Krokstad, and Henrik Bredmose. Critical Assessment of Hydrodynamic Load Models for a Monopile Structure in Finite Water Depth. *Marine Structures (submitted)*, April 2019

Relevance to the thesis: This paper suggests a way of implementing the newly developed KF model (Kristiansen and Faltinsen 2017) for irregular waves. By comparing experimental results to numerical simulations, it shows that this model has the potential to predict extreme responses of bottom-fixed offshore wind turbines in intermediate water depths but that it generally overpredicts first mode response and underpredicts second mode response. The paper also demonstrates that the KF model and the well-known Rainey model (Rainey 1989) produce similar excitation forces for large waves.

My contribution: The experimental data was produced by DHI Denmark and the Technical University of Denmark (DTU) for the Wave Loads project (Bredmose et al. 2013a). The fully non-linear kinematics were produced by DTU and the second order wave kinematics were produced by Erin Bachynski. I implemented the numerical load models, post-processed the experimental and numerical results and analyzed the data.

In addition to these publications, the following paper was presented at the 2014 IWEC conference, but is not included in the thesis as it it considered a preliminary study:

C1 Loup Suja-Thauvin, Lene Eliassen, and Jørgen Krokstad. The scalability of loads on large diameter monopile offshore wind support structures. In *International Wind Engineering Conference*, Hannover, September 2014

An overview of how the publications relate to the research objectives and to different topics explored in the thesis is given in Figure 1.7.

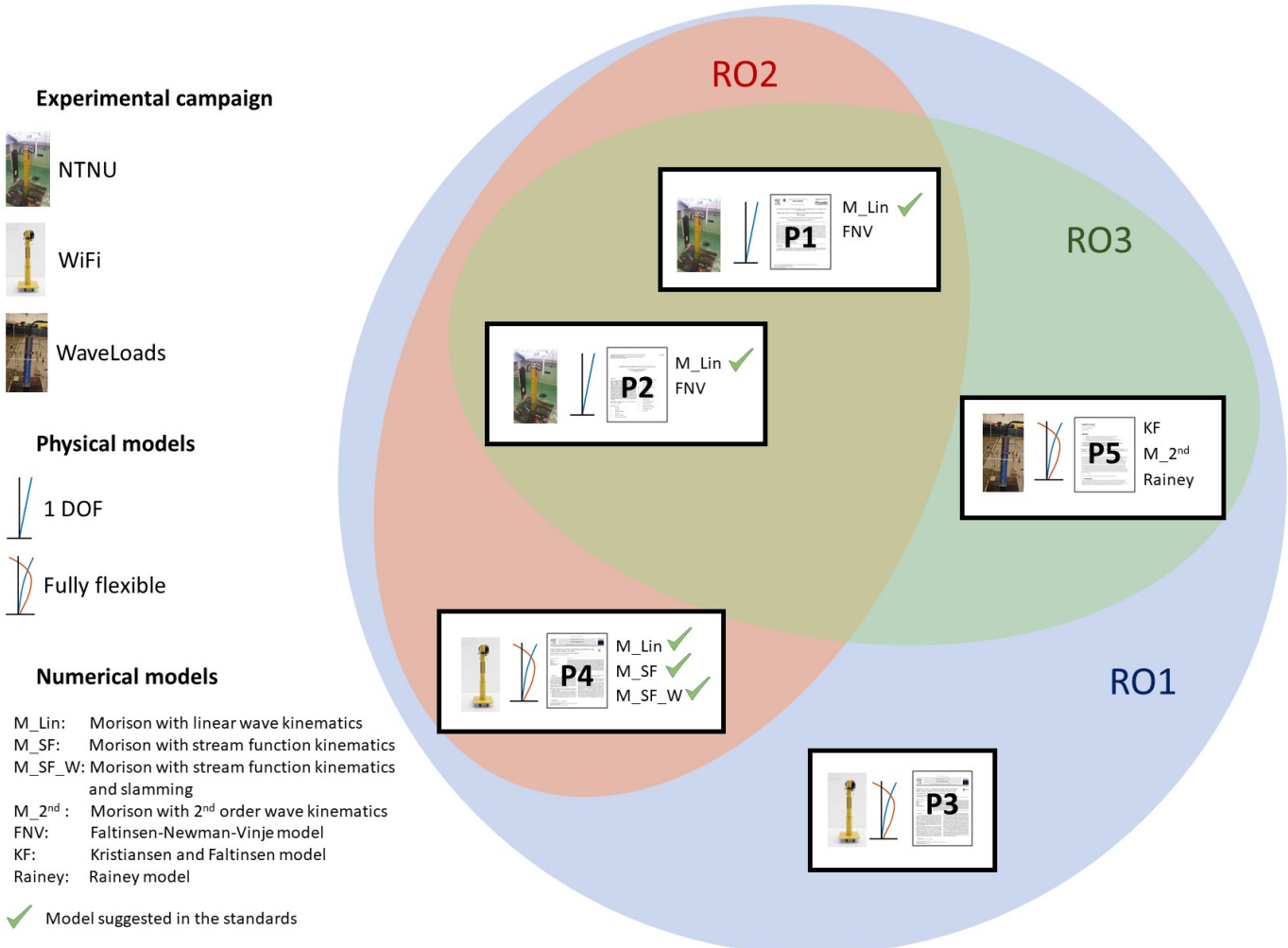

Figure 1.7: Overview of publications during the PhD

Chapter 2

Background

2.1 Dynamic analysis of an offshore wind turbine

In the design process of a bottom-fixed offshore wind turbine, as will be explained in Section 2.5, it is necessary to analyze the response of the structure in different environmental conditions. Offshore wind turbines are typically subjected to various sources of loading, due to the environmental conditions and to the operation of the turbine itself. When carrying out the dynamic analysis of a turbine in operating conditions, the following elements will affect the response:

- **Aerodynamics:** the loads from the air on the blades and the support structure.
- **Hydrodynamics:** the loads from the waves and current on the structure.
- **Controller:** depending on the environmental conditions, the controller will adjust parameters such as the generator torque exerted on the rotor of the turbine or the pitch angle. These will affect the behaviour of the system.
- **Geotechnics:** the monopile is piled into the ground, and the interaction between the soil and the structure needs to be accounted for.
- **Structure:** the dimensions and characteristics of the structure, such as stiffness or damping, will drive the response of the system.

Note that this list is not exhaustive, as several other sources can produce loads on the structure, such as marine growth, icing, the electrical grid, etc. During operation, many of the effects mentioned above interact, therefore models that simulate all these effects simultaneously are in principle required. Coupling effects include

- the aerodynamic loads influence the damping on the structure (so-called *aerodynamic damping*)
- the waves radiated by the monopile influence the damping of the structure
- the presence of the monopile influences the waves
- the motion of the structure influences the relative wind and wave kinematics. For the wave kinematics, this effect is negligible for bottom-fixed turbines
- the controller influences the dynamic response and the aerodynamic loads
- the soil-structure interaction influences the dynamic response, the stiffness and the damping
- the deflections of the blades affect the aerodynamic loads

In this thesis, Ultimate Limit State conditions are assumed, and the main focus is on the response of the structure due to hydrodynamic loads. Therefore, several of the coupled effects listed above can be neglected, as will be shown in Chapter 3.

2.2 Wave theory

The goal of this section is to provide a theoretical basis for the rest of the thesis. To do so, a summary of the assumptions and equations that depict the physics of water waves is given. Many authors have detailed the derivation of these equations much better than what could be done in this thesis, and the reader is therefore referred to these works for the complete picture. Among the books that provide a good overview of wave theory, Faltinsen (1990), Dalrymple and Dean (1991) or Mei et al. (2005) are especially recommended.

It is common in offshore environments to divide waves into deep water waves, intermediate water waves and shallow water waves, depending on the water depth and the wave characteristics. Figure 2.1 represents a snapshot of a wave and describes its main characteristics. Note that Figure 2.1 is taken at an instant t, which shows the wavelength λ but does not show the variation in time of the wave. If the time-evolution of the wave is studied instead, one can define the wave period T as the period of time between the occurrence of two successive wave crests at a given point in space.

Sarpkaya (2010) classifies the waves depending on their wavelength λ and the site depth h as follows:

- Deep water waves: $h/\lambda > 0.5$
- Intermediate water waves: $0.5 > h/\lambda > 1/20$
- Shallow water waves: $h/\lambda < 1/20$

Note that it is common to refer to deep water waves as *infinite water waves* and to group intermediate and shallow water under the *finite water waves* category.

Another relevant parameter to consider when studying waves is the so-called wave steepness, defined as $s = kH$ where $k = 2\pi/\lambda$ is called *wave number*. In finite water conditions, the interaction between the sea bottom and the wave tends to increase the wave steepness. When the wave steepness is above a certain limit (which depends on the water depth), the wave will become unstable and break (Dalrymple and Dean 1991).

When the wave steepness is small, which occurs when the wave height H is small compared to the wavelength λ and the water depth h, the waves are called *linear*. This implies that the position, velocity and acceleration of the water particles composing the wave (so-called wave kinematics) are proportional to the steepness of the wave s. This greatly simplifies the equations describing the wave kinematics shown for example in Faltinsen (1990). In addition, the kinematics of the wave oscillate at the wave's fundamental frequency, $\omega = 2\pi/T$, also called the wave first harmonic. A mathematical definition of the concept of linear waves is given in Section 2.2.2.

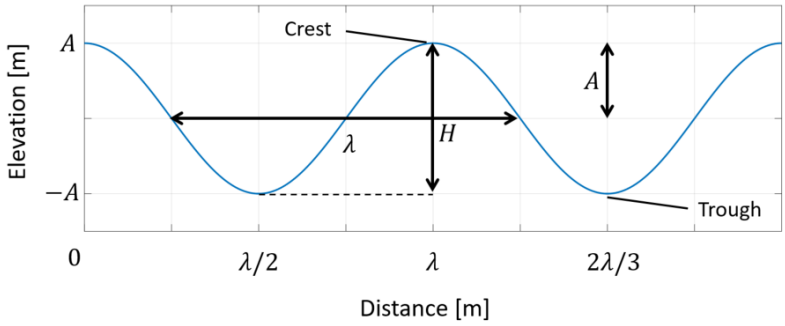

Figure 2.1: Definition of the characteristics of a wave, with A the amplitude of the wave, H the wave height and λ the wave length.

If the conditions for a small steepness wave are not fulfilled, the waves are called *non-linear*. Non-linear waves are steeper and have higher crests and shallower troughs than linear waves. The kinematics of non-linear waves oscillate not only at the first harmonic of the wave, but also at multiples of this first harmonic, i.e. at 2ω, 3ω and so on. This implies that non-linear waves carry energy at higher frequencies than linear waves. In addition, the larger the non-linearities are, the more energy will be carried at higher harmonics.

It should be noted that this thesis deals with so-called gravity waves. Two underlying assumptions are thus that compressibility effects and surface tension are not significant.

2.2.1 Definition of the boundary value problem

In the following paragraphs, we place ourselves in a Cartesian coordinate system fixed in space, where $\vec{i}$, $\vec{j}$ and $\vec{k}$ are the unit vectors along the $x-$, $y-$ and $z-$ axes, respectively. The height $z = 0$ is chosen to be at the mean sea level (MSL), and for the present analysis the vertical axis $(x, y) = (0, 0)$ can be chosen arbitrarily. Figure 2.2 shows the analyzed domain and the corresponding boundaries, defined by the free surface and the sea bottom. The lateral boundaries, shown as dashed lines in Figure 2.2 can again be chosen arbitrarily for the present analysis.

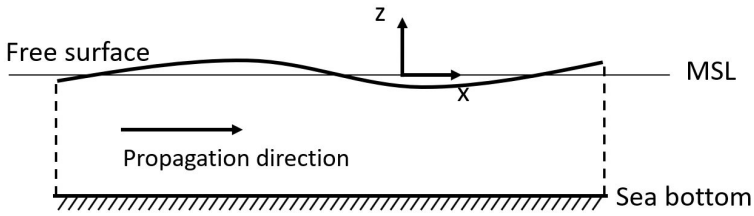

Figure 2.2: Domain of analysis of the water waves

Governing equation The starting assumption to derive the wave theory used in this thesis is that the water is an incompressible and inviscid medium. In addition, the flow is considered irrotational. Under these conditions, the fluid velocity at a point (x, y, z) at a time t, denoted $\vec{V}(x, y, z, t) = (u, v, w)$, can be described by a velocity potential Φ such as

$$\vec{V} = \nabla\Phi = \vec{i}\frac{\partial\Phi}{\partial x} + \vec{j}\frac{\partial\Phi}{\partial y} + \vec{k}\frac{\partial\Phi}{\partial z}. \tag{2.1}$$

Since the water is assumed incompressible, conservation of mass implies that $\nabla \cdot \vec{V} = 0$. The velocity potential Φ must therefore satisfy the well known Laplace equation:

$$\frac{\partial^2\Phi}{\partial x^2} + \frac{\partial^2\Phi}{\partial y^2} + \frac{\partial^2\Phi}{\partial z^2} = 0. \tag{2.2}$$

In order to describe the wave kinematics, one must therefore find a solution to the Laplace equation. This requires establishing the boundary conditions for the fluid domain defined in Figure 2.2.

Kinematic free surface boundary conditions The kinematic free surface boundary condition expresses the fact that a particle on the free surface remains on the free surface. We define the free surface of the water to be at $z = \zeta(x, y, t)$. The kinematic free surface boundary condition is then expressed as

$$\frac{\partial \zeta}{\partial t} + \frac{\partial \Phi}{\partial x}\frac{\partial \zeta}{\partial x} + \frac{\partial \Phi}{\partial y}\frac{\partial \zeta}{\partial y} - \frac{\partial \Phi}{\partial z} = 0 \quad \text{at} \quad z = \zeta(x, y, t). \tag{2.3}$$

Dynamic free surface boundary condition The dynamic boundary condition expresses the fact that the water pressure is equal to the atmospheric pressure at the free surface. It is obtained by applying the Bernoulli equation at the free surface and is expressed as

$$g\zeta + \frac{\partial \Phi}{\partial t} + \frac{1}{2}\left(\left(\frac{\partial \Phi}{\partial x}\right)^2 + \left(\frac{\partial \Phi}{\partial y}\right)^2 + \left(\frac{\partial \Phi}{\partial z}\right)^2\right) = 0 \quad \text{at} \quad z = \zeta(x, y, t). \tag{2.4}$$

Bottom boundary condition The sea bottom is considered impermeable, which means that no water particle can go through it. For a constant water depth h, this translates into the following condition:

$$\frac{\partial \Phi}{\partial z} = 0 \quad \text{at} \quad z = -h. \tag{2.5}$$

2.2.2 Linear wave kinematics

In the following section we consider two-dimensional waves, i.e. we neglect all variations in the y-direction. Expanding the theory to three-dimensional waves is trivial but would make the equations in the following section unnecessarily complicated.

The free surface boundary conditions established in the previous section should be applied at the free surface $z = \zeta(x, t)$, which is a priori unknown. A way to overcome this problem is to take the Taylor expansion of the free surface elevation around $z = 0$ to express those conditions. For example, this process applied to the kinematic free surface boundary condition in two dimensions yields

$$\begin{aligned}\left(\frac{\partial \zeta}{\partial t} + \frac{\partial \Phi}{\partial x}\frac{\partial \zeta}{\partial x} - \frac{\partial \Phi}{\partial z}\right)_{z=\zeta} &= \left(\frac{\partial \zeta}{\partial t} + \frac{\partial \Phi}{\partial x}\frac{\partial \zeta}{\partial x} - \frac{\partial \Phi}{\partial z}\right)_{z=0} \\ &\quad + \zeta\frac{\partial}{\partial z}\left(\frac{\partial \zeta}{\partial t} + \frac{\partial \Phi}{\partial x}\frac{\partial \zeta}{\partial x} - \frac{\partial \Phi}{\partial z}\right)_{z=0} + \ldots = 0.\end{aligned} \tag{2.6}$$

Next, if the wave amplitude is assumed to be small such that $kA \ll 1$, then the wave elevation, water particle velocities and other kinematics are small as well. This implies $k\zeta \ll 1$ and therefore $(k\zeta)^2 \ll k\zeta$, $k^2 u\zeta \ll k\zeta$ and so on. This enables to separate the terms into two categories: small first-order quantities such as $\partial\zeta/\partial t$ or $u = \partial\Phi/\partial x$ are

called *linear terms*. The rest of the terms, such as ζ^2 or $u\zeta$ are called *non-linear*. The assumption of small waves implies that the non-linear terms are negligible compared to the linear terms. The linear kinematic free surface boundary condition then becomes

$$\frac{\partial \zeta}{\partial t} - \frac{\partial \Phi}{\partial z} = 0 \quad \text{at} \quad z = 0. \tag{2.7}$$

Similarly, the linear dynamic free surface boundary condition becomes

$$g\zeta + \frac{\partial \Phi}{\partial t} = 0 \quad \text{at} \quad z = 0 \tag{2.8}$$

The bottom boundary condition remains the same if we only consider linear terms.

The full derivation of the linear solution to the velocity potential can be found for example in Mei et al. (2005), only the main assumptions are summarized here. In the following we assume that the time dependency of the velocity potential can be described with one single oscillatory frequency ω, which will produce so-called *regular waves*. By using the linear boundary conditions given above, one can show that the velocity potential for regular linear waves propagating in the positive x-direction can be expressed as

$$\Phi = \frac{gA}{\omega} \frac{\cosh\left[k(z+h)\right]}{\cosh(kh)} \cos(\omega t - kx) \tag{2.9}$$

with A the wave amplitude. With this definition of Φ, the linear dynamic free surface boundary condition yields

$$\zeta = A \sin(\omega t - kx). \tag{2.10}$$

The wave frequency ω and the wave number k are linked through the so-called linear dispersion relationship

$$\omega^2 = gk \tanh(kh) \tag{2.11}$$

Equations 2.9, 2.10 and 2.11 fully define the wave kinematics that will be used to calculate the loads on linear regular waves in Section 2.3.

Note that for infinite water depth, $kh \gg 1$ and the velocity potential reduces to

$$\Phi = \frac{gA}{\omega} e^{kz} \cos(\omega t - kx) \tag{2.12}$$

and the dispersion relationship becomes

$$\omega^2 = gk. \tag{2.13}$$

2.2.3 Non-linear wave kinematics

In the previous section, the free surface boundary conditions have been linearized by Taylor expanding them around $z = 0$ and keeping only linear terms. As explained, this is consistent if the wave elevation is very small, which implies that the regular wave amplitude is also very small, $kA \ll 1$.

The waves that produce loads relevant to ULS analysis are generally too large for the assumption $kA \ll 1$ to hold. Neglecting non-linear terms in the evaluation of the boundary conditions will then lead to significant inaccuracies in the estimation of the velocity potential. In this case, it is necessary to take into account higher order terms. The higher the order of the terms retained, the more accurate the velocity potential is. However, retaining more terms makes the equations more complex.

Different theories have been derived for determining the kinematics of steep regular waves and are appropriate for different wave characteristics. Figure 2.3 shows the domain of application of the wave theories commonly used to calculate the wave kinematics depending on the wave characteristics. Non-linear wave kinematics are generally computed based on Stokes wave theory (see for example Fenton John D. 1985) or stream function wave theory (see Rienecker and Fenton 1981).

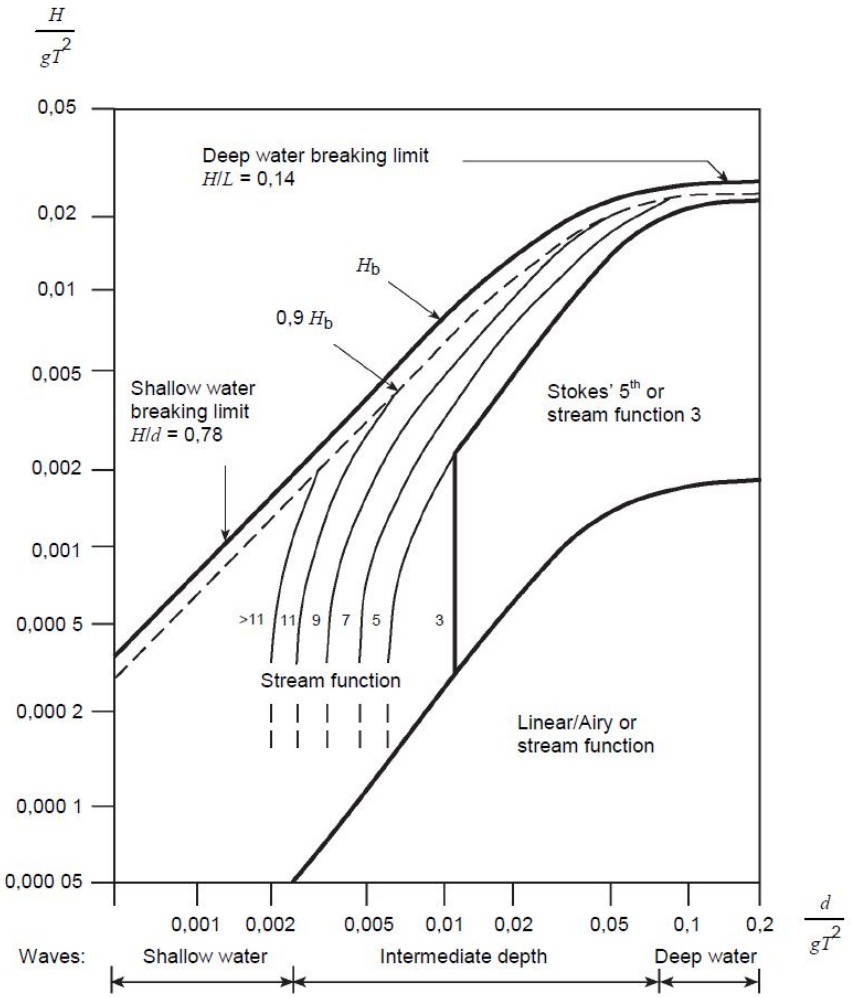

Figure 2.3: Selection of different wave theories for regular waves depending on the wave characteristics (taken from IEC-61400-3 2009). Note that in this figure, the water depth is denoted d

The following paragraphs give a non-exhaustive list of theories that have been developed to model non-linear wave kinematics.

Stoke's theory: perturbation approach

In Section 2.2.2, only the linear terms of the boundary conditions 2.3 to 2.5 defining the problem were kept. Solving the Laplace equation 2.2 for these boundary conditions yields the linear velocity potential $\Phi^{(1)}$.

If the terms of second order in the boundary conditions are kept, we obtain a new system

of equations. The solution of this new system of equations is known as the second order velocity potential $\Phi^{(2)}$. Note that the system of equations defining $\Phi^{(2)}$ is dependent on $\Phi^{(1)}$. The sum of the first and second order velocity potentials satisfies the Laplace equation and the boundary conditions to second order.

This makes it possible to obtain kinematics for regular waves with larger steepness than what linear theory would accurately describe. However, second order theory can produce nonphysical kinematics in finite water if the waves are too steep. A common way to assess whether a given wave is within the range of validity of second order theory is to use the Ursell number (Ursell 1953), defined as

$$U_r = \frac{kA}{(kh)^3}. \tag{2.14}$$

For $U_r \leq 0.33$, second order wave theory is generally considered to be valid (Dalrymple and Dean 1991).

It is in theory possible to reproduce this process and obtain velocity potentials to any order, but the equations become rapidly too complex to be of practical use. In practice, it is common to find second order and fifth order Stokes theory derivations (see Fenton John D. 1985).

Note that for irregular waves (see Section 2.2.4), it is possible to use second order theory, but to the knowledge of the author no general third order theory has been developed.

Stream function wave theory

In this thesis, a number of regular waves were modelled with the stream function implemented according to Rienecker and Fenton (1981). Similarly to what was done in Section 2.2.2, if the fluid is incompressible, it is possible to define a stream function Ψ such that the horizontal and vertical water particle velocities u and w are given by

$$u = \frac{\partial \Psi}{\partial z} \quad \text{and} \quad w = -\frac{\partial \Psi}{\partial x}. \tag{2.15}$$

If in addition the fluid is irrotational, the governing equation becomes, as in 2.2.2, the Laplace equation:

$$\frac{\partial^2 \Psi}{\partial z^2} + \frac{\partial^2 \Psi}{\partial x^2} = 0. \tag{2.16}$$

The boundary conditions can be established following the same process as in Section 2.2.2. The stream function wave theory solves the governing equation with the boundary condi-

tions for the stream function instead of the velocity potential. The problem is solved in a frame that moves at the celerity of the wave c, and the stream function is expressed as a Fourier series of finite number of terms N, such as

$$\Psi(x,z) = B_0 y + \sum_{n=1}^{N} B_n \frac{\sinh nky}{\cosh nkD} \cos nkx \tag{2.17}$$

where B_n are the Fourier coefficients of the stream function and D is an arbitrary reference level. N is called the *order* of the stream function and higher order means that the boundary conditions are solved at a higher order. Consequently, more non-linear waves require higher order in the stream function to correctly depict the wave kinematics.

This expression for Ψ is then inserted into the boundary conditions. If the water depth, the wave height and the wave period are known, and by assuming that there is no current under the wave, a solution that describes the wave kinematics as a sum of $N+1$ components can be found. Note that the first component corresponds to a constant, so for a regular wave of circular frequency ω, the highest harmonics will oscillate at $N\omega$.

Fully non-linear kinematics

Another possibility to approach non-linear waves is to solve the equations that define the problem without carrying out the linearization process described in Section 2.2.1, i.e. solving equations 2.2 to 2.5. The kinematics thus obtained are referred to as *fully non-linear*.

This approach is generally very computationally intensive and requires an empirical approach to model breaking waves, but describes very steep (non breaking) waves without making assumptions on their order. In addition, while the stream function or the Stokes wave theories higher than second order only describe regular waves, this method can be used on irregular waves.

2.2.4 Irregular waves

In the previous section, the assumption was made that the wave could be described with a single oscillatory frequency ω, producing a regular wave. In order to describe the free surface of the ocean, it is common to assume a superposition of linear regular waves, the waves thus obtained are called *linear irregular* waves. The velocity potential becomes the sum of the regular velocity potentials and can be expressed by the following equation:

$$\Phi = \sum_{n=1}^{N} \frac{gA_n}{\omega_n} \frac{\cosh\left[k_n(z+h)\right]}{\cosh(k_n h)} \cos(\omega_n t - k_n x + \epsilon_n) \tag{2.18}$$

where A_n, ω_n, k_n and ϵ_n are respectively the wave amplitude, wave frequency, wave

number and wave phase of the nth component of the irregular waves. The free surface is then given by

$$\zeta = \sum_{n=1}^{N} A_n \sin(\omega_n t - k_n x + \epsilon_n). \tag{2.19}$$

The phase angles ϵ_n are well represented by a uniform distribution between $-\pi$ and π. The amplitude of each component is given by a wave spectrum $S(\omega)$ such that

$$\frac{1}{2} A_n^2 = S(\omega_n) d\omega \tag{2.20}$$

where $d\omega$ is the difference frequency between two successive wave frequencies in the spectrum. Different spectra can be used to represent irregular wave seas. In the North Sea, it is common to use the so-called JONSWAP spectrum (see Hasselmann et al. 1973) for fully developed seas. A common definition of the JONSWAP spectrum is given in DNV-RP-C205 (2017) as

$$S_J(\omega) = (1 - 0.278 \ln \gamma) \frac{5}{16} H_S^2 \cdot \omega_P^4 \cdot \omega^{-5} \exp\left(-\frac{5}{4}\left(\frac{\omega}{\omega_P}\right)^{-4}\right) \cdot \gamma^B \tag{2.21}$$

with

$$B = \exp\left(-\frac{1}{2}\left(\frac{\omega - \omega_P}{\sigma \cdot \omega_P}\right)^2\right) \tag{2.22}$$

where $\sigma = 0.07$ for $\omega \leq \omega_P$
$\sigma = 0.09$ for $\omega > \omega_P$

Equations 2.21 and 2.22 show that this variant of the JONSWAP spectrum can be defined by three parameters: the significant wave height H_S which corresponds to the average height of the third of the waves with the highest wave height, the spectral peak period $T_P = 1/\omega_P$ which corresponds to the period containing the most energy in the spectrum and the the non-dimensional peak shape parameter γ (also called *peakedness* or *gamma factor*).

Note that the JONSWAP spectrum provides an accurate description of the waves for fully developed seas and deep water.

Wave statistics

As will be seen in Section 2.5, the standards commonly used in the design phase of offshore wind turbines recommend describing the statistical variation of the long-term wave statistics as a scatter diagram with the significant wave height H_S on the y-axis and the spectral peak period T_P on the x-axis. Each $(H_S - T_P)$ pair corresponds to a so-called *short-term wave condition*. Short-term conditions represent the wave elevation for a certain period (generally 20 minutes to 3 hours) during which the sea state can be characterized by a constant H_S and T_P and represented by a spectrum such as the JONSWAP spectrum. The $H_S - T_P$ diagram then shows the probability of occurrence of each short-term condition.

Once the $H_S - T_P$ graph has been established, it is possible to plot the *probability contours*, which show all the sea states that have a given probability of occurrence. Note that it is usual to talk about *return period* rather than probability of occurrence. For example, a 50-year return sea state will occur on average once every 50 years, and its probability of occurring within a year will be $1/50 = 0.02$.

This concept is illustrated in Figure 2.4. This figure shows the contour lines of the $H_S - T_P$ scatter diagram for the Dogger Bank Creyke Beck B site off the coast of the UK (Frimann-Dahl 2015). Here one can see the sea states with a return period of 1 and 5 years.

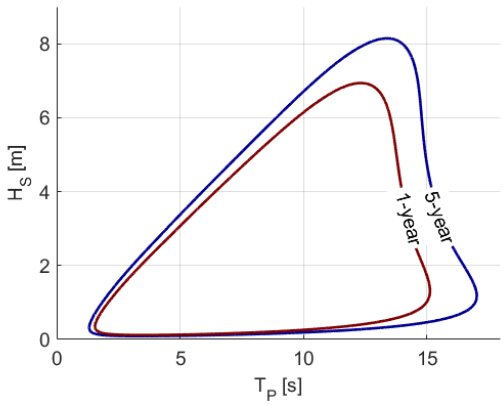

Figure 2.4: Contour plots for the Dogger Bank Creyke Beck B site

Similarly to the return period of a sea state, the return period of a wave can be defined. As will be seen in Section 2.5, it is common to use the 50-year return wave, defined by the wave with a height that will be exceeded on average once every 50 years.

It is possible to include the average wind speed in the statistical description of the sea, thus yielding a 3D scatter diagram (H_s, T_P, U). In this thesis, the turbine is considered idling, and the effects of the wind were neglected. Therefore, (H_S, T_P) scatter diagrams were sufficient to describe the long-term variations of the sea.

Embedding of a regular non-linear wave into a linear irregular wave realization

Irregular waves are generally modelled as a superposition of linear regular waves. However, as seen in Section 2.2.3, linear wave theory is generally not sufficient to depict the kinematics of steep waves, as explained in Section 2.5. In order to study the influence of a non-linear wave in irregular waves, the standards suggest inserting the kinematics of the non-linear wave into the irregular kinematics. This process is called *embedding* and was performed according to the process described in Rainey and Camp (2007).

Figure 2.5 gives an example where the surface elevation of a stream function wave is inserted into a linear irregular sea. In the area with the white background, the final solution is equal to the linear irregular wave. In the area with the yellow background, the final solution is equal to the stream function wave. To ensure a smooth transition between the linear and the non-linear wave elevation, two blending zones (with a grey background) are defined at each side of the non-linear wave.

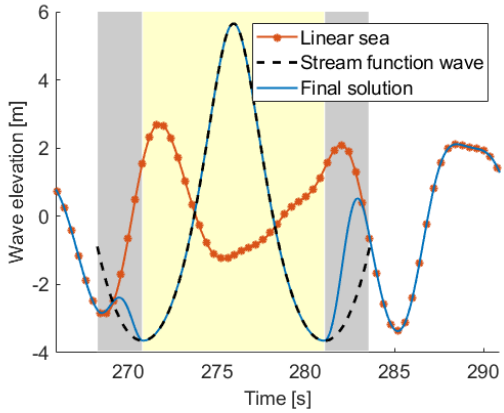

Figure 2.5: Illustration of the embedding process (following the description in Rainey and Camp 2007)

2.3 Wave loads on a surface piercing circular cylinder

Once the kinematics have been established, different models can be applied to compute the hydrodynamic loads on the structure. This section describes different models that were used throughout this thesis.

In order to select relevant theories to depict the wave kinematics, it is convenient to classify the wave conditions with two non-dimensional parameters. i) The non-dimensional water depth kh, where $k = 2\pi/\lambda$ is the wave number and h is the water depth. Sites can then be classified as having *infinite* or *finite* water depths for given waves. ii) The wave steepness kA where A is the wave amplitude, which is a good indicator of the wave non-linearity.

In addition, the non-dimensional cylinder radius can be defined as kR, where R is the cylinder radius. This parameter is especially relevant to determine the importance of the influence of the cylinder on the wave: for cylinders small compared to the wave length, the wave passes the cylinder undisturbed. For wavelength comparable to the cylinder diameter, the wave will be affected by the structure and so-called diffraction effects are to be considered. Faltinsen (1990) suggests a limit $kR < \pi/5$ to consider first order diffraction effects of importance.

2.3.1 Loads from small amplitude waves

In this section we assume deep water conditions ($kh \gg 1$) and small wave steepness ($kA \ll 1$). In these conditions, linear theory is sufficient to depict the wave kinematics. In addition, we place ourselves in the long-wavelength regime ($kR \ll 1$).

For such waves and structure dimension, it is common to use the so-called Morison equation (Morison et al. 1950) to compute the wave loads on offshore structures. The Morison equation gives the force on a section of a stationary vertical cylinder of length dz as

$$dF = \rho R C_D u(z)|u(z)|dz + \rho\pi R^2 C_M a(z)dz \tag{2.23}$$

with	ρ	the water density
	R	the cylinder radius
	C_D	the drag coefficient
	C_M	the inertia coefficient
	$u(z)$	the horizontal water particle velocity at height (z)
	$a(z)$	the horizontal water particle acceleration at height (z)

The coefficients C_M and C_D are experimentally determined and vary depending on the characteristics of the wave. It is common to refer to the first term of the equation as the *drag term* and to the second as the *inertia term*. The inertia coefficient can be split into two contributions, such as

$$C_M = 1 + C_a \tag{2.24}$$

where C_a is the added mass coefficient. The inertia term of the Morison equation can then be rewritten as

$$dF_I = \rho\pi R^2 a(z)dz + \rho\pi R^2 C_a a(z)dz. \tag{2.25}$$

The first term of equation 2.25, so-called *Froude-Krylov* force, results from the pressure from the undisturbed wave on the cylinder section. The second term is called the *added-mass* force and is due to the diffraction effects of the cylinder on the wave. If viscous effects are neglected, potential flow theory can be applied and $C_a = 1$ is obtained (Faltinsen 1990).

It is possible to account for the motion of the cylinder section into the Morison equation. In the present work, the motion of the cylinder was negligible compared to the wave kinematics and this effect is not accounted for.

In this work, the acceleration is taken as the Lagrangian derivative of the particle velocity, such as

$$a = \frac{\partial u}{\partial t} + u\frac{\partial u}{\partial x} + w\frac{\partial u}{\partial z}. \tag{2.26}$$

Note that even though linear wave kinematics are used, second order loads will appear due to the convective terms in the acceleration, and third order loads will appear due to the drag term.

Linear theory is generally not applicable when carrying out ULS analyses, but is relevant for Fatigue Limit State (FLS) analyses where waves are typically smaller. Hydrodynamic loads produced by linear waves are well understood and will not be analyzed in detail in this thesis.

2.3.2 Loads from steep waves

As explained in Section 2.2.3, linear wave theory is insufficient to describe the kinematics of steep waves. In this section, we describe four methods to compute wave loads from non-linear non-breaking waves on a circular cylinder.

1. Non-linear wave kinematics applied to the Morison equation

A common method to calculate loads on circular cylinder from regular steep waves is to compute the kinematics of the wave using a non-linear wave theory such as the stream function wave theory described in Section 2.2.3 or fully non-linear kinematics. These are then input into the Morison equation 2.23 under the assumption that the wavelength is large compared to the cylinder diameter.

2. Model from Faltinsen et al. (1995)

The FNV model was developed by Faltinsen et al. (1995) for regular waves in deep waters, and later extended to irregular waves by Newman (1996). This model is based on a perturbation approach on a small parameter ϵ, such that $kA = \mathcal{O}(\epsilon)$ (small wave steepness), $kR = \mathcal{O}(\epsilon)$ (long wavelength regime) and $A/R = \mathcal{O}(1)$.

The velocity potential is divided into a linear and a non-linear contribution, denoted ψ. The linear contribution is equal to the sum of the linear incident potential derived in Section 2.2.2 and the linearized scattered potential derived by MacCamy and Fuchs (1954), and presented for example in Sarpkaya (2010). The non-linear potential ψ is of third order in terms of ϵ and satisfies the free-surface boundary conditions approximated to third order.

The excitation loads are then obtained by integrating the pressure term of the Bernoulli equation along the cylinder. This has the two following implications:

- as opposed to computing the loads from the Morison equation and non-linear wave kinematics, the loads from the FNV model will include long wavelength diffraction effects
- the model includes all loads due to the the velocity potential up to third order, but will miss some higher order loads. For example, loads due to the fourth order incident potential will not be included. Therefore, loads of order higher than three that result from the pressure integration are disregarded. The model is said to be *consistent to third order*

The hydrodynamic loads as calculated by the FNV method are given in Newman (1996) by the following equation: $F_{FNV} = F^{(1)} + F^{(2)} + F^{(3)} + F^{\psi}$ with

$$F^{(1)} = 2\pi\rho R^2 \int_{-\infty}^{0} u_t(z)dz \tag{2.27}$$

$$F^{(2)} = 2\pi\rho R^2 u_t|_{z=0}\zeta^{(1)} + \pi\rho R^2 \int_{-\infty}^{0} \left(2w(z)w_x(z) + u(z)u_x(z)\right) dz \tag{2.28}$$

$$F^{(3)} = \pi\rho R^2 \left[\zeta^{(1)} \left(u_{tz}\zeta^{(1)} + 2ww_x + uu_x - \frac{2}{g}u_t w_t\right) - \left(\frac{u_t}{g}\right)(u^2 + w^2)|_{z=0}\right] \tag{2.29}$$

$$F^{\psi} = \pi\rho\frac{R^2}{g}u^2 u_t|_{z=0}\beta\left(\frac{h}{R}\right) \tag{2.30}$$

with
	ρ	the water density
	R	the cylinder radius
	u, v	the horizontal and vertical first order velocity components
	$\zeta^{(1)}$	the first order wave elevation

Subscript indicates differentiation. β is given by

$$\beta\left(\frac{h}{R}\right) = \int_0^{h/R} \left(3\Psi_1(Z) + 4\Psi_2(Z)\right) dZ \tag{2.31}$$

with Ψ_1 and Ψ_2 defined in Newman (1996). Note that in deep water, $\beta = 4$.

The force $F^{(1)}$ is of first order (i.e. proportional to ϵ) and equivalent to the inertia term of the Morison equation with $C_M = 2$. The force $F^{(2)}$ is of second order (proportional to ϵ^2). The first term of $F^{(2)}$ in equation 2.28 corresponds to the linear potential integrated from the mean water level to the first order wave elevation. The second term corresponds to the quadratic term of the Bernoulli equation integrated from the sea bed to the mean water level. The force $F^{(3)}$ is of third order and due to the linear potential and includes the static pressure integrated up to second order wave elevation. The force F^{ψ}, also of third order, results from the non-linear velocity potential.

Even though the FNV was initially developed for infinite waters, an attempt was made in P1 and P2 to adapt it to finite waters, by bringing the following three modifications:

- the wave kinematics were computed using the finite water velocity potential
- the finite water dispersion relationship was used
- the lower limit of the integral in terms $F^{(1)}$ and $F^{(2)}$ was taken as $-h$ instead of $-\infty$

This modification of the FNV presents two main sources of inaccuracies. First, the original equations were developed assuming the infinite depth velocity potential as described in equation 2.12. Therefore there is no mathematical basis for using finite water wave kinematics and the finite depth dispersion relationship. Second, the incident potential used to derive the FNV equations is linear. In deep water, the higher order incident potentials are not significant and can be neglected, but in intermediate water they contribute to the incident potential. This influence is not accounted for by the attempted modification of the FNV. Kristiansen and Faltinsen (2017) showed that in shallow waters, at the third harmonic, the loads due to the third order incident potential are the dominant contribution to the total load, which shows that the higher order potential cannot be neglected.

3. Model from Kristiansen and Faltinsen (2017)

The FNV model for infinite waters presented in the previous section was generalized to finite waters by Kristiansen and Faltinsen (2017), hereafter referred to as KF model. This model is also based on a perturbation approach on ϵ and assumes $kA = \mathcal{O}(\epsilon)$ (small wave steepness), $kR = \mathcal{O}(\epsilon)$ (long wavelength regime) and $A/R = \mathcal{O}(1)$. The excitation loads from the KF method are given by

$$F_{KF} = \int_{-h}^{\eta} F'(z,t)dz + F^{\psi}. \tag{2.32}$$

F' is a distributed load given by

$$F'(z,t) = \rho\pi R^2 \left(\frac{\partial u}{\partial t} + u\frac{\partial u}{\partial x} + w\frac{\partial u}{\partial z} \right) + m_a \left(\frac{\partial u}{\partial t} + w\frac{\partial u}{\partial z} \right) \tag{2.33}$$

where $m_a = C_a \rho\pi R^2$ is the added mass in surge with C_a the added mass coefficient. The point force F^ψ does not change compared to the infinite water case and is

$$F^\psi = \rho\pi R^2 \frac{4}{g} u^2 \frac{\partial u}{\partial t}. \tag{2.34}$$

Note that F^ψ is calculated with the kinematics taken at the MSL and applied at the MSL.

As opposed to the deep water case, the non-linear incident potentials must now be considered. As stated by Kristiansen and Faltinsen (2017), the loads produced by the KF model are consistent up to third order if kinematics of at least third order are used. It should be noted that the scattered potential is correct only up to third order. This means that fourth order loads resulting from these formulae (for example from a fourth order incident potential) will be incomplete since they will miss the contribution of the scattered potential. Therefore the model is not consistent to orders higher than three.

By applying the KF model to a large number of regular waves with varying heights and steepnesses, Kristiansen and Faltinsen (2017) showed that the contribution of the third order incident potential, which is negligible in deep water, becomes dominant in shallow water. On the contrary, the influence of the F^ψ term decreases with decreasing water depth.

4. Model from Rainey (1989)

Rainey (1989) developed a model to calculate loads on a slender surface-piercing body based on energy balance arguments. For a vertical circular cylinder, his model reduces to the inertia term of the Morison equation as presented in Section 2.3.1 with two additions. The first addition accounts for the fact that the cylinder is not slender in its axial direction (Manners and Rainey 1992) by adding the term

$$m_a u \frac{\partial w}{\partial z}. \tag{2.35}$$

The second addition corresponds to a point force at the free surface to account for the change in fluid kinetic energy due to the variation in time of the submerged portion of the cylinder (corresponding to equation (7.4) in the original paper by Rainey 1989). This force is given by

$$F^{\eta} = -\frac{1}{2} m_a u^2 \frac{\partial \eta}{\partial x}. \tag{2.36}$$

The point force F^{η} is calculated with the kinematics taken at the free surface elevation and applied at the free surface elevation.

2.3.3 Loads from breaking waves

For calculating slamming loads on slender structures, it is common to use the model developed by Wienke and Oumeraci (2005), so called *Wienke model*. This model consists of adding a slamming load F_{slam} to the Morison equation, defined by

$$F_{slam} = C_S \rho R c^2 \lambda_c \zeta_m \tag{2.37}$$

with
- C_S the slamming coefficient
- c the celerity of the wave
- λ_c the curling factor
- ζ_m the maximum wave elevation for the slamming event

The curling factor λ_c defines the portion of the wave that is impacting the cylinder, therefore $\lambda_c \zeta_m$ indicates the height over which the impact is assumed to happen. Based on experimental data, Burmester et al. (2017) found values of λ_c varying between 0.28 and 0.56 depending on the type of breaking wave and the characteristics of the bottom. For irregular waves on a flat sea bed, they report $\lambda_c = 0.28$.

Defining $t = 0$ as the time of impact of the wave on the cylinder, the slamming coefficient is defined as

$$C_S = \cos\alpha \left[2\pi \cos(\alpha) - 2\sqrt{\cos(\alpha)\frac{c}{R}t} \cdot \tanh^{-1}\left(\sqrt{1 - \frac{1}{4}\frac{1}{\cos\alpha}\frac{c}{R}t} \right) \right] \quad \text{for } 0 \le t \le \frac{1}{8}\frac{1}{\cos\alpha}\frac{R}{c} \tag{2.38}$$

$$C_S = \cos\alpha \left[\pi\sqrt{\frac{1}{6}\cos\alpha\frac{R}{ct'}} - \sqrt[4]{\frac{8}{3}\cos\alpha\frac{c}{R}t'} \cdot \tanh^{-1}\left(\sqrt{1 - \frac{c}{R}t'\sqrt{\frac{6}{\cos\alpha}\frac{c}{R}t'}} \right) \right] \quad \text{for } \frac{3}{32}\frac{1}{\cos\alpha}\frac{R}{c} \le t' \le \frac{12}{32}\frac{1}{\cos\alpha}\frac{R}{c} \text{ with } t' = t - \frac{1}{32}\frac{1}{\cos\alpha}\frac{R}{c} \tag{2.39}$$

with α the angle between the water surface and the axis of the cylinder as shown in Figure 2.6 and c the wave celerity.

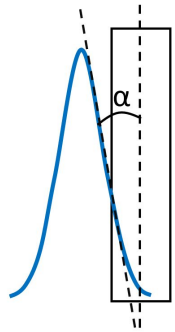

Figure 2.6: Illustration of the angle α

2.4 Response of a surface piercing circular cylinder

Once the loads on the structure have been determined, it is necessary to calculate the response of the structure to these loads.

2.4.1 Dynamic amplification

It is important to have a correct description of the structure because of the dynamic nature of the system. The characteristic time of variation of several aerodynamic and hydrodynamic loads applied to wind turbines is within the order of magnitude or smaller than the eigenperiods of the system, therefore dynamic effects can amplify the response of the structure.

The *dynamic load factor* (DLF, also referred to as *dynamic amplification factor* in the literature) is defined as the ratio of the response of a system to a given time-varying load over the response the system would have if a load of same magnitude was applied in a static manner (Biggs 1964). For transient loads, it is common to compute the DLF using the largest response and dividing it by the static response. This is denoted DLF_{max}.

Figure 2.7 illustrates this concept: a one degree of freedom system of eigenperiod T_1 is subjected to a triangular impulse load of duration t_d. The response of the system is computed and the DLF is calculated based on the maximum response and the characteristic load F. This procedure is repeated for varying load durations and DLF_{max} is plotted for each t_d.

Different load shapes will give different DLF_{max} curves (Biggs 1964), however some general results can be drawn from Figure 2.7:

- the highest DLF_{max} corresponds to a load with a duration close to the eigenperiod

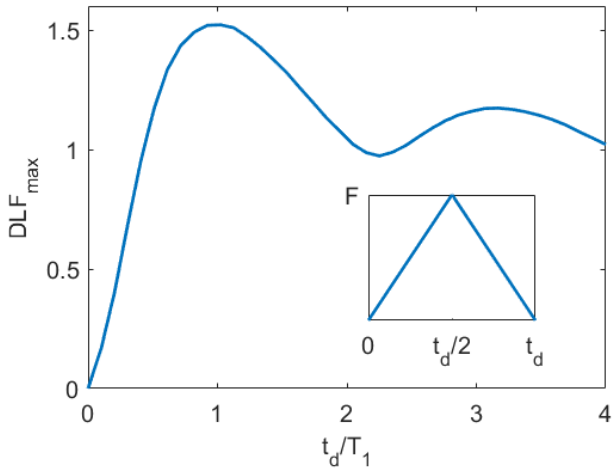

Figure 2.7: Maximum response of a one degree of freedom system depending on the duration of a triangular impulse load. The shape of the load is given in the box within the graph.

of the system

- for a given amplitude, a load with a very short duration compared to the eigenperiod of the system will not produce significant response

2.4.2 Structural models

Different structural models have been used throughout this thesis to compute the response of the structure. The details of these models are given below, while their validation is given in Appendix B.1.

Single degree of freedom equation

For systems that can be defined with a single degree of freedom, it is common to calculate the response with a single degree of freedom equation. Here we take the example of a system that oscillates around an axis x. Its position in time is determined by an angle $\theta(t)$. If the excitation moment $M_{exc}(t)$ is known, the equation of motion derived from Newton's second law is then

$$M_{exc}(t) = I\ddot{\theta}(t) + B\dot{\theta}(t) + C\theta(t) \tag{2.40}$$

with I the moment of inertia around x
B the damping coefficient
C the stiffness

The dot over a variable means differentiation with respect to time. Note that I, B and C are here assumed to be constant. If the initial conditions $\theta(0)$ and $\dot{\theta}(0)$ are known, the equation can be solved and the response of the system can be found.

Mode shape solver

For a system with multiple degrees of freedom, it is possible to decompose the response into the response of each of the eigenmodes of the system. For example, the deflection Ψ_d of a structure slender in the vertical direction can be assumed to be the sum of the deflections of each individual mode, such as

$$\Psi_d(z,t) = \sum_{n=1}^{N} \psi_n(z)\xi_n(t) \tag{2.41}$$

with ψ_n the mode shape of the n$^{\text{th}}$ mode
ξ_n the modal displacement of the n$^{\text{th}}$ mode
N the number of modes considered

Note that the more modes are considered, the more accurate the response will be. The modal displacement for each mode is determined solving the single degree of freedom equation with:

$$f_n = m_n\ddot{\xi}_n + b_n\dot{\xi}_n + c_n\xi_n \tag{2.42}$$

with f_n the modal excitation for the n$^{\text{th}}$ mode
m_n the modal mass for the n$^{\text{th}}$ mode
b_n the modal damping for the n$^{\text{th}}$ mode
c_n the modal stiffness for the n$^{\text{th}}$ mode

The modal mass and the modal stiffness are given by the following equations:

$$m_n = \int_l m(z)\left[\psi_n(z)\right]^2 dz \tag{2.43}$$

$$c_n = \int_l EI(z)\left[\frac{\partial^2\psi_n(z)}{\partial z^2}\right]^2 dz \tag{2.44}$$

with $m(z)$ the linear mass at height z
E the Young's modulus
l the length of the structure

To obtain the modal damping, the damping ratio for each mode shape η_n is measured from decay tests on the physical model. The modal damping for mode n is then computed as

$$b_n = 2\eta_n\sqrt{m_n c_c}. \tag{2.45}$$

For slender structures, the modal excitation for each mode is obtained by integrating the product of the excitation force times the mode shape over the length of the structure.

$$f_n = \int_l F(z)\psi_n(z)dz \tag{2.46}$$

where F is the hydrodynamic excitation load.

Once the deflection Ψ_d has been calculated, the response is obtained with the Euler-Bernoulli beam equation. The response bending moment is given by

$$M(z,t) = EI\frac{\partial^2\Psi_d(z,t)}{\partial z^2}. \tag{2.47}$$

Note that to obtain accurate responses, a higher number of mode shapes is required for moments than for displacements.

Finite element method

Another way to compute the response of a structure is to discretize the structure into a number of elements and establish the equations of motion of each of the elements. These equations are then assembled into a system of equations that represents the whole structure. Solving this system gives the response of each element of the model. Using finite element models generally implies having a large number of elements compared to the number of modes in a mode shape solver. This increases the computational time and the accuracy of the solution.

In this thesis, the finite element software Ashes, specialized in simulation of wind turbines, was used (Thomassen et al. 2012).

2.5 Design process for bottom-fixed offshore wind turbines

Within the offshore wind industry, it is common to use the DNV-RP-C205 (2017), DNV-OS-J101 (2014) and IEC-61400-3 (2009) standards when designing bottom-fixed offshore wind turbines in the North sea. These standards typically suggest to carry out simulations with different sets of environmental and operational conditions (called design load cases, denoted DLC). These load cases aim at simulating all the critical conditions a wind turbine will experience during its lifetime. A safe design of the structure must therefore withstand all load cases.

In this thesis, special attention is brought to DLC6.1, as this load case was identified by de Ridder et al. (2017) as driving the design for the experiments analyzed in P3 and described in Section 3.2. The objective of using DLC6.1 is to design the wind turbine so that it withstands the largest response it will experience over a 50-year period, so-called the *50-year response* (DNV-OS-J101 2014).

To calculate the largest response over a 50-year period, the standard IEC-61400-3 (2009) suggests simulating the environmental conditions that have a 50-year return period and taking the largest response as the 50-year response. It should be noted that the 50-year response does not necessarily occur during the 50-year return environmental conditions, but this process is generally used to assess DLC6.1. In the following, we refer to the largest response occurring during the 50-year environmental conditions as the 50-year response. Note that under these conditions, the rotor of the turbine will be idling, which means that the blades will not be facing the wind. This drastically reduces the aerodynamic loads and aerodynamic damping. In the rest of the thesis, it is assumed that the aerodynamic loads on idling rotors can be neglected.

To define the 50-year environmental conditions, it is common to use the scatter diagram as defined in Section 2.2.4. In principle, the most accurate way to calculate the 50-year response is to simulate all environmental conditions with a 50-year return period, but as most of these sea states will not produce large responses of the structure, it is common to select only the most unfavourable sea state (Naess and Moan 2012). A stationarity period is then assumed, usually 3 hours, and a random realization of that sea state for this duration is carried out. However, this approach poses the following problems: i) since the response from very steep waves is studied, the kinematics used must be non-linear. Non-linear methods for obtaining irregular wave kinematics are computationally intensive (see Section 2.2.3). ii) It can be inefficient to simulate 3 hours of environmental conditions since the largest response will by definition happen only once, often for the most extreme wave.

To tackle these issues, the approach suggested by IEC-61400-3 (2009) is to establish the largest expected wave for the given 50-year sea state by assuming a certain distribution for the wave heights. Two common distributions are the Rayleigh distribution and the Battjes and Groenendijk distribution (Battjes and Groenendijk 2000). Once the largest expected wave of the 50-year return sea state has been established, its kinematics are calculated

with a non-linear wave theory and embedded in a 10-minute linear realization of the sea state at a random instant. With this method, the simulation time is drastically reduced and includes the largest expected wave.

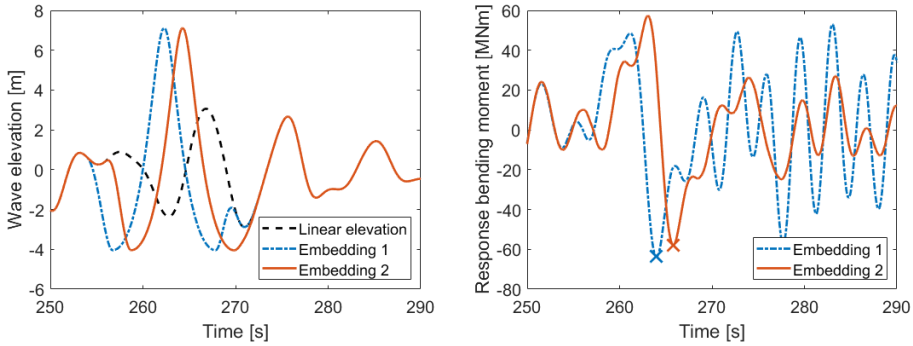

(a) Wave elevation **(b)** Responses

Figure 2.8: Illustration of the embedding procedure at two different time instants. The maxima of the responses is marked with an 'x'

With this method, however, the largest simulated response over the 10-minute time series will be dependent on the time of embedding because of the time history of the response. Figure 2.8 shows the embedding procedure for a given 50-year return wave modelled with the stream function wave theory embedded into a given linear realization of a 50-year return sea state at two different instants. As can be seen in Figure 2.8(b), the difference in time of embedding produces a response magnitude 10% larger for the first case compared to the second.

To address this issue, 20 realizations of the linear sea state are generated and the 50-year wave is embedded in each of them. The average of the 20 maxima thus obtained is taken as the 50-year response. The process, as suggested by IEC-61400-3 (2009), is performed through the following five steps:

1. Establishing the characteristics of the 50-year return sea state and the 50-year return wave at the site based on available metocean data.
2. Carrying out 20 realizations of the extreme sea state with different seeds. Each realization is a superposition of linear regular waves.
3. In each of the 20 realizations, embedding a 50-year wave. The kinematics of the wave are calculated with the stream function theory (see Section 2.2.3) and the order of the stream function wave depends on the wave and site characteristics as described in Figure 2.3.
4. Simulating the response of the structure. The hydrodynamic loads are calculated with the Morison equation. For breaking waves, the slamming loads are calculated with Wienke's model (Wienke and Oumeraci 2005).

5. Averaging the maximum responses obtained for each of the twenty realizations.

The average of the maximum responses is then taken as the driving response for DLC6.1. This process is summarized in Figure 2.9.

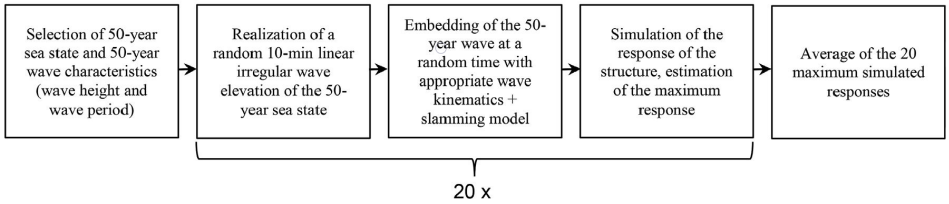

Figure 2.9: Procedure for estimating the 50-year response, according to IEC-61400-3 (2009).

Note that in step 3, the time of embedding has to be such that the transients due to the start of the simulation have died out. In this thesis, a period of 60 seconds was added at the beginning of all simulations during which the stream function was not embedded for any of the realizations.

Chapter 3

Model testing of monopile bottom-fixed offshore wind turbines

Within the work carried out in this thesis, the data recorded during three experimental campaigns has been analyzed. The first one of these three campaigns was carried out at the 'Lilletanken' wave flume at the Norwegian University of Science and Technology (NTNU)/Sintef Ocean facilities. The second one was carried out within the Wave Impact on Fixed turbines Joint Industry Project (WiFi project, see de Ridder et al. 2017). The last experimental campaign was carried out within the Wave Loads project (Bredmose et al. 2013a). These three experimental campaigns are referred to as the *NTNU*, the *WiFi* and the *Wave Loads* experimental campaigns, respectively.

The structures that have been studied in these campaigns have been models of idling bottom fixed wind turbines with rated powers between 4 and 6 MW. Table 3.1 summarizes the main structural characteristics of the three models that have been experimentally tested (detailed information about the experimental campaigns is given in the following subsections). Note that the model for the NTNU campaign was attempted to be built as a one degree of freedom system. For that purpose, a stiff cylinder was mounted on a rotational spring, which explains the high frequency of the second mode. This frequency is not representative of full scale wind turbines, and the damping ratio at that mode was not measured. More details are provided in Section 3.1.

Damping levels For all the environmental conditions analyzed in the presented experimental campaigns, it was assumed that the wind speed is above the cut-out limit, meaning that the blades will be pitched into the wind and the rotor will be idling or parked. In order to validate the damping levels used in the experimental campaigns, data from full-scale

Table 3.1: Range of characteristics of the different models used in the thesis. Values are given in full-scale

		NTNU	WiFi	WaveLoads
Scale [-]		48	30.6	80
Diameter at the mean sea level [m]		6.9	5.8	6
Tested water depths [m]		20.9, 30	27	20.9, 31, 40.8
First mode	Eigenfrequency [Hz]	0.26	0.29	0.28
	Damping ratio [%]	2.4	1.1	1.7
Second mode	Eigenfrequency [Hz]	11.5	1.21	2
	Damping ratio [%]	-	1.1	2.7

offshore turbines were analyzed.

Table 3.2 summarizes the damping ratios reported in five papers for turbines with similar characteristics and in the same conditions as the one used in the experimental campaigns. In all the cited work, the damping ratio was established from measuring the response of the turbine after a rotor stop sequence. At the beginning of such a sequence, the turbine is operating. At a given time, the blades are pitched towards the wind and the brakes are applied onto the main shaft. This will stop the rotor from rotating and provoke the structure to oscillate in its first mode (Damgaard et al. 2013). By analyzing the oscillations in the response and establishing the logarithmic decrement, it is possible to determine the damping ratio of the turbine.

Table 3.2: Damping ratios measured on full-scale offshore wind turbines

Source	Damping ratio [%]
Damgaard et al. (2013)	2.4 - 2.5
Damgaard and Andersen (2012)	2.25
Devriendt et al. (2014)	1.86
Shirzadeh et al. (2015)	1.7 - 2.8
Versteijlen et al. (2011)	3

The damping ratios used within the experimental campaigns are within the lower end of the damping ratios range given in Table 3.2. This means that the responses measured during the experimental campaigns will decay more slowly than for full-scale wind turbines.

Assumptions Consistently with the scope of the thesis, some assumptions were made in all three experimental campaigns:

- Froude scaling
- the aerodynamic loads can be neglected because the blades are pitched into the wind. Therefore no rotor was modelled, and no wind was applied to the models

- no action from the controller was modelled
- no geotechnical modelling was implemented. The models were fixed at their lower end, except for the NTNU test, where the model was pinned at its lower end (see 3.1)
- long-crested waves. The waves are assumed not to vary in the direction perpendicular to their propagation
- no current

3.1 NTNU experimental campaign

The data from this experimental campaign was used in P1 and P2. More information about the experimental campaign can be found in these papers,

Experimental set-up

This experimental campaign was carried out between April and May 2015 in the small wave flume of the NTNU/Sintef Ocean facilities. This flume, illustrated in Figure 3.1, is 28 m long and 2.5 m wide with a constant water depth. One end of the flume was equipped with a piston-type wave maker, consisting of a flat plate forced into translational motion by an electric actuator. At the other end, an absorbing parabolic beach consisting of a perforated plate was fitted in order to reduce wave reflection. The highest part of this beach was a few centimeters above the mean sea level, and the height of the beach was adjusted when the water depth was changed. A number of capacitance wave gauges, marked in red in Figure 3.1, were placed in the flume to measure the wave elevation. The wave gauges were calibrated every 48 hours to account for changes in the water temperature or other unknown changes that could affect the set-up.

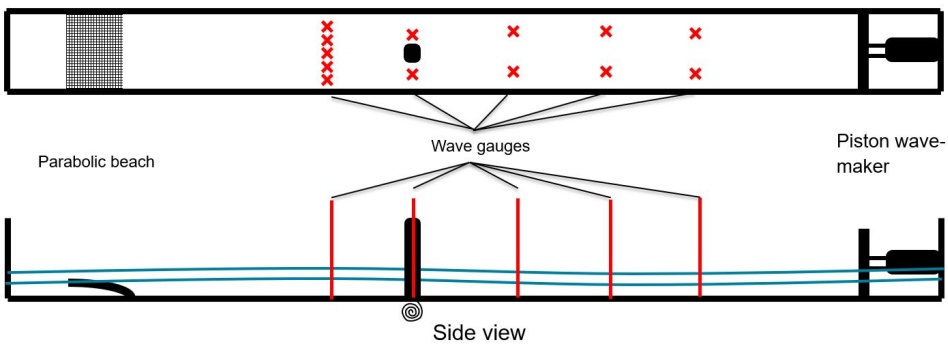

Figure 3.1: Experimental set-up of the NTNU campaign

Model

At about 15 m from the wave maker, a pit was constructed in which the model was placed. This paragraph gives the characteristics of the model, in full-scale values unless otherwise specified. The model, illustrated in Figure 3.2 consisted of a 1:48 representation of an offshore wind turbine. It was a stiff (i.e. rigid) cylinder with a 6.9 m diameter and a 0.28 mm thickness. A mass of 557 t was placed on top of the cylinder to obtain an eigenfrequency representative of a full-scale offshore wind turbine. Note that for practical reasons, the height of the model (1.54 m model scale, 73.9 m full scale) was significantly smaller than that of a full scale turbine, therefore the top mass was significantly larger than typical values of a full scale turbine. A series of decay tests were conducted on the model, for different water depths and in dry conditions. For the data presented in this thesis, the full-scale first wet eigenfrequency was found to be $f^{(1)}_{NTNU} = 0.26$ Hz (1.78 Hz model scale) and the damping ratio was 2.4 % of the critical damping. The second eigenfrequency was obtained through hammer tests and found to be around $f^{(2)}_{NTNU} = 11.5$ Hz (80 Hz in model scale).

The model was held onto the bottom of the pit by a rotational spring which blocked all degrees of freedom except for pitch. The spring was mounted onto a force and moment transducer. Two accelerometers measured the accelerations at the top, in the longitudinal and traversal directions of the flume.

An attempt was made to study the influence of damping on the response by adding an adjustable damper. However, during the experiments where this damper was used, the rotational spring became damaged, rendering the results unusable.

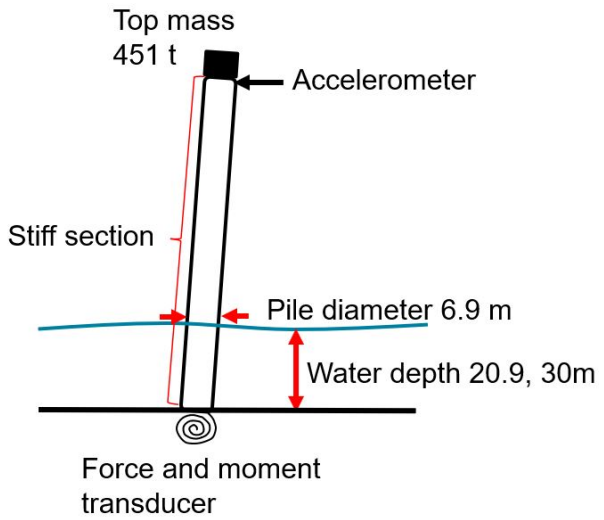

Figure 3.2: Model used during the NTNU experimental campaign

Environmental conditions

Two water depths were tested, at 20.9 m and 30 m in full scale (0.435 m and 0.625 m model scale). A large number of regular and irregular waves were tested, but only results from irregular waves are presented here. Eight sea states were tested for each water depth, corresponding to a combination of two significant peak periods $T_P = (15, 11.25)$ s with fours significant wave heights $H_S = (9.04, 8.22, 7.69, 6.71)$ m. All the sea states were realized following a JONSWAP spectrum with a spectral peak shape $\gamma = 3.3$. The waves were calibrated by removing the model and running the tests. A high level of repeatability was found for the wave elevation.

Limitations

- the mode shape of this model does not correspond to that of a wind turbine. For a full-scale wind turbine, most of the motion occurs on the higher part of the structure, while the displacement at the MSL is significantly smaller. This is not correctly captured by the present model, which will experience large displacements at the MSL. This will produce more radiated waves than a full scale turbine.

- as no second or higher modes are modelled, the influence of these modes on the response is not accounted for.

3.2 WiFi

This experimental campaign was carried out in the context of the Wave impact on Fixed foundations (WiFi) Joint Industry Project (WP3), where the objective was "to increase the understanding of breaking and steep wave impact's on fixed foundations of offshore wind turbines." (de Ridder et al. 2017). The data from these experiments were used in P3 and P4.

Experimental set-up

The experimental campaign was carried out in the shallow water basin at the Maritime Research Institute Netherlands (MARIN). This tank, illustrated in Figure 3.3, is 220 m long and 15.8 m wide with a flat bottom. It is equipped with a parabolic absorbing beach at one end to minimize wave reflection and a piston-type wave maker at the other end. The waves were generated following the second order wave generation technique presented in Schäffer (1996) to correct for the difference between the oval motion of the water particles in intermediate water and the horizontal motion of the piston. Two pits were dug into the ground and two models were mounted onto two 6-component force frames that measured the response of the models.

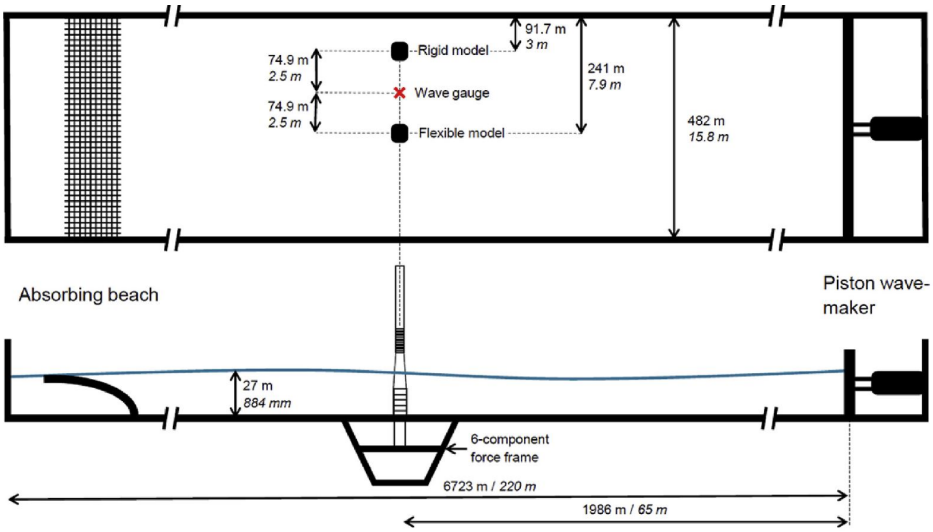

Figure 3.3: Experimental set-up of the WiFi experimental campaign

Model

Two models were used to produce the data used in this work. The models are a flexible and a stiff representation of a 4 MW wind turbine mounted on a monopile at a 1:30.6 scale. The two models are presented in the following paragraphs. All values are given full-scale, unless otherwise specified.

Flexible model: the fully flexible model was composed of two cylindrical sections of 5.5 m and 7 m, respectively, linked through a conical section which gave a diameter at the MSL of 5.8 m (see Figure 3.4). The model extended 10.1 m below the sea bed at a water depth of 27 m and reached a height of 87 m above the MSL. Special effort was put into achieving similar first and second eigenfrequencies and first mode shape as the full-scale model. For that purpose, a top mass of 276 t (9.5 kg model scale) was placed on top of the structure to model the RNA, and some sections of the cylinder were partially cut transversely to reduce their stiffness. The first and second eigenfrequencies thus obtained were $f_{WiFi}^{(1)} = 0.29$ Hz and $f_{WiFi}^{(2)} = 1.21$ Hz. Figure 3.5 shows the targeted mode shapes (i.e. the mode shapes of the full-scale turbine) and the obtained mode shapes (i.e. the mode shapes of the model).

Stiff model: the stiff model had the same diameter and conical section as the flexible model but only extended up to the expected maximum wave run-up. The goal of having a stiff model was to be able to measure the excitation loads. For that purpose, the first eigenfrequency of the structure should be as high as possible. In practice, the achieved eigenfrequency was 1.8 Hz.

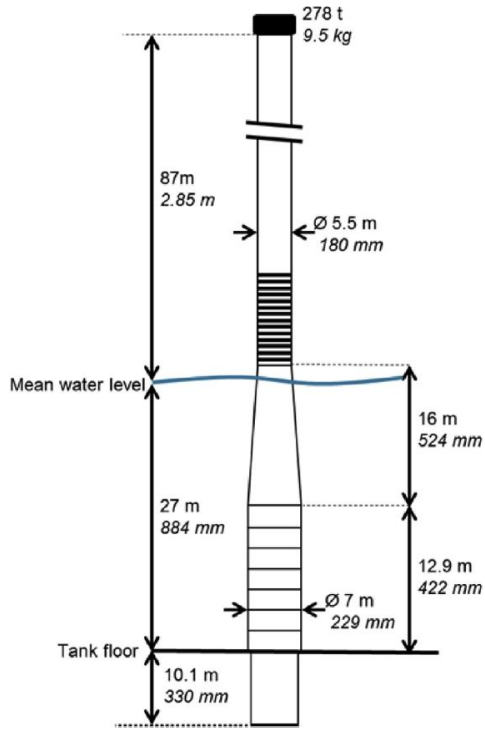

Figure 3.4: Model used during the WiFi experimental campaign

The wave elevation and the bending moments at the bottom of the structure for both models were measured. In addition, video cameras recorded the complete experimental campaign.

Environmental conditions

A large number of wave conditions were produced during this campaign, including regular waves, focused waves and irregular waves. Only the data produced during the irregular wave tests are analyzed in this thesis. All the irregular sea states were generated following a JONSWAP spectrum with a spectral peakedness factor of 3.3. The characteristics of the sea states are given in Table 3.3.

Limitations

- as seen in Figure 3.5, the discrepancies between the targeted and obtained second mode shapes at the top were significant. This had little influence on the response to hydrodynamic loads.
- the modes higher than second were not tuned to match those of the full-scale turbine. Therefore, the influence of those higher modes was not representative of the full-scale situation

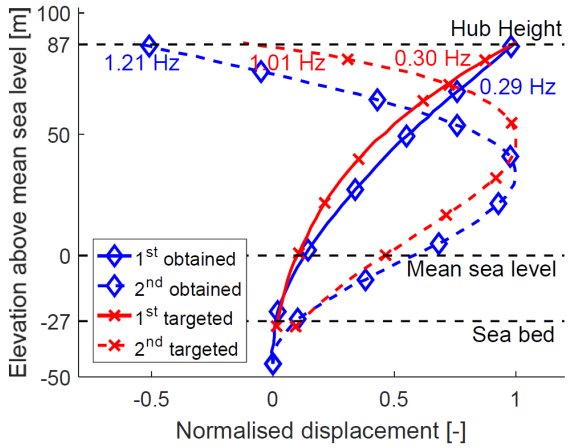

Figure 3.5: Dimensionless mode shapes. Blue colour represents the obtained mode shapes and red colour represents the targeted ones.

Table 3.3: Characteristics of the sea states from the WiFi experimental campaign used in this thesis

H_S [m]	T_P [s]
3.5	8.5
5.81	10.93
5.89	10
6.18	10
5	8.5
6.5	10
9	13
9	11

- the eigenperiod of the stiff model was relatively high compared to the duration of a slamming event. This means that the dynamic response of the stiff structure will be visible during wave breaking events.
- the mildest sea states presented in Table 3.3 did not correspond to extreme storms. In these conditions, it is likely that the turbine is not idling but rather operating. The assumption that aerodynamic loads are not significant might therefore not hold.
- no wave measurements without the structure were available. The wave elevation used for the numerical models was taken from a wave gauge placed 13 diameters away from the models and it was assumed that the influence of the models at that location was not significant and that the waves were long-crested.

3.3 Wave Loads Project

This experimental campaign was carried out as part of the Wave Loads Project (Bredmose et al. 2013a) and the data it produced have been used in P5 as well as in other research such as Bredmose et al. (2013b) or Robertson et al. (2016).

Experimental set-up

The experiments were carried out at the shallow water basin of DHI Denmark. The dimensions of the experimental set-up are given in Figure 3.6. This basin was equipped with a piston wave maker on one side and an absorbing rock berm on the other side to minimize wave reflection. A 1:25 slope was fixed onto the bottom, on which the structure was mounted. More information on the experimental set-up can be found in the Wave Loads project report (Bredmose et al. 2013a).

Model

A fully flexible model was used in this campaign, representing the NREL 5 MW wind turbine (Jonkman et al. 2009) at a 1:80 scale. The main characteristics of the model are given in full scale (unless specified otherwise). The model was a cylinder of constant diameter of 6 m, with two point masses of about 937 t (1.78 kg in model scale) added 87 m and 128.6 m above the sea bed (108.75 cm 160.75 cm, respectively). The two first eigenfrequencies of the model were $f_{WL}^{(1)} = 0.28$ Hz and $f_{WL}^{(2)} = 2.0$ Hz. More information about the model can be found in Robertson et al. (2016).

A stiff model was also used during the experimental campaign, but the data measured on the stiff model were not used in this thesis.

Environmental conditions

In the tests used in this thesis, three water depths were considered, at 40.8 m, 31 m and 20.9 m. At each depth, two irregular sea states were generated following the JONSWAP spectrum, defined by ($H_S = 8.3$ m; $T_P = 12.6$ s) and ($H_S = 11$ m; $T_P = 14$ s), respectively. Both sea states had a spectral peakedness factor of 3.3.

Limitations

- as for the WiFi experimental campaign, the modes higher than second were not tuned to match those of the full-scale turbine. Therefore, the influence of those higher modes is not representative of the full-scale situation
- the slope of 1:25 is larger than typical values (around 1:1000, see Bredmose et al. 2013a), which will create more plunging-type breaking waves. This can increase the number of events with a large excitation of the second mode.

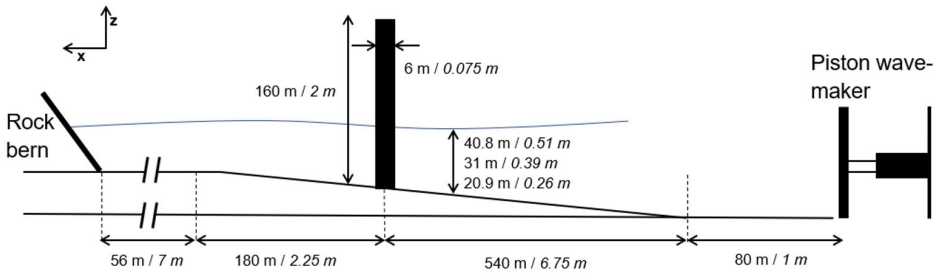

Figure 3.6: Set-up of the Wave Loads experimental campaign

Chapter 4

Dynamic response analysis of monopile bottom-fixed offshore wind turbines

This chapter lists the main findings from the thesis. For all the experiments in chapter 3, the general approach has consisted of two steps:

- Analyze the measured data, to describe the relative importance of different phenomena and hypothesize as to what causes them
- Compare the measurements with numerical simulations, to assess how different numerical models perform when predicting the structural responses.

For the NTNU and WiFi campaigns, the bending moment at the sea bed was measured, while for the Wave Loads campaign, the shear force at the sea bed was measured. For simplicity, we refer to both these measurements as *response* in the following sections.

4.1 Experimentally determined response to steep and breaking waves

For all experimental campaigns, significant first mode response was observed even in non-extreme waves. This was attributed to a springing-type of response. During the campaigns, it was observed that ringing produced larger responses than springing. However, the springing response prior to a ringing event will affect the maximum response depending on the phasing of the prior response and the ringing event (P1): if the structure is

pitched towards an incoming wave that will produce ringing response, the springing and the ringing responses will add-up. In the other extreme, if the structure is pitched away from the wave, the springing response will cancel part of the ringing response. The latter situation is referred to as *non-additive* or *favorable* by Bachynski et al. (2017) and the former is referred to as *additive* or *unfavorable*.

The analysis of the measured response produced during the Wave Loads experiments (P5) showed that for waves producing low responses, the amplitude of the response is driven by the water depth: structures in larger depths experience larger response due to i) a larger water column acting on the structure and ii) a larger mode shape displacement away from the sea bed, which implies a larger modal excitation as can be seen from equation 2.46.

For waves producing a large response however, structures in shallower water experienced larger responses than structures in deeper water. This is explained by the fact that waves become more non-linear with decreasing water depth.

Figure 4.1 illustrates this phenomenon with data from the Wave Loads campaign. The exceedance probability p_{exc} of the measured responses from the same sea state at three different depths is shown, and it can be seen that for the largest part of the population ($p_{exc} > 0.2$), the sea state at the largest depth (40.8 m) produces the largest responses, followed by the medium depth (31 m) and the shallowest depth (20.9 m). For the largest measured responses however, the order is inverted, with the shallowest depth producing the largest responses and the deepest producing the smallest responses.

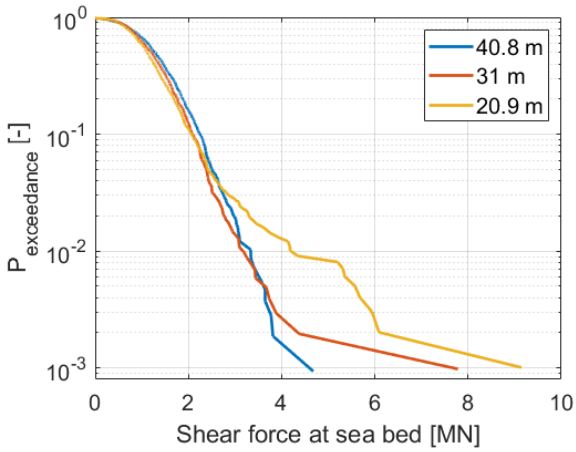

Figure 4.1: Exceedance probability plot for the measured base shear force for one sea state at three different depths

In all campaigns, the largest responses were measured for steep and breaking waves. This is illustrated in Figure 4.2, which shows the wave elevation and measured bending moment at the sea bed for an event with a large response recorded during the WiFi campaign.

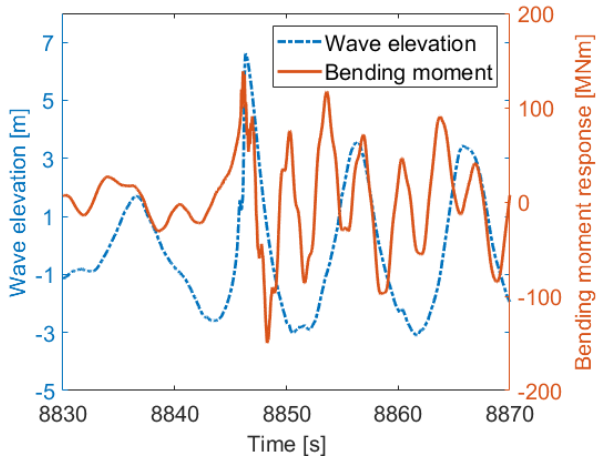

Figure 4.2: Example of the bending moment measured during an event with a large response.

For the models with a realistic second mode (i.e. from the WiFi and the Wave Loads campaigns, in P3 and P5), a spectral analysis showed that both the first and the second modes were triggered in such events. For these two campaigns, the response was decomposed into so called *quasi-static*, *first mode* and *second mode* contributions (note that contributions from higher modes were removed by low-pass filtering out the measured response). The first and second mode contributions were obtained using a band-pass filter around the first and second eigenfrequencies of the structure. The quasi-static response was the result of subtracting the first and second mode responses from the total response (here and in the rest of the chapter, *total response* refers to the response filtered out for modes higher than second). Figure 4.3 shows an example of this decomposition for the measured response during an event of the WiFi campaign.

This decomposition shows the contribution of the different modes to the total response. Note that with this method, all the response at an eigenfrequency is attributed to the corresponding mode, which is not correct in general. For example, by assuming that all the response around the first eigenfrequency corresponds to the first mode, we omit that the second mode can also produce a response at the first eigenfrequency. The decomposition also emphasizes the responses which are in phase at the instant of maximum response.

This decomposition was applied to a large number of events that produced large responses. In such events from the WiFi campaign, it was found that the quasi-static response contributed between 40 and 50 % of the total response, the first mode contributed between 30 and 40 % and the second mode up to 20% (P3). A similar decomposition was performed on the acceleration close to the top of the structure of the Wave Loads campaign (P5): for the largest measured acceleration over the whole campaign, the second mode contributed to about 30% of the total acceleration.

In addition, a comparison between the second mode response and a video recording of

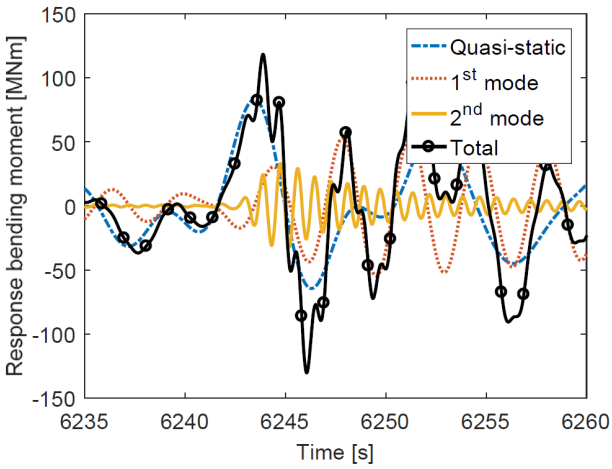

Figure 4.3: Example of decomposition of the response around the eigenfrequencies of the structure

the experimental campaign was carried out in the NTNU and the WiFi campaigns (P2, P3). This comparison showed that significant second mode response only occurred when waves were breaking at the structure, therefore the hypothesis was made that second mode response can only be triggered by slamming events. This was later confirmed by numerically simulating the response of the structure with and without slamming load models (P4, see Section 4.2). However, not all slamming events triggered significant second mode response.

Figure 4.4 shows four snapshots of a breaking wave impacting the structure. The presence of water particles ejected upwards and sideways, visible in the fourth image, are a visual indicator that the wave has broken at the cylinder, as explained in P3.

Secondary Load Cycle

By analyzing the loads on the stiff model of the WiFi campaign, it was also possible to study the excitation force and in particular the secondary load cycle phenomenon, referred to as SLC. Figure 4.5 shows the wave elevation, the excitation force measured on the stiff structure and the first mode response measured on the flexible structure. No correlation between the SLC characteristics and the magnitude of the first mode response could be established. However, some of the events presented a clear ringing response but did not have a SLC, such as the one shown in Figure 4.5(b). This suggests that in the WiFi experimental campaign, the SLC was not a necessary load attribute to generate ringing responses.

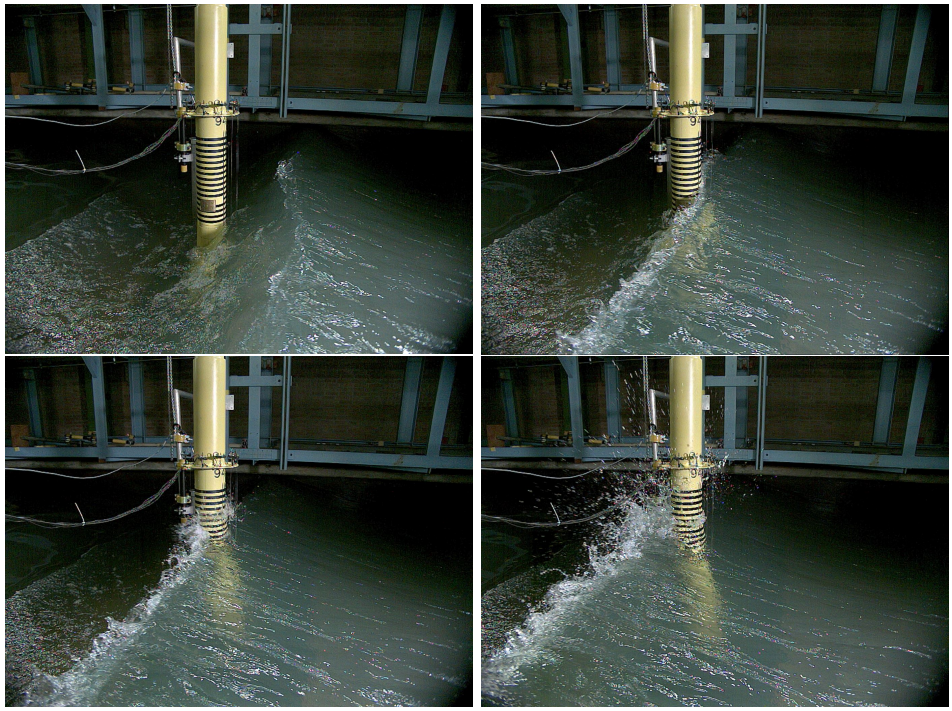

Figure 4.4: Snapshots of a steep wave breaking at the structure, recorded during the WiFi campaign

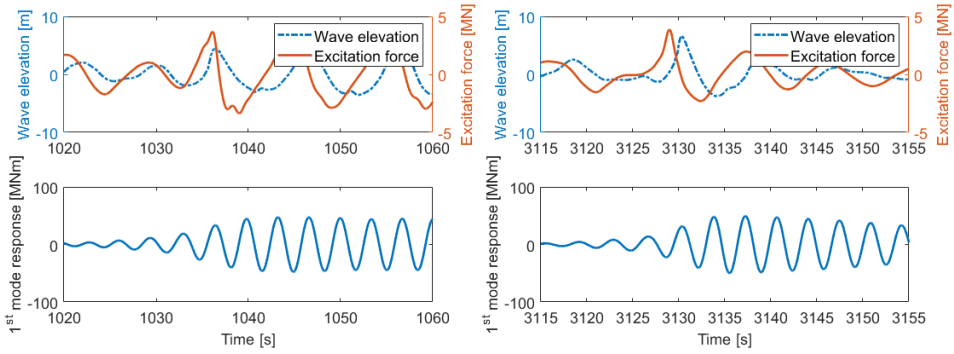

(a) Event with a SLC

(b) Event without a SLC

Figure 4.5: Example of two events with a large measured response. The first mode response is measured on the flexible structure, the excitation force is measured on the stiff structure

4.2 Simulation of the response to steep and breaking waves

The second step of the analyses consisted in reproducing the data produced during the experimental campaigns with different models. As explained in Section 3, the aerodynamic and geotechnic effects were neglected in the present test, and since the turbine was assumed to be idling no controller was modelled. The structural models used to calculate the responses (see Section 2.4) do not present any major challenge, the focus of this work was therefore in the hydrodynamic load models. In this section we assess how the models used in this thesis compare, both at a deterministic and statistical level, to the experimental data.

Note that comparing experimental data to simulations is not in general part of the design process for offshore wind turbines (see Section 2.5). Making this comparison at a deterministic level introduces the added difficulty of having to match the measured wave kinematics.

4.2.1 Individual assesment of the models

The following paragraphs summarize the general conclusions that were drawn for each of the numerical models and provide a comparison between the simulated response and the measurements for the event with the largest response measured during the Wave Loads campaign.

4.2.1.1 Linear kinematics applied to the Morison equation

The measured wave kinematics were linearized following the process described in the appendix A of P4. The hydrodynamic loads were then calculated with the Morison equation as described in 2.3. This model was used in P1, P2 and P4.

This model generally underestimated the largest measured responses because it did not trigger significant first and second mode response. This was expected as the calculated loads did not have the frequency content necessary to significantly excite the modes of the structure. This result is well-known (see for example Paulsen et al. 2013 or Marino et al. 2013) and will not be discussed in further detail.

4.2.1.2 Second order kinematics applied to the Morison equation

This model was used to try to match the measured responses of the Wave Loads campaign in P5. The wave kinematics used included components up to second order in terms of wave steepness. This set of kinematics was obtained by first linearizing the measured wave elevation. The linearization was carried out by first removing the difference-frequency wave components from the measurements, and then iteratively selecting the cut-off frequency of a low-pass filter such that the reconstructed wave spectrum (including first and second order terms) gave the best possible match to the measured spectrum. Further details can be found in Bachynski et al. (2017).

For the two cases in the shallowest water depth, the irregular Ursell number as defined by Stansberg (2011) was above the classical limit of 0.33, beyond which second order theory is not expected to depict accurately the wave kinematics. The responses calculated for these cases therefore largely underpredicted the measurements and were not considered in the analysis.

For the other cases, the Morison equation with second order wave kinematics matched the main population of events but generally underestimated the largest responses. This is due to the fact that the kinematics did not include harmonics higher than second and therefore lack some components of the high frequency loads which trigger the largest dynamic responses.

Figure 4.6 shows a comparison between this model and the measurements. The upper plot shows the wave elevation obtained from the second order wave kinematics. The measured wave is significantly steeper than the simulated one due to the lack of higher harmonics in the simulated wave. The lower plot compares the response obtained with this model to the measurement. The simulated response does not include any second mode response, therefore underestimating the total response.

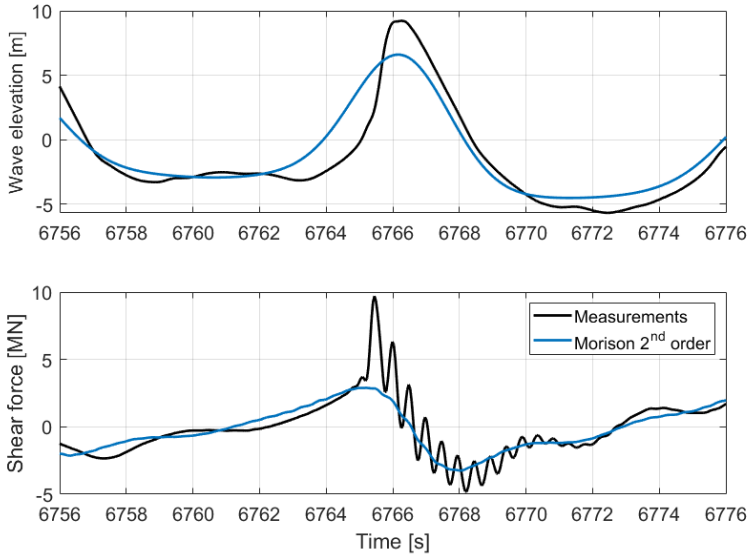

Figure 4.6: Comparison of the measurements and the Morison equation with second order wave kinematics

4.2.1.3 Stream function wave kinematics applied to the Morison equation

Without slamming model This model is referred to as the **M_SF** model and was used to calculate the responses measured in the WiFi campaign in P4. This model was assessed at a deterministic level by selecting the waves that produced the largest responses, finding

their period and height and modeling them with the stream function wave theory described in Section 2.2.3. The kinematics thus obtained were embedded into a linearization of the measured wave and applied to the Morison equation.

This model was able to produce ringing responses due to the higher harmonics contained in the wave kinematics. However, at a deterministic level, there was no general trend as to over- or underestimation of the first mode response: the first mode response was underestimated for some events and overestimated for others.

This model was not able to trigger significant second mode response. This is consistent with the findings from the measured data, which suggest that second mode response is a consequence of slamming loads, which were not included in this model.

With Wienke's slamming model This model is referred to as the **M_SF_W** model and was assessed in P4 following the same procedure as for M_SF. A comparison was made between the responses produced by this model and the previous one, where the only difference is the slamming model. The first mode responses produced by both models were very similar, which suggests that the slamming model did not significantly influence the first mode response. This is consistent with the basic structural dynamics theory discussed in Section 2.4.1: it was shown in P2 that the duration of a slamming force calculated with Wienke's model was about two orders of magnitude shorter that the first eigenperiod of the structure, which implies, as illustrate in Figure 2.7, that no significant first mode response will be triggered.

Significant second mode response was triggered by this model. Figures 4.7(c) and 4.7(d) show the continuous wavelet transform of the measured response and the response simulated with the M_SF_W model for an extreme event, respectively. Figure 4.7(c) shows that the first and second mode of the structure at 0.29 Hz and 1.21 Hz were triggered during the experiments. Figure 4.7(d) shows that the M_SF_W model was capable of triggering both the first mode and the second mode. By comparing with the results from the M_SF model, it was concluded that the Morison equation with stream function wave kinematics was able to produce the first mode response and that Wienke's slamming model was able to trigger second mode response.

However, by comparing a large number of extreme responses simulated with the M_SF_W model to measured responses, it was found that the simulated amplitude of the second mode response did not generally match the measured one. By performing this comparison for the total response, it was found that the M_SF_W model was overpredicting the response for some extreme events and underpredicting it for others, with no clear trend.

This is also illustrated in Figure 4.8, which compares both models to the measurements. The upper plot shows the wave elevation, where the stream function wave has been embedded into a linearization of the wave measured elevation following the process described in Figure 2.5. Note that both models use the same wave kinematics, therefore the wave elevation is equal for both. Here it can be seen that the stream function exhibits a symmetry

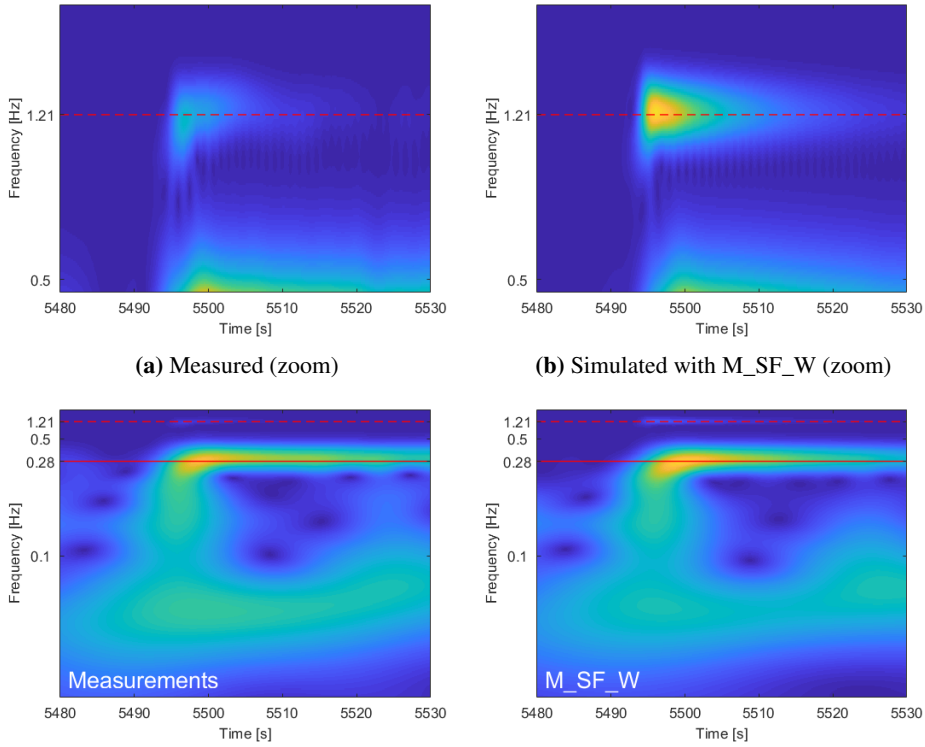

(a) Measured (zoom)

(b) Simulated with M_SF_W (zoom)

(c) Measured

(d) Simulated with M_SF_W

Figure 4.7: Continuous wavelet transform of the response measured and simulated with the M_SF_W model in the WiFi campaign. The upper plots are a zoom of the lower ones around the second eigenfrequency of the structure. Warm colors indicate a high energy content, while cold colors indicate a low energy content. For visualization purposes, the color scale of the upper plots is different from the lower plots.

around the crest, while the measured wave does not.

The lower plot shows that although both models underestimate the measured response, the M_SF_W model triggers some second mode response, which increases the maximum response by about 20% compared to the M_SF model. This is an example where the M_SF_W model underestimates the second mode response, which can not be generalized to all events.

Statistical assessment In P4, the M_SF_W model was also assessed at a statistical level, following the procedure suggested in DNV-RP-C205 (2017), DNV-OS-J101 (2014) and IEC-61400-3 (2009) to simulate DLC6.1 and described in Section 2.5.

Each of the sea states of P4 was assumed to correspond to the 50-year return sea state at a

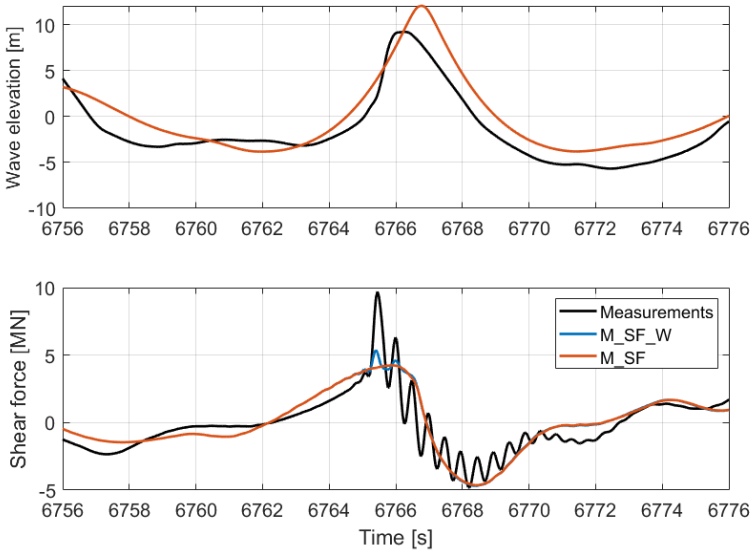

Figure 4.8: Comparison of the measurements and the Morison equation with stream function wave kinematics, with and without slamming model

fictitious location. Following IEC-61400-3 (2009), the height of the 50-year wave was calculated assuming that the sea state had a 3-hour stationarity during which the wave heights followed a given distribution (two distributions were analyzed: the Rayleigh distribution and the Battjes and Groenendijk distribution presented in Battjes and Groenendijk (2000) and noted *BG*). The kinematics of the 50-year wave were then calculated with the stream function theory and embedded at a random time into a realization of the 50-year return sea state. The loads were then calculated with the Morison equation with Wienke's slamming model addition, and the maximum simulated response was taken. For each sea state, this procedure was repeated 20 times, and the average of the 20 maxima was taken as the 50-year response, i.e. the driving response for DLC6.1.

The 50-year response thus calculated was compared to the largest measured response for each sea state. Note that the 50-year response does not generally correspond to the response to the 50-year return wave nor to the largest response during the 50-year return sea state. However, this comparison provides a good indication of how the M_SF_W mode performs.

Figure 4.9(a) shows the height of the 50-year return wave for the different sea states for the Rayleigh and the BG distributions. The BG and the Rayleigh distribution produced similar results in deep water, where the numerical predictions matched the measurements. The wave heights predicted by the BG distribution were generally smaller than the Rayleigh distribution for intermediate waters.

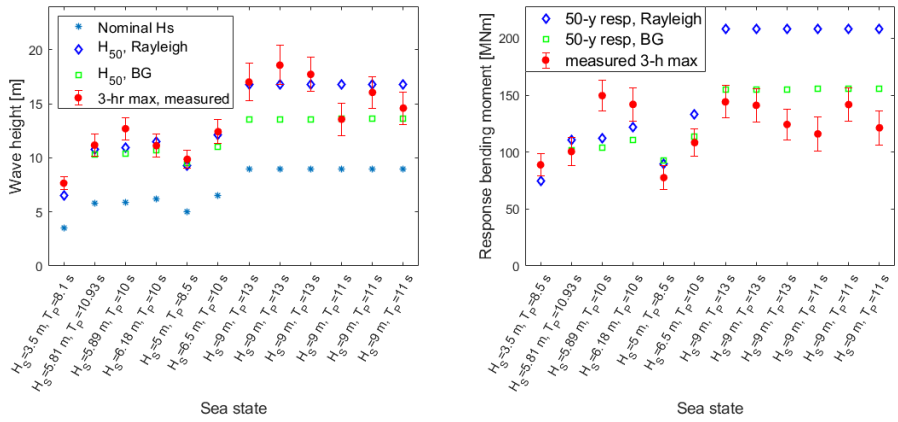

(a) Wave heights **(b)** Responses

Figure 4.9: Comparison between the estimated 50-year wave heights (in Figure a) and the corresponding responses (in figure b) with the measurements for different wave height distributions. The error bars around the measured maxima correspond to 2 standard deviations of the maximum.

Figure 4.9(b) shows the 50-year return responses estimated using the procedure described in Section 2.5 for the different distributions and compares them to the measurements. For the sea states with a large significant wave height, the M_SF_W model overpredicts the responses compared to the experimental measurements when using the Rayleigh distribution. The overprediction is reduced by using the BG distribution since this distribution leads to lower estimates of the 50-year return wave height, as seen in Figure 4.9(a). For lower sea states, the predicted response is closer to the measurements. It was shown in P4 that the overprediction was mainly related to the response at the second mode of the structure, which depends strongly on the celerity of the stream function wave.

4.2.1.4 KF and Rainey model

In this section the KF model and the Rainey model are discussed simultaneously. These models were used to simulate the response in P5. The kinematics input into both models were fully non-linear wave kinematics computed with the OceanWave3D software (Engsig-Karup et al. 2009) within the Wave Loads Project. Note that these models do not include any slamming force term. For both models, a drag term equal to that of the Morison equation was added. The loads from the KF model then become

$$F_{KF} = \int_{-h}^{\eta} \left(2\rho\pi R^2 \left(\frac{\partial u}{\partial t} + w\frac{\partial u}{\partial z} \right) + \rho\pi R^2 u \frac{\partial u}{\partial x} + \rho C_D R u|u| \right) dz + F^{\psi} \qquad (4.1)$$

By noting that conservation of mass for the present two-dimensional waves yields $\partial u/\partial x = -\partial w/\partial z$ and using $C_M = 2$, the force from the Rainey model can be written as

$$F_{Rainey} = \int_{-h}^{\eta} \left(2\rho\pi R^2 \left(\frac{\partial u}{\partial t} + w\frac{\partial u}{\partial z} \right) + \rho\pi R^2 u \frac{\partial u}{\partial x} + \rho C_D R u|u| \right) dz + F^{\eta} \quad (4.2)$$

In order to calculate the point force F^{ψ} of the KF model, the kinematics at the mean sea level must be used. The fully non-linear kinematics provided for the Wave Loads Project only included data for wet parts of the monopile, so no kinematics were available at the MSL when a trough was passing the monopile. To solve this issue, the kinematics at the free surface were Taylor expanded to approximate the kinematics at the MSL and used to calculate F^{ψ}.

In addition, the KF model is consistent to third order only. To be consistent with the theory, contributions higher than third order should be removed from the hydrodynamic loads thus calculated. This is not trivial and was not carried out in this work.

The analysis carried out in P5 suggests that these two approximations did not introduce a significant error compared to the original formulation of Kristiansen and Faltinsen (2017).

The KF and the Rainey models produced responses that matched the measurements reasonably well both for the main population of events as well as for extreme events, although they did not generally overpredict or underpredict the measured responses. A general observation is that the KF model produced larger responses than the Rainey model.

This is illustrated in Figure 4.10. The wave elevation in the upper plot shows that the fully non-linear kinematics produced a higher but less steep wave than the measurements. Note that both models use the same wave kinematics, therefore the wave elevation is equal for both.

The lower plot shows the measured and simulated responses, and illustrates how for this event the responses simulated with the KF and the Rainey model underestimate the measured responses by 11% and 20%, respectively.

Equations 4.1 and 4.2 show that the only difference between the models are the point forces F^{ψ} and F^{η}. As shown in Section 2.3.2, these two point forces are given by

$$F^{\psi} = \rho\pi R^2 \frac{4}{g} u^2 \frac{\partial u}{\partial t} \quad (4.3)$$

$$F^{\eta} = -\frac{1}{2} m_a u^2 \frac{\partial \eta}{\partial x} \quad (4.4)$$

It is a well known result that in the small wave amplitude limit, F^{ψ} is eight times larger than F^{η} (Chaplin et al. 1997, Faltinsen et al. 1995, Rainey 1995). The similarity between

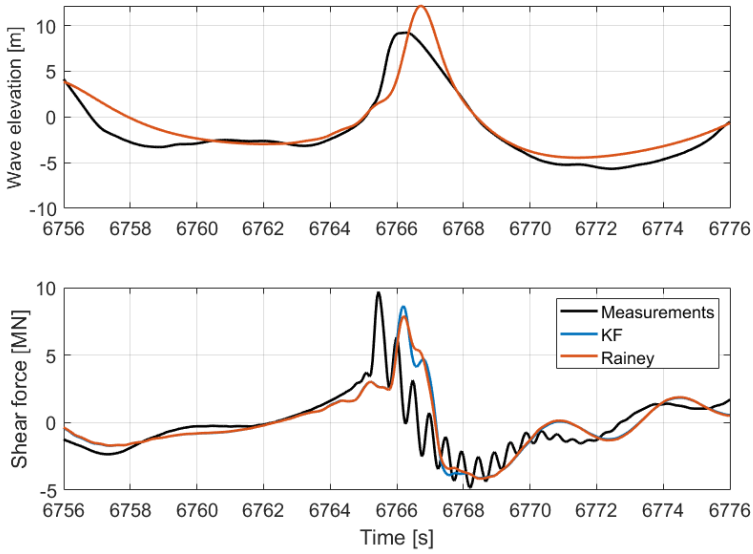

Figure 4.10: Comparison of the measurements and the Rainey and KF models

the responses produced by these two models suggested that this eightfold difference must somehow be compensated in the present case. The third harmonic of the excitation force produced by these two point loads for regular waves of different amplitudes and at different depths was analyzed in P5. As shown in Figure 4.11(a), the eightfold difference at small wave amplitudes tends towards unity for larger waves, which explains why the results produced by the two models are similar.

By taking the derivative of the linear dynamic free surface boundary condition (given in equation 2.7) with respect to x, it can be found that $g\partial\eta/\partial x = -\partial u/\partial t$. Inserting this expression in the definition of F^{η} given in equation 4.4 yields $F^{\psi} = 8F^{\eta}$ and explains the difference for small amplitude waves. This is illustrated in Figure 4.11(b), where the third harmonic of $u^2\partial u/\partial t$ is analyzed. This figure shows that for small amplitude waves, taking the kinematics at $z = 0$ or at $z = \eta$ does not have a significant impact. However, for large waves, the kinematics at $z = \eta$ are significantly larger, which partly compensates for the eightfold difference between the linear expressions of F^{ψ} and F^{η}.

By decomposing the measured structural acceleration at a point close to the top of the structure around the first and second eigenfrequencies, it was found that for extreme events, both models generally overpredicted the first mode acceleration while the second mode acceleration was underpredicted. The latter was expected since the results from P4 show that slamming models are necessary to significantly trigger second mode response. The former is a known limitation and has been discussed by Kristiansen and Faltinsen (2017), who showed that the KF model overpredicts the third harmonic excitation for steep waves such as those analyzed in this experimental campaign.

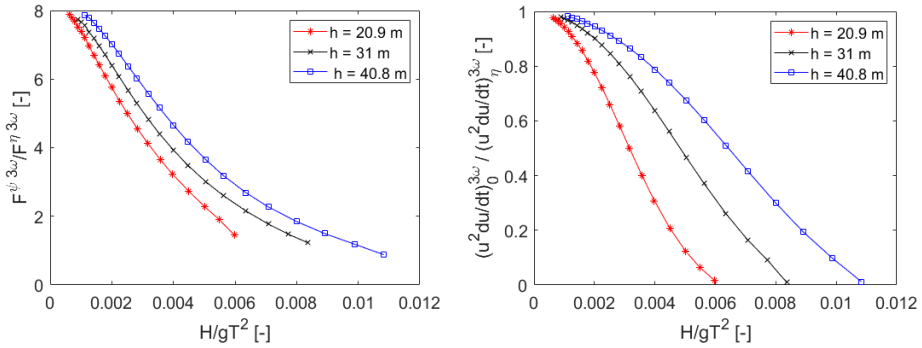

(a) Ratio of F^{ψ} and F^{η} **(b)** Ratio of $u^2 \partial u/\partial t$ taken at $z = 0$ and $z = \eta$

Figure 4.11: Comparison of the third harmonic excitation force for F^{ψ} and F^{η} and of the kinematic term $u^2 \partial u/\partial t$ taken at $z = 0$ and $z = \eta$

4.2.2 Comparison of numerical models

In this section the numerical results are compared to the measurements for the KF, Rainey, Morison second order and M_SF_W models. Figure 4.12 compares the measurements and the numerical models for the event shown in Figures 4.6, 4.8 and 4.10 (i.e. the event that produced the largest response in the Wave Loads campaign). The three time series represent, from top to bottom:

- The wave elevation. Note that the KF and the Rainey models use the same kinematics and therefore show the same wave elevation.
- The modal excitation of the first mode. Note that no measurement of the excitation force was available.
- The shear force at the sea bed.

None of the simulated wave elevations matches the steepness of the measured waves. The steepest wave is obtained from the fully non-linear kinematics, followed by the stream function wave theory and the second order kinematics. There is a slight delay in the wave simulated using the fully non-linear kinematics and the stream function theory. This delay is also visible in the response in the third plot.

In the second plot showing the excitation force, it can be seen that the M_SF_W model contains an impulse force, resulting from the slamming model. If this impulse force is excluded, the KF and Rainey models produce the largest excitation forces, followed by the M_SF_W model and the Morison second order model.

Note that the slamming force calculated with Wienke's model was applied when the wave reached its maximum steepness, as the results from P4 showed that this generally gave

the closest temporal match between the simulated and measured second mode responses. This produces a peak in the excitation force that is not in phase with the maximum of the force from the Morison equation alone. This is due to the fact that the shape of the stream function wave does not match the measured wave: while the measured wave is asymmetric and sees the slamming load roughly in phase with the maximum particle acceleration, the stream function wave is symmetric.

The third plot in Figure 4.12 shows that for this event, the largest response is produced by the KF model, followed by the Rainey model, the M_SF_W model and the Morison second order model. The order of the largest responses follows that of the excitation forces (with the slamming impulse load excluded). For this event, none of the models match the second mode response.

Figure 4.13 shows the same comparison for a different event. In this event, the second mode response is largely overestimated by the M_SF_W model, and the response simulated by this model is the largest of all responses. The accuracy of the total response produced by the M_SF_W model depends strongly on the amplitude of the second mode response.

A statistical comparison of these models is shown in Figure 4.14, where the exceedance probability plot of the response is given for the 3-hour sea state with $H_S = 11$ m, $T_P = 14$ s at $h = 31$ m during which the largest response was measured. This figure shows that all models match the main part of the population except M_SF_W. This model largely underestimates the response for the lower events because the kinematics for non-extreme waves are a linearization of the measured wave. Therefore, the model used in non-extreme events is effectively the Morison equation applied to linear wave kinematics. In this plot, only the 10 waves that produced the largest 10 responses are simulated with stream function kinematics and have a slamming load added to the Morison equation. For these events, as stated earlier, some events are underestimated while some are overestimated by the M_SF_W model. The number of events simulated with the M_SF_W model was selected to obtain a sample that could be compared to the other models for the most extreme events.

Note that the order in which the events are plotted along the y-axis is not generally the same for the different models and the measurements. Indeed, for the largest measured response shown in Figure 4.12, the M_SF_W model underestimated the measured results.

As explained previously, the Morison second order model can accurately predict the lowest responses but largely underestimates the most extreme events. For this sea state, the Morison equation with second order kinematics matches the measurements for $p_{exc} > 0.02$. The portion of the population for which the simulation was close to the measurements improved for milder sea states but decreased for more extreme sea states (P5). For more extreme sea states, the irregular Ursell number was above 0.33 and this model was not valid.

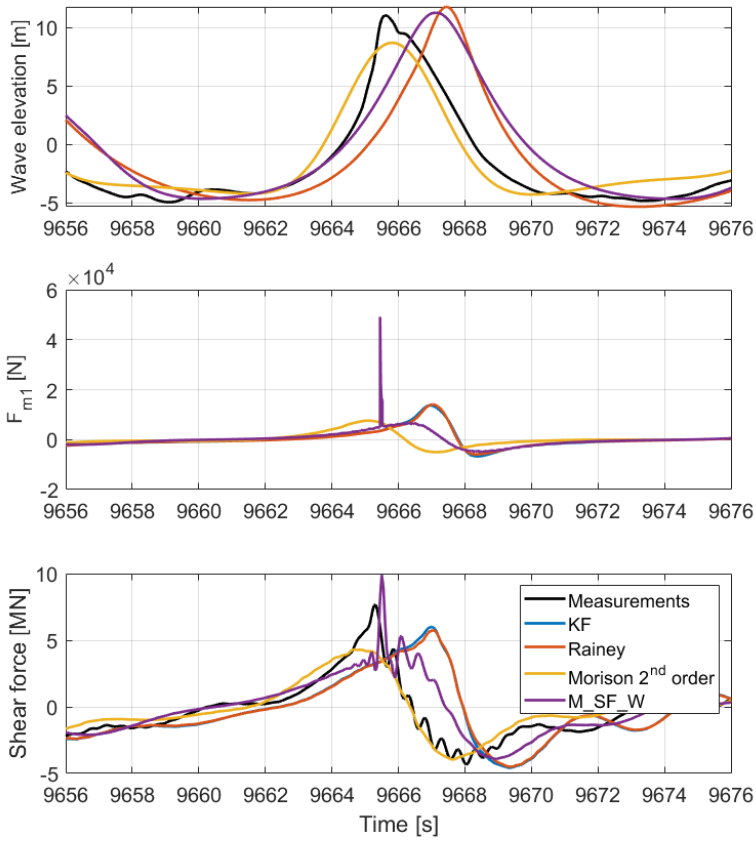

Figure 4.13: Comparison between the measurements and the numerical models, example 2: $H_S = 8.3$ m, $T_P = 12.6$ s, $h = 40.8$ m

The KF model produces responses that lie within 12% of the measured forces, with the KF model generally producing larger responses than the Rainey model. However, as explained previously, this figure does not keep the order of the events along the y-axis. Therefore, the largest measured response and the largest response simulated by the KF model, which appear reasonably close in Figure 4.14, do not correspond to the same event. The conclusions about the KF and Rainey models drawn from this sea condition can be applied to the other sea conditions as well (P5).

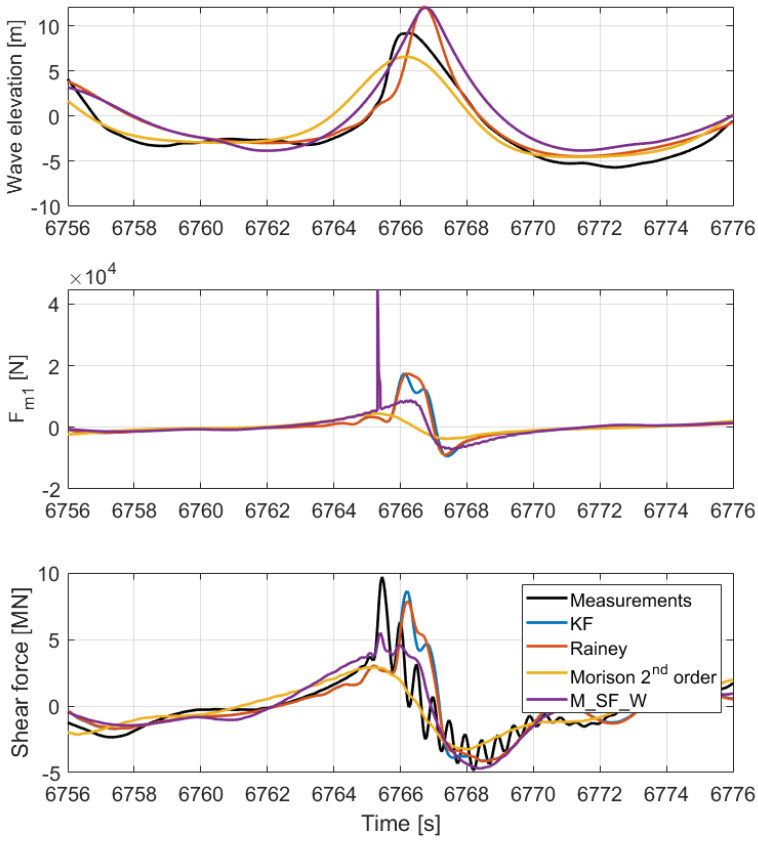

Figure 4.12: Comparison between the measurements and the numerical models, example 1: $H_S = 11$ m, $T_P = 14$ s, $h = 31$ m

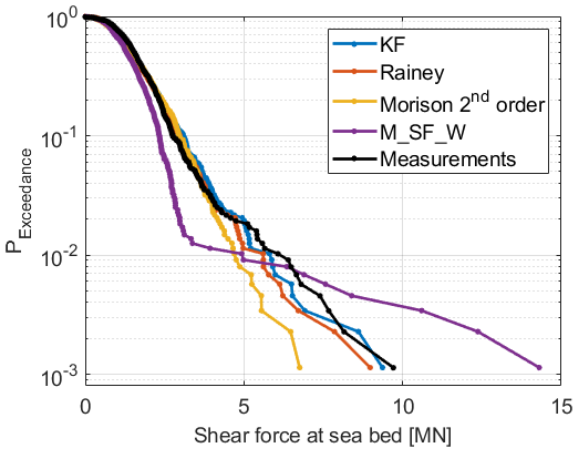

Figure 4.14: Exceedance probability plot for the measured and simulated responses

Chapter 5

Conclusions and future work

This chapter gives a summary of the contributions to the scientific community that resulted from the work presented in this thesis, as well as suggestions for future work based on the challenges that were encountered while carrying out this work.

5.1 Conclusions

This thesis addresses research questions about the design of monopile bottom-fixed offshore wind turbines in Ultimate Limit State. It studies the response of such turbines in extreme sea states and how to simulate the loads that produce such responses. This work has focused on two non-linear phenomena that affect offshore structures in steep waves, namely ringing (transient excitation of the first mode of the structure) and slamming (steep wave breaking at the structure).

Data measured during three experimental campaigns were used to validate different hydrodynamic load models. A number of conclusions were drawn from this comparison, which are listed below:

- the maximum responses consistently occurred during steep waves breaking at the structure. In such events, the first mode response characteristic of ringing events could be seen combined with second mode response (P1, P2, P3, P5).

- by band-pass filtering the response around the first and second eigenfrequencies, it was possible to decompose the response into quasi-static, first and second mode responses, to quantify the contributions of these modes to the total response in extreme events. For the response bending moment at the sea bottom, it was found that the quasi-static response contributed between 40 and 50% of the total response, the first mode contributed between 30 and 40% and the second mode up to 20%. This

shows the necessity of having an accurate second mode when carrying out model tests or numerical simulations in order to not underestimate the extreme responses (P3).

- the first mode of the structure was excited by second and third order hydrodynamic loads only. It was not influenced by slamming loads because their duration is too short to significantly excite the first mode of the structure (P1, P2).

- the second mode of the structure was excited by slamming loads. Waves that did not break did not significantly trigger second mode response, but not all breaking waves excited the second mode of the structure (P2, P3).

- as shown in previous research, linear wave kinematics applied to the Morison equation did not produce loads with the frequency content necessary to produce ringing responses or excite the second mode of the structure (see for example Paulsen et al. 2013). Therefore, this model largely underestimated the response of the structure in extreme events (P1, P2, P4).

- second order linear kinematics applied to the Morison equation can trigger ringing responses, but this model generally underpredicted extreme events. For very steep waves in shallow waters, the Ursell number was above the classical limit $U_r < 0.33$ where second order theory accurately depicts the kinematics of a wave. It was therefore expected that this model did not accurately predict extreme responses (P5).

- the FNV model, initially developed by Faltinsen et al. (1995) for deep water, can qualitatively produce ringing responses in intermediate water as well. However, this model does not include any non-linear incident potential. As shown by Kristiansen and Faltinsen (2017), the contribution from the non-linear incident potentials is dominant in shallow water. Therefore, it is not consistent to use the FNV model in finite water (P2).

- the model suggested by the common standards (IEC-61400-3 2009, DNV-RP-C205 2017, DNV-OS-J101 2014) is the Morison equation with stream function kinematics (Rienecker and Fenton 1981) and Wienke's slamming model (Wienke and Oumeraci 2005). The Morison loads with the stream function kinematics could produce ringing responses while the slamming model could trigger second mode response, therefore the combination of the two had the capability to match the measured responses. However, this model generally missed the balance between first and second mode response and the results it produced were not in general conservative (P4).

- the KF model is a generalization of the FNV to finite waters recently derived by Kristiansen and Faltinsen (2017). The input to this model are third order wave kinematics, and the model is consistent to third order. It requires separating the wave kinematics into different orders, which is not trivial for irregular waves. It also requires kinematics at the MSL, which, depending on the model used to generate the kinematics, is not always possible. In the work presented in this thesis, the input wave kinematics were not split into orders, which means that loads of order higher than third were included, and therefore the loads are not consistent. In addition,

the kinematics at the free surface were Taylor expanded to obtain the kinematics at the MSL as required. These two modifications, although not consistent, showed a reasonable agreement with the original formulation. (P5)

- the KF model with the modifications mentioned in the previous point matched the extreme responses reasonably well but was not in general conservative. For most extreme events it overpredicted the first mode response. This is expected as Kristiansen and Faltinsen (2017) showed that this model overpredicts the excitation loads for very steep waves. The model also underpredicted second mode response as it lacks a slamming model (P5).

- the Rainey model presented by Rainey (1989) is equal to the KF model if the same kinematics are used as input, apart from a point load. As for the KF model, the Rainey model generally overpredicted the first mode contribution but underpredicted the second mode contributions for event with large responses. The responses induced by the Rainey model were generally 5 to 10% lower than those induced by the KF model (P5).

- for small amplitude waves, previous research has shown that the point force of the KF model is eight times larger than the point force of the Rainey model. The work presented in this thesis shows that this ratio reduces towards unity for steep waves (P5).

5.2 Original contributions

The main contributions of this thesis are summarized below.

- *Quantification of the contribution of the first and second modes to the extreme responses in ULS*

  By analyzing time series of measured response bending moment at the sea bottom for a fully flexible model, it was possible to investigate the relative contributions of the first and second modes of the structure in the total response. This enables quantifying the importance of the second mode for the total response.

- *Assessment of the Kristiansen and Faltinsen model in extreme irregular waves*

  Kristiansen and Faltinsen (2017) validated the KF model against regular waves. This thesis tests the validity of the model in the context of extreme irregular waves by comparing numerical predictions to measurements obtained during model tests.

- *Development of an approach to to apply the Kristiansen and Faltinsen model in irregular waves*

  It is not straightforward to apply the KF model to irregular waves. In this thesis we suggest and implement an approach for using fully non-linear irregular wave kinematics as an input to the KF model.

- *Analysis of the eightfold ratio between the point loads of the FNV and Rainey models*

  The eightfold ratio between the point loads of the FNV and Rainey models is shown to decrease towards unity for large waves, which explains why both models produce similar results in ULS conditions.

- *Critical assessment of the models suggested by the design standards*

  The response produced by the model suggested by the standards for computing loads in ULS conditions, namely the stream function wave with Wienke's slamming model, is compared to experimental data.

- *Evaluation of the importance of the secondary load cycle for ringing responses*

  The discussion on whether the secondary load cycle is a necessary attribute of the excitation force to produce ringing responses has been ongoing in the last decades. Here we show that for the considered conditions, ringing can occur without the secondary load cycle.

- *Development and implementation of a method to extract linear seas from wave measurements*

  Several hydrodynamic load models, including the FNV model developed by Faltinsen et al. (1995), require linear waves as input. When comparing measurements to numerical modelling, it is therefore necessary to linearize the measured wave elevation. The method proposed in P4 filters out the waves of third and higher order and then iteratively removes the second order wave contribution.

5.3 Future work

Based on the conclusions drawn in this thesis and the limitations encountered, several extensions of the work presented here can be envisaged. The following topics of investigation are suggested:

1. *Consistent use of the wave kinematics for the KF model*

   In this work, fully non-linear kinematics were used as input to the KF model. This is not consistent with the original formulation as it does not allow to separate hydrodynamic loads by order, therefore loads of order higher than third were present in the excitation calculated in this thesis. This limitation was assessed for regular waves in P5 but its influence could not be quantified for irregular waves. A model that sorts the kinematics by order, such as the Stokes fifth order theory for regular waves, would make is possible to keep the results consistent with the KF theory and therefore assess the inaccuracies of the method applied in this work.

2. *Slamming model consistent with the KF model*

   In order to produce a realistic second mode response, the KF model should be complemented with a consistent slamming model. This is not trivial because the KF

model is based on perturbation theory consistent to third order, while slamming loads are strongly non-linear (Rainey 2007). As shown in P3, second mode response can account for up to 20% of the response of a wind turbine in extreme conditions, which shows that capturing that response is crucial to endure a safe design of the structure.

3. *Influence of the embedding process*

   The design process suggested by IEC-61400-3 (2009) and described in Section 2.5 implies using the same wave characteristics for 20 different realizations of a sea state. Since the embedded wave is the same for all realizations, the only variability in the response comes from the response history of the structure. From a statistical point of view, using the same wave could remove the randomness that is sought when using different realizations of the irregular waves. This effect should be assessed.

4. *Analysis of the response for different damping levels*

   Bachynski and Moan (2014) analyzed tension leg platform floating wind turbines and found that aerodynamic damping had a major role in the damping of the oscillations produced by a ringing event. An attempt to study the influence of damping was made during the NTNU experimental campaign, but the set-up got damaged and the results could not be used. Such a study would be relevant to close this knowledge gap.

5. *Fully integrated analysis*

   As explained in Section 3, in the presented experimental campaign, the influence of aerodynamic loads was neglected, and the soil-structure interaction was greatly simplified. A fully integrated analysis of the ULS response of the wind turbine should be performed with the hydrodynamic load models presented in this thesis.

6. *Influence of larger rotors*

   The flexible models used in the WiFi and the Wave Loads experimental campaigns represented a 4 MW and a 5 MW wind turbine, respectively. Larger turbines have since then been designed and installed, and it is likely that the eigenfrequencies of the structure will change. This can potentially change the relative contributions of the different modes, and these should be updated with the current and future sizes of wind turbines.

7. *Evaluation of experimental methods and uncertainties*

   The uncertainties inherent to model scale testing were not quantified or analyzed in detail for the presented experimental campaigns. In order to assess the degree of validity of the conclusions of this thesis, such analyses should be carried out.

8. *Distributed response*

   The work presented in this thesis only deals with the response of the structure at the sea bed. In order to verify the numerical models presented in this thesis, it is necessary to check that they are able to correctly predict the stress distribution along the support structure of the turbine.

9. *Full scale measurement*

   Model scale experiment might miss physical phenomena due to scaling issues or incorrect environmental conditions. To validate the numerical models presented in this thesis, they should be checked against full-scale measurements.

Bibliography

Erin E. Bachynski and Torgeir Moan. Ringing loads on tension leg platform wind turbines. *Ocean Engineering*, 84:237–248, July 2014. ISSN 0029-8018. doi: 10.1016/j.oceaneng.2014.04.007. URL http://www.sciencedirect.com/science/article/pii/S0029801814001371.

Erin E. Bachynski, Trygve Kristiansen, and Maxime Thys. Experimental and numerical investigations of monopile ringing in irregular finite-depth water waves. *Applied Ocean Research*, 68:154–170, October 2017. ISSN 0141-1187. doi: 10.1016/j.apor.2017.08.011. URL http://www.sciencedirect.com/science/article/pii/S0141118716305284.

Jurjen A Battjes and Heiko W Groenendijk. Wave height distributions on shallow foreshores. *Coastal Engineering*, 40(3):161–182, June 2000. ISSN 0378-3839. doi: 10.1016/S0378-3839(00)00007-7. URL http://www.sciencedirect.com/science/article/pii/S0378383900000077.

John M. Biggs. *Introduction to structural dynamics*. McGraw-Hill College, 1964.

Henrik Bredmose, Bjarne Jensen, Signe Schløer, Torben Juul Larsen, Taesong Kim, and Anders Melchior Hansen. The Wave Loads Project. Technical report, DTU Vindenergi, December 2013a.

Henrik Bredmose, Peter Slabiak, Lasse Sahlberg-Nielsen, and Flemming Schlütter. Dynamic Excitation of Monopiles by Steep and Breaking Waves: Experimental and Numerical Study. *Proceedings of the ASME 2013 32nd International Conference on Ocean, Offshore and Arctic Engineering*, page V008T09A062, June 2013b. doi: 10.1115/OMAE2013-10948. URL http://dx.doi.org/10.1115/OMAE2013-10948.

Per Ivar Bruheim. Development and validation of a finite element software facilitating large-displacement aeroelastic analysis of wind turbines. *83*, 2012. URL https://brage.bibsys.no/xmlui/handle/11250/232200.

Tim Bunnik, Joop Helder, and Erik Jan de Ridder. Simulation of the Flexible Response of a Fixed Offshore Wind Turbine subject to Breaking Waves. In *7th International Conference on HYDROELASTICITY IN MARINE TECHNOLOGY*, September 2015.

Simon Burmester, Erik-Jan de Ridder, Christof Wehmeyer, Erik Asp, and Philipp Gujer. Comparing Different Approaches for Calculating Wave Impacts on a Monopile Turbine Foundation. *Proceedings of the ASME 2017 36th International Conference on Ocean, Offshore and Arctic Engineering*, page V010T09A063, June 2017. doi: 10.1115/OMAE2017-61182. URL http://dx.doi.org/10.1115/OMAE2017-61182.

J. R. Chaplin, R. C. T. Rainey, and R. W. Yemm. Ringing of a vertical cylinder in waves. *Journal of Fluid Mechanics*, 350:119–147, 1997. doi: 10.1017/S002211209700699X.

Felix Creutzig, Blanca Fernandez, Helmut Haberl, Radhika Khosla, Yacob Mulugetta, and Karen C. Seto. Beyond Technology: Demand-Side Solutions for Climate Change Mitigation. *Annual Review of Environment and Resources*, 41(1):173–198, 2016. doi: 10.1146/annurev-environ-110615-085428. URL https://doi.org/10.1146/annurev-environ-110615-085428.

Robert A. Dalrymple. Stream Function Wave Theory, 1996. URL http://homepages.cae.wisc.edu/~chinwu/Coastal_Java/streamless.html.

Robert A. Dalrymple and Robert George Dean. *Water wave mechanics for engineers and scientists*. Prentice-Hall, 1991. URL http://www.asianscientist.com/books/?book=1232.

M. Damgaard, L. B. Ibsen, L. V. Andersen, and J. K. F. Andersen. Cross-wind modal properties of offshore wind turbines identified by full scale testing. *Journal of Wind Engineering and Industrial Aerodynamics*, 116:94–108, May 2013. ISSN 0167-6105. doi: 10.1016/j.jweia.2013.03.003. URL http://www.sciencedirect.com/science/article/pii/S0167610513000603.

Mads Damgaard and Jacob K. F. Andersen. Natural Frequency And Damping Estimation of an Offshore Wind Turbine Structure. In *Proceedings of the Twenty-second (2012) International Offshore and Polar Engineering Conference*. International Society of Offshore and Polar Engineers, January 2012. URL https://www.onepetro.org/conference-paper/ISOPE-I-12-126.

Erik Jan de Ridder. WP3 MONOPILE FOUNDATION MODEL TESTS MARIN. Technical Report 25236-2-BT, MARIN, Wageningen, February 2015.

Erik Jan de Ridder, Pieter Aalberts, Joris van den Berg, Bas Buchner, and Johan Peeringa. The Dynamic Response of an Offshore Wind Turbine With Realistic Flexibility to Breaking Wave Impact. *Proceedings of the ASME 2011 30th International Conference on Ocean, Offshore and Arctic Engineering*, pages 543–552, January 2011. doi: 10.1115/OMAE2011-49563. URL http://dx.doi.org/10.1115/OMAE2011-49563.

Erik Jan de Ridder, Tim Bunnik, Johan M. Peeringa, Bo Terp Paulsen, Christof Wehmeyer, Philipp Gujer, and Erik Asp. Summary of the Joint Industry Project Wave Impact on Fixed Foundations (WiFi JIP). *Proceedings of the ASME 2017 36th International Conference on Ocean, Offshore and Arctic Engineering*, page V010T09A081, June 2017. doi: 10.1115/OMAE2017-62040. URL http://dx.doi.org/10.1115/OMAE2017-62040.

C. Devriendt, W. Weijtjens, M. El-Kafafy, and G. D. Sitter. Monitoring resonant frequencies and damping values of an offshore wind turbine in parked conditions. *IET Renewable Power Generation*, 8(4):433–441, May 2014. ISSN 1752-1416. doi: 10.1049/iet-rpg.2013.0229.

DNV-OS-J101. DNV-OS-J101 Design of offshore wind turbine structures. Technical report, DNV, May 2014.

DNV-RP-C205. DNV-RP-C205 Environmental Conditions and Environmental Loads. Technical report, DNV, August 2017.

A. P. Engsig-Karup, H. B. Bingham, and O. Lindberg. An efficient flexible-order model for 3d nonlinear water waves. *Journal of Computational Physics*, 228(6):2100–2118, April 2009. ISSN 0021-9991. doi: 10.1016/j.jcp.2008.11.028. URL http://www.sciencedirect.com/science/article/pii/S0021999108006190.

O. M. Faltinsen and A. N. Timokha. Undamped eigenperiods of a sea-based gravity monotower. *Applied Mathematical Modelling*, 40(19–20):8217–8243, October 2016. ISSN 0307-904X. doi: 10.1016/j.apm.2016.04.003. URL http://www.sciencedirect.com/science/article/pii/S0307904X16302037.

O. M. Faltinsen, J. N. Newman, and T. Vinje. Nonlinear wave loads on a slender vertical cylinder. *Journal of Fluid Mechanics*, 289:179–198, 1995. doi: 10.1017/S0022112095001297.

O.M. Faltinsen. *Sea loads on ships and offshore structures*. Ocean Techmology. Cambridge, 1990. ISBN 0-521-45870-6.

John Fenton. Steady water waves - Programs FOURIER, STOKES and CNOIDAL - Homepage, 2015. URL http://johndfenton.com/Steady-waves/Fourier.html.

Fenton John D. A Fifth-Order Stokes Theory for Steady Waves. *Journal of Waterway, Port, Coastal, and Ocean Engineering*, 111(2):216–234, March 1985. doi: 10.1061/(ASCE)0733-950X(1985)111:2(216). URL http://ascelibrary.org/doi/abs/10.1061/(ASCE)0733-950X(1985)111:2(216).

Joakim Frimann-Dahl. *Experimental Validation and Design Review of Wave Loads on Large-Diameter Monopiles*. PhD thesis, NTNU, Marine Technology, June 2015.

Roger F. Gans. *Mechanical Systems*. Springer, 2015. URL http://link.springer.com/content/pdf/10.1007/978-3-319-08371-1.pdf.

John Grue and Morten Huseby. Higher-harmonic wave forces and ringing of vertical cylinders. *Applied Ocean Research*, 24(4):203–214, August 2002. ISSN 0141-1187. doi: 10.1016/S0141-1187(02)00048-2. URL http://www.sciencedirect.com/science/article/pii/S0141118702000482.

John Grue, Gunnhild Bjørshol, and Øyvind Strand. Higher harmonic wave exciting forces on a vertical cylinder. *Applied Mathematics*, 1993. URL https://www.duo.uio.no/handle/10852/48919.

GWEC. Global Wind Report. Technical report, Global Wind Energy Council, 2017. URL http://gwec.net/publications/global-wind-report-2/.

S. Hallowell, A. T. Myers, and S. R. Arwade. Variability of breaking wave characteristics and impact loads on offshore wind turbines supported by monopiles. *Wind Energy*, pages n/a–n/a, February 2015. ISSN 1099-1824. doi: 10.1002/we.1833. URL http://onlinelibrary.wiley.com/doi/10.1002/we.1833/abstract.

K. Hasselmann, T. P. Barnett, E. Bouws, H. Carlson, D. E. Cartwright, K. Enke, J. A. Ewing, H. Gienapp, D. E. Hasselmann, P. Kruseman, A. Meerburg, P. Müller, I. Love, U Diana, D. J. Olbers, K. Richter, W. Sell, and H. Walden. Measurements of wind-wave growth and swell decay during the Joint North Sea Wave Project (JONSWAP), January 1973. URL http://resolver.tudelft.nl/uuid:f204e188-13b9-49d8-a6dc-4fb7c20562fc.

Arjen Y. Hoekstra and Thomas O. Wiedmann. Humanity's unsustainable environmental footprint. *Science (New York, N.Y.)*, 344(6188):1114–1117, June 2014. ISSN 1095-9203. doi: 10.1126/science.1248365.

Morten Huseby and John Grue. An experimental investigation of higher-harmonic wave forces on a vertical cylinder. *Journal of Fluid Mechanics*, 414:75–103, 2000. doi: 10.1017/S0022112000008533.

IEC-61400-3. IEC 61400-3: Wind Turbines–Part 3: Design Requirements for Offshore Wind Turbines. *International Electrotechnical Commission, Geneva*, February 2009.

IPCC. *Climate Change 2014: Impacts, Adaptation, and Vulnerability. Part A: Global and Sectoral Aspects. Contribution of Working Group II to the Fifth Assessment Report of the Intergovernmental Panel on Climate Change [Field, C.B., V.R. Barros, D.J. Dokken, K.J. Mach, M.D. Mastrandrea, T.E. Bilir, M. Chatterjee, K.L. Ebi, Y.O. Estrada, R.C. Genova, B. Girma, E.S. Kissel, A.N. Levy, S. MacCracken, P.R. Mastrandrea, and L.L. White (eds.)]*. Cambridge University Press, Cambridge, United Kingdom and New York, NY, USA, 2014.

Jason Jonkman, S. Butterfield, Walt Musial, and G. Scott. Definition of a 5-MW Reference Wind Turbine for Offshore System Development. Technical Report NREL/TP-500-38060, NREL, February 2009.

T. Kristiansen and O. M. Faltinsen. Higher harmonic wave loads on a vertical cylinder in finite water depth. *Journal of Fluid Mechanics*, 833:773–805, December 2017. ISSN 0022-1120, 1469-7645. doi: 10.1017/jfm.2017.702. URL https://www.cambridge.org/core/journals/journal-of-fluid-mechanics/article/higher-harmonic-wave-loads-on-a-vertical-cylinder-in-finite-water-depth/D7A563005EF0F28B7F55FAC708C6BB20.

J. R. Krokstad and C. T. Stansberg. RINGING LOAD MODELS VERIFIED AGAINST EXPERIMENTS. *Proceedings of the International conference on offshore mechanics and arctic engineering (1995)*, 1995. URL http://trid.trb.org/view.aspx?id=456094.

R. C. MacCamy and R. A. Fuchs. WAVE FORCES ON PILES: A DIFFRACTION THEORY. Technical report, Corps of Engineers, Washington DC, December 1954.

Š. Malenica and B. Molin. Third-harmonic wave diffraction by a vertical cylinder. *Journal of Fluid Mechanics*, 302:203–229, 1995. doi: 10.1017/S0022112095004071.

W. Manners and R. C. T. Rainey. Hydrodynamic Forces on Fixed Submerged Cylinders. *Proceedings of the Royal Society of London. Series A: Mathematical and Physical Sciences*, 436(1896):13–32, January 1992. ISSN 1364-5021, 1471-2946. doi: 10.1098/rspa.1992.0002. URL http://rspa.royalsocietypublishing.org/content/436/1896/13.

Enzo Marino, Claudio Lugni, and Claudio Borri. A novel numerical strategy for the simulation of irregular nonlinear waves and their effects on the dynamic response of offshore wind turbines. *Computer Methods in Applied Mechanics and Engineering*, 255:275–288, March 2013. ISSN 0045-7825. doi: 10.1016/j.cma.2012.12.005. URL http://www.sciencedirect.com/science/article/pii/S0045782512003751.

Chiang C. Mei, Michael Stiassnie, and Dick K.-P. Yue. *Theory and Applications of Ocean Surface Waves: Linear aspects*. World Scientific, 2005. ISBN 978-981-256-156-5.

J.R. Morison, J.W. Johnson, and S.A. Schaaf. The Force Exerted by Surface Waves on Piles. *Journal of Petroleum Technology*, 2(05):149–154, May 1950. ISSN 0149-2136. doi: 10.2118/950149-G. URL http://www.onepetro.org/doi/10.2118/950149-G.

Arvid Naess and Torgeir Moan. *Stochastic Dynamics of Marine Structures*. Cambridge University Press, October 2012. ISBN 978-0-521-88155-5.

B. J. Natvig and P. Teigen. Review Of Hydrodynamic Challenges In Tlp Design. *International Journal of Offshore and Polar Engineering*, 3(04), December 1993. ISSN 1053-5381. URL https://www.onepetro.org/journal-paper/ISOPE-93-03-4-241.

J. N. Newman. Nonlinear Scattering of Long Waves by a Vertical Cylinder. In John Grue, Bjørn Gjevik, and Jan Erik Weber, editors, *Waves and Nonlinear Processes in Hydrodynamics*, number 34 in Fluid Mechanics and Its Applications, pages 91–102. Springer Netherlands, January 1996. ISBN 978-94-010-6597-9 978-94-009-0253-4. URL http://link.springer.com/chapter/10.1007/978-94-009-0253-4_8.

Bo Terp Paulsen, Henrik Bredmose, Harry B. Bingham, and Signe Schløer. Steep Wave Loads From Irregular Waves on an Offshore Wind Turbine Foundation: Computation and Experiment. *Proceedings of the ASME 2013 32nd International Conference on Ocean, Offshore and Arctic Engineering*, page V009T12A028, June 2013. doi: 10.1115/OMAE2013-10727. URL http://dx.doi.org/10.1115/OMAE2013-10727.

Bo Terp Paulsen, Henrik Bredmose, Harry B. Bingham, and Niels Gjøl Jacobsen. Forcing of a bottom-mounted circular cylinder by steep regular water waves at finite depth. *Journal of Fluid Mechanics*, 755:1–34, 2014. ISSN 00221120. doi: 10.1017/jfm.2014.386.

Johan Peeringa. Stream Function Wave Program User's manual. Technical report, ECN, February 2005.

Johan M. Peeringa and Koen W. Hermans. Impact of New Slamming Wave Design Method on the Structural Dynamics of a Classic, Modern and Future Offshore Wind Turbine. *Proceedings of the ASME 2017 36th International Conference on Ocean, Offshore and Arctic Engineering*, page V010T09A071, June 2017. doi: 10.1115/OMAE2017-61654. URL http://dx.doi.org/10.1115/OMAE2017-61654.

P. J. Rainey and T. R. Camp. Constrained non-linear waves for offshore wind turbine design. *Journal of Physics: Conference Series*, 75(1):012067, 2007. ISSN 1742-6596. doi: 10.1088/1742-6596/75/1/012067. URL http://stacks.iop.org/1742-6596/75/i=1/a=012067.

R. C. T. Rainey. A new equation for calculating wave loads on offshore structures. *Journal of Fluid Mechanics*, 204:295–324, 1989. doi: 10.1017/S002211208900176X.

R. C. T. Rainey. The hydrodynamic load at the intersection of a cylinder with the water surface. In *Proceedings of 10th International Workshop on Water Waves and Floating Bodies*, pages 207–210, 1995. URL http://yghacxx.iwwwfb.org/Abstracts/iwwwfb10/iwwwfb10_42.pdf.

R. C. T. Rainey. Weak or strong nonlinearity: the vital issue. *Journal of Engineering Mathematics*, 58(1-4): 229–249, August 2007. ISSN 0022-0833, 1573-2703. doi: 10.1007/s10665-006-9126-2. URL http://link.springer.com/article/10.1007/s10665-006-9126-2.

R. C. T. Rainey and J. R. Chaplin. Wave Breaking and Cavitation Around a Vertical Cylinder: Experiments and Linear Theory. In *18th IWWWFB*, 2003.

M. M. Rienecker and J. D. Fenton. A Fourier approximation method for steady water waves. *Journal of Fluid Mechanics*, 104:119–137, March 1981. ISSN 1469-7645. doi: 10.1017/S0022112081002851. URL http://journals.cambridge.org/article_S0022112081002851.

Bjørn Hervold Riise, John Grue, Atle Jensen, and Thomas B. Johannessen. A note on the secondary load cycle for a monopile in irregular deep water waves. *Journal of Fluid Mechanics*, 849, August 2018. ISSN 0022-1120, 1469-7645. doi: 10.1017/jfm.2018.450. URL https://www.cambridge.org/core/journals/journal-of-fluid-mechanics/article/note-on-the-secondary-load-cycle-for-a-monopile-in-irregular-deep-water-waves/9E466D919B4C2C677C0A15765AD270E4.

Amy N. Robertson, Fabian Wendt, Jason M. Jonkman, Wojciech Popko, Michael Borg, Henrik Bredmose, Flemming Schlutter, Jacob Qvist, Roger Bergua, Rob Harries, Anders Yde, Tor Anders Nygaard, Jacobus Bernardus de Vaal, Luca Oggiano, Pauline Bozonnet, Ludovic Bouy, Carlos Barrera Sanchez, Raul Guanche García, Erin E. Bachynski, Ying Tu, Ilmas Bayati, Friedemann Borisade, Hyunkyoung Shin, Tjeerd van der Zee, and Matthieu Guerinel. OC5 Project Phase Ib: Validation of Hydrodynamic Loading on a Fixed, Flexible Cylinder for Offshore Wind Applications. *Energy Procedia*, 94:82–101, September 2016. ISSN 1876-6102. doi: 10.1016/j.egypro.2016.09.201. URL http://www.sciencedirect.com/science/article/pii/S1876610216308700.

Mary Robinson and Tara Shine. Achieving a climate justice pathway to 1.5 degrees. *Nature Climate Change*, 8(7):564–569, July 2018. ISSN 1758-6798. doi: 10.1038/s41558-018-0189-7. URL https://www.nature.com/articles/s41558-018-0189-7.

Turgut Sarpkaya. *Wave forces on offshore structures*. Cambridge University Press, 2010.

Hemming A. Schäffer. Second-order wavemaker theory for irregular waves. *Ocean Engineering*, 23(1): 47–88, January 1996. ISSN 0029-8018. doi: 10.1016/0029-8018(95)00013-B. URL http://www.sciencedirect.com/science/article/pii/002980189500013B.

Rasoul Shirzadeh, Wout Weijtjens, Patrick Guillaume, and Christof Devriendt. The dynamics of an offshore wind turbine in parked conditions: a comparison between simulations and measurements. *Wind Energy*, 18(10):1685–1702, October 2015. ISSN 1099-1824. doi: 10.1002/we.1781. URL http://onlinelibrary.wiley.com/doi/10.1002/we.1781/abstract.

Carl Trygve Stansberg. Characteristics of Steep Second-Order Random Waves in Finite and Shallow Water. *Proceedings of the ASME 2011 30th International Conference on Ocean, Offshore and Arctic Engineering*, pages 859–869, January 2011. doi: 10.1115/OMAE2011-50219. URL http://dx.doi.org/10.1115/OMAE2011-50219.

Aina Stensgård, Kjersti Prestrud, Jørgen Hanssen, and Pieter Callewaert. Matsvinn i Norge: Rapportering av nøkkealt 2015-2017. Technical Report OR.28.18, Matvett AS, October 2018. URL https://www.matvett.no/uploads/documents/Matsvinn-i-Norge-Rapportering-av-nokkeltall-2015-2017.pdf.

Loup Suja-Thauvin and Jørgen Ranum Krokstad. Simplified Bottom Fixed Offshore Wind Turbine in Extreme Sea States. In *The 26th International Ocean and Polar Engineering Conference*, Rhodos (Greece), June 2016. International Society of Offshore and Polar Engineers. ISBN 978-1-880653-88-3. URL https://www.onepetro.org/conference-paper/ISOPE-I-16-468.

Loup Suja-Thauvin, Lene Eliassen, and Jørgen Krokstad. The scalability of loads on large diameter monopile offshore wind support structures. In *International Wind Engineering Conference*, Hannover, September 2014.

Loup Suja-Thauvin, Jørgen R. Krokstad, and Joakim Frimann-Dahl. Maximum loads on a one degree of freedom model-scale offshore wind turbine. *Energy Procedia*, 94:329–338, 2016.

Loup Suja-Thauvin, Jørgen R. Krokstad, Erin E. Bachynski, and Erik-Jan de Ridder. Experimental results of a multimode monopile offshore wind turbine support structure subjected to steep and breaking irregular waves. *Ocean Engineering*, 146:339–351, December 2017. ISSN 0029-8018. doi: 10.1016/j.oceaneng.2017.09.024. URL http://www.sciencedirect.com/science/article/pii/S0029801817305437.

Loup Suja-Thauvin, Jørgen R. Krokstad, and Erin E. Bachynski. Critical assessment of non-linear hydrodynamic load models for a fully flexible monopile offshore wind turbine. *Ocean Engineering*, 164: 87–104, September 2018. ISSN 0029-8018. doi: 10.1016/j.oceaneng.2018.06.027. URL https://www.sciencedirect.com/science/article/pii/S0029801818310515.

Loup Suja-Thauvin, Erin Elizabeth Bachynski, Fabio Pierella, Michael Borg, Jørgen Ranum Krokstad, and Henrik Bredmose. Critical Assessment of Hydrodynamic Load Models for a Monopile Structure in Finite Water Depth. *Marine Structures (submitted)*, April 2019.

Paul E Thomassen, Per Ivar Bruheim, Loup Suja, and Lars Frøyd. A Novel Tool for FEM Analysis of OffshoreWind TurbinesWith Innovative Visualization Techniques. *Proceedings of the Twenty-second (2012) International Offshore and Polar Engineering Conference*, page 1, 2012.

F. Ursell. The long-wave paradox in the theory of gravity waves. *Mathematical Proceedings of the Cambridge Philosophical Society*, 49(4):685–694, October 1953. ISSN 1469-8064, 0305-0041. doi: 10.1017/S0305004100028887.

W. G. Versteijlen, A. Metrikine, J. S. Hoving, E. H. Smidt, and W. E. De Vries. Estimation of the vibration decrement of an offshore wind turbine support structure caused by its interaction with soil. In *Proceedings of the EWEA Offshore 2011 Conference, Amsterdam, The Netherlands, 29 November-1 December 2011*. European Wind Energy Association, 2011. URL http://repository.tudelft.nl/assets/uuid:1b9b84a8-148e-4250-82cb-306435dea7ad/279265.pdf.

Herbrt Wagner. Über Stoß- und Gleitvorgänge an der Oberfläche von Flüssigkeiten. *ZAMM - Journal of Applied Mathematics and Mechanics / Zeitschrift für Angewandte Mathematik und Mechanik*, 12 (4):193–215, January 1932. ISSN 1521-4001. doi: 10.1002/zamm.19320120402. URL http://onlinelibrary.wiley.com/doi/10.1002/zamm.19320120402/abstract.

S. Welch, C. Levi, E. Fontaine, M. P. Tulin, and others. Experimental Study of the Ringing Response of a Vertical Cylinder in Breaking Wave Groups. *International Journal of Offshore and Polar Engineering*, 9(4):276–282, 1999.

Adrian Whiteman, Javier Esparrago, Sonia Rueda, Samah Elsayed, and Iana Arkhipova. Capacity Statistics 2019. Technical report, IRENA, March 2019. URL /publications/2019/Mar/Capacity-Statistics-2019.

J. Wienke and H. Oumeraci. Breaking wave impact force on a vertical and inclined slender pile—theoretical and large-scale model investigations. *Coastal Engineering*, 52(5):435–462, May 2005. ISSN 0378-3839. doi: 10.1016/j.coastaleng.2004.12.008. URL http://www.sciencedirect.com/science/article/pii/S0378383904001735.

WindEurope. Offshore Wind in Europe, Key trends and statistics 2017. Technical report, WindEurope, February 2018. URL https://windeurope.org/wp-content/uploads/files/about-wind/statistics/WindEurope-Annual-Offshore-Statistics-2017.pdf.

Appendix A

Appended papers

Paper 1: Maximum loads on a one degree of freedom model-scale offshore wind turbine

By Loup Suja-Thauvin, Jørgen R. Krokstad and Joakim Fürst Frimann-Dahl

In Elsevier Energy Procedia, vol 94, p 329-338, 2016

Available online at www.sciencedirect.com

ScienceDirect

Energy Procedia 94 (2016) 329 – 338

Energy Procedia

[S1]13th Deep Sea Offshore Wind R&D Conference, EERA DeepWind'2016, 20-22 January 2016, Trondheim, Norway

Maximum loads on a one degree of freedom model-scale offshore wind turbine

Loup Suja-Thauvin*[ab], Jørgen Ranum Krokstad[ab], Joakim Fürst Frimann-Dahl[b]

[a]*Statkraft AS, Offshore Wind Department,Sluppenveien 17B, Trondheim 7005, Norway*
[b]*NTNU, Department of Marine Technology, Trondheim 7491, Norway*

Abstract

This paper presents the results of an experiment carried out in a wave flume aiming at reproducing a 50-year wave condition on an extra-large bottom-fixed offshore wind turbine mounted on a monopile. The model is a stiff cylinder mounted on a spring allowing rotation of the system around its base only in the wave propagation direction. Under these conditions, the turbine is assumed to be idling, and the damping ratio of the system is 2.4%. The overturning moment at the base of the cylinder is measured, and it is found that the maximum responses are recorded when long steep breaking or near-breaking waves hit the cylinder and excite the first eigenperiod of the structure. For a selected event involving a breaking wave, the response of the system is compared to numerical simulations using the FNV method. The higher order excitation loads from the FNV are approximated as sinusoid pulse loads, and it is shown that since the duration of these pulses lies close to the eigenperiod of the structure, they suffice to trigger the first mode motion, without the need for a slamming model. A consequence of the low damping is that if the structure has been previously excited at its 1st mode (linearly or by higher order phenomena such as springing), the structure can already have a motion that adds up to the transient response to the pulse loads. The findings of this study also challenge some of the load models currently used by the industry to estimate the response of offshore wind turbines during extreme events.

Peer-review under responsibility of SINTEF Energi AS

Keywords: extra-large monopile, 50-year storm, low damping

1. Introduction

Offshore wind turbines in extreme weather often encounter steep or breaking waves that produce high response loads threatening the structural integrity of the foundation. Under these conditions the blades are typically pitched so that the turbine is idling, decreasing the total damping on the first mode for the whole structure.

Peer-review under responsibility of SINTEF Energi AS
doi:10.1016/j.egypro.2016.09.191

During model tests performed in a wave flume at the Norwegian University of Science and Technology (NTNU) in Trondheim in April-May 2015, a one degree of freedom model composed of a stiff cylinder mounted on a rotational spring was exposed to 50-years wave conditions. Due to low damping, a lot of first mode oscillation could be observed through the experiment, and it was not clear whether these oscillations were due to linear excitation, non-linear excitation or slamming events. The structure was hit by a number of steep and breaking waves that produced oscillations of the whole structure and induced the maximum recorded loads.

This paper challenges the physics behind the maximum events and how the low damping has a primary effect on them. It is organized as follow: Section 2 is a short presentation of the experiment and section 3 is a presentation of the numerical model used to represent the system and the hydrodynamic loads. In section 4 we try to match the experimental results with a simple model that can explain the behavior of the turbine and how the maximum loads are reached, and section 5 concludes on the findings of this paper.

2. Presentation of the experiments

This model test was carried out in the small wave flume at NTNU in April and May 2015. This flume is 28m long and 2.5m wide with a constant water depth. One end of the flume is fitted with a perforated parabolic absorbing beach and the other end is equipped with a piston-type wave maker, consisting on a flat plate forced into translational motion by an electric actuator. At about 15m from the wave maker, a pit has been constructed where the model is fixed.

The model is a representation of a bottom-fixed extra-large offshore wind turbine mounted on a monopile with a scale of 1:48. It is a stiff cylinder 1.54m long with a 0.144m diameter and 6mm thick, attached to a force and moment transducer via an intermediate piece that behaves as a spring. These parts are dimensioned so that the bottom of the cylinder is exactly at the mudline. The transducer is then mounted on a stiff truss structure which is solidly anchored to the ground. The spring has been designed to model the stiffness of the soil, and enables the cylinder to rotate around its base in the wave direction but not in the transverse direction. The stiffness of the spring is 3300 Nm/rd. A mass of 5.04kg was added to the top of the model in order to model the mass of the rotor-nacelle assembly and get the correct eigenperiod for the system. The values given in this paragraph are model scale values; their full-scale equivalent is given in table 1.

Decay test were performed on the structure, and it was found that the whole system (with the correct water depth) had a damping ratio of 2.4%. [1] and [2] estimated the total damping of offshore wind turbines based on rotor-stop sequences for five wind parks and found mean damping ratios varying between 2.3 and 2.5%. The water depths of the considered wind parks were between 6 and 27m, which shows that these damping ratios are realistic for a wide range of water depths. On a different wind farm, [3] found that for low wind speeds and with the tuned mass damper blocked, the damping ratio was 1.1%. For the same turbine, [4] found that fore-aft damping ratios could vary from 1.7 to 2.8% depending on the wind speed, with the highest values corresponding to the highest wind speeds and with the tuned mass damper on. The values used in the presented experiments lie within the range of full-scale wind turbine in idling conditions.

Two different water depths with 8 sea states and 20 seeds per sea state were run. Only one run is studied in details in this paper, and was aimed at modelling 50-year storm at the Dogger Bank Creyke Beck B site [5]. The waves were randomly generated following a JONSWAP spectrum with a significant wave height H_S = 0.171m and a spectral peak period T_P = 1.62s at a water depth of 0.625m (corresponding to full scale values of H_S = 8.22m, T_P = 11.25s and h = 30m). Under these conditions, the turbine will be idling, so no aerodynamic modelling is implemented.

The tank flume was equipped with pairs of capacitance wave gauges at different positions along its length, which were used to measure the wave elevation input into the numerical model (see section 3.2.1). Two accelerometers were placed at the top of the cylinder and confirmed that the model experienced motion only in the wave direction. The force and moment transducer aforementioned was used to calculate the response of the structure to the incoming waves. Two cameras recorded the whole duration of the test enabling a visual check of the wave. Focus was on whether the wave had broken when exciting the cylinder.

Table 1. characteristics of the model test

	Diameter	Water depth	Rotational stiffness	Damping ratio	Eigenperiod
Full scale	6.9m	30m	1.75e7 kNm/rad	2.4%	3.89s
Model scale	144mm	625mm	3300 Nm/rad	2.4%	0.562s

Table 1 shows the characteristics of the model and their equivalent in full scale. A more exhaustive description of the model test can be found in [6].

3. Description of the numerical model

3.1. Model of the structure

The structure is represented by the classical single degree of freedom equation:

$$M_{hydro} = (I_P + I_A)\ddot{\theta} + C\dot{\theta} + K\theta \quad (1)$$

with M_{hydro} excitation moment due to the waves
I_P moment of inertia of the pile
I_A moment of inertia due to the added mass
C damping coefficient
K rotational stiffness of the spring
θ angular displacement of the structure

The dot over a variable means differentiation. The moment of inertia was calculated using an added mass coefficient of 1. Wavelet analysis showed small or close to negligible changes in the first mode frequency throughout all the recorded tests. The rotational stiffness was calculated based on the material and geometrical properties of the spring and tuned to fit the eigenperiod of the structure. The damping coefficient was estimated from the logarithmic decrement of the decay tests. Figure 1 shows the overturning moment measured at the base of the cylinder during the decay test and the simulation with the fitted parameters.

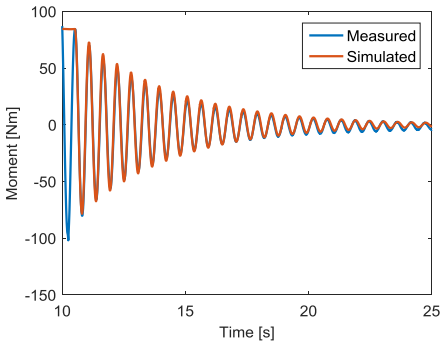

Fig 1. Decay test, experimental and numerical

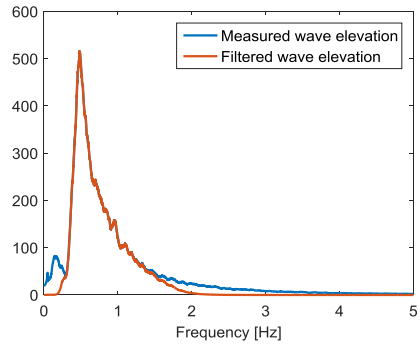

Fig 2. Spectra of the filtered and unfiltered measured wave elevation

3.2. Hydrodynamic load model

The input to equation (1) is the hydrodynamic excitation loads, which were calculated from the wave elevation measured during the model tests. The first part of this section will present the simple method used to obtain a linear

wave time series from the measured wave elevation (the concept of a linear wave time series and the reason for this being required are explained in the next section). The linear wave time series is then used as an input to the load model, which is developed in the second part of this section.

3.2.1. Linear input wave

The model used in this analysis is the FNV model, a weakly nonlinear model which will be presented in the next section. This model calculates 2nd and 3rd order hydrodynamic loads (in terms of wave steepness) from linear wave kinematics. If the wave kinematics used as input contain higher order terms, for instance 2nd order wave kinematics, 2nd order hydrodynamic loads would be calculated from two contributions: (i) from the linear term of the FNV (see first line of equation (3)) applied to 2nd order wave kinematics, and (ii) from the 2nd order term of the FNV (see second line of equation (3)) applied to linear wave kinematics. This would be inconsistent and produce conservative hydrodynamic excitation loads.

As a wave travels from the wave-maker to the model, non-linearities start to develop, and even more so due to the shallow waters considered. These are therefore found in the measured wave and should be removed before inputting the wave elevation into the FNV model. For the present paper, an attempt to linearize the measured wave elevation was made by filtering out the difference- and the sum-frequencies present in the wave spectrum.

The waves due to difference-frequencies do not present a major difficulty, as they lie distinctively from the linear wave in the spectrum. It can be seen in figure 2 how applying a high-pass filter to the measured wave elevation suffices to eliminate the difference-frequencies.

The waves due to second-order sum-frequencies require a much more elaborated method. Most of the energy from sum-frequency waves lies at about twice the spectral peak period which in a JONSWAP spectrum also contains energy from linear waves. Completely filtering out the energy at those frequencies would therefore result in a loss of information coming from the linear waves. For the present analysis, a simple method consisting in applying a Butterworth low-pass filter was used. The cut-off frequency, as suggested in [7] is defined by

$$\omega_{cut-off} = \sqrt{2g/H_S} \tag{2}$$

where g is the gravitational acceleration. Figure 2 shows the spectrum of the measured wave elevation in blue, and the same spectrum once the filtering has been applied. As can be seen from the figure, there is a significant difference between the filtered and unfiltered spectra at high frequencies (so-called tail of the spectra). According to [8], weakly nonlinear models are strongly dependent on the cutoff frequency, which means that the results from the present analysis must be used carefully. However, the results presented here are qualitative, and attention is given to the phasing of nonlinear terms rather than their amplitude. More accurate ways of obtaining the linear wave elevation from a measured time series can be found in [9] or [10].

3.2.2. Excitation loads: FNV model

The model used to calculate the excitation loads is the Faltinsen-Newman-Vinje model (hereafter referred as FNV, see [11]), which accounts for loads up to 3rd order in terms of wave steepness (referred as ϵ hereafter). The FNV was developed in the 90s when ringing was first observed in basin experiments (see [12]) first for regular waves and further developed for irregular waves by [13]. The hydrodynamic excitation force calculated by the FNV method as found in [13] is given by the following equation:

$$\begin{aligned} F_{FNV} = \; & 2\pi\rho R^2 \textstyle\int_{-h}^{0} u_t(z)dz && O(\epsilon) \\ & + 2\pi\rho R^2 u_t|_{z=0}\zeta^{(1)} + \pi\rho R^2 \textstyle\int_{-h}^{0} [2w(z)w_x(z) + u(z)u_x(z)]dz && O(\epsilon^2) \\ & + \pi\rho R^2 \left[\zeta^{(1)}\left(u_{tz}\zeta^{(1)} + 2ww_x + uu_x - \frac{2}{g}u_t w_t\right) - \left(\frac{u_t}{g}\right)(u^2+v^2)\Big|_{z=0}\right] && O(\epsilon^3) \\ & + \pi\rho\frac{R^2}{g}u^2 u_t|_{z=0}\beta\left(h/R\right) && O(\epsilon^3) \end{aligned} \tag{3}$$

Where ρ is the water density, u and w are the horizontal and vertical first order velocity components, $\zeta^{(1)}$ is the first order wave elevation, h is the mean water depth, R is the cylinder radius, and subscripts indicate differentiation. β is given by

$$\beta\left(h/R\right)=\int_0^{h/R}\left(3\Psi_1(Z)+4\Psi_2(Z)\right)dZ \tag{4}$$

with Ψ_1 and Ψ_2 defined in [13]. These functions represent the steady state and near field non-linear interaction with the cylinder for a deeply penetrating and constant diameter cylinder. The slenderness parameter, δ, has been omitted for simplicity. It is shown in [14] that all terms of equation (3) are of the order of δ^2. The FNV formulation assumes that $\epsilon\sim\delta$, which is equivalent to saying that the wave amplitude is close to the cylinder diameter. In the implementation of the model, the deep water assumption was used for β as indicated in [13], giving $\beta = 4$.
The FNV equations do not model any breaking wave loading effect, i.e. they do not model load events related to rapid change of added mass impacting the cylinder. The reason for using this model, as will be discussed in detail later, is to show that the higher order excitation loads (proportional to ϵ^2 and ϵ^3) can predict the response measured during the experiments.

The original formulation for the FNV, as shown in equation (3), gives a lumped force whose application point is at the mean free surface. The overturning moment at the mudline is then simply obtained by multiplying this force by the arm. In the present model, the two terms of equation (3) that require integration from the mudline to the mean water level, have been calculated as a distributed force. Each contribution has been multiplied by the corresponding arm to obtain the distributed moment. The first term for the overturning moment, which is equivalent to the inertia term of the classical Morison load, is then

$$Mf1 = 2\pi\rho R^2\int_{-h}^{0}\left(zu_t(z)\right)dz \tag{5}$$

And the second term is

$$Mf21 = \pi\rho R^2\int_{-h}^{0}z\left[2w(z)w_x(z)+u(z)u_x(z)\right]dz \tag{6}$$

The first term of second order of equation (3) corresponds to the contribution of the linear potential integrated from the mean water depth to the first order wave elevation. In the present model, this force will be applied at the mean water level and the moment from this force will be

$$Mf2Free = 2\pi\rho R^2 u_t\big|_{z=0}\zeta^{(1)}\cdot h \tag{7}$$

The terms in the third and fourth line of equation (3) are third order term and will be multiplied by the mean water depth to obtain moments respectively named $Mf31$ and $Mf3Xsi$.

The FNV model was initially developed for infinite water depth. Under the current setting, with a water depth of 30m and a spectral peak period of 11.25s, the ratio between water depth and wavelength is about 0.18, which according to [15] is in the intermediate water depth range. An attempt to account for some finite water depth effects was made by using a finite water potential when calculating the wave kinematics, integrating $Mf1$ and $Mf21$ over a finite depth and using the finite water depth dispersion relationship (found for instance in [16]).

The FNV is known to overestimate the loads, and it is inconsistent to use finite water depth kinematics since the formulas were developped assuming a deep water potential. However, as mentioned in section 3.2.1, this analysis aims at giving a qualitative explanation of the loading process with special focus on the phasing of different excitation loads and the response. The results, as will be seen in figure 3, fit the experiment sufficiently well to be considered valid as a parametric and efficient non-linear model.

4. Numerical results

The FNV model was run with all the modelled sea states. It is known to be too conservative in general, but in the present analysis there were some events that were accurately depicted by the FNV. The maximum moment recorded for the sea state H_S = 0.171m, T_P = 1.62s and h = 0.625m occurred at about t = 994s and is shown in figure 3. During this event, it was visible from the video recording that a breaking wave impacted the turbine, and that the turbine started oscillating at its eigenperiod. In [17], slamming tests were carried out in a wave flume, and it was shown that the time duration of the impact is very small compared to the first eigenperiod of the structure. According to classical structure theory (see for example [18] p47), this will not create significant response of the system in its first mode compared to the quasi-static response due to non-breaking waves. In the following we try to show that non-impact higher order loads alone can explain the observed first mode motion.

It appears from this figure 3 that the FNV gives a good approximation of the maximum moment whereas the Morison model (applied here with the same linear wave kinematics as the FNV model and with Wheeler stretching) underpredicts it. This is described in [16]. As the structure continues oscillating at its eigenfrequency, the FNV model starts to clearly overpredict the results while a closer fit is obtained with the Morison equation. As this paper analyses the maximum load and the mechanism that triggers the first mode motion of the structure, we focus on the first seconds of the event described here, which are correctly depicted by the FNV.

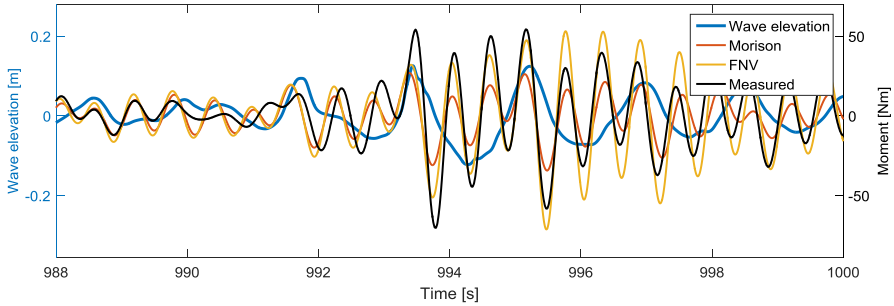

Fig 3. Maximum recorded event from measurements and simulated, for H_S = 0.171m, T_P = 1.62s and h = 0.625m

Figure 4 shows the different terms of the FNV for the maximum event ($Mf1$ is not shown as it is already clear from figure 3 that the Morison equation alone is not able to fully capture the first mode motion). From this figure one can see that $Mf2Free$, $Mf31$ and $Mf3Xsi$ experience a dramatic increase around 993s. These moments are referred to later in this paper as higher order moments. As a first approximation, these three excitation loads are represented by a pulse load with a sinusoidal shape and variying periods (by pulse load we refer to a load that has zero amplitude except for a duration of the order of magnitude of a characteristic period of the system or smaller, like the load showed in figures 5 and 6). The aim of this approximation is to assess whether these loads are able to trigger the 1st mode motion.

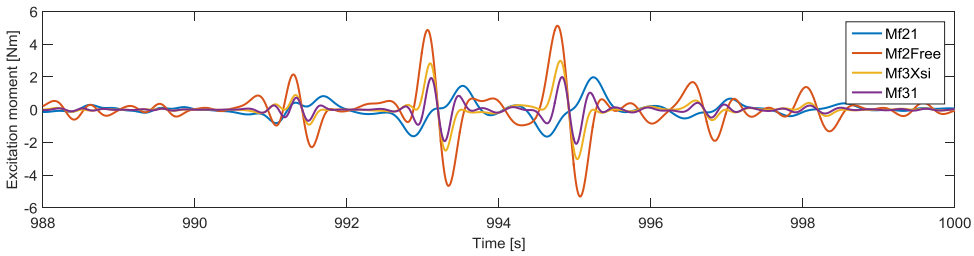

Fig 4. Excitation moments derived from the FNV

A pulse load of sinusoidal shape and arbitrary amplitude M_i is input to the numerical model. This simulation is ran many times with the pulse load duration t_d as a parameter. The maximum measured response is then divided by the static response (response to a constant load of same amplitude), giving the maximum dynamic load factor DLF_{max} (see [18]). Figure 5 shows the maximum dynamic load factor as a function of the pulse load duration (on the x axis, the load duration has been normalized by the eigenperiod of the system). The important point of this figure is that one can compare relative values of the response of the system for different duration of the pulse. Trying to fit a sinusoidal shape on the loads of figure 4, we find that the pulse loads equivalent to $Mf2Free$, $Mf31$ and $Mf3Xsi$ have durations of 0.6s, 0.45s and 0.36s respectively. With an eigenperiod of 0.56s, that gives for $Mf2Free$, $Mf31$ and $Mf3Xsi$ an amplification of 2.8, 2.2 and 1.7 respectively. This shows that for a load duration close to the eigenperiod of the system, the response will experience a significant amplification, which can partly explain the high values of the overturning moment after a steep wave.

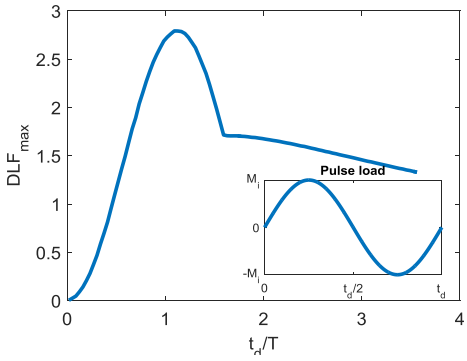

Fig 5. DLF max depending on pulse load duration

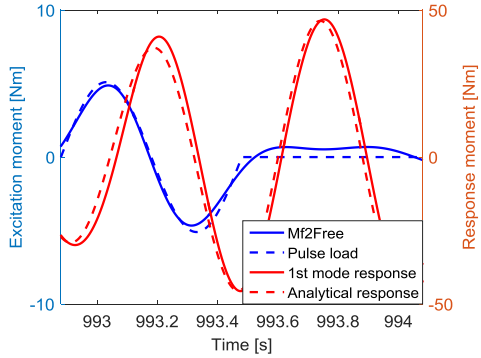

Fig 6. Comparison between the analytical response to a pulse load and the measured 1st mode response

In order to verify the assumption just formulated, an attempt to separate the 1st mode motion from the total response was made. In theory, since the model is a stiff cylinder mounted on a rotational spring, it should have only one degree of freedom and therefore only one eigenmode. However, due to the impossibility of having an infinitely stiff structure in reality, a second mode could be measured with a 2nd eigenfrequency lying around 80 Hz. It should be noted that this second mode has no full-scale meaning and is therefore not representative of the 2nd mode of a full-scale turbine. The response at the second mode was also extracted and contributed very little to the total moment, but it was seen by comparing it to the video recording that slamming events triggered second mode motion. This can also be seen in the third plot of figure 7, where the second mode response experiences a sudden increase when the breaking wave impacts the model.

In the following part, we focus on $Mf2Free$ since it is the load that will produce the highest response, but it should be noted that the other higher order loads will also produce a dynamic amplification of the first mode motion, as was shown in the previous paragraph. It is known that for short waves, diffraction effects will reduce the 2nd order force (see [14]). For the studied event, and estimated from zero-upcrossing of the local wave period, the wave number-radius product is $kR = 0.13$, which lies within the range where $Mf2Free$ is expected to give accurate results.

Figure 7 shows the mode decomposition of the response for the maximum event. The decomposition was obtained by filtering the measured moment, and was shown to be very little sensitive to the filtering methods used.

The second plot of figure 7 shows $Mf2Free$ and the 1st mode motion response. As suggested by the previous analysis, it seems like the 1st mode motion is greatly amplified by $Mf2Free$, with a delay of about 0.16 s. This delay can be explained mathematically using the classical equation for the response of an undamped linear system, that can be found in [18]:

$$M(t) = M_0 \cos(\omega t) + \frac{\dot{M}_0}{\omega} \sin(\omega t) + \omega M_a \int_0^t f(\tau) \sin[\omega(t-\tau)] d\tau \tag{8}$$

with
- M the response moment of the structure
- M_0 response moment at the initial state
- M_a load amplitude
- f load shape function
- ω eigenperiod of the system

We use the same assumption for the load shape than previously, that is, that the load from 0 to td is a sinusoid of period 0.6s. From figure 4 we find that the amplitude of $Mf2Free$ which we will take as the amplitude of the sinusoidal load is about $M_a = 5Nm$ (model scale). We take as the initial conditions the situation of the structure at the upscrossing time of $Mf2Free$, around 992.9s, which gives $M_0 = -27.1Nm$ and $\dot{M}_0 = -119.5Nm \cdot s^{-1}$ (model scale). The displacement from t = 0 to t = 0.6 is then

$$M(t) = M_0 \cos(\omega t) + \frac{\dot{M}_0}{\omega} \sin(\omega t) + \omega M_a \frac{\left(2\pi / t_d\right) \sin(\omega t) - \omega t \cdot \cos(\omega t)}{2\pi / t_d} \tag{9}$$

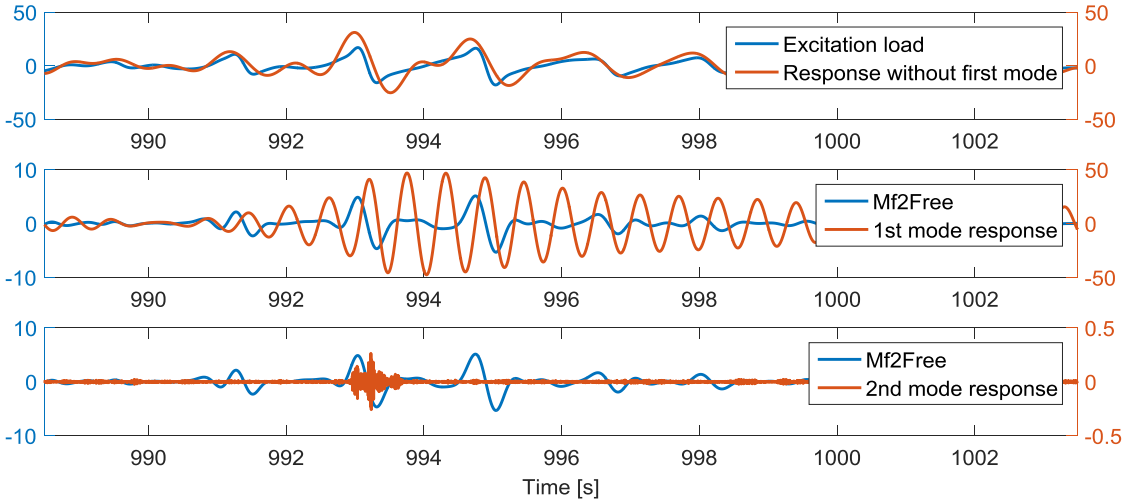

Fig 7. Response decomposition for the maximum event

Figure 6 shows the sine approximation for $Mf2Free$ and the corresponding response. The maximum for the impulsive excitation load occurs at t = 993.03s and the maximum for the analytical response occurs around t = 993.19s, which gives a time delay of 0.16s, equal to what was previously found.

After t = 0.6s, the approximated excitation load is equal to 0 and the structure starts oscillating at its eigenfrequency, without decaying since this model does not include damping. This is similar to what can be seen from figure 7, with some differences due to the fact that the shape of $Mf2Free$ is not a true sinusoid.

The value of the first maximum from figure 7 also fits well the value of figure 6. In order to have an accurate approximation of this maximum, it is critical to have the correct initial conditions. These initial conditions are determined by the history of the response, which is itself highly dependent on damping. The presented experiment

was carried with very low damping. This implies that when the first mode is excited, either by short linear waves or by a previous non-linear wave loading, it is likely that it is still oscillating when a load like the one studied in this event occurs. The response to a new sudden excitation load will then occur on top of the free decay oscillations, potentially increasing the maxima if they occur in phase.

It can be seen from figure 7 and figure 4 that a second impulsive-like 2^{nd} order load occurs around 995s. This load has a longer duration and different initial conditions than the one studied in this analysis, both of which explain that there is not a significant increase in the 1^{st} mode motion. This was checked with the proposed approximation and gave good quantitative results but a too high amplitude in the analytical response. This is in agreement with figure 3, where it can be seen that the FNV method overestimates the response around 995s.

5. Conclusion

The second order term of the FNV equation (equation 3) corresponding to the contribution of the linear potential integrated from the mean water level to the 1^{st} order wave elevation was represented as a pulse load of sinusoidal shape. This simple approximation can explain the phasing and the amplitude of the responses found in the experiment. The observed oscillations appear to be the transient response to a short pulse load (of a time duration close to the eigenperiod of the structure) due to higher order hydrodynamic contributions rather than the response to a slamming load. The steady state response to the second order load term is still relevant but cannot explain extreme load responses in a close to breaking or combined breaking loading situation.

It is important to account for the right damping when assessing these maximum loads, because it defines the state (position and velocity) of the structure when it is hit by the pulse load. A strongly damped structure will most likely decay into a resting position quickly after a transient response. This will induce lower loads when a new pulse load excites it. This will be investigated in further tests with varying damping.

A commonly used method to estimate the response of a bottom-fixed offshore wind turbine to a breaking wave is to add a pulse load to the classical Morison equation (see[7]). It is shown in the present paper that none of these two models suffices to explain the first mode motion occurring after a breaking or near breaking wave hits the cylinder. The study presented brings some new insight into the process of maximum loading by showing that in order to correctly capture the first mode motion of the system, higher order excitation hydrodynamic loads are required.

No slamming model was required to match the experiments, which suggests that a slamming load occurs too rapidly to trigger the first mode motion. However, this study does not aim at replacing state of the art theoretical models for estimating maximum loads on offshore wind turbines. A more thorough analysis, especially in a statistical perspective, is required to further validate it. Furthermore, it is important to recall that the presented experiments were carried out with a single degree of freedom system, with a conservative linear mode shape and where the second mode was not modelled. The second mode motion of the structure can be excited by slamming events and may increase the maximum loads. The latter will be presented in future studies.

Acknowledgements

This study has been financed by Statkraft and the Norwegian Research Council. The authors are grateful to the support brought by Marintek during the realization of the experiments, both in terms of working hours and relevant input to the presented discussion. The model setup was originally financed by Statoil and Statkraft through the Dudgeon offshore wind project.

References

[1] M. Damgaard, L.B. Ibsen, L.V. Andersen, J.K.F. Andersen, Cross-wind modal properties of offshore wind turbines identified by full scale testing, J. Wind Eng. Ind. Aerodyn. 116 (2013) 94–108. doi:10.1016/j.jweia.2013.03.003.

[2] M. Damgaard, J.K.F. Andersen, Natural Frequency And Damping Estimation of an Offshore Wind Turbine Structure, in: International Society of Offshore and Polar Engineers, 2012. https://www.onepetro.org/conference-paper/ISOPE-I-12-126 (accessed July 9, 2015).

[3] C. Devriendt, M. El-Kafafy, G. De Sitter, P. Guillaume, Estimating damping of an offshore wind turbine using an overspeed stop and ambient excitation, in: Proc. 15th Int. Conf. Exp. Mech., 2012. http://www.vliz.be/imisdocs/publications/265470.pdf (accessed September 25, 2015).

[4] R. Shirzadeh, W. Weijtjens, P. Guillaume, C. Devriendt, The dynamics of an offshore wind turbine in parked conditions: a comparison between simulations and measurements, Wind Energy. 18 (2015) 1685–1702. doi:10.1002/we.1781.
[5] Forewind - Dogger Bank Creyke Beck, (n.d.). http://www.forewind.co.uk/projects/dogger-bank-creyke-beck.html (accessed January 19, 2016).
[6] J. Frimann-Dahl, Experimental Validation and Design Review of Wave Loads on Large-Diameter Monopiles, NTNU, Marine Technology, 2015.
[7] Environmental Conditions and Environmental Loads DNV-RP-C205, DNV, 2014.
[8] T.B. Johannessen, Nonlinear Superposition Methods Applied to Continuous Ocean Wave Spectra, J. Offshore Mech. Arct. Eng. 134 (2011) 011302–011302. doi:10.1115/1.4003518.
[9] T.B. Johannessen, On the Use of Linear and Weakly Nonlinear Wave Theory in Continuous Ocean Wave Spectra: Convergence With Respect to Frequency, (2008) 211–217. doi:10.1115/OMAE2008-57355.
[10] A.K. Jha, S.R. Winterstein, Wavemaker 2.0: Simulation and Identification of Second-Order Random Waves, 1996.
[11] O.M. Faltinsen, J.N. Newman, T. Vinje, Nonlinear wave loads on a slender vertical cylinder, J. Fluid Mech. 289 (1995) 179–198. doi:10.1017/S0022112095001297.
[12] B.J. Natvig, A Proposed Ringing Analysis Model For Higher Order Tether Response, Fourth Int. Offshore Polar Eng. Conf. (1994). https://www.onepetro.org/conference-paper/ISOPE-I-94-005 (accessed June 10, 2014).
[13] J.N. Newman, Nonlinear Scattering of Long Waves by a Vertical Cylinder, in: J. Grue, B. Gjevik, J.E. Weber (Eds.), Waves Nonlinear Process. Hydrodyn., Springer Netherlands, 1996: pp. 91–102. http://link.springer.com/chapter/10.1007/978-94-009-0253-4_8 (accessed June 23, 2014).
[14] J.R. Krokstad, C.T. Stansberg, A. Nestegård, T. Marthinsen, A New Nonslender Ringing Load Approach Verified Against Experiments, J. Offshore Mech. Arct. Eng. 120 (1998) 20–29. doi:10.1115/1.2829515.
[15] O. Faltinsen, A. Timokha, Sloshing, Cambridge University Press, 2009.
[16] O.M. Faltinsen, Sea loads on ships and offshore structures, Cambridge, 1990.
[17] J. Wienke, H. Oumeraci, Breaking wave impact force on a vertical and inclined slender pile—theoretical and large-scale model investigations, Coast. Eng. 52 (2005) 435–462. doi:10.1016/j.coastaleng.2004.12.008.
[18] J.M. Biggs, Introduction to structural dynamics, 1964.

Paper 2: Simplified Bottom Fixed Offshore Wind Turbine in Extreme Sea States

By Loup Suja-Thauvin and Jørgen R. Krokstad

In the proceedings of the 26th International Ocean and Polar Engineering Conference, 2016

Paper 3: Experimental results of a multimode monopile offshore wind turbine support structure subjected to steep and breaking irregular waves

By Loup Suja-Thauvin, Jørgen R. Krokstad, Erin E. Bachynski and Erik-Jan de Ridder

In the Journal of Ocean Engineering, vol 146, p 339-351, 2017

Ocean Engineering 146 (2017) 339–351

Contents lists available at ScienceDirect

Ocean Engineering

journal homepage: www.elsevier.com/locate/oceaneng

Experimental results of a multimode monopile offshore wind turbine support structure subjected to steep and breaking irregular waves

Loup Suja-Thauvin [a,*], Jørgen R. Krokstad [a], Erin E. Bachynski [a], Erik-Jan de Ridder [b]

[a] NTNU, Department of Marine Technology, Trondheim, Norway
[b] MARIN, Wageningen, The Netherlands

ARTICLE INFO

Keywords:
Offshore wind turbine
Monopile
Ringing
Slamming
Modal decomposition
Experimental hydrodynamics

ABSTRACT

We present experimental data from MARIN on a bottom-fixed offshore wind turbine mounted on a monopile in intermediate water depth subjected to severe irregular wave conditions. Two models are analysed: the first model is fully flexible and its 1st and 2nd eigenfrequencies and 1st mode shape are representative of those of a full-scale turbine. This model is used to study the structural response with special focus on ringing and response to breaking wave events. The second model is stiff and is used to analyse the hydrodynamic excitation loads, in particular the so-called secondary load cycle. The largest responses are registered when the second mode of the structure is triggered by a breaking wave on top of a ringing response. In such events, the quasi-static response accounts for between 40 and 50% of the total load, the 1st mode response between 30 and 40%, and the 2nd mode response up to 20%. A statistical analysis on the occurrences and characteristics of the secondary load cycle shows that this phenomenon is not directly linked to ringing.

1. Introduction

Over their lifetime, many bottom-fixed offshore wind turbines will encounter steep or breaking waves that might produce large structural responses. A number of offshore wind farms are planned or being developed in the North Sea, in water depths between 20 and 50 m (Ho et al., 2016). At these depths, interaction with the sea bottom enhances the wave nonlinearity, increasing the likelihood of breaking waves (Dalrymple and Dean, 1991). When designing the support structure of an offshore wind turbine for a specific site, the industry has to assess the maximum expected response that the structure will experience over its lifetime (so-called Ultimate Limit State (ULS) analysis, DNV, 2014a; DNV, 2014b; IEC, 2009).

Under ULS conditions, experiments have shown that the natural period of the structure can be suddenly excited by non-breaking waves whose fundamental period lies far from the structure's eigenperiod (Marthinsen et al., 1996; Stansberg et al., 1995; Welch et al., 1999). This phenomenon, called 'ringing', is characterized by a fast build-up of transient resonant vibrations (only a few oscillations; Chaplin et al., 1997) and a much slower decay (Natvig and Teigen, 1993). In the case of a monopile type of support structure such as the one studied in this paper, ringing occurs during the passage of steep waves whose height is of the same order of magnitude as the diameter of the cylinder and whose fundamental period is around 3 times the natural period of the structure. Fig. 1 shows an illustration of a ringing event. The bending moment has been filtered to show only the response of the first mode of the structure (this procedure is explained in section 4). After the passage of a very steep wave, the first mode gets suddenly excited and then decays slowly.

The ringing phenomenon started gaining attention in the 1990s when it was first observed on model tests of the Hutton and Heidrun TLP offshore oil and gas platforms, and then on the deep water concrete towers of the Draugen and Troll A platforms (Natvig and Teigen, 1993). Recently, the increase in size of offshore wind turbines combined with the limitation of the blade tip velocity has led to decreasing natural frequencies of the support structure down to a level where the 3rd harmonic of large waves (i.e. three times the fundamental frequency) coincides with the first structural natural frequency. This intensifies the risk of ringing response when subjected to extreme storms (see Suja-Thauvin et al., 2014). In addition to higher order hydrodynamic loads, breaking wave events have been a major concern for offshore structures. Both de Ridder et al. (2011) and Bredmose et al. (2013) carried out experiments on a bottom-fixed responding structure (as opposed to a stiff structure) whose characteristics were similar to those of an idling extra-large wind turbine (i.e. with the blades completely pitched to feather to limit the aerodynamic loading) and found that breaking waves could lead to extreme accelerations of the nacelle.

* Corresponding author.
E-mail address: loups@stud.ntnu.no (L. Suja-Thauvin).

https://doi.org/10.1016/j.oceaneng.2017.09.024
Received 7 November 2016; Received in revised form 12 September 2017; Accepted 16 September 2017
Available online 7 October 2017

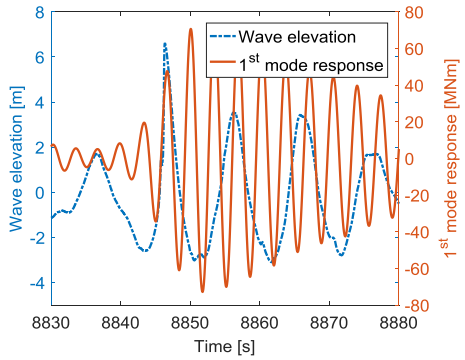

Fig. 1. Illustration of a ringing event. A surface-piercing vertical cylinder is exposed to a steep wave, and the bending moment is measured at the sea bottom. The 1st mode is suddenly triggered and slowly decays, which is a typical characteristic of ringing events.

The main objective of this paper is to examine the process of maximum response of monopile offshore wind turbines under extreme stochastic sea states, in particular assessing the importance of the second mode of the structure and the characteristics of the measured excitation. In order to do so, we analyse data from experiments carried out in the Maritime Research Institute Netherlands (MARIN). The tests were performed within the project Wave Impact on Fixed structures (WiFi JIP). The characteristics of the model used for the experiments are those of an idling 4 MW bottom-fixed offshore wind turbine mounted on a monopile. These tests were performed with both a flexible and a stiff model in order to be able to measure the response and the excitation of the structure. Here, we focus on the measured excitation and response rather than on the wave kinematics. A correct understanding of the most important physical effects is an important first step in developing and validating engineering models which incorporate the relevant nonlinearities in the wave kinematics and in the wave-structure interaction.

In addition to the response analysis, we examine the phenomenon known as "secondary load cycle", or SLC, which appears as a rapid and high frequency increase of the excitation force, as Grue et al. (1993) described from their experiments. An occurrence of a SLC (sometime referred to as 'hydraulic jump') is highlighted in Fig. 2. The SLC typically occurs about one quarter wave period after the main peak of the excitation force (Grue and Huseby, 2002) and lasts for about 15% of the wave period (Grue et al., 1993).

Occurrences of SLCs have been extensively reported for steep waves

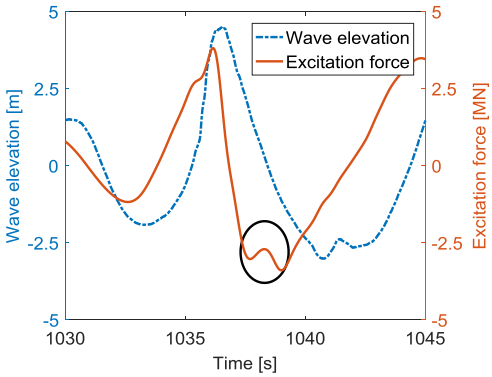

Fig. 2. Occurrence of secondary load cycle, visible on the excitation force (circled in black).

in experiments in infinite water depths (see Chaplin et al., 1997; Grue et al., 1993; Grue and Huseby, 2002; Stansberg et al., 1995; Welch et al., 1999). Grue and Huseby (2002) also summarized the experimental data from those papers to establish a trend of occurrences of the SLC. One of their conclusions is that flow separation effects might reduce the likelihood of SLCs on small cylinders, and they suggest that for experimental analysis of the SLC the β-number should be larger than 15 000 ($\beta = (2R)^2/\nu T$, with R the cylinder radius, T the local period of the wave, and ν the kinematic viscosity of the water). For the events presented in this paper, the longest wave corresponds to $\beta \approx 19\,000$ and the Keulegan-Carpenter number is approximately 5, which places us in what they describe as cylinders of moderate size.

There has been a lot of work published around the relevance of the SLC for ringing responses. Grue and Huseby (2002) used the experimental data of the above-mentioned papers to show that SLCs and ringing responses are correlated, and state that "The secondary load cycle gives an important contribution to build-up of resonant body responses […]". High speed photography from the experiments of Chaplin et al. (1997) and Rainey and Chaplin (2003) was used by Rainey (2007) to conclude that "the rapid loading cycle causing the "ringing" vibration is traceable to local wave breaking around the cylinder […]". However, in a recent study, Paulsen et al. (2014) investigate the SLC numerically by solving the two-phase incompressible Navier-Stokes equations and conclude that "[…] the secondary load cycle is thus an indicator of strongly nonlinear flow rather than a direct contributor to the resonant forcing". This agrees with earlier findings from Krokstad and Solaas (2000), where a study of the phasing between the SLC and the ringing response led them to conclude that "The hydraulic jump [i.e. secondary load cycle] has no direct connection with the non-linear behaviour of the ringing force […]".

The paper is organized as follows: in Section 2 we describe the experimental set up and the models used during the tests and Section 3 gives a simple justification of how to estimate slamming events from video recording. Section 4 presents the analysis of the response of the flexible structure. Section 5 combines results from the stiff and the flexible structure to establish the link between secondary load cycle and ringing events. Conclusions of this study are drawn in Section 6.

2. Presentation of the model test

The model tests were carried out at 1:30.6 scale, and Froude scaling was applied in order to correctly generate gravity waves. For the considered model and wave conditions, inertia forces dominate compared to viscous forces (DNV, 2014a; DNV, 2014b; IEC, 2009) and the effects of the Reynolds number mismatch are not examined here. All the values given in the paper are full-scale unless specified otherwise.

2.1. Test facilities

The tests were performed at the shallow water basin of MARIN, a 220 m long and 15.8 m wide wave flume (model scale) with constant water depth. One end of the flume was equipped with a piston-type wavemaker, consisting of a flat plate forced into horizontal translational motion by an electrical actuator. The wave maker includes 2nd order wave generation techniques that enable a correction for the difference between the oval motion of water particles in shallow/intermediate waters and the horizontal motion induced by the flat plate. It is possible to suppress parasitic wave generation using this technique (see Schäffer, 1996). On the other side of the flume, an absorbing parabolic beach was fitted in order to minimize wave reflection. Two pits were dug into the ground approximately 65 m (model scale) from the wave maker, and the two models were mounted onto two 6-component force frames solidly anchored into the pits. Fig. 3 shows the layout of the experiment. No aerodynamic loading was modelled during the tests.

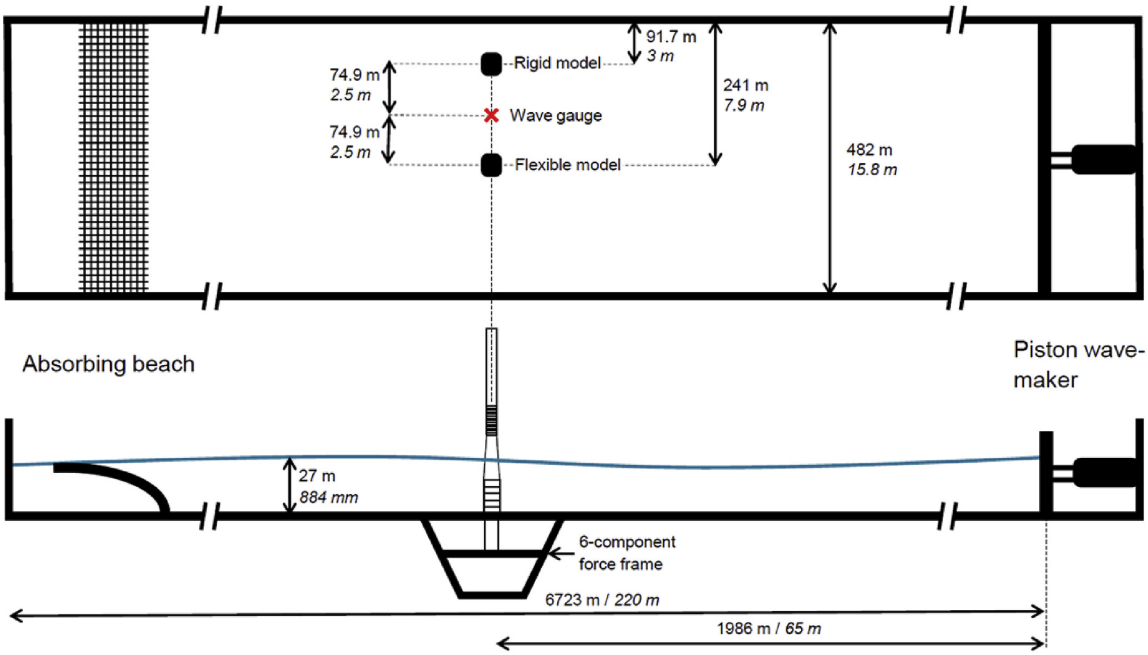

Fig. 3. Top and side view of the experimental set-up (values are given both in full and model scale).

2.2. Physical models

2.2.1. Flexible model

A flexible model of an extra-large bottom-fixed offshore wind turbine mounted on a monopile was built according to typical dimensions of a 4 MW turbine. The model is composed of two cylindrical sections of diameters 7 m and 5.5 m, linked via a conical section (see Fig. 4). This gives a diameter at the mean sea level of 5.8 m. The pile reaches 10.1 m below seabed at a water depth of 27 m and extends up to 87 m above the mean sea level, for a total length of 124 m. The rotor-nacelle assembly is modelled by a mass of 278 tons placed at the top of the tower.

Special emphasis was put on achieving correct 1st and 2nd eigenfrequencies and the 1st mode shape. Table 1 gives the eigenfrequencies and damping values derived from hammer tests in water (Bunnik et al., 2015), and Fig. 5 shows the targeted and obtained mode shapes of the flexible model. Due to physical restrictions in the laboratory, it is not straightforward to exactly match all mode shapes. The largest discrepancies occur at hub height which has little influence on the response to hydrodynamic loads. The obtained deflections at the mean sea level and down to the sea bed are seen to be acceptable.

The measured 3rd and 4th mode characteristics are also shown in Table 1 but they are not representative of the full-scale wind turbine. More details about the physical meaning of the 3rd and 4th mode are given in Section 4.4.

The damping for the first and second modes is found to be 1.1% of the critical damping. For the first mode, this is somewhat lower than the damping ratios measured on similar idling full-scale wind turbines (1.7–2.8% depending on the wind speed, Damgaard et al., 2013; Damgaard and Andersen, 2012; Shirzadeh et al., 2015). As a result, the obtained responses are expected to be slightly conservative, but previous research suggests that the damping is more important for the decay of the response than for the maximum values (Bachynski and Moan, 2014; Schløer et al., 2016).

2.2.2. Stiff model

A stiff model was also constructed, whose geometry is the same as the flexible model but extended only up to the expected maximum wave run-up. The objective of having a non-responding model was to be able to measure the hydrodynamic excitation.

Ideally, the 1st eigenfrequency of the stiff model should be as high as possible, such that it responds as little as possible to the hydrodynamic loading. The obtained fundamental eigenfrequency was 1.8 Hz (full-scale value). Fig. 6 shows the smoothed spectrum of the measured wave elevation of one of the studied sea states (with a spectral peak period $T_P = 10$ s, see section 2.3). The wave spectrum does not contain significant energy at or above 0.4 Hz, i.e. one-third of the eigenfrequency of the stiff model, so 2nd and 3rd order excitation loads are not expected to excite significant response.

During the tests, it was observed that the stiff model was nonetheless responding at times in its 1st mode. The loads measured on the stiff model can therefore not be taken as the excitation loads because they contain the dynamic amplification of the 1st mode of the structure. In order to remove the response of the stiff model from the measured response and keep only the excitation loads, a low-pass 6th order Butterworth filter was applied with a cut-off frequency at 1.2 Hz. This simple technique brings a major limitation: loads from breaking waves typically have very short durations, so by removing high frequencies from the excitation loads, the load contribution from breaking waves is potentially removed as well. The data from the stiff model therefore cannot be used to study slamming loads, but it can be used to examine 2nd and 3rd order loads.

2.2.3. Data acquisition

Foundation loads: Both models were placed on a 6 component measurement frame that enabled recording of forces and moments at the seabed.

Wave probes: 4 resistance-type wave probes were placed around the

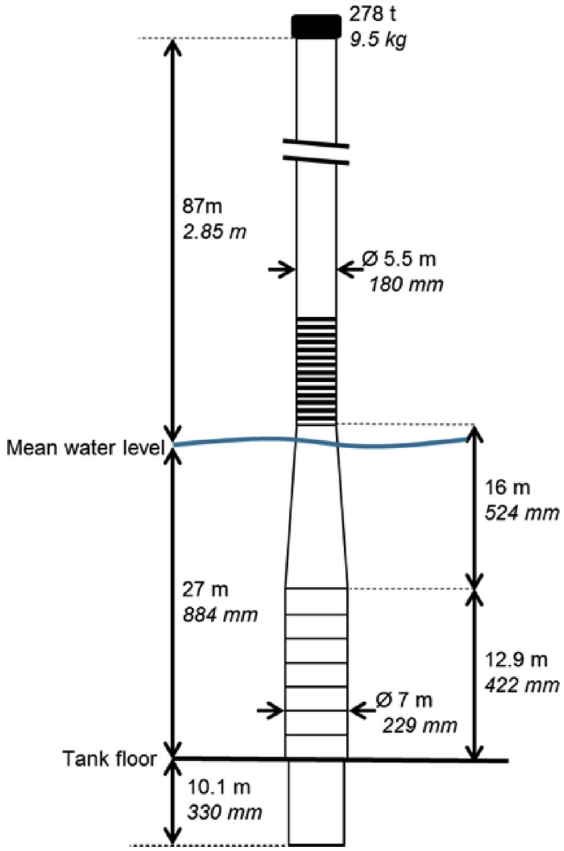

Fig. 4. Characteristics of the flexible model (values are given both in full and model scale).

Table 1
Achieved frequencies and damping ratios of the flexible model (obtained from hammer tests).

	1st mode	2nd mode	3rd mode	4th mode
Eigenfrequency [Hz]	0.29	1.21	3.11	7.24
Damping (% of critical)	1.1	1.1	2	2

models to measure the wave elevation. One of the wave probes (marked with a red cross in Fig. 3) was placed between the 2 models, at 2.4 m (model scale) from both of them (corresponding to around 13 diameters). It is expected that this wave probe is far enough from the models to not be affected by radiated and diffracted waves.

Video recording: Most sea states were recorded with two above-water cameras, one for each model. These video recordings were used to visually check whether a wave has broken when a large response of the structure was recorded (see section 3).

Accelerations: both models were fitted with accelerometers along their length. In the present study, those accelerometers were used to confirm that the flexible monopile only experienced significant displacement in the wave direction and to derive its mode shapes.

The wave elevations, loads and accelerations were recorded at a sampling rate of 200 Hz (model scale value), resulting in a time step of 5 ms in model scale, or 0.028 s in full scale.

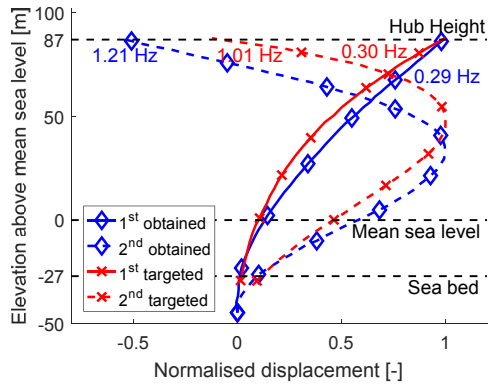

Fig. 5. Dimensionless mode shapes. Blue colour represents the obtained mode shapes and red colour represents the targeted ones. (For interpretation of the references to colour in this figure legend, the reader is referred to the web version of this article.)

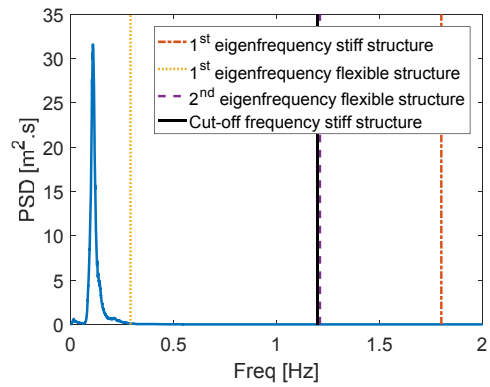

Fig. 6. Example of an incoming wave spectrum.

2.3. Sea states

During the experiments, different irregular sea states were generated following a JONSWAP spectrum (Hasselmann et al., 1973). The JONSWAP spectrum describes sea conditions that are likely to occur for severe sea states in the North Sea and is typically recommended by the standards for ULS analysis (DNV, 2014a; DNV, 2014b; IEC, 2009). Table 2 shows the sea states that are analysed in this paper. For each sea state, only one realization was performed. Each sea state is characterized by a spectral peak period T_P and a significant wave height H_S. All sea states were realized with a spectral peak enhancement factor of 3.3.

We define an average wave steepness s_P for irregular seas based on (DNV, 2014b):

$$s_P = \frac{k_P H_s}{2\pi} \tag{1}$$

where k_P is an average wave number obtained from T_P from the dispersion relationship (DNV, 2014b uses a linear dispersion relationship but we here apply eq (1) in Kirby and Dalrymple, 1986, which is based on 2nd order theory). For the analysed spectral peak periods, at the considered water depths, sea states with a steepness larger than 0.059 are not possible (DNV, 2014b). The average steepnesses used in this paper are well below this limit.

In addition, we calculate an averaged Ursell parameter Ur for the

Table 2
Selected sea states.

H_S	T_P	s_P	Ur
5.89	10	0.043	0.070
6.18	10	0.045	0.074
5.81	10.93	0.038	0.088

presented sea states. The Ursell parameter is typically defined for regular waves, but here we use the method given by Stansberg (2011) to calculate an average value for irregular seas:

$$\mathrm{Ur} = \frac{k_p H_s}{2\left(k_p h\right)^3} \tag{2}$$

where h is the water depth. The average Ursell numbers thus calculated are well below the classical limit of 0.33, above which 2nd order wave kinematic models are no longer valid and fully non-linear models are suggested.

To give an indication of what these sea states represent in terms of return period, the H_S-T_P graph based on the metocean conditions at the Dogger Bank Creyke Beck B site is given in Fig. 7 (see Frimann-Dahl, 2015). The yellow and blue lines correspond to 1-year and 5-year return period sea states, respectively, and the sea states are indicated with asterisks. More sea states than the ones analysed in this paper were run, but they are not presented here as they did not produce large responses of the structure.

When carrying out ULS analysis, the standards commonly used by the industry in the North Sea (DNV, 2014a; DNV, 2014b; IEC, 2009) recommend assessing sea states corresponding to 50-year return storms. The sea states considered in this paper correspond to generally much lower sea states, as illustrated by Fig. 7, which is a limitation of this study. More extreme sea states were later tested with the same experimental set-up and will be included in future work.

It should also be noted that the wind conditions for the analysed sea states have not been determined. For the present paper and in the experiments, the turbine is assumed to be idling, which is likely not to be the case under the studied wave conditions. On an idling turbine, aerodynamic damping is usually small compared to an operating turbine (Shirzadeh et al., 2015) which makes 1st mode oscillations due to ringing decay slower than on an operating turbine (Bachynski and Moan, 2014; Schløer et al., 2016). This means that the ringing events observed during the experiments would decay faster if the turbine was operating.

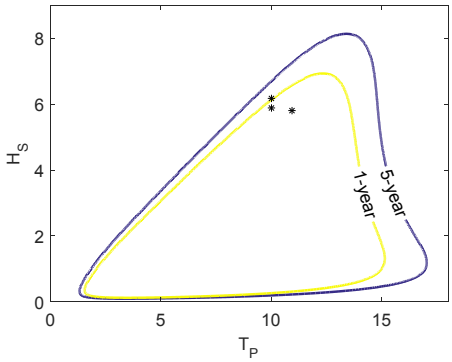

Fig. 7. Contour lines for the metocean conditions at the Dogger Bank Creyke Beck B site. The asterisks represent the studied sea states.

3. Use of video recording to detect slamming on the flexible structure

Loads from breaking waves have been a major concern in the design of offshore structures over the past decades. We define 'slamming loads' for this paper using the explanation provided by Sarpkaya (1979): we consider a cylinder of radius R fixed to the sea bottom that we divide vertically into strips of length dz. We assume now that a vertical wall of incompressible water parallel to the cylinder with a control volume of constant mass per unit length M approaches a strip at a velocity u_0, the mass of water has then a horizontal momentum per unit length $p = Mu_0$. The duration of the impact being very short (Faltinsen, 1990; Sarpkaya, 2010) compared to the eigenperiod of the structure, it is reasonable to assume that, during the impact, no significant response will occur (according to classical structural theory, see for example Biggs, 1964) and that the cylinder will thus behave as a stiff structure. If we neglect nonconservative forces, the momentum of the water will remain constant during penetration. After the breaking wave has impacted the structure, because the fluid is in motion in the vicinity of the cylinder, a positive 2D added-mass term m_a appears, thus reducing the velocity to u and giving a new equation for the momentum $p = Mu_0 = (M + m_a)u$. Here m_a is taken as the high-frequency asymptote for the added mass (Faltinsen, 1990). Fig. 8 illustrates the terms defined here, with the expression of the momentum p before and after impact. We can calculate the horizontal force using Newton's second law:

$$dF = \frac{dp}{dt}dz = \left((m_a + M)\frac{du}{dt} + u\frac{dm_a}{dt}\right)dz \tag{3}$$

The first term of the above equation, proportional to the acceleration of the fluid, is the classical added mass load (see for example Faltinsen, 1990). The second term incorporating the time derivative of the added mass is the so-called slamming load dF_{slam}. If the latter is non-negligible compared to the former, the event is considered a slamming event.

This derivation provides a good mathematical understanding of slamming but is of little use in practice because the evaluation of the time-varying added mass is rather complex (Sarpkaya, 2010). However, it provides a way to visually check whether slamming loads occur. In order to have a large slamming force on a cylinder strip, we need to have a large velocity u in the horizontal direction and a rapidly changing two-dimensional added mass in the horizontal plane. For the considered monopile, the most suitable situation for slamming loads to occur is when a breaking wave impacts on the cylinder.

Under these conditions, most of the momentum of the water in motion will be in the horizontal direction. When the water particles impact the cylinder, they are restricted in the horizontal direction by the incoming water on the back side and by the cylinder itself on the front side. In order to conserve the total momentum, these particles must be deflected and ejected upwards and sideways, which gives a good visual indication of whether a slamming load has occurred. In the present paper, video recordings of the experiments are used to check whether slamming has occurred using the above hypothesis. Fig. 10a and b shows two such events.

4. Maximum response analysis

This section deals with the response of the flexible model and only data measured on this model is used here. Here and in the rest of the paper, the term 'response' corresponds to the bending moment of the flexible model taken at the seabed. A positive bending moment corresponds to the structure being deflected in the direction of the wave propagation. Since the amplitude of the moment is what is relevant to the design of a monopile rather than its direction, we compare absolute values of those moments. We therefore refer to 'maximum' or 'highest' moments even when the moment is negative.

In order to study the influence of different modes on the response of

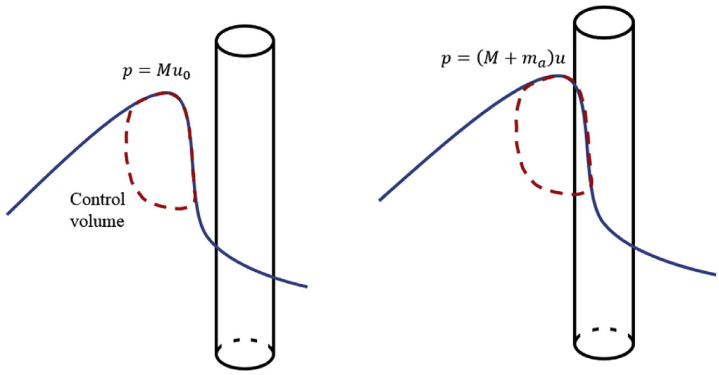

Fig. 8. Breaking wave on circular cylinder before impact (left) and after impact (right).

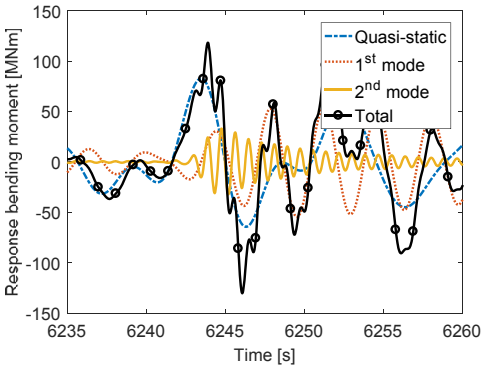

Fig. 9. Example of decomposition of the response around the eigenfrequencies of the structure.

the structure, the measured bending moment in the frequency domain was split into responses around different frequencies corresponding to the eigenfrequencies of the system. Fig. 9 below is the result of such decomposition performed on one of the events studied in this paper. The sum of the quasi-static, 1st and 2nd mode responses equal the total response. This figure enables us to assess the relative importance of the responses of different modes of the structure.

4.1. Maximum responses

In this section, the two events with the largest responses of all three sea states (named event 1 and event 2 and shown in Fig. 10a and b respectively) are analysed in detail. Table 3 gives the characteristics of these two events. The trough-to-trough period is measured for each event and used to calculate the wave number k based on 2nd order theory (calculated with eq (1) in Kirby and Dalrymple, 1986), and η_m is the maximum wave elevation of the given event. The trough-to-trough period rather than the up- or down-crossing period was chosen because this type of wave is typically approximated by embedded stream function waves in design practices. The embedding process commonly uses the trough-to-trough period (Rainey and Camp, 2007).

Fig. 10 shows these two events side to side. The figures from top to bottom correspond to snapshots of the cylinder at the time of impact, the measured response and wave elevation, the frequency decomposition (as shown in Fig. 9) and the continuous wavelet transform (cwt) of the measured response. Responses from the 3rd and 4th modes of the structure have been removed by low-pass filtering, see Section 4.4. Even though the contribution of these modes has been removed, we still refer to this filtered response as 'total response'.

For these events, the maximum response is measured when a steep and breaking wave passes the structure (see Fig. 10c and d). The wave excites the 1st mode of the structure, which starts oscillating and decays in similar fashion to the ringing phenomenon described in section 1. As shown in Fig. 10e and f, the structure also oscillates in its 2nd mode, but in a different way than the 1st mode response: the 2nd mode resonant oscillations occur suddenly after the breaking wave has passed, whereas the 1st mode response experiences a build-up over one wave period and then slowly decays. The influence of the second mode is studied in more detail in the following section.

The cwt plots of Fig. 10g and h also show that the structure responds at the frequency of the wave (about 0.1 Hz for the selected events) and that its 1st and 2nd modes are triggered (respectively at 0.29 and 1.21 Hz). The snapshots of Fig. 10a and b indicate that the wave breaks at the cylinder. As explained in the previous section, the water particle ejection visible in the photographs is characteristic of slamming events.

In addition to the two events shown in Fig. 10, the 21 events with the largest responses were analysed. For all events it was found that the 1st and 2nd mode responses were triggered after the passage of a steep and breaking wave, as described above. The characteristics of these 21 events are given in Table 5.

Previous work done by Suja-Thauvin et al. (2016) and further developed by Suja-Thauvin and Krokstad (2016), showed that the first mode response of a similar structure can be explained solely by 2nd and 3rd order hydrodynamic excitation loads, without the need to account for slamming loads. We apply their findings to the present study to conclude that the ringing response observed for large events is mainly due to 2nd and 3rd order hydrodynamic loads and not to slamming loads. However, as their work is done on a one degree-of-freedom system, it does not include any consideration of the 2nd mode of the structure.

4.2. Contributions to the total response

In this section, we analyse the contribution of the different modes of the structure to the total response. To do so, we decompose the response as shown in Figs. 9 and 10c and d and evaluate the value of the response at different modes at the instant of maximum total response. Their relative importance for events 1 and 2 is given in Table 4. Moments (here and in the rest of the paper) are given within an accuracy of 3%.

Fig. 11 offers a graphical interpretation of Table 4 for the 21 largest events. This figure shows the different contributions to the total response: quasi-static response accounts for between 40 and 60%, 1st mode response accounts for between 30 and 40% and the second mode contributes up to 20%. The numerical values for each event are given in Table 5.

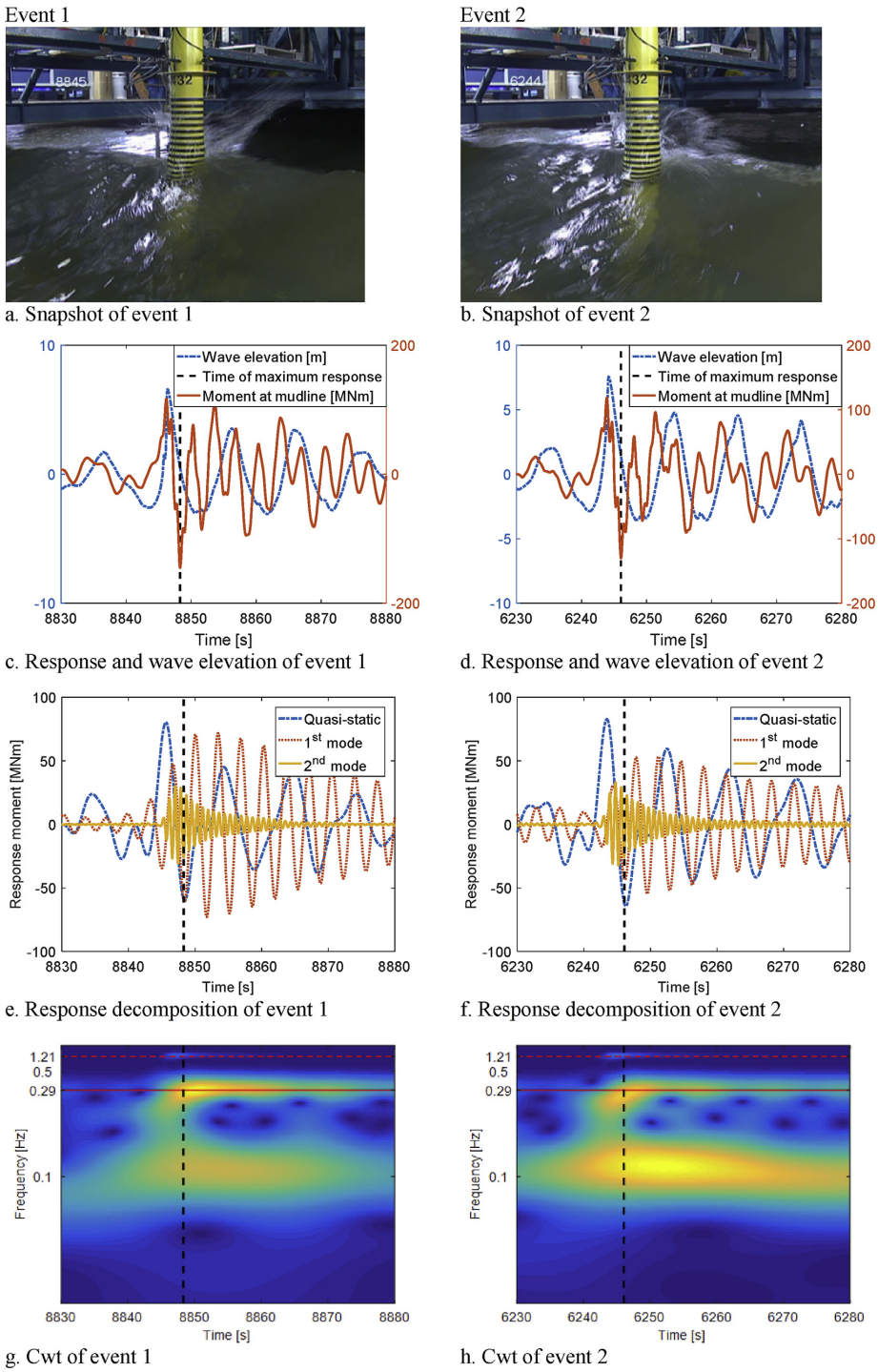

Fig. 10. Characteristics of the largest and 2nd largest measured responses, respectively Event 1 and 2.

Table 3
Events with maximum bending moments.

Event	Sea state	Max [*MNm*]	Time [*s*]	Period [*s*]	η_m [*m*]	k [m^{-1}]
1	$H_S = 5.89\ m, T_P = 10s$	−145	8848	7.80	6.61	0.0599
2	$H_S = 6.18\ m,\ T_P = 10\ s$	−130	6246	8.13	7.57	0.0550

Table 4
Different contributions to the maximum load.

Event	Total moment [MNm]	% quasi-static	% 1st mode	% 2nd mode
1	−145	41.1	41.6	17.2
2	−130	48.3	33.2	18.5

These observations suggest, as was also found in de Ridder et al. (2011), that not taking into account the 2nd mode of the structure when assessing ULS leads to underestimation of the total response. For these 21 events, we also note that the maximum response is negative, i.e. it corresponds to the structure moving against the wave propagation direction.

It should be noted that Table 5 only shows the characteristics of the individual waves that occur at the same time as the maximum response.

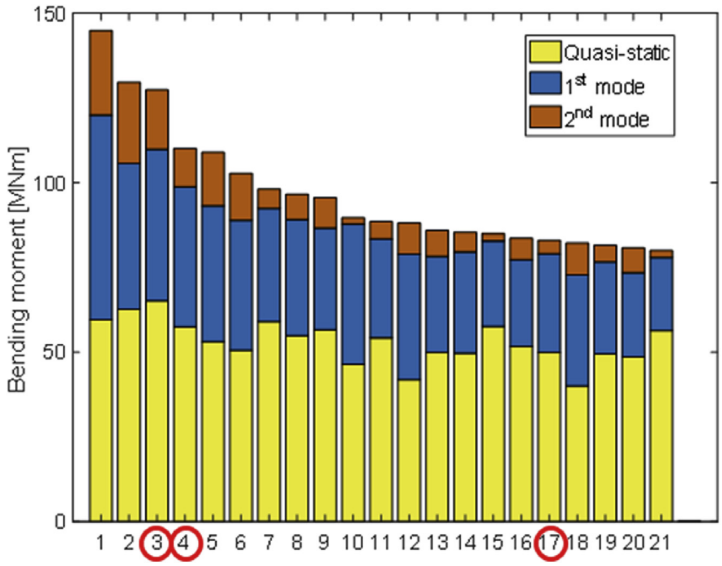

Fig. 11. Decomposition of the largest responses into quasi-static, 1st and 2nd mode response. The red circles correspond to events where no secondary load cycle was observed (see section 5). (For interpretation of the references to colour in this figure legend, the reader is referred to the web version of this article.)

Table 5
Characteristics of the 21 highest recorded responses. $\boldsymbol{T}$, $\boldsymbol{\eta_m}$, $\boldsymbol{H}$ and $\boldsymbol{k}$ correspond to the trough-to-trough wave period, the crest elevation, the wave height and the wave number, respectively.

Event	Max [*MNm*]	Contribution to total moment [%]			Time [*s*]	Sea state H_S - T_P	T [s]	η_m [*m*]	H [*m*]	k [m^{-1}]
		Quasi-static	1st mode	2nd mode						
1	−145	41.1	41.6	17.2	8848	5.89 m–10 s	7.82	6.61	9.32	0.0599
2	−130	48.3	33.2	18.5	6246	6.18 m–10 s	8.15	7.57	10.6	0.055
3	−127	51.1	35.1	13.7	1046	5.89 m–10 s	8.76	8.06	11.96	0.0492
4	−111	52.2	37.6	10.2	3132	6.18 m–10 s	7.24	6.65	9.02	0.0664
5	−110	48.8	36.7	14.5	6962	6.18 m–10 s	9.34	6.33	9.67	0.0474
6	−103	49.2	37.3	13.5	10688	5.89 m–10 s	7.57	5.85	8.45	0.0642
7	−98.2	60.2	34.0	5.8	340	6.18 m–10 s	8.62	6.43	9.53	0.0527
8	−97.0	56.8	35.5	7.7	6961	5.89 m–10 s	9.29	7.4	10.23	0.0465
9	−95.7	59.2	31.4	9.4	4217	5.81 m–10.93 s	7.96	6.52	8.57	0.0587
10	−88.6	51.8	46.1	2.1	6482	5.89 m–10 s	8.82	6.12	9.51	0.0516
11	−88.6	61.3	32.9	5.8	8748	5.89 m–10 s	7.63	5.67	8.3	0.064
12	−86.3	47.5	42.1	10.4	4514	5.81 m–10.93 s	10.59	6	8.64	0.0405
13	−86.0	58.2	33.0	8.9	6685	6.18 m–10 s	7.96	5.83	8.01	0.0599
14	−85.7	58.2	34.9	6.9	5293	6.18 m–10 s	8.71	7.08	10.06	0.0511
15	−85.1	67.8	29.6	2.6	6245	5.89 m–10 s	8.71	6.57	10.09	0.0518
16	−83.6	61.8	30.6	7.6	6562	5.89 m–10 s	8.46	5.79	8.53	0.0551
17	−83.2	60.2	35.1	4.8	8583	5.89 m–10 s	7.43	7	9.54	0.0633
18	−82.5	48.7	39.9	11.4	8616	5.81 m–10.93 s	10.14	5.69	7.74	0.0431
19	−81.6	60.6	33.3	6.1	2304	6.18 m–10 s	7.13	4.67	6.5	0.073
20	−80.9	60.2	30.8	9.0	9499	5.89 m–10 s	8.12	6.09	8.82	0.0578
21	−80.1	70.5	267.0	2.5	11492	5.81 m–10.93 s	10.06	7.18	10.41	0.0421

However, a wave with a given height could produce less response than a wave with smaller height if, for the latter case, the structure was already responding to a previous wave. This "memory effect" is relevant for dynamic systems with low damping. Peng et al. (2013) showed that wave groups could produce larger responses than individual regular waves with the same characteristics as the largest wave of the wave group.

4.3. Physics of the second mode response

Fig. 12 shows the full time series of the 2nd mode response of sea state $H_S = 6.18$ m and $T_P = 10$ s. In this plot, independent peak occurrences of 2nd mode response higher than half of the standard deviation of the quasi-static response have been marked with a red dot. From comparison with the video recordings, it appears that these large second mode responses only occur when a breaking wave hits the cylinder. Indeed, as pointed out by Hallowell et al. (2015), loads from breaking waves have two characteristics that make them especially relevant when analysing 2nd mode motion:

- They have a very short duration (as shown for instance by Wienke and Oumeraci, 2005) compared to 1st, 2nd or 3rd order loads (Suja--Thauvin and Krokstad, 2016). With such a duration, according to classical structure theory (see for example Biggs, 1964), these loads have the potential to trigger significant 2nd mode response.
- They are concentrated around the free water surface, where 2nd mode shape displacement is the highest (see Fig. 5) whereas loads from non-breaking waves are distributed between the free surface and the sea bed.

This visual check was performed for all sea states mentioned in this paper, and it was consistently found that responses of the 2nd mode above the selected threshold corresponded to breaking wave events. We therefore suggest that large 2nd mode responses only occur when a wave breaks at the cylinder. However, it should be noted that not all breaking wave events produce such a large response in the 2nd mode.

The empirical cumulative distribution function of the 2nd mode response is given in Fig. 13 in terms of exceedance probability. Exceedance probabilities for total and the quasi-static response are also shown for comparison. There is a qualitative difference between the 2nd mode response and the other responses: for the main part of the observations (for an exceedance probability higher than about 3% for the most severe sea states or even than 0.5% for the mildest sea state), the probability of exceedance curve of the 2nd mode response follows a linear variation (in

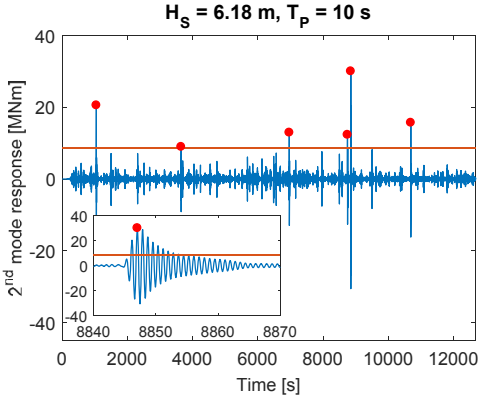

Fig. 12. Response of the structure in its 2nd mode. A zoom of the 2nd mode response of event 1 is also shown. The red line corresponds to half of the standard deviation of the quasi-static response. (For interpretation of the references to colour in this figure legend, the reader is referred to the web version of this article.)

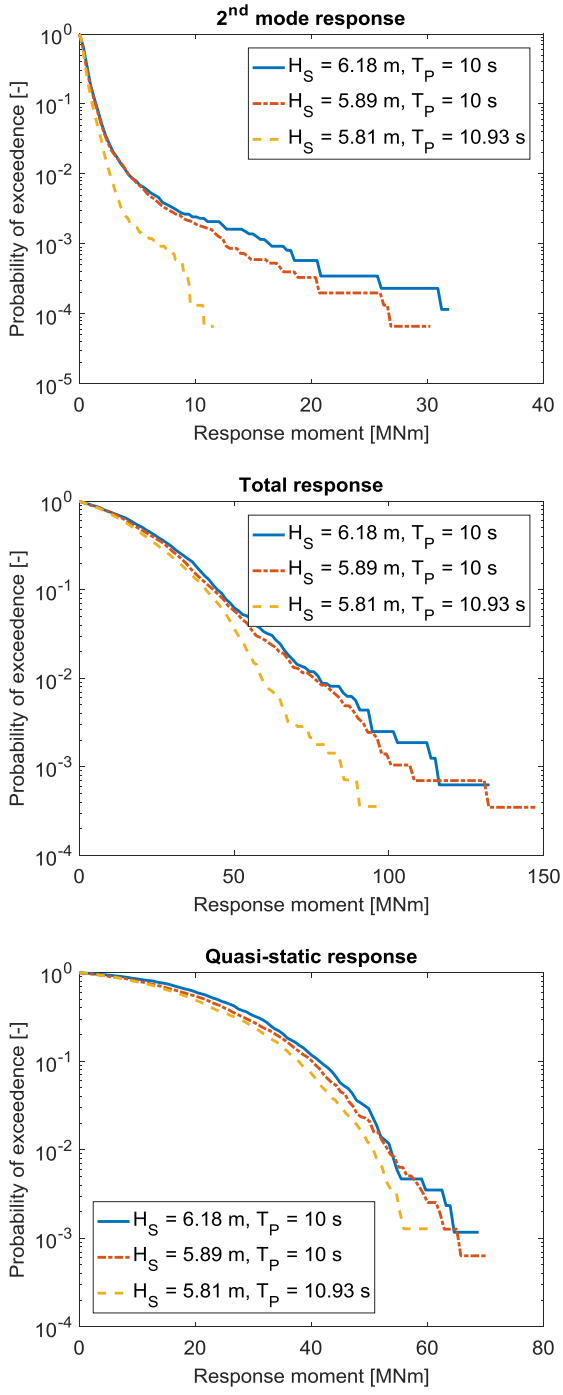

Fig. 13. Empirical exceedance probability curve for response moments.

the logarithmic plot). For lower exceedance probabilities, the 2nd mode response significantly increases. This sudden change in the slope of the probability of exceedance curve is not visible for the total or the quasi-static response.

In order to explain this observation, we compare the 2nd mode response to the quasi-static response. A given wave produces a quasi-static response proportional to the wave particle acceleration for an inertia-dominated structure such as the one presented here. The quasi-static response is therefore roughly linear in terms of wave steepness. The 2nd mode, however, is only triggered by breaking waves, which means that below a certain steepness threshold, no 2nd mode response is expected, but past this threshold the 2nd mode gets excited and large responses will occur. This confirms the non-linear behaviour of 2nd mode response and shows that there will be a large number of outliers in the peak distribution.

In addition, the excess kurtosis gives a good indicator of the behaviour of the outliers of a given distribution. The excess kurtosis (calculated for each sea state using all data points) is calculated by Matlab® with the following formula:

$$k_1 = \frac{\frac{1}{n}\sum_{i=1}^{n}(x_i-\bar{x})^4}{\left(\frac{1}{n}\sum_{i=1}^{n}(x_i-\bar{x})^2\right)^2} - 3 \quad (4)$$

where n is the number of samples, x is the set of data points and $\bar{x}$ is the average of x. A large excess kurtosis means that the distribution produces a large number of outliers and that their value will be more extreme than for a normal distribution. For the presented sea states, the 2nd mode response has a very large excess kurtosis compared to the total and quasi-static responses, as shown in Table 6. This confirms what was suggested in the previous paragraph, i.e. that the extremes of the 2nd mode response lie far from the rest of observations.

4.4. 3rd and 4th modes

The previous analysis considered measured responses after filtering out the 3rd and 4th mode. However, these modes are in fact present and they contribute to the total measured response. As exemplified in Fig. 14 (a zoom of event 2), structural modes higher than the 2nd mode influence the response. These modes decay quickly after the slamming impact.

Fig. 15 shows a zoom of the wavelet plot for event 2 (the scaling of the colours has been changed compared to Fig. 10 for clarity). This plot shows that the 3rd and 4th modes, respectively at 3.11 and 7.24 Hz are also excited by the breaking wave but that their influence is limited compared to the 2nd mode response at 1.21 Hz.

The 3rd and 4th modes on the model were not tuned to fit the modes of a full-scale wind turbine, so the response at these modes is not representative of that of a full-scale wind turbine. Further analysis of the influence of higher modes is needed to assess their influence on the total response of an offshore wind turbine, and whether not including 3rd and 4th modes might lead to non-conservative results.

5. Secondary load cycle analysis

In this section we use data measured on the stiff model and on the flexible model. Both models were in the basin at the same time and experienced the same sea states.

5.1. Occurrences in the present study

The secondary load cycle (SLC) appears as a rapid and high-frequency variation in the excitation force. Fig. 16 shows an occurrence of a SLC together with the definitions of its magnitude (F_{SLC}) and the peak-to-peak force (F_{PP}). The SLC ratio is defined as F_{SLC}/F_{PP} (Grue and Huseby, 2002).

The occurrences of SLCs are found by analysing the force measured by the stiff structure. As explained in Section 2.2.2, this measured force is first low-pass filtered at a frequency of 1.2 Hz to remove the response of the structure, giving the time-series obtained in Fig. 16. Grue et al. (1993) state that the SLC has a duration of about 15% of the wave period. For the present experiments, this corresponds to durations of about 1.5 s. The cut-off frequency is about twice the expected frequency of the SLC; it is therefore expected that the SLC is not removed or significantly altered by the filtering. A visual check of the excitation force time series is performed on each of the events selected hereafter to ensure they correspond to SLCs.

For each of the three sea states, the 25 occurrences of SLCs with the highest magnitudes are kept and plotted in the $kR - kn_m$ plane in Fig. 17. Our observations of SLCs are within the same range as those reported by

Table 6
Excess kurtosis of the measured wave ($\boldsymbol{W}_{meas}$), of the total ($\boldsymbol{M}_{tot}$), quasi-static ($\boldsymbol{M}_0$) 1st mode ($\boldsymbol{M}_1$) and 2nd mode ($\boldsymbol{M}_2$) moments.

	W_{meas}	M_{tot}	M_0	M_1	M_2
$H_S = 6.18\,m,\ T_P = 10\,s$	−0.0543	0.787	0.0667	3.83	190
$H_S = 5.89\,m,\ T_P = 10\,s$	0.0538	0.915	0.185	4.91	147
$H_S = 5.81\,m,\ T_P = 10.93\,s$	0.0020	0.370	0.0704	1.10	33.3

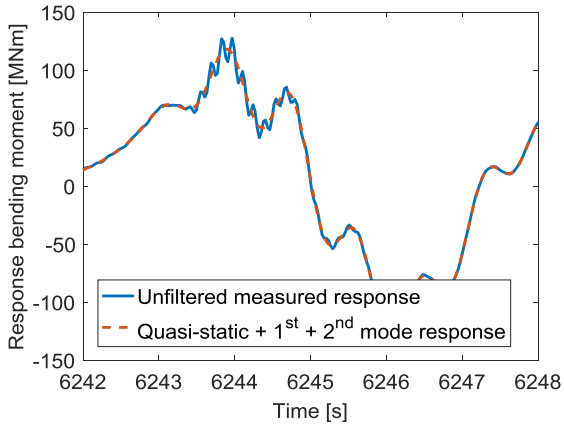

Fig. 14. Zoom of the response of event 2. The difference between the two curves is due to modes higher than 2nd.

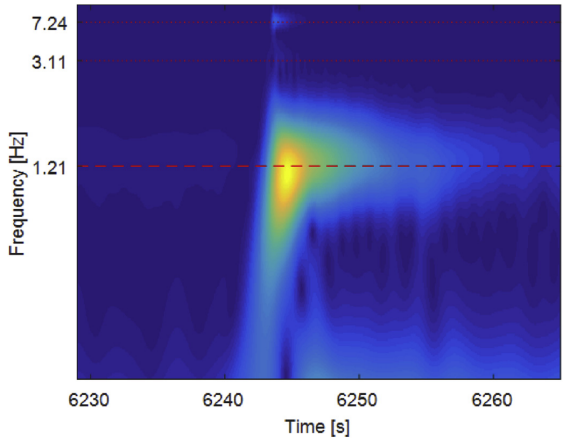

Fig. 15. Zoom of the cwt plot of the unfiltered measured response of event 2.

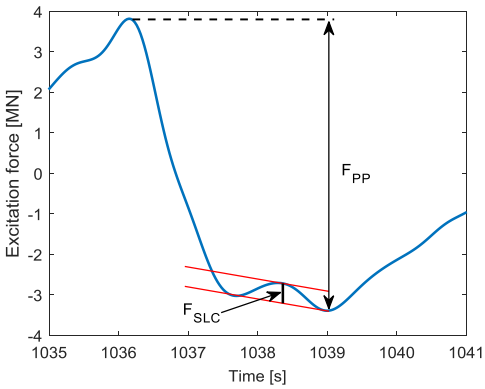

Fig. 16. Example of a secondary load cycle occurrence with the definitions of the magnitude and the peak-to-peak force.

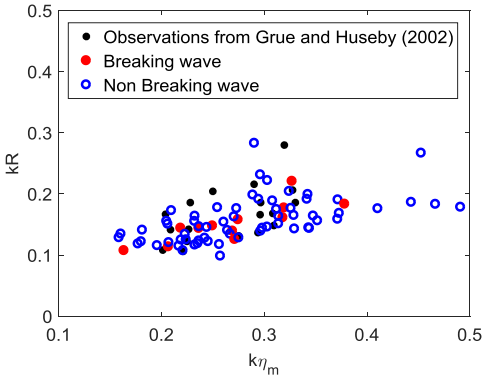

Fig. 17. Occurrences of secondary load cycle in the kR - $k\eta_m$ plane. The 25 largest occurrences (i.e. with highest magnitudes) of each of the 3 sea states are kept.

Grue and Huseby (2002) where they report SLCs for $0.1 < kR < 0.21$ and $0.2 < k\eta_m < 0.33$. They analysed the SLC phenomenon based on experiments carried out in deep water, whereas the experiments of the present paper were performed in finite water. It should be noted that due to finite water, we observe SLC for waves steeper than those reported in Grue and Huseby (2002). This is the only noticeable difference between SLC occurrences in deep water and finite water.

5.2. Link with maximum responses

The correlation between SLC and ringing responses was examined in the present experiments. For each of the 75 occurrences, the response of the structure in its 1st mode is analysed: the maximum of the 1st mode response (measured on the flexible structure) occurring immediately after the SLC is normalized by dividing it by the excitation moment (measured on the stiff structure). The obtained result is plotted as a function of the SLC ratio in Fig. 18.

Fig. 18 shows that the highest 1st mode amplifications are not provoked by the largest SLC ratios. Breaking waves usually provoke large 1st mode amplification, but as explained previously, there is no causality link between the two phenomena: both are a consequence of a wave being very steep.

Another correlation that was explored is the time of occurrence of the SLC against the 1st mode response amplification. The time of occurrence is defined as the time between the maximum of the excitation force and

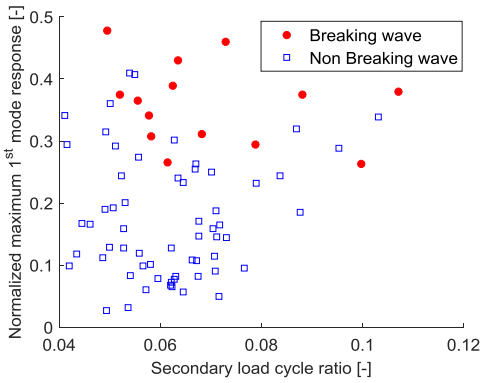

Fig. 18. Correlation between the secondary load cycle ratio and the 1st mode amplification. The 25 largest occurrences (i.e. with highest magnitudes) of each of the 3 sea states are kept.

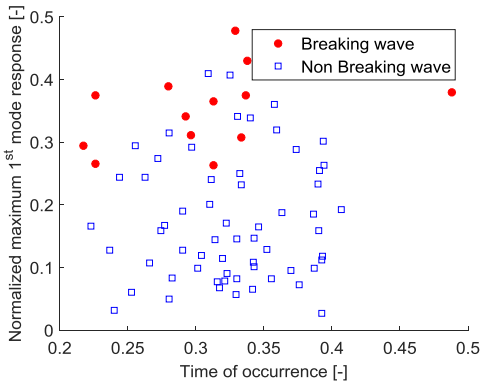

Fig. 19. Correlation between the time of occurrence of the secondary load cycle and the 1st mode amplification. The 25 largest occurrences (i.e. with highest magnitudes) of each of the 3 sea states are kept.

the maximum of the SLC, and is normalized by the wave period. As shown in Fig. 19, there is no clear trend between the time of occurrence and the 1st mode amplification.

In addition, some events did not present a SLC but a ringing type of response was still visible in the bending moment (these events are marked with a red circle in Fig. 11). Fig. 20 shows events 3 and 4 (respectively 3rd and 4th highest total responses) in detail. No SLC was seen in the measured excitation for either event. However, the lower plots of Fig. 20 clearly show a resonant response of the structure around its first eigenfrequency, characteristic of ringing responses.

These observations suggest that in the present experiment, the SLC is not a necessary load attribute to generate ringing response. This statement has important implications in terms of what is necessary to accurately model the response of offshore wind turbines in ULS conditions. Faltinsen et al. (1995) and Malenica and Molin (1995) developed third-order hydrodynamic models based on a perturbation approach (with the wave steepness as the perturbation parameter) in order to model ringing events. These models, as was shown in Paulsen et al. (2014), cannot depict the SLC because it is a phenomenon of even higher order. However, as discussed in this paragraph, the SLC is not required in the excitation force to produce ringing responses, meaning that these models that cannot predict SLCs can still potentially predict ringing responses, as seen for deep water (Gaidai and Krokstad, 2014).

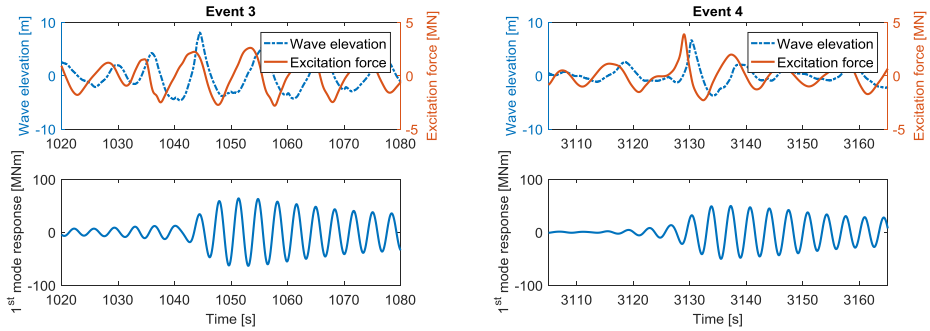

Fig. 20. Large response events with no visible secondary load cycle. The response is measured on the flexible model while the excitation is measured on the stiff one.

6. Conclusions

Experimental data of a bottom-fixed offshore wind turbine mounted on a monopile and subjected to extreme weather conditions in finite water are analysed in this paper. Two models of the support structure are presented: one is a fully flexible model whose 1st and 2nd eigenfrequencies and 1st mode shape were tuned to fit those of a full scale 4 MW wind turbine and the other one is a stiff model with the same dimensions as the flexible model. Both models were in the tank at the same time and therefore experienced the same incoming waves.

The flexible model is used to study the bending moment response at the seabed of the structure in ULS conditions. Over the whole set of experiments, the 21 events with largest responses are analysed and the bending moment is decomposed into response around the 2nd eigenfrequency, response around the 1st eigenfrequency (which highlights ringing responses) and quasi-static response. It is found that for every event, in addition to the quasi-static response, the structure experiences ringing and that its second mode is triggered, contributing to up to 20% of the total response. In line with what was found in Suja-Thauvin and Krokstad (2016) and by comparing the bending moment time series with video recordings, the conjecture is made that ringing responses are induced by 2nd and 3rd order hydrodynamic loads and that the 2nd mode is excited by slamming loads. The 2nd mode response exhibits behaviour qualitatively different than the total response or the quasi-static response. By analysing the excess kurtoses of the 2nd mode response of different sea states and the exceedance probability, it is shown that there are more outliers with more extreme values in the 2nd mode response than in the total or quasi-static response.

The excitation force is obtained by measuring the force at the stiff structure. This enables study of the phenomenon known as secondary load cycle, where shortly after the passage of a steep wave, a high frequency increase of the excitation force occurs. It has been conjectured in previous work that the secondary load cycle could be a cause of ringing responses. In the present paper, however, no correlation is found between the characteristics of secondary load cycles and ringing responses. Furthermore, some events with a strong ringing response do not present a secondary load cycle in the excitation force, indicating that the secondary load cycle is not a necessary load attribute to trigger ringing responses.

There are several important limitations to the present work, which is based on a limited number of experimental realizations at 1:30.6 scale. In addition to the limitations and uncertainties associated with small-scale testing and wave generation, this study only deals with one pair of values for 1st and 2nd eigenfrequencies. With the current trend of rotors getting larger (Ho et al., 2016), it is expected that the mass and moment of inertia on top of the tower will increase differently, thus changing the ratio of 1st over 2nd eigenfrequency. This could potentially change the relative contributions of the 1st and 2nd mode responses to the total response and therefore modify Fig. 11. A more detailed assessment of this phenomenon is left for further studies. The presence of the 3rd and 4th mode in the response, and the use of visual detection of slamming also represent limitations in the present work. Furthermore, the sea states considered here are not associated with a 50-year return period. As such, the considered conditions are not necessarily representative of typical ULS assessment, and the assumption of an idling turbine may not be correct. Finally, memory effects (i.e. the fact that the response to one wave depends on the response to previous waves) are not studied in this paper. As explained in section 4.2, wave groups can produce larger responses than individual regular waves with the same characteristics as the largest wave of the wave group.

This study explains the mechanism of large responses in ULS conditions for offshore wind turbines and shows the necessity of having both a non-linear hydrodynamic load model and a slamming model for the excitation loads, and at least 1st and 2nd structural modes accurately represented. The finite water conditions make it likely that more and steeper breaking waves will occur at the support structure of the turbine compared to deep water. In order to account for the phenomena described in this paper, a common practice in the industry is to simulate the wave kinematics using the stream function theory (Rienecker and Fenton, 1981) and adding a slamming model on top of it. This model will be studied in depth in future work.

Acknowledgments

This study has been financed by Statkraft and the Norwegian Research Council, project number 237192. The authors are grateful to the WiFi project for providing the experimental data used for this paper as well as for support and relevant input to the presented discussion. The participants of the WiFi project, in alphabetical order, are Ballast Nedam, Deltares, DNV, Dong, ECN, EON, GL, MARIN, Ramboll, Royal HaskoningDHV, RWE, Savannah River National Laboratory, Siemens, Sirris/OWI-lab, Statkraft, Statoil, STX, Van Oord, Vattenfall and Volker InfraDesign bv.

References

Bachynski, E.E., Moan, T., 2014. Ringing loads on tension leg platform wind turbines. Ocean Eng. 84, 237–248. https://doi.org/10.1016/j.oceaneng.2014.04.007.
Biggs, J.M., 1964. Introduction to Structural Dynamics. McGraw-Hill College.
Bredmose, H., Slabiak, P., Sahlberg-Nielsen, L., Schlütter, F., 2013. Dynamic Excitation of Monopiles by Steep and Breaking Waves: Experimental and Numerical Study. https://doi.org/10.1115/OMAE2013-10948. V008T09A062.
Bunnik, T., Helder, J., de Ridder, E.J., 2015. Simulation of the flexible response of a fixed offshore wind turbine subject to breaking waves. In: Presented at the 7th International Conference on HYDROELASTICITY IN MARINE TECHNOLOGY.
Chaplin, J.R., Rainey, R.C.T., Yemm, R.W., 1997. Ringing of a vertical cylinder in waves. J. Fluid Mech. 350, 119–147. https://doi.org/10.1017/S002211209700699X.
Dalrymple, R.A., Dean, R.G., 1991. Water Wave Mechanics for Engineers and Scientists. Prentice-Hall.
Damgaard, M., Andersen, J.K.F., 2012. Natural frequency and damping estimation of an offshore wind turbine structure. In: Presented at the the Twenty-second International Offshore and Polar Engineering Conference, International Society of Offshore and Polar Engineers.

Damgaard, M., Ibsen, L.B., Andersen, L.V., Andersen, J.K.F., 2013. Cross-wind modal properties of offshore wind turbines identified by full scale testing. J. Wind Eng. Ind. Aerodyn. 116, 94–108. https://doi.org/10.1016/j.jweia.2013.03.003.
de Ridder, E.J., Aalberts, P., van den Berg, J., Buchner, B., Peeringa, J., 2011. The Dynamic Response of an Offshore Wind Turbine with Realistic Flexibility to Breaking Wave Impact, pp. 543–552. https://doi.org/10.1115/OMAE2011-49563.
DNV, 2014a. DNV-OS-J101 Design of Offshore Wind Turbine Structures. DNV.
DNV, 2014b. DNV-RP-C205 Environmental Conditions and Environmental Loads. DNV.
Faltinsen, O.M., 1990. Sea Loads on Ships and Offshore Structures. Ocean Technology. Cambridge.
Faltinsen, O.M., Newman, J.N., Vinje, T., 1995. Nonlinear wave loads on a slender vertical cylinder. J. Fluid Mech. 289, 179–198. https://doi.org/10.1017/S0022112095001297.
Frimann-Dahl, J., 2015. Experimental Validation and Design Review of Wave Loads on Large-diameter Monopiles. NTNU, Marine Technology.
Gaidai, O., Krokstad, J., 2014. Extreme response statistics of fixed offshore structures subjected to ringing loads. J. Offshore Mech. Arct. Eng. 136 https://doi.org/10.1115/1.4027542, 031604–031604.
Grue, J., Bjørshol, G., Strand, Ø., 1993. Higher Harmonic Wave Exciting Forces on a Vertical Cylinder.
Grue, J., Huseby, M., 2002. Higher-harmonic wave forces and ringing of vertical cylinders. Appl. Ocean Res. 24, 203–214. https://doi.org/10.1016/S0141-1187(02)00048-2.
Hallowell, S., Myers, A.T., Arwade, S.R., 2015. Variability of breaking wave characteristics and impact loads on offshore wind turbines supported by monopiles. Wind Energy. https://doi.org/10.1002/we.1833 n/a-n/a.
Hasselmann, K., Barnett, T.P., Bouws, E., Carlson, H., Cartwright, D.E., Enke, K., Ewing, J.A., Gienapp, H., Hasselmann, D.E., Kruseman, P., Meerburg, A., Müller, P., Olbers, D.J., Richter, K., Sell, W., Walden, H., 1973. Measurements of Wind-wave Growth and Swell Decay during the Joint North Sea Wave Project. JONSWAP.
Ho, A., Mbistrova, A., Corbetta, G., 2016. The European Offshore Wind Industry - Key Trends and Statistics 2015 [WWW Document]. WindEurope. https://windeurope.org/about-wind/statistics/offshore/key-trends-2015/ (Accessed October 10 16).
IEC, 2009. IEC 61400–61403: Wind Turbines–part 3: Design Requirements for Offshore Wind Turbines. Int. Electrotech. Comm, Geneva.
Kirby, J.T., Dalrymple, R.A., 1986. An approximate model for nonlinear dispersion in monochromatic wave propagation models. Coast. Eng. 9, 545–561. https://doi.org/10.1016/0378-3839(86)90003-7.
Krokstad, J.R., Solaas, F., 2000. Study of nonlinear local flow. In: Tenth Int. Offshore Polar Eng. Conf.
Malenica, Š., Molin, B., 1995. Third-harmonic wave diffraction by a vertical cylinder. J. Fluid Mech. 302, 203–229. https://doi.org/10.1017/S0022112095004071.
Marthinsen, T., Stansberg, C.T., Krokstad, J.R., 1996. On the ringing excitation of circular cylinders. In: Presented at the the Sixth International Offshore and Polar Engineering Conference. International Society of Offshore and Polar Engineers.
Natvig, B.J., Teigen, P., 1993. Review of hydrodynamic challenges in tlp design. Int. J. Offshore Polar Eng. 3.
Paulsen, B.T., Bredmose, H., Bingham, H.B., Jacobsen, N.G., 2014. Forcing of a bottom-mounted circular cylinder by steep regular water waves at finite depth. J. Fluid Mech. 755, 1–34. https://doi.org/10.1017/jfm.2014.386.
Peng, Z., Raaijmakers, T., Wellens, P., 2013. Nonlinear Wave Group Impact on a Cylindrical Monopile. https://doi.org/10.1115/OMAE2013-10838. V001T01A044.
Rainey, P.J., Camp, T.R., 2007. Constrained non-linear waves for offshore wind turbine design. J. Phys. Conf. Ser. 75, 12067. https://doi.org/10.1088/1742-6596/75/1/012067.
Rainey, R.C.T., 2007. Weak or strong nonlinearity: the vital issue. J. Eng. Math. 58, 229–249. https://doi.org/10.1007/s10665-006-9126-2.
Rainey, R.C.T., Chaplin, J.R., 2003. Wave breaking and cavitation around a vertical cylinder: experiments and linear theory. In: 18th IWWWFB.
Rienecker, M.M., Fenton, J.D., 1981. A Fourier approximation method for steady water waves. J. Fluid Mech. 104, 119–137. https://doi.org/10.1017/S0022112081002851.
Sarpkaya, T., 2010. Wave Forces on Offshore Structures. Cambridge University Press.
Sarpkaya, T., 1979. Wave Impact Loads on Cylinders.
Schäffer, H.A., 1996. Second-order wavemaker theory for irregular waves. Ocean Eng. 23, 47–88. https://doi.org/10.1016/0029-8018(95)00013-B.
Schløer, S., Bredmose, H., Bingham, H.B., 2016. The influence of fully nonlinear wave forces on aero-hydro-elastic calculations of monopile wind turbines. Mar. Struct. 50, 162–188. https://doi.org/10.1016/j.marstruc.2016.06.004.
Shirzadeh, R., Weijtjens, W., Guillaume, P., Devriendt, C., 2015. The dynamics of an offshore wind turbine in parked conditions: a comparison between simulations and measurements. Wind Energy 18, 1685–1702. https://doi.org/10.1002/we.1781.
Stansberg, C.T., 2011. Characteristics of Steep Second-order Random Waves in Finite and Shallow Water, pp. 859–869. https://doi.org/10.1115/OMAE2011-50219.
Stansberg, C.T., Huse, E., Krokstad, J.R., Lehn, E., 1995. Experimental study of non-linear loads on vertical cylinders. In: Steep Random Waves. Presented at the the Fifth International Offshore and Polar Engineering Conference. International Society of Offshore and Polar Engineers.
Suja-Thauvin, L., Eliassen, L., Krokstad, J., 2014. The scalability of loads on large diameter monopile offshore wind support structures. In: Presented at the International Wind Engineering Conference, Hannover.
Suja-Thauvin, L., Krokstad, J.R., 2016. Simplified bottom fixed offshore wind turbine in extreme sea states. In: Presented at the the 26th International Ocean and Polar Engineering Conference. International Society of Offshore and Polar Engineers, Rhodos (Greece.
Suja-Thauvin, L., Krokstad, J.R., Frimann-Dahl, J., 2016. Maximum loads on a one degree of freedom model-scale offshore wind turbine. In: Energy Procedia, EERA DeepWind' 2016, 13th Deep Sea Offshore Wind R&D Conference.
Welch, S., Levi, C., Fontaine, E., Tulin, M.P., others, 1999. Experimental study of the ringing response of a vertical cylinder in breaking wave groups. Int. J. Offshore Polar Eng. 9, 276–282.
Wienke, J., Oumeraci, H., 2005. Breaking wave impact force on a vertical and inclined slender pile—theoretical and large-scale model investigations. Coast. Eng. 52, 435–462. https://doi.org/10.1016/j.coastaleng.2004.12.008.

Paper 4: Critical assessment of non-linear hydrodynamic load models for a fully flexible monopile offshore wind turbine

By Loup Suja-Thauvin, Jørgen R. Krokstad and Erin E. Bachynski

In the Journal of Ocean Engineering, vol 164, p 87-104, 2018

Ocean Engineering 164 (2018) 87–104

Contents lists available at ScienceDirect

Ocean Engineering

journal homepage: www.elsevier.com/locate/oceaneng

Critical assessment of non-linear hydrodynamic load models for a fully flexible monopile offshore wind turbine

Loup Suja-Thauvin*, Jørgen R. Krokstad, Erin E. Bachynski

NTNU, Department of Marine Technology, Trondheim, Norway

ARTICLE INFO

Keywords:
Offshore wind turbine
Ringing
Slamming
Engineering models
Experimental hydrodynamics
Modal decomposition

ABSTRACT

This paper presents a comparison between experimental data of a model-scale 4 MW monopile offshore wind turbine subjected to extreme irregular sea states in finite water and the numerical models suggested in offshore wind energy standards to assess ULS conditions. The model is fully flexible with its 1st and 2nd eigenfrequencies and 1st mode shape tuned to fit those of the full-scale turbine. The measured and simulated bending moments at the sea bottom are decomposed around the eigenfrequencies of the structure, and the Morison equation with stream function wave kinematics is found to trigger transient 1st mode response (so-called ringing response). The amplitude of the simulated 1st mode response is proportional to the incoming wave steepness; such a relationship is not observed experimentally. Similarly, 2nd mode response is triggered by Wienke's slamming model, but generally does not match the experimental data. Although the numerical models from the design standards (Morison's equation with stream function kinematics, plus a slamming model) can give conservative estimates of the extreme responses, the models miss the balance between 1st and 2nd mode responses. The simplification of the physics in the numerical models can thus lead to inaccuracies in response prediction, such as the stress distribution along the monopile.

1. Introduction

Offshore wind turbines mounted on monopiles are currently being built or planned in the North Sea in water depths between 20 and 50 m (Ho et al., 2016). In order to safely design the monopiles, the maximum load effect that the structure will experience over its lifetime has to be assessed (so-called Ultimate Limit State (ULS) analysis). A number of standards suggest hydrodynamic load models for such a study for different situations (for example DNV-OS-J101, 2014; DNV-RP-C205, 2014a; IEC 61400-3, 2009). These standards are mostly adapted from experience from the oil and gas industry, whose structures differ from offshore wind turbines in two important aspects:

- The depths considered for oil and gas platforms are much larger than those of offshore wind turbines, enabling the simplification of 'infinite water depth'.
- For offshore wind turbines, the displacement of the 2nd mode shape near the mean sea level is large compared to oil and gas platforms. This means that the 2nd mode of the structure will be excited by breaking wave events (which induce loads around the mean sea level), as shown for instance by Peeringa and Hermans (2017). For bottom-fixed oil and gas platforms, breaking wave loads act close to the maximum of the 1st mode shape, but are unlikely to excite global 1st mode response due to the short load duration.

Fig. 1 illustrates the concepts explained above. The largest contribution from hydrodynamic loads is around the mean sea level, which means that for a wind turbine it will be low (in relative heights) compared to an offshore oil and gas platform.

The main aim of this paper is to assess how well the standards used by the offshore wind industry predict the response of the support structure in ULS conditions. Experimental data produced by the Maritime Research Institute Netherlands (MARIN) is compared to the numerical models proposed in the standards. In these experiments, a fully flexible model of an idling 4 MW bottom-fixed offshore wind turbine mounted on a monopile was subjected to extreme weather conditions. Suja-Thauvin et al. (2017) analysed these experiments and showed that the largest responses for an offshore wind turbine in the above-mentioned conditions were provoked by steep and breaking waves. 2nd and 3rd order hydrodynamic loads from the wave trigger the 1st mode of the structure and produce the response phenomenon known as 'ringing', characterized by a build-up of the resonant vibration over about one wave period which then slowly decays (Natvig, 1994) and illustrated in Fig. 2. The bending moment in Fig. 2 has been

* Corresponding author.
E-mail address: loups@stud.ntnu.no (L. Suja-Thauvin).

https://doi.org/10.1016/j.oceaneng.2018.06.027
Received 14 December 2017; Received in revised form 11 May 2018; Accepted 9 June 2018
Available online 22 June 2018

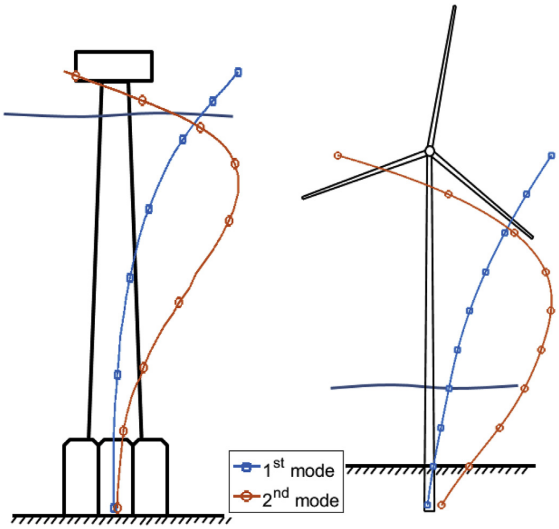

Fig. 1. Schematic representation of the Draugen platform (Natvig and Teigen, 1993) and the offshore wind turbine used in the present paper (not to scale). The lines represent the 1st and 2nd mode shapes normalized against their maximum value (the mode shapes of the Draugen platform are taken from Faltinsen and Timokha, 2016).

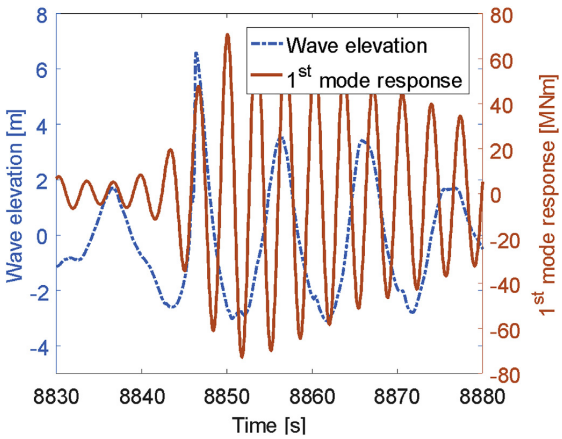

Fig. 2. Illustration of a ringing event. A surface-piercing vertical cylinder is exposed to a steep wave, and the bending moment is measured at the sea bottom.

filtered to show only the response of the 1st mode of the structure, this procedure is explained in section 5.2. The loads due to the impact of the breaking wave on the structure (so-called slamming loads) excite the 2nd mode of the structure, which can account for up to 20% of the maximum response (Suja-Thauvin et al., 2017). Slamming loads excite all modes of the structure, but only higher modes will be significantly excited due to (i) the very short slam duration compared to the 1st eigenperiod and (ii) the shape of the 2nd mode compared to the 1st mode. A conclusion of Suja-Thauvin et al. (2017) is thus that in order to correctly depict the maximum responses experienced by the support structure of offshore wind turbines, one has to account for both ringing responses and responses to breaking waves.

Numerical models for predicting ringing gained attention in the 1990s, when ringing was first observed during model tests of the Hutton and Heidrun TLP offshore oil and gas platforms and of the deep water concrete towers of the Draugen and Troll A platforms (Natvig and Teigen, 1993). For offshore wind turbines, the necessity of using non-linear wave kinematics when calculating hydrodynamic loads for capturing this phenomenon was shown for example by Marino et al. (2013a). This agrees well with Paulsen et al. (2013), who showed by using a CFD solver that the excitation force based on linear wave kinematics does not have the frequency content necessary to excite the 1st mode of the structure. Bredmose et al. (2012) used a simple cantilever beam numerical model to assess the importance of wave height and water depth with respect to ringing responses and to show how this phenomenon can dominate the total response due to dynamic amplification.

In addition to ringing responses, breaking wave events have also been studied for offshore wind turbines. Both de Ridder et al. (2011) and Bredmose et al. (2013) carried out experiments on a bottom-fixed responding structure whose characteristics were similar to those of an idling extra-large wind turbine and found out that breaking waves could lead to extreme accelerations of the nacelle. Bredmose and Jacobsen (2010) carried out a CFD analysis where focused waves were forced to break at different locations in the vicinity of the turbine in order to assess the hydrodynamic loads at different stages of the breaking process. Marino et al. (2013a) applied a fully nonlinear high-order boundary-element solver to a series of realistic sea states and showed that the bending moment at the tower base could be six times larger compared to a linear model.

The numerical models presented in the aforementioned works provide accurate predictions of the response of a bottom-fixed offshore wind turbine to steep breaking waves but are too computationally expensive to be used by the industry for design, where typically thousands of load cases need to be assessed. The standards commonly used by the industry to calculate hydrodynamic loading under steep breaking waves (DNV-OS-J101, 2014; DNV-RP-C205, 2014a; IEC 61400-3, 2009) suggest simpler models, such as the stream function theory (Rienecker and Fenton, 1981) and Wienke's slamming model (Wienke and Oumeraci, 2005). To assess the validity of these models for calculating the turbine's response under steep/breaking wave loads, the above-mentioned models have been implemented in Matlab® and used to try to match the experiments carried out by MARIN.

Other theories that attempt to reproduce ringing responses have been developed by Faltinsen et al. (1995), so-called FNV model, and Malenica and Molin 1995, so-called MM model. Both these theories were developed based on a perturbation approach and estimate the excitation load up to third order in terms of wave steepness. Krokstad et al. (1998) presented a validation of the response predicted by the FNV model in deep water, and Kristiansen and Faltinsen (2017) further developed the model for finite water. Paulsen et al. (2014) showed that the 3rd order excitation loads from both the FNV and the MM models, within their range of validity, match those predicted by CFD. Both models account for hydrodynamic-structural interaction by considering the diffracted wave from the cylinder. On the contrary, the models presented in this paper – and commonly used in design – do not account for the presence of the structure, and only estimate the kinematics of the undisturbed wave.

The paper is organized as follows: section 2 briefly presents the experiments carried out by MARIN, and in section 3 we introduce the structural model used in the paper. In section 4 we use the models proposed by the standards to carry out the ULS analysis under the environmental conditions of the MARIN experiments, and section 5 compares the same models on a single event basis to assess how the models perform. Conclusions are drawn in section 6.

2. Presentation of the model test

A more detailed description of the experiments is given by Suja-Thauvin et al. (2017); only the most relevant points are given here. The

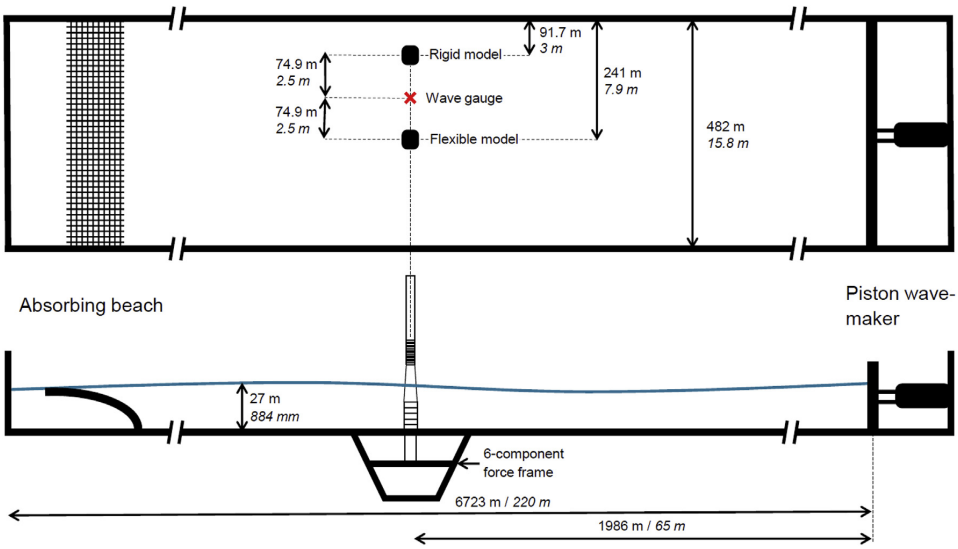

Fig. 3. Top and side view of the experimental set-up (values are given both in full and model scale).

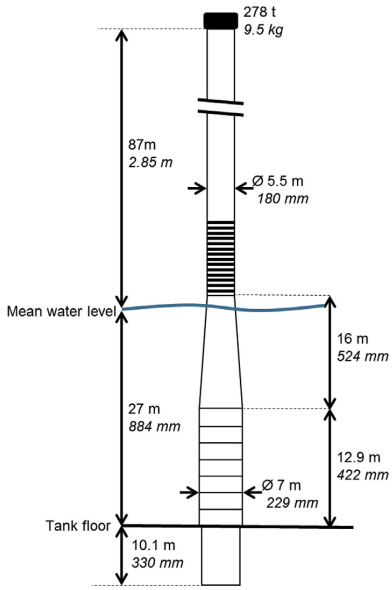

Fig. 4. Flexible model (values are given both in full and model scale).

dimensions of the experimental set-up and the flexible model are given in Fig. 3 and Fig. 4. The values given in the paper are full-scale, unless specified otherwise. The fully flexible model was held by a 6-component force frame and placed in a pit dug into the shallow water basin of MARIN, a rigid model was also constructed and placed in the basin but is not analysed in this study. The force frame was calibrated by pulling on it with known weights and showed an accuracy in measured moments of 2–3%. The fore-aft bending moment was measured at the sea bed and is simply referred to as 'response' in the rest of the paper.

4 wave gauges were placed in the basin. The accuracy of the wave gauges was not reported, but a typical value is approximately 1 mm in model scale (Steen, 2014), or 5 cm in full scale. Only one wave gauge (marked in Fig. 3) was used in this study. This wave gauge was placed about 13 diameters from both models, so it is expected that the diffracted and reflected waves can be neglected. The elevation measured by this wave gauge is used as an input for the numerical models after linearization (see appendix A). The waves were generated by a piston-type wave-maker, consisting of a flat plate forced into horizontal motion by an electrical actuator.

The prototype is a 1:30.6 Froude scaled model of a 4 MW wind turbine. The diameter at the mean sea level is 5.78 m and the water depth is 27 m. Special effort was put into achieving the correct 1st and 2nd eigenfrequencies and correct 1st mode shape. Table 1 shows the eigenfrequencies and damping ratios of the model (derived from hammer tests in water, see Bunnik et al., 2015), and Fig. 5 shows the mode shapes of the 1st and 2nd mode.

It should be noted that the damping values are low compared to idling full-scale wind turbine (Damgaard et al., 2013; Damgaard and Andersen, 2012; Shirzadeh et al., 2015 report 1.7–2.8% of critical damping for the first mode, depending on the wind speed). Considerations regarding very lightly damped systems are briefly discussed in section 5.4.

The 3rd and 4th modes measured on the experimental model have not been tuned to fit those of the full-scale model, which implies that conclusions based on the analysis of these two modes (and even higher) could not be applied to a full-scale wind turbine. Therefore these higher modes have been left out of the study. All the measured data presented in this work has been low-pass filtered to remove the response of the structure at these higher modes. More details are given in Suja-Thauvin et al. (2017).

In this paper, we analyse selected sea states from the experiments, summarized in Table 2 and plotted in Fig. 6. The experimental campaign was divided into Part A and Part B as they were different stages of the same project, but the experimental set-up remained unchanged between these two parts. Fig. 6 shows the $H_S - T_P$ graph of the Dogger-

Table 1
Frequencies and damping ratios of the model (full-scale values).

	1st mode	2nd mode	3rd mode	4th mode
Eigenfrequency [Hz]	0.29	1.21	3.11	7.24
Damping (% of critical)	1.1	1.1	2	2

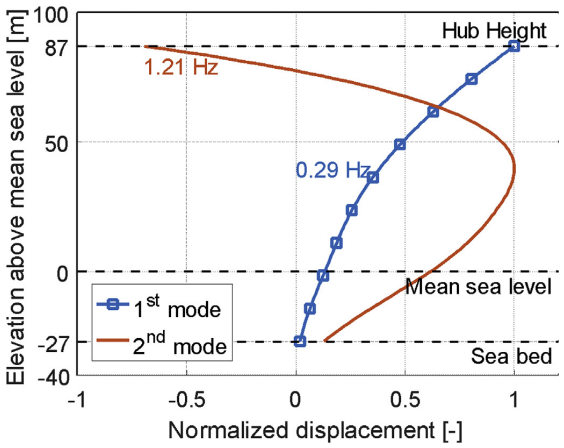

Fig. 5. Normalized mode shapes of the model. These mode shapes are also used in the structural model (see section 3).

Table 2
Selected sea states.

H_S	T_P	γ	Number of realizations
Part A			
3.5	8.5	3.3	1
5.81	10.93	3.3	1
5.89	10	3.3	1
6.18	10	3.3	1
Part B			
5	8.5	3.3	1
6.5	10	3.3	1
9	13	3.3	3
9	11	3.3	3

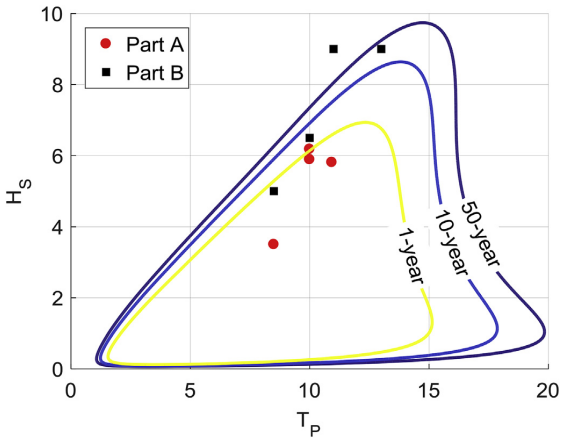

Fig. 6. H_S-T_P plot for the DoggerBank Creyke Beck B location. Contour lines for 1, 10 and 50-year return period.

Bank Creyke Beck B site (see Frimann-Dahl, 2015) and gives an indication of the return periods of the analysed sea states. It should be noted that the wind conditions for the selected sea states have not been determined. Under all sea states analysed in the paper, the turbine is assumed idling and no aerodynamics are modelled (except estimated damping from an idling turbine). In reality, the mildest sea states are probably associated with an operational turbine.

3. Structural model

The numerical tool developed for modelling the response of the structure is a simple mode shape solver (see for example Gans, 2015). The mode shapes and damping levels were provided by Bunnik et al. (2015). The response bending moment of the structure is calculated with the Euler-Bernoulli beam equation assuming a slender structure in the vertical direction z:

$$M(z,t) = EI\frac{\partial^2 \Psi(z,t)}{\partial z^2} \tag{1}$$

where M is the response bending moment, E is the Young's modulus, I is the area moment of inertia of the cross-section and Ψ is the deflection of the system. The deflection is assumed to be the sum of the deflections of each individual mode:

$$\Psi(z,t) = \sum_{i=1}^{N} \psi_i(z)\xi_i(t) \tag{2}$$

where ψ_i is the mode shape of the i^{th} mode and ξ_i is the modal displacement of the i^{th} mode. The modal displacement for each mode is determined solving the simple one degree of freedom equation with Matlab®:

$$f_i = m_i\ddot{\xi}_i + b_i\dot{\xi}_i + c_i\xi_i \tag{3}$$

where f_i is the modal excitation for the i^{th} mode and m_i, b_i and c_i are respectively the modal mass (including added mass), the modal damping and the modal stiffness of mode i. The modal excitation for each mode is obtained by integrating the product of the excitation force times the mode shape over the instantaneous wetted surface:

$$f_i = \int_h^{z_0} F(z)\psi_i(z)dz \tag{4}$$

where F is the hydrodynamic load, calculated with one of the models described in section 4.1.4, z_0 is the instantaneous wave elevation and h is the water depth.

4. Standards – statistical analysis

4.1. Procedure to estimate ULS response

In this section we evaluate the characteristic response for ULS design (shortened to "ULS response") of the structure using three standards commonly used in the offshore wind industry, namely DNV-OS-J101 (2014); DNV-RP-C205 (2014a); IEC 61400-3 (2009). We investigate load case 6.1 from these standards, which was established by de Ridder et al. (2017) as the design driver for the present experimental campaign. The standards prescribe 20 realizations of the 50-year return sea state corresponding to the desired location, each including a wave with the characteristics of a 50-year return wave embedded at a random time. If the wave is breaking at the structure, a slamming load model has to be added to account for the impact-like load on the structure (more details are given in section 4.1.4).

Each realization has a 10-min duration and corresponds to a linear superposition of regular wave components according to a JONSWAP spectrum (see Hasselmann et al., 1973) as suggested in all three standards. The average of the 20 maxima obtained from the simulated response time-series is interpreted as the ULS response. This response is commonly referred to as the '50-year response' even though it is rather the response to 50-year return environmental conditions. In this paper, in order to align with the common terminology, we denote the response estimated following the aforementioned procedure the '50-year response'. Fig. 7 illustrates this procedure.

In this paper, we assume that each of the analysed sea states (given in Table 2) corresponds to a 50-year return sea state at a fictitious location. Once the 50-year return sea state has been determined, one must

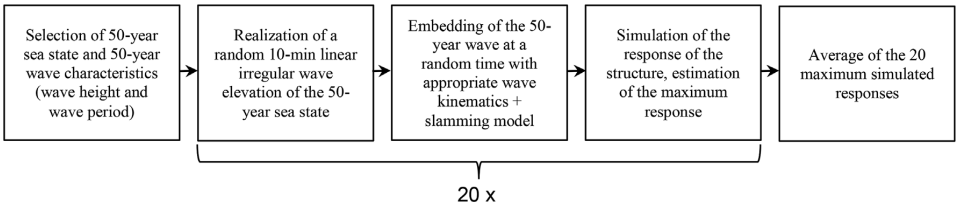

Fig. 7. Procedure for estimating the 50-year response.

define the characteristics of the 50-year return wave and the wave kinematics used to model this wave. The next four subsections deal respectively with.

- determining the characteristics of the 50-year wave
- choosing the kinematics model used to simulate the 50-year wave
- the embedding procedure
- the hydrodynamic load models.

4.1.1. 50-year return wave characteristics

To define the height of the 50-year return wave based on the 50-year return sea state, IEC 61400-3 (2009) assumes that the sea state has a 3-h stationarity during which the wave elevation follows a Gaussian distribution and the wave heights follow a given distribution (in this paper either a Rayleigh or a Battjes and Groenendijk distribution, see Battjes and Groenendijk, 2000). We denote hereafter H_{50} the height of the 50-year return wave and H_{S50} the significant wave height of the 50-year return sea state. IEC 61400-3 (2009) shows in detail how to estimate H_{50} assuming a Rayleigh distribution of the wave elevation. This assumption yields the classical result $H_{50} = 1.86H_{S50}$. The same derivation can be carried out assuming a Battjes and Groenendijk distribution (hereafter noted BG). The details of the derivation can be found in Battjes and Groenendijk (2000).

Fig. 8 shows the calculated H_{50} assuming the two different wave height distributions for each sea state. In addition, we show the significant wave height for each sea state and the maximum measured wave height. In order to find the maximum wave height, two maxima are measured per sea state, corresponding to trough-to-crest and crest-to-trough wave heights, and then the maximum of the two is taken. The error bars for the measured values correspond to two standard deviations of the 3-h maximum, as estimated for a Rayleigh distribution of the peaks, above and below the measured value (see for example Naess and Moan, 2012). The measured maximum wave height is only given as an indication, since the maximum wave of a 3-h realization of the 50-year return sea state is in general not the same as the 50-year return wave.

The Rayleigh distribution is known to be a good approximation for wave height distribution in deep water. The BG distribution takes depth into consideration and converges towards the Rayleigh distribution in deep waters. This is confirmed by Fig. 8, where for lower sea states both models give similar results. The method presented by Battjes and Groenendijk (2000) uses a look-up table and does not provide an estimate for the lowest sea state (H_S = 3.5 m, T_P = 8.5 m). For such conditions, it is reasonable to assume that the wave height distribution is well represented by a Rayleigh distribution.

In addition to determining the H_{50}, it is necessary to determine the period of the 50-year return wave, hereafter noted T_{50}. T_{50} can be taken within the range given by the following formula, according to IEC 61400-3 (2009).

$$11.1\sqrt{\frac{H_{S50}}{g}} < T_{50} < 14.3\sqrt{\frac{H_{S50}}{g}} \tag{5}$$

For each sea state, different values of T_{50} varying within the range given by equation (5) were tested and the most conservative results

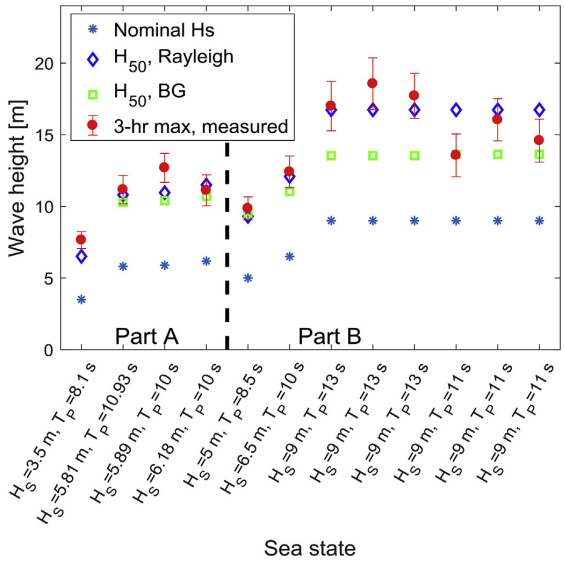

Fig. 8. Estimated 50-year wave heights (open symbols) and measured 3-h maximum wave height (red circle). (For interpretation of the references to colour in this figure legend, the reader is referred to the Web version of this article.)

were always obtained with the shortest T_{50} (corresponding to the steepest 50-year return wave). Only results for the steepest 50-year return wave are shown in this paper. It should be noted that this equation provides T_{50} depending only on H_{S50}. In this paper, the 2 highest sea states have the same H_S and will therefore have the same T_{50}.

4.1.2. Determination of the wave kinematics

In order to accurately model the kinematics of a single wave, different theories suggest different approaches. Fig. 9 is common to all three standards and suggests which theory can be used to describe a given regular wave depending on the wave height, wave period, and water depth. All these theories provide a solution for the Laplace equation and boundary conditions that can be found in most text books (e.g. Faltinsen, 1990). The main difference between these theories is the order to which they satisfy the dynamic and kinematic boundary condition at the free surface, higher order meaning more accuracy but also higher computational time.

In Fig. 9, the 'x' and the '+' represent the 50-year return waves shown in Fig. 8. It can be seen in Fig. 9 that a stream function of order between 3 and 9 is required to accurately model the 50-year return waves analysed in this study. For the following simulations, a 9th order stream function was used to model the 50-year return waves. The kinematics of the stream function waves were computed following Rienecker and Fenton (1981).

Fig. 9 also shows dots which correspond to the individual events studied in section 5.

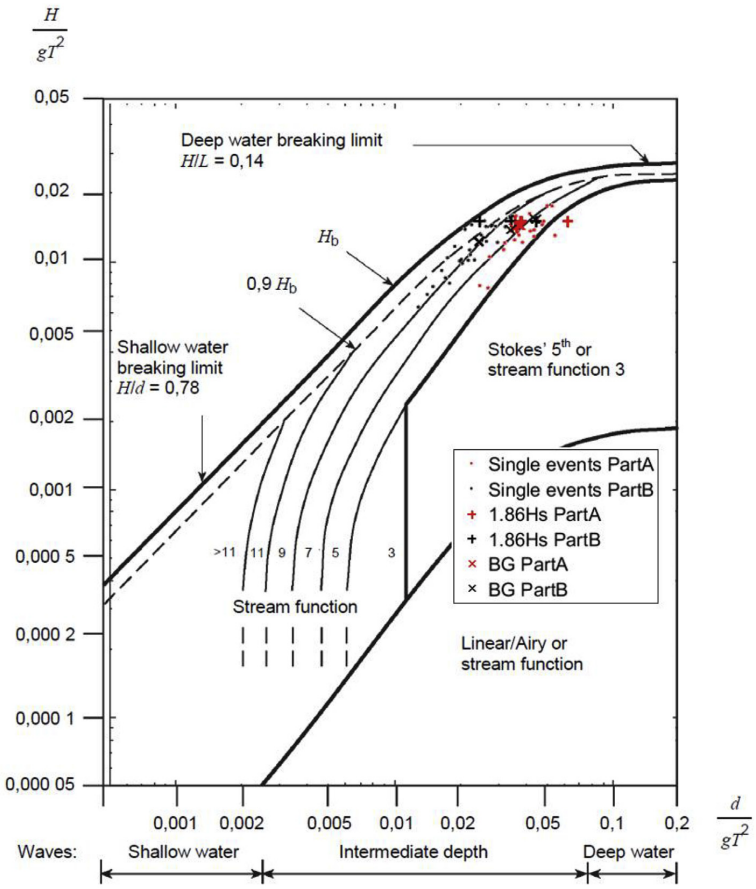

Fig. 9. Wave kinematic models depending on wave characteristics (taken from IEC 61400-3, 2009).

4.1.3. Embedding procedure

For the present paper, the embedding of the stream function is done following Rainey and Camp (2007), as shown in Fig. 10. This figure shows how the stream function wave is smoothly embedded into the linear irregular sea by defining two blending areas (marked in grey) where the linear and the stream function wave are multiplied by weighting functions. These weighting functions ensure a transition without discontinuities between the stream function and the linear kinematics. The weighting functions are applied to the wave elevation, the particle velocity and the particle acceleration.

According to IEC 61400-3 (2009), the instant when the 50-year wave is embedded into the linear irregular sea is randomly selected for each realization of the 50-year sea state. The effect of the time of embedding on the estimation of the ULS load can be seen by comparing the responses of the structure to the same realization of a 10-min sea state with a stream function randomly embedded with 2 s of difference (no slamming model is applied in this simulation). Fig. 11a shows the wave elevation of the linear realization and with the two different embeddings, while Fig. 11b shows the response of the structure.

As shown in Fig. 11b the difference of maximum bending moments between the two embeddings is about 13%. 10 realizations of 2 time series with 2-s separated embeddings have been carried out, and the average difference between the 2 embeddings was about 9%. This is caused by the response history of the structure, i.e. its position, velocity and acceleration when the wave passes through it, as well as the wave

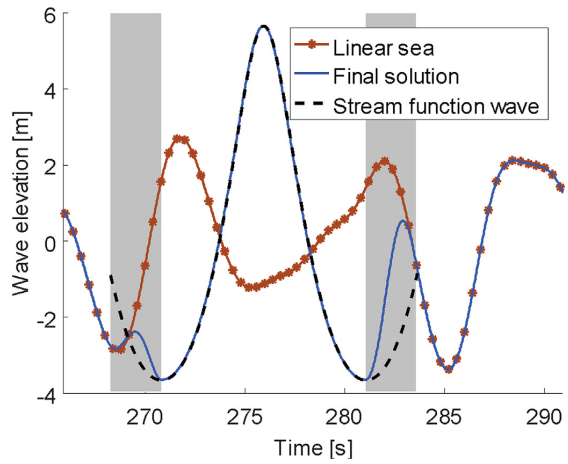

Fig. 10. Embedding process (following the description in Rainey and Camp, 2007).

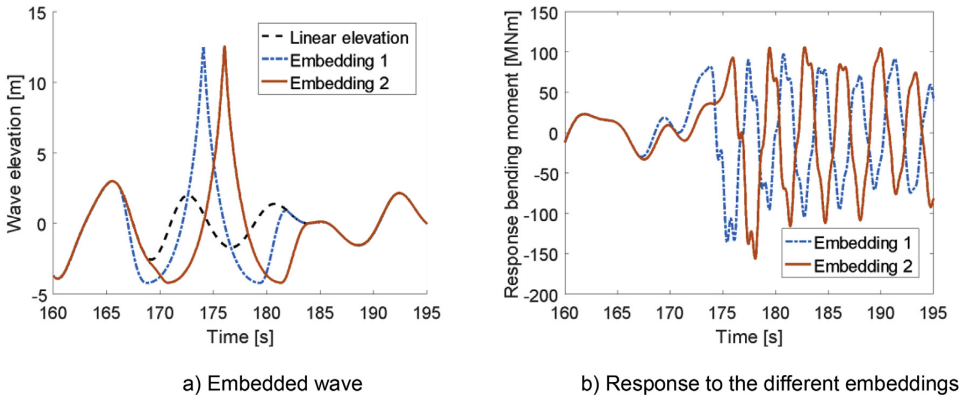

Fig. 11. Illustration of the embedding procedure at two slightly different instants.

kinematics induced by sewing together the time histories. Since the time of embedding is random, the kinematics of the structure at the time of embedding vary from one realization to the next. Furthermore, the process of embedding introduces different wave kinematics in the overlap region. By averaging the maxima over 20 realizations, the result accounts for some of these uncertainties.

4.1.4. Hydrodynamic load models

The considered 50-year return waves all have a wavelength longer than 10 times the radius of the cylinder, which implies that near-field first-order diffraction effects from the structure can be neglected (Faltinsen, 1990). Therefore, as suggested by all three standards, the numerical model of the structure is vertically divided into strips of length dz and the well-known Morison equation (Morison et al., 1950) is used to calculate the hydrodynamic loads dF on each strip:

$$dF = \rho\pi C_M R^2 a dz + \rho R C_D u|u|dz \tag{6}$$

with ρ the water density, R the cylinder radius, a and u the particle acceleration and velocity in the horizontal direction respectively, and C_M and C_D the inertia and drag coefficients. The particle acceleration and velocity are obtained from the kinematic model as explained above. The inertia and drag coefficients are determined empirically. For the Reynolds and Keulegan-Carpenter numbers relevant to this study, Sarpkaya (2010) recommends $C_M = 1.8$ and $C_D = 0.8$.

A slamming load is added to the Morison equation to account for the impact of the breaking wave on the structure. This load is calculated according to "Wienke's model" developed in Wienke and Oumeraci (2005) and given by the following equation:

$$F_{slam} = C_S \rho R c^2 \lambda \eta_m \tag{7}$$

with C_S the slamming coefficient, c the wave celerity, λ the curling factor and η_m the maximum wave elevation for the given slamming event. The slamming coefficient is time dependent and is given by (assuming $t = 0$ corresponds to the time of impact)

$$C_S = 2\pi \cdot \cos\gamma - 2\sqrt{\cos\gamma \cdot \frac{c}{R}t} \cdot \tanh^{-1}\sqrt{1 - \frac{1}{4}\cdot\frac{1}{\cos\gamma}\cdot\frac{c}{R}t} \quad \text{for } t \le \frac{1}{8}\cdot\frac{R}{c}\cdot\frac{1}{\cos\gamma}$$

and

$$C_S = \pi\sqrt{\frac{1}{6}\cdot\cos\gamma\cdot 1/\frac{c}{R}t'} - \sqrt[4]{\frac{8}{3}\cdot\cos\gamma\cdot\frac{c}{R}t'} \cdot \tanh^{-1}\sqrt{1 - \frac{c}{R}t'\sqrt{\frac{6}{\cos\gamma}\cdot\frac{c}{R}t'}}$$

$$\text{for } \frac{3}{32}\cdot\frac{R}{c}\cdot\frac{1}{\cos\gamma} \le t' \le \frac{12}{32}\cdot\frac{R}{c}\cdot\frac{1}{\cos\gamma} \text{ and } t' = t - \frac{1}{32}\cdot\frac{R}{c}\cdot\frac{1}{\cos\gamma} \tag{8}$$

with γ the angle between the water surface and the axis of the cylinder.

In the present paper, the slamming load is applied when the slope of the wave elevation is maximum (as this was found to fit the experimental data by comparing the excitation loads measured on some of the small sea states to the numerical models) and at the free surface elevation. Both the duration and the amplitude of the slamming load are dependent on the celerity of the wave, which in the present study is calculated with the stream function theory. In another study using the same experimental data as this paper, Burmester et al. (2017) report a curling factor of 0.28. This value is used in the present study.

4.2. Analysis of the statistical results

In the data provided by MARIN, we interpret each wave elevation time series as a 3-h realization of a 50-year sea state and look at the maximum response over this realization. We then compare this maximum to the estimation of the 50-year response obtained following the procedure explained above and summarized in Fig. 7. This comparison is plotted in Fig. 12. The calculated 50-year responses correspond to estimations of H_{50} considering the two mentioned wave height distributions (Rayleigh and BG). As in Fig. 8, the error bars for the measured values correspond to two standard deviations of the 3-h maximum, as estimated for a Rayleigh distribution of the peaks, above and below the measured value.

For the sea states with a large significant wave height, the models suggested by the standards overpredict the responses compared to the experimental measurements. The overprediction is reduced by using the BG distribution since this distribution leads to lower estimates of H_{50} (as seen in Fig. 8). For lower sea states, the predicted response is closer to the measurements. The overprediction is mainly related to the 2nd mode response, which depends strongly on the celerity of the stream function wave. In order to understand the difference of prediction between low and high sea states, individual events where a large response of the structure was measured are analysed in section 5.

It should be noted that the maximum response of the structure during a 50-year sea state does not generally correspond to the response of the structure to a 50-year return wave: it is therefore not strictly correct to compare the measurements and the estimations. However, such a comparison provides an indication of whether the numerical simulations are conservative.

5. Single event simulation

In this section, we analyse how the models suggested by the industry perform when assessing extreme responses by considering individual events. We focus on the events that produced the largest measured responses of part A and part B. For Part A, that event occurred during sea state $H_S = 5.89\,m$, $T_P = 10\,s$ and for Part B, it

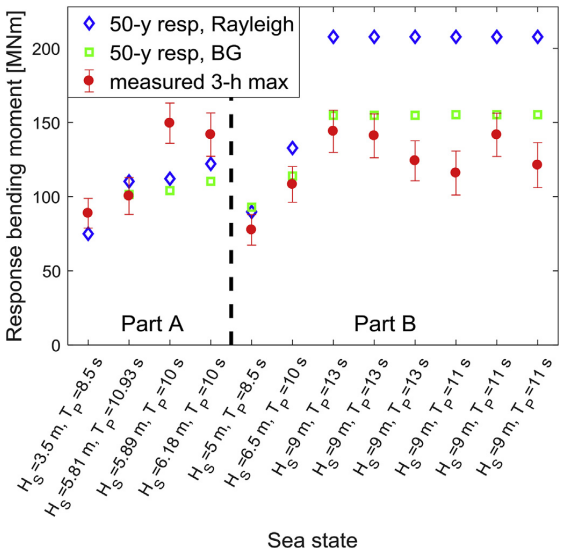

Fig. 12. 50-year responses obtained for the different wave height distributions (open symbols) and 3-h maximum measured response (red circles). (For interpretation of the references to colour in this figure legend, the reader is referred to the Web version of this article.)

occurred during sea state $H_S = 9\ m,\ T_P = 13\ s$. These events are named events A1 and B1 respectively, and are simulated using the following three models:

- **M_Lin**: Morison with linear kinematics. The wave kinematics are obtained from a linearization of the wave elevation measured during the experiments (see appendix A). Wheeler stretching (Wheeler, 1969), non-linear wave models and slamming models are not applied.
- **M_SF**: Morison with stream function wave kinematics. The wave immediately preceding the measured large response is replaced with a 9th order stream function wave. The wave height and wave period of the embedded stream function wave are taken as the measured wave height and trough-to-trough period, as shown in Fig. 13.
- **M_SF_W**: Morison with stream function wave kinematics and Wienke's slamming model. As in M_SF, with the addition of Wienke's slamming model at the instant where the slope of the wave elevation is maximum. For the slamming model, the wave celerity is obtained from the stream function theory.

5.1. Largest responses

Fig. 14 shows the simulated and measured responses of events A1 and B1. The upper plot shows the time series of the response, and the following plots are the continuous wavelet transforms (cwt, see Daubechies, 1992) of the measured and simulated responses. The colour scale is kept the same over all events, with warm colours corresponding to high energy content.

Fig. 14a and b and Fig. 14c and d shows that during the experiments the structure oscillates in its 1st and 2nd mode (with eigenperiods of 3.44 and 0.82 s, respectively). This confirms what was found by Suja-Thauvin et al. (2017), i.e. that the passage of a steep and breaking wave triggers both 1st and 2nd mode response.

The time series in Fig. 14a and b and the cwt plots in Fig. 14e and f shows that for both events, using the M_Lin model does not match the measured response. Neither the 1st nor the 2nd mode are triggered. The limitations of using linear wave kinematics to simulate extreme waves

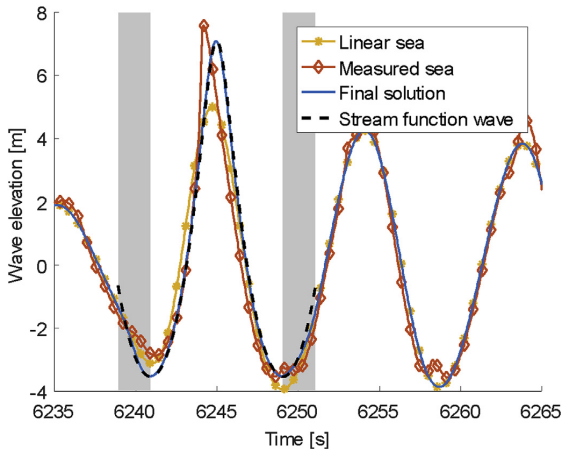

Fig. 13. Embedding of a stream function wave onto the linearization of the measured wave elevation.

are well known (Marino et al., 2013a; Paulsen et al., 2013; Suja-Thauvin et al., 2014).

For event A1, it can be seen from Fig. 14a and the cwt plots in Fig. 14g that the 1st mode response is not triggered correctly using the M_SF model. As seen in Fig. 15 (zoom of Fig. 14i), adding Wienke's slamming model triggers 2nd mode response but does not change the 1st mode response. Indeed, the duration of the slamming load estimated by Wienke's model is too short to significantly trigger 1st mode response (see Suja-Thauvin and Krokstad, 2016).

For event B1, the time series in Fig. 14b and the cwt plot in Fig. 14h show that the 1st mode response is triggered by the M_SF model. As for event A1, Fig. 14j shows that the M_SF_W model triggers 2nd mode response.

Fig. 16 shows the modal excitation force for the first mode simulated with M_SF and M_L for event B1. The cwt plots show that the excitation force of the M_SF model contains higher frequencies than that of the M_L, which explain its ability to trigger 1st mode response in the structure. The trough-to-trough period of the wave provoking event B1 is 11.25 s, which for the 9th order stream function wave gives a 9th harmonic at 0.8 Hz. The ability of the stream function to trigger 1st mode response is analysed in more detail in section 5.3.1.

These results suggest that the studied non-linear wave kinematic model can qualitatively produce 1st mode response, and that Wienke's model can trigger the 2nd mode of the structure. A combination of the two models therefore has the potential to match the experimental data. To assess the models in more detail, the next section examines a larger number of events.

5.2. Response decomposition by modes

For the 21 largest events of part A and the 30 largest events of part B (in terms of measured response), the responses were decomposed into quasi-static, 1st mode and 2nd mode response. Two Butterworth band pass filters were applied around the 1st and 2nd eigenfrequencies of the structure to extract the 1st and 2nd mode responses, and the remaining signal was taken as the quasi-static response. Fig. 17 shows the decomposition of the response for event A1. The vertical dotted line corresponds to the time T_{max} where the total response is maximum. By evaluating the amplitude of the responses of different modes at T_{max} it is possible to determine the contribution of the different modes to the maximum response.

Fig. 18 shows the contribution of the different modes for the simulated responses and how they compare to the measured responses

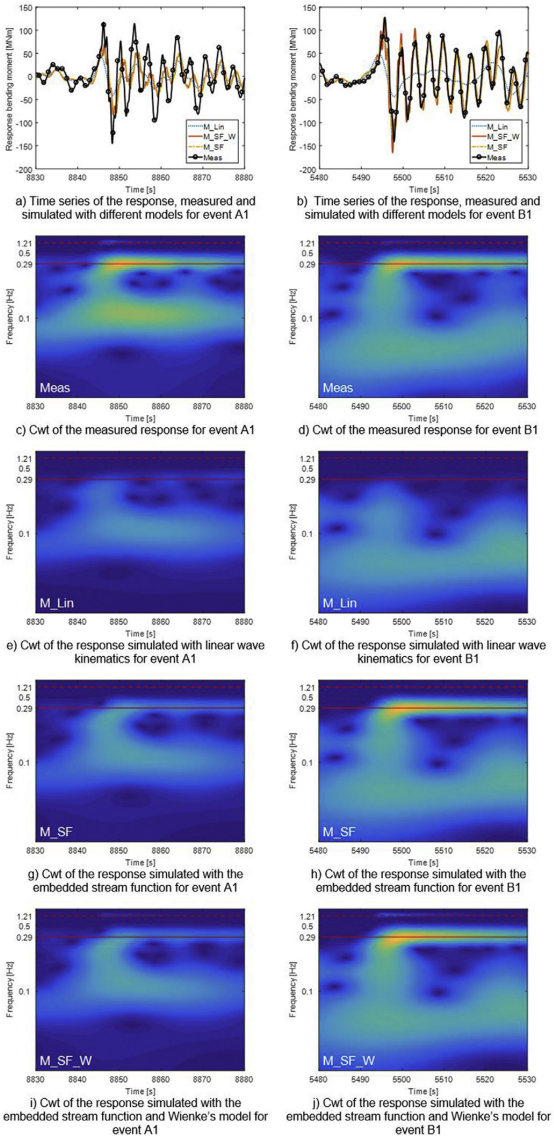

Fig. 14. Analysis of individual events: the plots on the left and on the right correspond events A1 and B1 respectively.

for part A. Fig. 18a shows that all models reproduce the quasi-static response reasonably well, with M_Lin slightly underestimating it. The differences in quasi-static response between M_Lin and the models including stream function kinematics are due to the vertical length of integration of the loads on the structure: M_Lin assumes loads up to the mean water level whereas M_SF and M_SF_W assumes loads up to the measured wave elevation. As noted in section 5.1 and illustrated in Fig. 18b,c, M_Lin does not trigger 1st or 2nd mode response and therefore underestimates the total response, as shown in Fig. 18d and e. Fig. 18b also shows that both models using stream function wave kinematics do trigger 1st mode response to a larger extent than M_Lin but still underestimate it. As explained previously, only the slamming model has the capability to 2nd mode response, but the response from

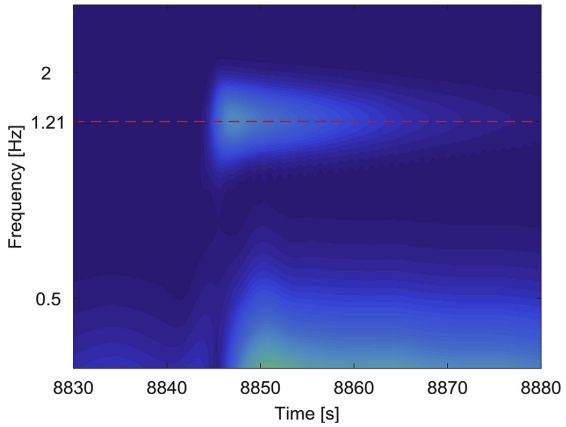

Fig. 15. Zoom of Fig. 14i (cwt of the response simulated with the embedded stream function and Wienke's model for event A1).

the simulations is significantly larger than the experiments.

It appears from Fig. 18 that 1st mode and quasi-static response are affected by the presence of the slamming model. The time of occurrence of the maxima when the slamming model is applied is slightly different than without slamming model, and therefore the contributions of the different modes vary slightly. There was no indication that the slamming model significantly affected the 1st mode and the quasi-static response.

Fig. 18 indicates that stream function wave kinematics with Wienke's slamming model have the potential to correctly predict the total response of the structure, but generally do not capture the balance between 1st and 2nd mode response. This leads to an inaccurate distribution of the stresses along the monopile.

Fig. 19 shows the same results as Fig. 18 for the largest 30 events of part B. The conclusions regarding the M_Lin model and the quasi-static and 2nd mode response drawn for part A also apply for part B. When it comes to 1st mode response however, there is no clear trend of how well the models using the stream function (models M_SF and M_SF_W) capture it: for some events, they produce conservative results while for others they are non-conservative.

Fig. 19e shows that the stream function with Wienke's model does not give a conservative estimate of the total response of the structure when the 1st mode response is underestimated. This underestimation can in some cases be compensated by an overestimation of the 2nd mode response using the slamming model, but the physics of the process of maximum response are not correctly captured.

5.3. Analysis of the models

In this part we try to explain the discrepancies observed between the models and the experimental data. In the following, we define the wave steepness as the steepness of the highest third of the wave, equal to $\frac{(H/3)}{(c * T_{1/3})}$, where $H/3$ and $T_{1/3}$ are defined in Fig. 20 and c is the wave celerity, taken equal to the stream function wave celerity for simulated waves and estimated with the nonlinear dispersion relationship for measured waves.

5.3.1. Stream function – ringing response

Here we assess how the frequency content of the excitation affects the 1st mode response. We evaluate the energy content of the modal excitation force for mode 1 (obtained from equation (4)) at the 1st eigenfrequency by calculating the cwt and taking its maximum along the 1st eigenfrequency of the structure, indicated by a red dot in Fig. 16.

From Fig. 21 to Fig. 26, the data points correspond to the events

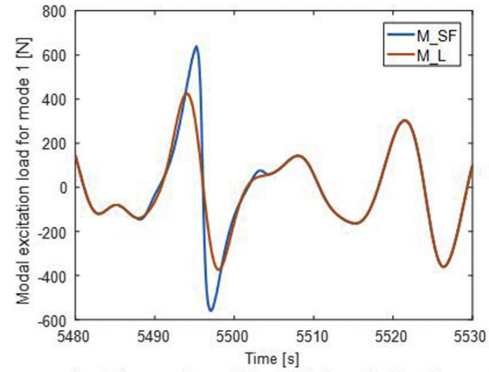

a) Time series of the modal excitation forces for event B1, for M_SF and M_L

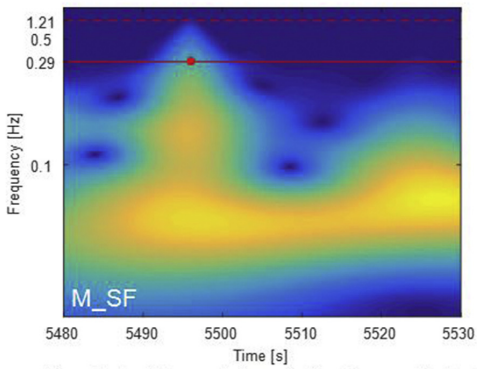

b) Cwt of the modal excitation force with the M_SF model

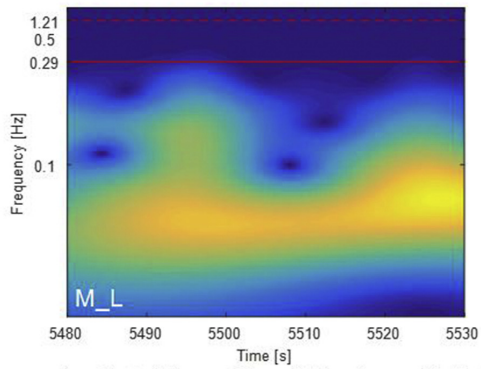

c) Cwt of the modal excitation force with the M_L model

Fig. 16. Modal excitation load for mode 1 of event B1. The red dot in the cwt plot corresponds to the maximum energy content at the 1st eigenfrequency of the structure (Section 5.3.1). (For interpretation of the references to colour in this figure legend, the reader is referred to the Web version of this article.)

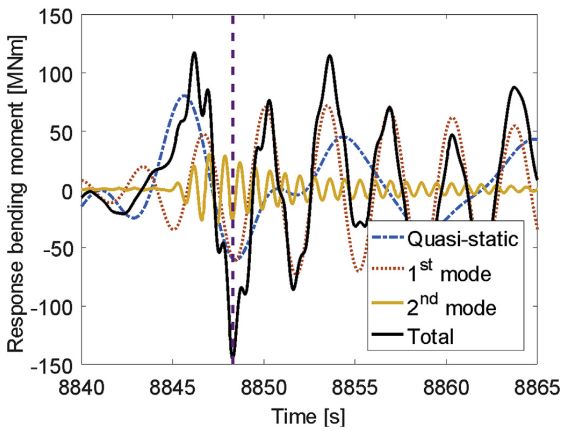

Fig. 17. Decomposition of the response around the eigenfrequencies of the structure for event A1.

analysed in section 5.1. Fig. 21 shows the correlation between the energy content of the modal excitation force at the 1st eigenfrequency (which has been normalized against its maximum value) and the maximum value of the simulated 1st mode response (this is different from previous figures, where the contribution of the 1st mode response at the instant where the total maximum was reached was shown). As expected, there is a strong correlation between these parameters.

Fig. 22 shows the correlation of the stream function wave steepness and the energy content of the excitation force at the 1st eigenfrequency. Waves get steeper as the influence of higher harmonics gets larger, therefore steeper waves have a higher energy content at high frequencies. The eigenfrequency of the structure (0.29 Hz) corresponds to harmonics between 3 and 5 for the considered waves. This explains why steeper waves produce excitation forces with larger energy content at 0.29 Hz, as can be seen in Fig. 22.

In Figs. 21 and 22 the black line is obtained from a linear regression of the data. The R^2 coefficient is given in the caption.

Fig. 23 shows that there is no clear correlation between the measured wave steepness and 1st mode response. Fig. 24 shows the same for a different definition of the wave steepness (wave height over wavelength). This suggests that the reason why the stream function model does not consistently capture 1st mode response is because it produces a response proportional to the wave steepness, which does not correspond to what is observed in the experiments.

5.3.2. *Slamming model – 2nd mode response*

By definition, the amplitude of the slamming load is proportional to the wave elevation times the wave celerity squared (see Wienke and Oumeraci, 2005). The impulse of the slamming load is proportional to its amplitude,

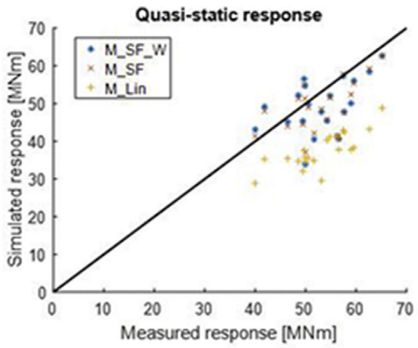

a) Comparison between quasi-static measured and simulated responses for Part A

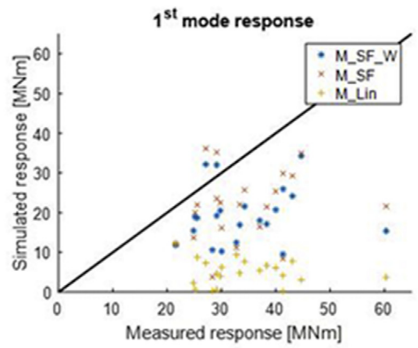

b) Comparison between 1st mode measured and simulated responses for Part A

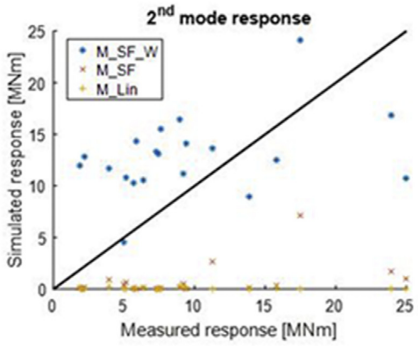

c) Comparison between 2nd mode measured and simulated responses for Part A

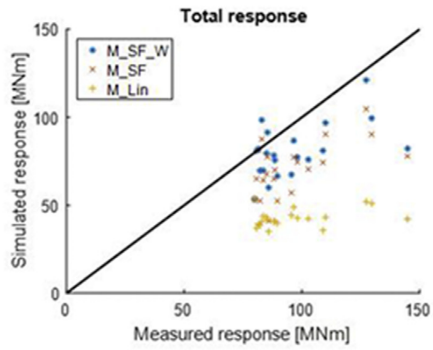

d) Comparison between total measured and simulated responses for Part A

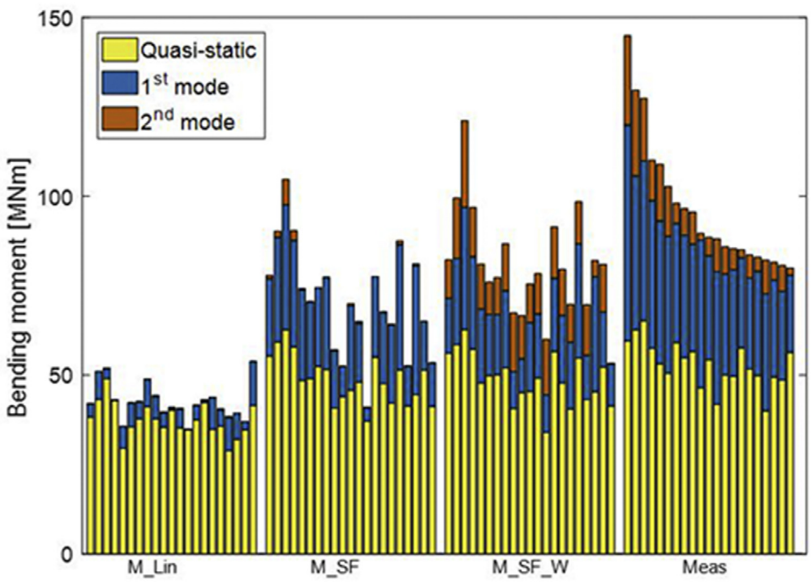

e) Summary of the measured and simulated responses for Part A

Fig. 18. Comparison of the simulated responses with the measured response for the largest events in Part A. The response has been decomposed into contributions of the different modes of the structure.

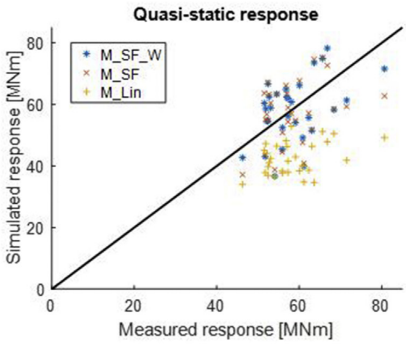

a) Comparison between quasi-static measured and simulated responses for Part B

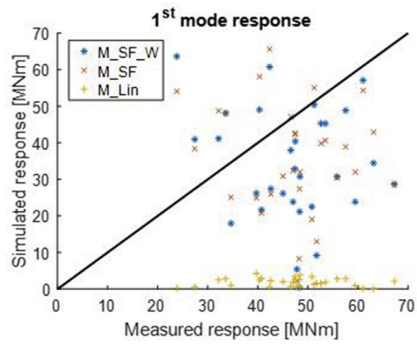

b) Comparison between 1st mode measured and simulated responses for Part B

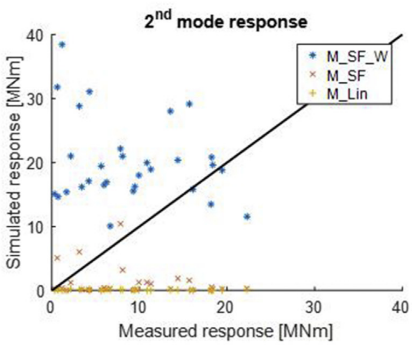

c) Comparison between 2nd mode measured and simulated responses for Part B

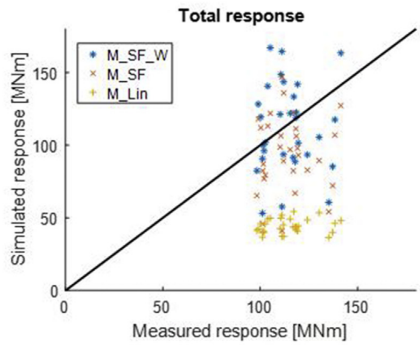

d) Comparison between total measured and simulated responses for Part B

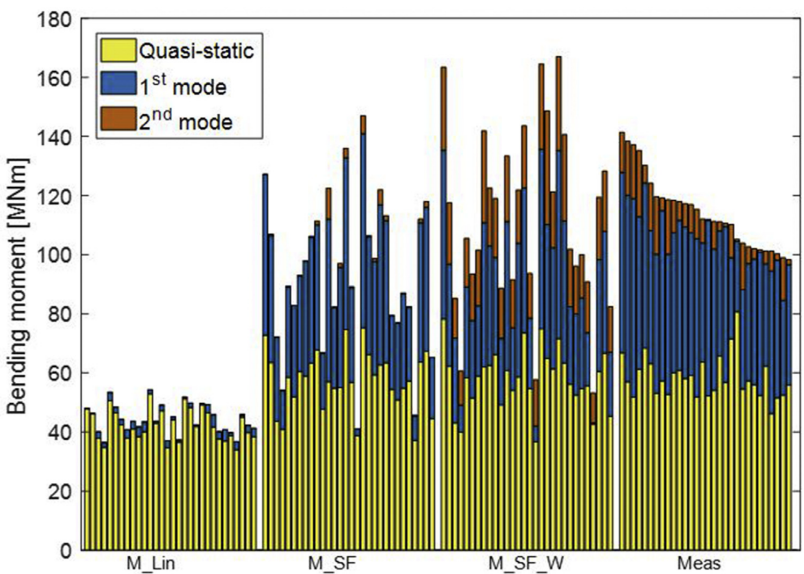

e) Summary of the measured and simulated responses for Part B

Fig. 19. Comparison of the simulated responses with the measured response for the largest events in Part B. The response has been decomposed into contributions of the different modes of the structure.

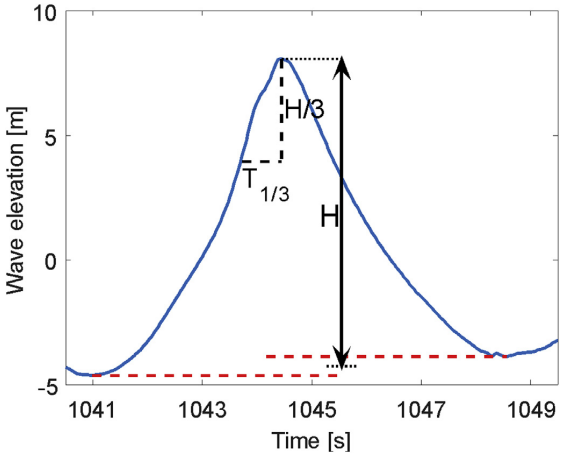

Fig. 20. Definition of the wave steepness at the highest third of the wave.

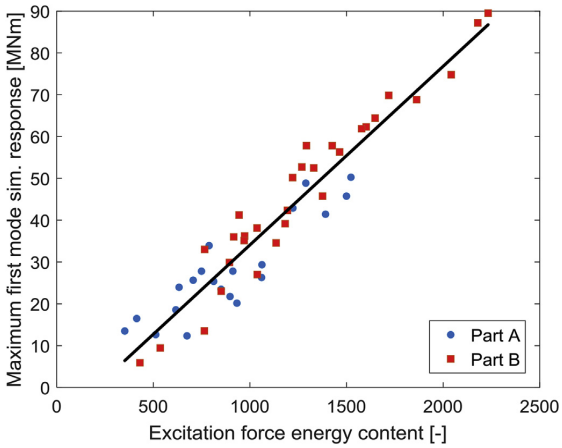

Fig. 21. Energy content of the excitation force at the 1st eigenfrequency against maximum 1st mode simulated response ($R^2 = 0.91$).

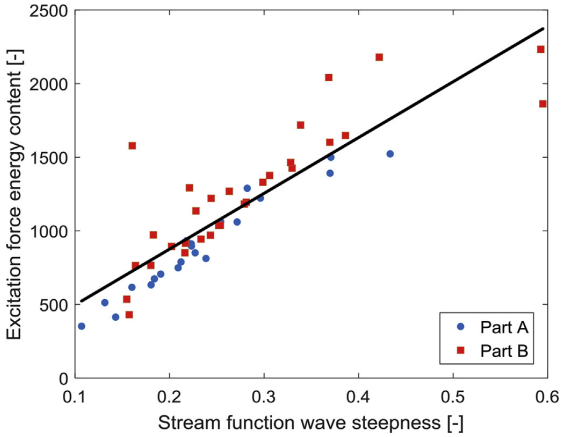

Fig. 22. Stream function wave steepness against energy content of the excitation force at the 1st eigenfrequency ($R^2 = 0.76$).

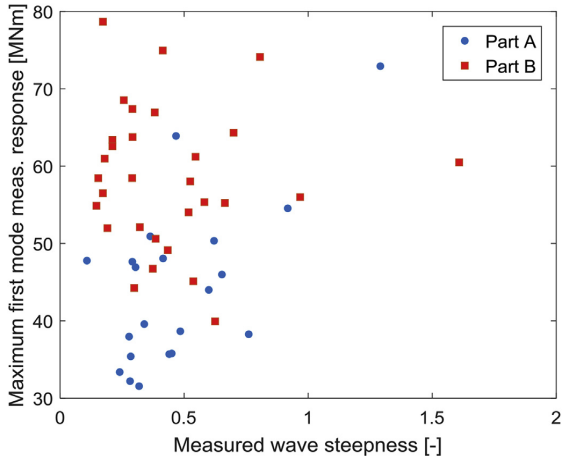

Fig. 23. Measured wave steepness against maximum 1st mode measured response.

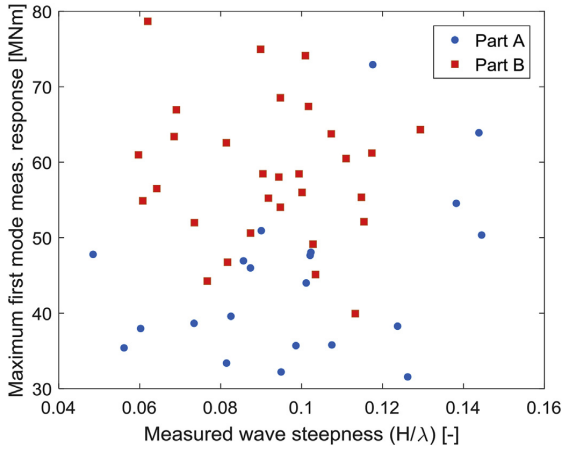

Fig. 24. Measured wave steepness (wave height over wavelength) against maximum 1st mode measured response.

and classical structure dynamics (see for example Biggs, 1964) shows that increasing impulse produces an increased response of the structure. This explains the linear trend in the correlation between the simulated 2nd mode response and the wave elevation times the wave celerity squared seen in Fig. 25. As in the analysis of 1st mode response in section 5.3.1, the trend in the simulations does not correspond to what can be observed from the experiments. Fig. 26 shows no apparent trend between the measured 2nd mode response and the wave elevation times the celerity squared. This can be due to (i) physical phenomena not considered in the theory (such as air entrapment, asymmetry of the load, imperfections on the surface), (ii) an inaccurate estimation of the wave celerity and (iii) an inaccurate representation of the shape of the impact load by the slamming model (given by equation (8)). A detailed analysis of the effect of the shape of the slamming load is beyond the scope of this paper, but classical structure dynamics (Biggs, 1964) shows that the response of a structure to a transient load depends on the shape of the load. It should be noted that the impulse could not be obtained from measurements with the given experimental setup.

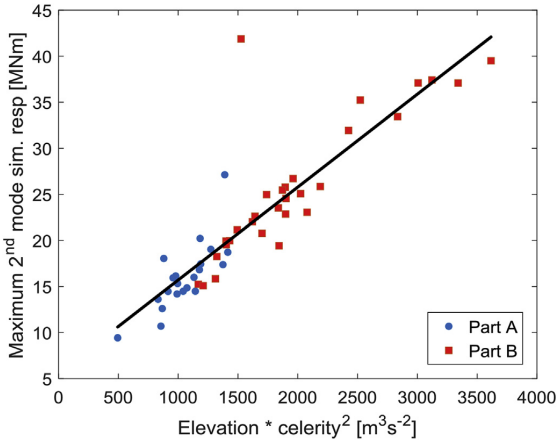

Fig. 25. Maximum 2nd mode simulated response against wave elevation * celerity squared (R^2 = 0.78).

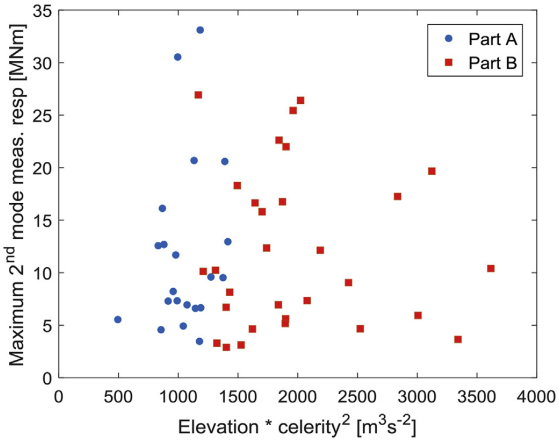

Fig. 26. Maximum 2nd mode measured response against wave elevation * celerity squared.

5.4. Discussion on damping

The damping of the 1st and 2nd mode was 1.1% of the critical damping. Research done by Bachynski and Moan (2014) and Schløer et al. (2016) suggests that damping is not critical for the maximum response but more relevant for fatigue damage. This agrees with the numerical simulations reported in Marino et al. (2013b) where it can be seen at an event level that the maximum bending moments at the tower bottom are not generally smaller in power production mode (which implies larger damping) compared to idling conditions. However, Suja-Thauvin et al. (2016) pointed out that for very lightly damped systems the 1st mode response produced by a ringing event will not decay quickly, so a new event may produce 1st mode response on top of these free decay oscillations, potentially increasing the maximum if the oscillations from the two events occur in phase. Bachynski et al. (2017) explored this issue further and showed that at a statistical level, increased damping would decrease the extreme bending moment at the tower bottom.

The present experimental set-up did not enable variation of the system damping. It was thus impossible to assess whether – for a very lightly damped structure – the response to non-linear loading might be somewhat hidden by the large responses at the 1st eigenmode. Indeed, if an event A induces a 1st mode response in the structure and that response has not dampened out by the time a later event B occurs, it will be challenging to assess the contribution of each event to the 1st mode response. The question of whether low damping decreases the sensitivity of the system to non-linearities is left for further studies.

6. Conclusion

Experimental data of a monopile offshore wind turbine subjected to severe irregular waves has been compared to the numerical models suggested by typical standards used in the offshore wind industry (namely DNV-OS-J101, 2014; DNV-RP-C205, 2014a; IEC 61400-3, 2009). The experimental campaign at MARIN consisted of a fully flexible monopile offshore wind turbine in finite water depth and subjected to extreme irregular sea states. The model was built so that its dimensions, its 1st and 2nd eigenfrequencies and 1st mode shape fit those of a full scale 4 MW wind turbine. During the experimental campaign, ULS conditions were found to be the design driver for the given structure (de Ridder et al., 2017), so this paper attempts to reproduce the characteristic response for ULS design, commonly referred to as the 50-year response. Both statistical and event-based comparisons were considered.

Several limitations to the present work should be noted. This analysis is based on experimental data from a limited number of sea state realizations at 1:30.6 scale, with the inherent limitations and uncertainties associated with wave generation and small-scale testing. In addition, due to the experimental set-up, only one combination of 1st and 2nd eigenfrequencies was analysed. As rotor size increases (Ho et al., 2016), the mass and moment of inertia on top of the tower may increase at different rates, thus changing the ratio of 1st to 2nd eigenfrequency. This could potentially change the relative contributions of the 1st and 2nd mode responses to the total response and therefore modify Figs. 18e and 19e. Furthermore, the wave elevation measured during the experiments is inherently nonlinear and had to be linearized to be a valid input to the hydrodynamic load models (see Appendix A). The 3rd and 4th modes of the structure were also disregarded in this study and might be relevant when assessing maximum responses. Finally, we did not consider memory effects (i.e. the fact that the response to previous events influences the response to a given wave). Peng et al. (2013) showed that it is possible to get larger responses from wave groups than from individual regular waves with the same characteristics as the largest wave of the group.

In order to determine the 50-year response, the standards suggest simulating the response of the structure over 20 realizations of the 50-year sea state with the 50-year wave randomly embedded. The 50-year wave kinematics are determined using the stream function and the hydrodynamic loads are computed with the Morison equation. During the experiments, large responses were provoked by steep and breaking waves, so Wienke's slamming model (see Wienke and Oumeraci, 2005) was added on top of the Morison loads. The numerical model gave a conservative estimate of the 50-year response for the largest sea states studied in this paper, but underpredicted the 50-year response for the milder sea states.

The events which produced a large response in the experiments were analysed individually, and the measured and simulated responses were decomposed into contributions around the 1st and 2nd eigenfrequencies of the structure. The results suggest that the numerical model does not correctly predict the relative contributions of the 1st and 2nd mode response to the total response. In particular, it was found that.

- The quasi-static response was in general accurately estimated by linear as well as non-linear wave kinematic models.
- The Morison equation with stream function wave kinematics inconsistently predicted ringing response (transient 1st mode response). The amplitude of the simulated response was roughly

proportional to the wave steepness, but this correlation was not found in the experimentally measured response.
- The 2nd mode of the structure was only excited by the slamming model. This is consistent with the findings of Suja-Thauvin et al. (2017), who show that during the experiments, 2nd mode response was triggered by waves breaking at the structure. However, according to the theory, the amplitude of the 2nd mode response is proportional to the wave elevation times the celerity squared, which was not observed in the experimental data.

Overall, the numerical model – with Morison's equation, stream function wave kinematics, and a slamming model – conservatively estimated the total maximum response on 3 out of 21 events for part A and 14 out of 30 events for part B. For all events where the total response was overestimated, the 2nd mode response was also overestimated, but there was no clear trend for the 1st mode response. These findings imply that even in a situation where the models give a conservative estimate of the 50-year response, the balance between 1st and 2nd mode response might not be realistic, and the stress distribution along the monopile can be inaccurate.

It should be noted that in this paper, the models were implemented to reproduce experimental data in order to allow an event-based comparison. In the estimation of 50-year response of offshore wind turbines, rather than using experimental data, the industry typically has access to metocean data to estimate the relevant extreme conditions. In order to select a relevant 50-year return wave in section 4.1.1, based on IEC 61400-3 (2009), we assumed both Rayleigh and Battjes and Groenendijk distributions for the wave heights for a 3-h sea state. In addition, several parameters required careful selection in order to provide trustworthy results. The assumptions made here are summarized in Table 3.

Table 3
Input to the numerical models.

Required input	Selected value	Reference
Load model	Morison with strip theory	(DNV-RP-C205, 2014; IEC 61400-3, 2009)
Hydrodynamic coefficients	$C_M = 1.8$ and $C_D = 0.8$.	(Sarpkaya, 2010)
Wave kinematic model	Stream function wave theory	(DNV-RP-C205, 2014; IEC 61400-3, 2009)
Wave embedding procedure	Method described by Rainey and Camp	(Rainey and Camp, 2007)
Slamming model	Wienke's model	(DNV-RP-C205, 2014)
Curling factor	$\lambda = 0.28$	(Burmester et al., 2017)

Acknowledgments

This study has been financed by Statkraft and the Norwegian Research Council, project number 237192. The authors are grateful to the WiFi project for providing the experimental data used for this paper as well as for support and relevant input to the presented discussion. The authors also want to thank Tim Bunnik for sharing information about the mode shape solver. The participants of the WiFi project, in alphabetical order, are Ballast Nedam, Deltares, DNV, Dong, ECN, EON, GL, MARIN, Ramboll, Royal HaskoningDHV, RWE, Savannah River National Laboratory, Siemens, Sirris/OWI-lab, Statkraft, Statoil, STX, Van Oord, Vattenfall and Volker InfraDesign bv.

Appendix A. wave linearization

A1 filtering

Difference-frequency waves are first removed from the measured signal using a simple high-pass filter. The difference-frequency waves are far from the linear waves (in the red circle in Figure 27a), making the filtering process straightforward.

Next, some of the higher order waves are removed by using a low-pass filter. We assume that 3rd and higher order waves have energy at frequencies that are higher than the linear wave, and will therefore simply be removed by the low-pass filter. However, removing second order sum-frequency waves is more complicated because some of these waves have frequencies that lie within the range of linear waves. If the cut-off frequency is too low, one might lose information from the linear waves. On the other hand, if the cut-off frequency is too high, part of the higher order waves will remain. The explanation of how this cut-off frequency is selected is given in appendix A2.

Once the high-pass and low-pass filters have been applied, we obtain the initial approximation $\zeta_{init}^{(1)}$ for the linear wave (red curve in Figure 27b). In this initial approximation, difference-frequency waves have been removed, but the sum-frequency waves whose frequencies lie within the linear waves remain. This unwanted energy is removed as follows: a second order wave (yellow curve in Figure 27c) is estimated from the initial approximation of the linear wave (Newman, 1996):

$$\zeta_1^{(2)} = -\frac{1}{g}\left[\frac{1}{2}(u^2 + w^2) + \zeta_{init}^{(1)} w_t\right] \tag{9}$$

with g the gravitational acceleration, u and w the horizontal and vertical water particle velocities, respectively and with subscript indicating differentiation.

We then want to remove this second order wave from $\zeta_{init}^{(1)}$. However, part of $\zeta_1^{(2)}$ is higher than the cut-off frequency (the region to the right of the black dotted line in Figure 27c) and will introduce higher frequencies into the linear wave if simply substracted. Therefore, $\zeta_1^{(2)}$ is first filtered in the same way as the measured wave elevation (the result of this filtering is the yellow curve in Figure 27d) and then substracted from $\zeta_{init}^{(1)}$. We then obtain the second approximation of the linear wave

$$\zeta_2^{(1)} = \zeta_{init}^{(1)} - \zeta_1^{(2)} \tag{10}$$

Equation (9) used to calculate $\zeta_1^{(2)}$ requires a linear wave elevation as input. However, $\zeta_{init}^{(1)}$ contains second order wave energy that was not removed by the initial filtering process, as explained above. This introduces an error in the second order wave $\zeta_1^{(2)}$ and therefore in the linear wave $\zeta_2^{(1)}$. In order to reduce this error, we use $\zeta_2^{(1)}$ to calculate a new estimation of the second order wave, using equation (9) with $\zeta_2^{(1)}$ instead of $\zeta_{init}^{(1)}$. We then obtain $\zeta_2^{(2)}$.

We iterate this process and compare $\zeta_{i-1}^{(1)}$ and $\zeta_i^{(1)}$ at each step. When the maximum of the difference is below a certain threshold (set to $\frac{H_S}{100}$ for the present study), we consider that the process has converged and we use the obtained linear wave as input for the numerical models.

The flow chart in Figure 28 describes the iterative process explained above. In this flow chart, the numbers of the figures illustrating the concepts are also given.

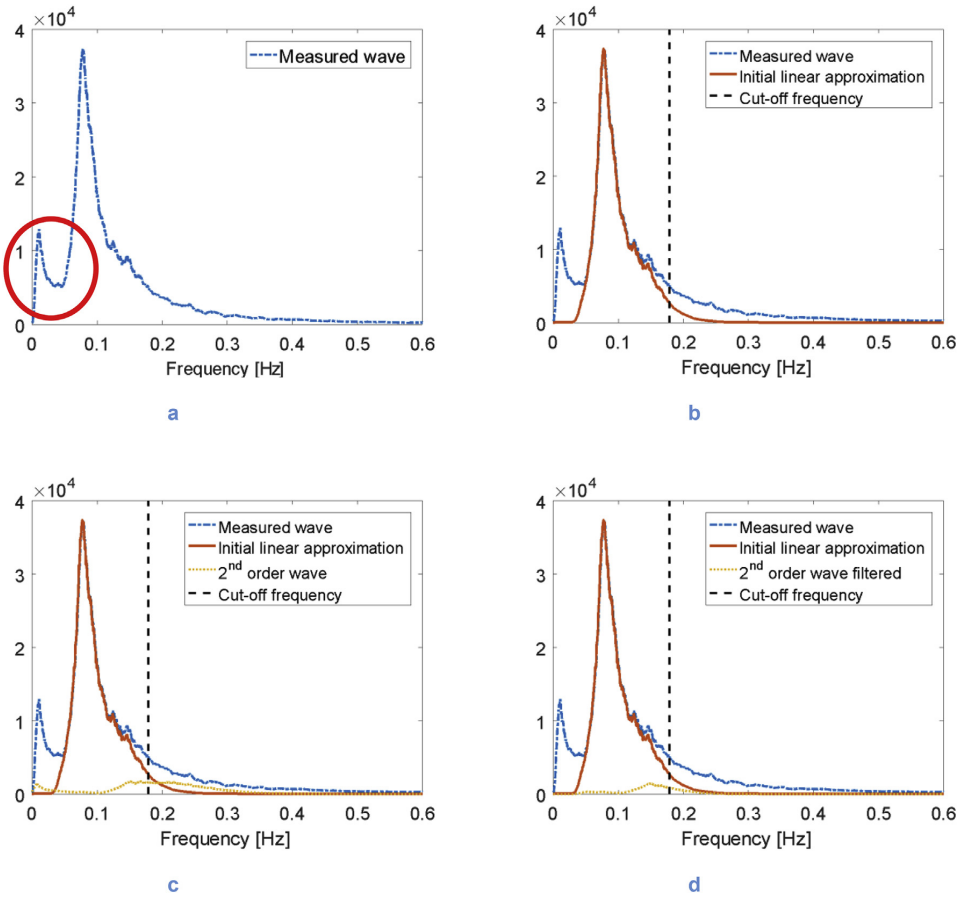

Fig. 27. Spectra of the wave elevation during filtering process.

A2 Selection of the cut-off frequency

As stated above, the selection of the cut-off frequency for the low-pass filter is not straight forward. It is specified in the standard DNV-RP-C205 (2014a) that if second order loads are to be calculated from a linear wave time series, a low-pass filter should be applied with the following cut-off frequency.

$$\omega_{DNV} = \sqrt{\frac{2g}{H_S}} \tag{11}$$

This cut-off frequency, developed for deep water, has to be applied because some kinematic terms used in non-linear hydrodynamic models can become unphysically large at the tail of the commonly used wave spectra (see Johannessen, 2008). For intermediate water conditions, the inherent non-linear behaviour of the waves implies that a lower cut-off frequency than the one presented in equation (11) has to be used.

The unwanted high-frequency energy is filtered out by use of a Butterworth filter. This filter is defined by two parameters: the cut-off frequency and the order of the filter, higher order meaning a sharper cut at the cut-off frequency. Suja-Thauvin and Krokstad (2016) varied these two parameters and a reconstructed linear wave was calculated for sea states of different severity. It was found that a 4th order Butterworth filter with a cut-off frequency $\omega_{cutoff} = 0.8 \cdot \omega_{DNV}$ gives the most accurate results. However, as pointed out by Johannessen (2011), the results are sensitive to the cut-off frequency selected. A careful assessment of the filter has to be carried out in order to get accurate results.

The linearization of the measured wave elevation introduces uncertainties into the estimation of the input to the hydrodynamic models, but these do not affect the computation of the loads that determine the 50-year response in the present study:

- For the stream function theory, the wave height is taken from the unfiltered measured wave elevation and the period from the linear wave is practically the same as for the measured wave. The kinematics of the stream function are only dependent on those two parameters and the water depth and therefore independent of the linearization process.
- Wienke's slamming model is only dependent on the wave elevation and the celerity of the wave (which depends on the stream function). Its ability to trigger 1st or 2nd mode motion is therefore not dependent on the linearization process

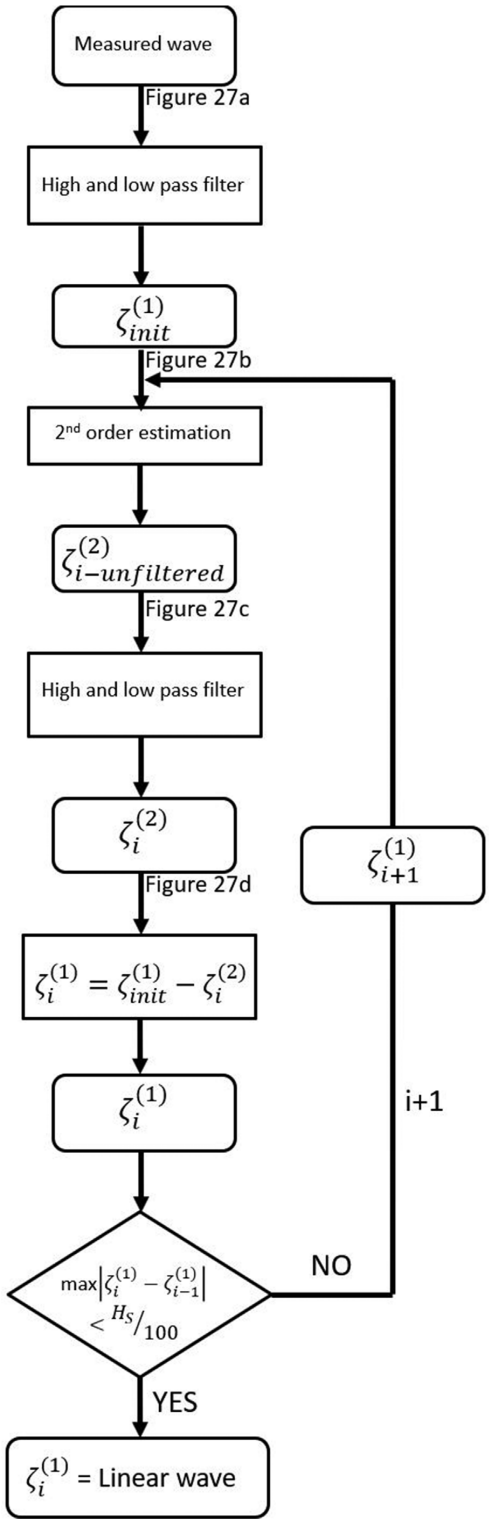

Fig. 28. Flow chart for the linearization process.

References

Bachynski, E.E., Kristiansen, T., Thys, M., 2017. Experimental and numerical investigations of monopile ringing in irregular finite-depth water waves. Appl. Ocean Res. 68, 154–170. https://doi.org/10.1016/j.apor.2017.08.011.

Bachynski, E.E., Moan, T., 2014. Ringing loads on tension leg platform wind turbines. Ocean Eng. 84, 237–248. https://doi.org/10.1016/j.oceaneng.2014.04.007.

Battjes, J.A., Groenendijk, H.W., 2000. Wave height distributions on shallow foreshores. Coast Eng. 40, 161–182. https://doi.org/10.1016/S0378-3839(00)00007-7.

Biggs, J.M., 1964. Introduction to Structural Dynamics. McGraw-Hill College.

Bredmose, H., Jacobsen, N.G., 2010. Breaking wave impacts on offshore wind turbine foundations: focused wave groups and CFD 397–404. https://doi.org/10.1115/OMAE2010-20368.

Bredmose, H., Schløer, S., Paulsen, B.T., 2012. Higher-harmonic response of a slender cantilever beam to fully nonlinear regular wave forcing 469–478. https://doi.org/10.1115/OMAE2012-83475.

Bredmose, H., Slabiak, P., Sahlberg-Nielsen, L., Schlütter, F., 2013. Dynamic excitation of monopiles by steep and breaking waves: experimental and numerical study V008T09A062. https://doi.org/10.1115/OMAE2013-10948.

Bunnik, T., Helder, J., de Ridder, E.J., 2015. Simulation of the flexible response of a fixed offshore wind turbine subject to breaking waves. In: Presented at the 7th International Conference on HYDROELASTICITY IN MARINE TECHNOLOGY.

Burmester, S., de Ridder, E.-J., Wehmeyer, C., Asp, E., Gujer, P., 2017. Comparing different approaches for calculating wave impacts on a monopile turbine foundation V010T09A063. https://doi.org/10.1115/OMAE2017-61182.

Damgaard, M., Andersen, J.K.F., 2012. Natural frequency and damping estimation of an offshore wind turbine structure. In: Presented at the the Twenty-second International Offshore and Polar Engineering Conference, International Society of Offshore and Polar Engineers.

Damgaard, M., Ibsen, L.B., Andersen, L.V., Andersen, J.K.F., 2013. Cross-wind modal properties of offshore wind turbines identified by full scale testing. J. Wind Eng. Ind. Aerod. 116, 94–108. https://doi.org/10.1016/j.jweia.2013.03.003.

Daubechies, I., 1992. Ten Lectures on Wavelets. SIAM.

de Ridder, E.J., Aalberts, P., van den Berg, J., Buchner, B., Peeringa, J., 2011. The dynamic response of an offshore wind turbine with realistic flexibility to breaking wave impact 543–552. https://doi.org/10.1115/OMAE2011-49563.

de Ridder, E.J., Bunnik, T., Peeringa, J.M., Paulsen, B.T., Wehmeyer, C., Gujer, P., Asp, E., 2017. Summary of the joint industry project wave impact on fixed foundations (WiFi JIP) V010T09A081. https://doi.org/10.1115/OMAE2017-62040.

DNV-OS-J101, 2014. DNV-OS-J101 Design of Offshore Wind Turbine Structures. DNV.

DNV-RP-C205, 2014. DNV-RP-C205 Environmental Conditions and Environmental loads. DNV.

Faltinsen, O.M., 1990. Sea Loads on Ships and Offshore Structures. Ocean Techmology, Cambridge.

Faltinsen, O.M., Newman, J.N., Vinje, T., 1995. Nonlinear wave loads on a slender vertical cylinder. J. Fluid Mech. 289, 179–198. https://doi.org/10.1017/S0022112095001297.

Faltinsen, O.M., Timokha, A.N., 2016. Undamped eigenperiods of a sea-based gravity monotower. Appl. Math. Model. 40, 8217–8243. https://doi.org/10.1016/j.apm.2016.04.003.

Frimann-Dahl, J., 2015. Experimental Validation and Design Review of Wave Loads on Large-diameter Monopiles. NTNU, Marine Technology.

Gans, R.F., 2015. Mechanical Systems. Springer.

Hasselmann, K., Barnett, T.P., Bouws, E., Carlson, H., Cartwright, D.E., Enke, K., Ewing, J.A., Gienapp, H., Hasselmann, D.E., Kruseman, P., Meerburg, A., Müller, P., Olbers, D.J., Richter, K., Sell, W., Walden, H., 1973. Measurements of Wind-wave Growth and Swell Decay during the Joint North Sea Wave Project (JONSWAP).

Ho, A., Mbistrova, A., Corbetta, G., 2016. The European offshore wind industry - key trends and statistics 2015 [WWW Document]. WindEurope. https://windeurope.org/about-wind/statistics/offshore/key-trends-2015/, Accessed date: 10 January 2016.

IEC 61400-3, 2009. IEC 61400–61403: Wind Turbines–part 3: Design Requirements for Offshore Wind Turbines. Int. Electrotech. Comm, Geneva.

Johannessen, T.B., 2011. Nonlinear superposition methods applied to continuous ocean wave spectra. J. Offshore Mech. Arctic Eng. 134 011302–011302. https://doi.org/10.1115/1.4003518.

Johannessen, T.B., 2008. On the use of linear and weakly nonlinear wave theory in continuous ocean wave spectra: convergence with respect to frequency 211–217. https://doi.org/10.1115/OMAE2008-57355.

Kristiansen, T., Faltinsen, O.M., 2017. Higher harmonic wave loads on a vertical cylinder in finite water depth. J. Fluid Mech. 833, 773–805. https://doi.org/10.1017/jfm.2017.702.

Krokstad, J.R., Stansberg, C.T., Nestegård, A., Marthinsen, T., 1998. A new nonslender ringing load approach verified against experiments. J. Offshore Mech. Arctic Eng. 120, 20–29. https://doi.org/10.1115/1.2829515.

Malenica, Š., Molin, B., 1995. Third-harmonic wave diffraction by a vertical cylinder. J. Fluid Mech. 302, 203–229. https://doi.org/10.1017/S0022112095004071.

Marino, E., Lugni, C., Borri, C., 2013a. A novel numerical strategy for the simulation of irregular nonlinear waves and their effects on the dynamic response of offshore wind turbines. Comput. Meth. Appl. Mech. Eng. 255, 275–288. https://doi.org/10.1016/j.cma.2012.12.005.

Marino, E., Lugni, C., Borri, C., 2013b. The role of the nonlinear wave kinematics on the global responses of an OWT in parked and operating conditions. J. Wind Eng. Ind. Aerodyn. In: The Twelfth Italian National Conference on Wind Engineering, IN-VENTO-2012, Venezia, Italy, October 7th–10th 2012 123, Part B, pp. 363–376. https://doi.org/10.1016/j.jweia.2013.09.003.

Morison, J.R., Johnson, J.W., Schaaf, S.A., 1950. The force exerted by surface waves on piles. J. Petrol. Technol. 2, 149–154. https://doi.org/10.2118/950149-G.

Naess, A., Moan, T., 2012. Stochastic Dynamics of Marine Structures. Cambridge University Press.

Natvig, B.J., 1994. A proposed ringing analysis model for higher order tether response. In: Fourth Int. Offshore Polar Eng. Conf.

Natvig, B.J., Teigen, P., 1993. Review of hydrodynamic challenges in tlp design. Int. J. Offshore Polar Eng. 3.

Newman, J.N., 1996. Nonlinear scattering of long waves by a vertical cylinder. In: Grue, J., Gjevik, B., Weber, J.E. (Eds.), Waves and Nonlinear Processes in Hydrodynamics, Fluid Mechanics and its Applications. Springer Netherlands, pp. 91–102.

Paulsen, B.T., Bredmose, H., Bingham, H.B., Jacobsen, N.G., 2014. Forcing of a bottom-mounted circular cylinder by steep regular water waves at finite depth. J. Fluid Mech. 755, 1–34. https://doi.org/10.1017/jfm.2014.386.

Paulsen, B.T., Bredmose, H., Bingham, H.B., Schløer, S., 2013. Steep wave loads from irregular waves on an offshore wind turbine foundation: computation and experiment V009T12A028. https://doi.org/10.1115/OMAE2013-10727.

Peeringa, J.M., Hermans, K.W., 2017. Impact of new slamming wave design method on the structural dynamics of a classic, modern and future offshore wind turbine V010T09A071. https://doi.org/10.1115/OMAE2017-61654.

Peng, Z., Raaijmakers, T., Wellens, P., 2013. Nonlinear wave group impact on a cylindrical monopile V001T01A044. https://doi.org/10.1115/OMAE2013-10838.

Rainey, P.J., Camp, T.R., 2007. Constrained non-linear waves for offshore wind turbine design. J. Phys. Conf. Ser 75 (012067). https://doi.org/10.1088/1742-6596/75/1/012067.

Rienecker, M.M., Fenton, J.D., 1981. A Fourier approximation method for steady water waves. J. Fluid Mech. 104, 119–137. https://doi.org/10.1017/S0022112081002851.

Sarpkaya, T., 2010. Wave Forces on Offshore Structures. Cambridge University Press.

Schløer, S., Bredmose, H., Bingham, H.B., 2016. The influence of fully nonlinear wave forces on aero-hydro-elastic calculations of monopile wind turbines. Mar. Struct. 50, 162–188. https://doi.org/10.1016/j.marstruc.2016.06.004.

Shirzadeh, R., Weijtjens, W., Guillaume, P., Devriendt, C., 2015. The dynamics of an offshore wind turbine in parked conditions: a comparison between simulations and measurements. Wind Energy 18, 1685–1702. https://doi.org/10.1002/we.1781.

Steen, S., 2014. Experimental Methods in Marine Hydrodynamics - Lecture Notes.

Suja-Thauvin, L., Eliassen, L., Krokstad, J., 2014. The scalability of loads on large diameter monopile offshore wind support structures. In: Presented at the International Wind Engineering Conference, Hannover.

Suja-Thauvin, L., Krokstad, J.R., 2016. Simplified bottom fixed offshore wind turbine in extreme sea states. In: Presented at the the 26th International Ocean and Polar Engineering Conference, International Society of Offshore and Polar Engineers, Rhodos (Greece).

Suja-Thauvin, L., Krokstad, J.R., Bachynski, E.E., de Ridder, E.-J., 2017. Experimental results of a multimode monopile offshore wind turbine support structure subjected to steep and breaking irregular waves. Ocean Eng. 146, 339–351. https://doi.org/10.1016/j.oceaneng.2017.09.024.

Suja-Thauvin, L., Krokstad, J.R., Frimann-Dahl, J., 2016. Maximum loads on a one degree of freedom model-scale offshore wind turbine. Energy Procedia, EERA DeepWind' 2016. In: 13th Deep Sea Offshore Wind R&D Conference.

Wheeler, J.D., 1969. Methods for calculating forces produced by irregular waves. In: Presented at the Offshore Technology Conference, Offshore Technology Conference, . https://doi.org/10.4043/1006-MS.

Wienke, J., Oumeraci, H., 2005. Breaking wave impact force on a vertical and inclined slender pile—theoretical and large-scale model investigations. Coast Eng. 52, 435–462. https://doi.org/10.1016/j.coastaleng.2004.12.008.

Paper 5: Critical assessment of hydrodynamic load models for a monopile structure in finite water depth

By Loup Suja-Thauvin, Erin E. Bachynski, Fabio Pierella, Michael Borg, Jørgen R. Krokstad and Henrik Bredmose

Submitted to the Journal of Marine Structures in April 2019

Critical assessment of hydrodynamic load models for a monopile structure in finite water depth

Loup Suja-Thauvin*[a]	Erin E. Bachynski[a]	Fabio Pierella[b]	Michael Borg[b]	Jørgen Krokstad[a]	Henrik Bredmose[b]

[a] NTNU, Department of Marine Technology, Trondheim, Norway

[b] DTU, wind energy, Nils Koppels Allé, Building 403, DK-2800 Kgs. Lyngby, Denmark

The response from steep and breaking waves for a monopile structure is investigated by analysis of experimental results and by application of numerical models for six sea states. The experimental monopile was designed to reproduce the first and second natural frequencies of the NREL 5 MW reference monopile wind turbine. The measured response is reproduced in a finite element model using the Morison equation extended to full Lagrangian acceleration with second-order wave kinematics, and with fully non-linear kinematics and the axial divergence term. For the fully nonlinear wave kinematics, the additional point forces of Rainey [1]and Kristiansen & Faltinsen (KF) [2] are further added. In the latter model, the kinematics at the still water level are obtained by Taylor expansion of the kinematics from the free surface.

The shear force at the sea bed and the structural accelerations are next compared between the force models and the experimental data. Among the findings are that the extreme force events are generally smallest for the second-order Morison approach, followed by the extended Morison model, the Rainey model and the KF model. While the total accelerations are found to generally match the measurements with fair accuracy, a modal decomposition shows that all models overpredict the response at the first eigenfrequency and underpredict it at the second eigenfrequency for extreme events. The latter is linked to the missing description of slamming loads in the modelling approach. The point force models of Rainey and KF are found to give quite similar results for the extreme events, the reasons for which are demonstrated by regular wave analysis.

Keywords: monopile wind turbine, wave loads, ringing, slamming, fully non-linear kinematics

1 Introduction

The number of bottom-fixed offshore wind turbines around the world has been increasing for the past decade and is expected to continue this trend in the years to come [3]. In Europe, 81.7% of all substructures for wind turbines are currently monopiles [4]. Over their lifetime, many of these structures will encounter extreme storms with steep and breaking waves. These waves may produce large responses thus threatening the structural integrity. In particular, two load effects have been the focus of several research projects over the last years, namely ringing and slamming.

Ringing responses are an intermittent excitation of the first mode of the structure by a steep wave, not necessarily breaking, whose fundamental frequency lies far from the first eigenfrequency of the structure. Figure 1 illustrates such an event: large first mode response is triggered by a very steep wave. The response builds up over one wave period and slowly decays. Ringing started gaining attention in the 1990s when it was observed during experimental campaigns on offshore oil and gas platforms [5], and has recently been observed in model tests of bottom-fixed offshore wind turbines as well [6]–[9]. Although the mechanisms producing ringing responses are not yet fully understood, all research agrees on the fact that it is a nonlinear phenomenon [2], [10]–[12], and that numerical models that only use linear wave kinematics to calculate the forcing on a structure cannot reliably reproduce the complete ringing response [13]–[16].

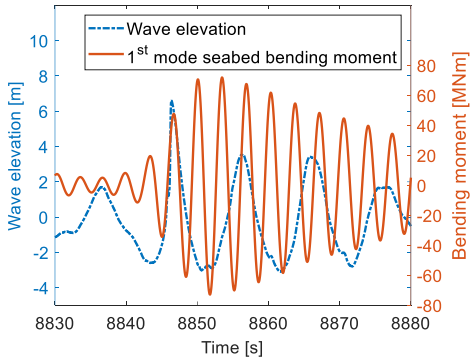

Figure 1. Illustration of a ringing event, recorded in the experiments presented by Suja-Thauvin et al. [17]. In this figure the quasi-static contribution to the bending moment has been filtered out to keep only responses near the first eigenfrequency of the structure.

Slamming events occur when a breaking or near-breaking wave impacts the monopile, producing an impulse load on the structure. The duration of slamming loads is usually very small compared to the first eigenfrequency of the structure [18] and it has therefore been argued that slamming loads alone are less important for the first-mode response, since this is to a large extent driven by ringing loads [8]. However, large responses around the second mode of the structure have been observed when slamming events occur, both on full-scale measurements [19] and during experiments [7], [9]. Suja-Thauvin et al. demonstrated that the dynamic amplification of the second mode of the structure can account for up to 20% of the maximum total response, thus showing that models that do not include slamming are likely to underestimate the response [17].

This discussion highlights the importance of having models for external forcing that predict the dynamic amplification of at least the first and second modes when designing a bottom-fixed offshore wind turbine. In the North Sea, the assessment of the response of the structure under extreme environmental conditions -so-called Ultimate Limit State (ULS) analysis- is commonly performed following the DNV-OS-J101, DNV-RP-C205 and IEC-61400-3 standards [20]–[22]. These standards suggest that the hydrodynamic loads produced by extreme waves are calculated with the Morison equation [23] applied with stream function theory wave kinematics [24]. In cases where the wave is breaking, a slamming model must be applied. For plunging breaking waves, the method derived by Wienke and Oumeraci [25] is usually applied; whereas for spilling breakers, the method developed by Nestegård et al. [26] is generally used (an overview of the different types of breaking waves is given by Galvin [27]).

The standard hydrodynamic load models used to predict ringing and slamming were initially developed for oil and gas platforms in deep waters and present some limitations regarding application to offshore wind turbines. These models fail to accurately depict the physics, as they generally do not reproduce the balance between the measured response of the first mode of the structure and that of the second mode [28]. In the present paper, four numerical models, briefly described hereafter, are analysed. The main goal of this paper is to assess how well these models predict the response of a bottom-fixed monopile offshore wind turbine subjected to extreme irregular waves. Experimental data produced by DHI Denmark as part of the Wave Loads project [29] are compared to the responses modelled with those numerical models.

The first model uses wave kinematics that include components up to second order in terms of wave steepness (hereafter referred to as second-order wave kinematics). The hydrodynamic loads are then computed applying those kinematics to the well-known Morison equation [23]. Compared to a traditional application of the Morison equation, the wave kinematics applied here include convective acceleration terms.

The second model uses fully non-linear wave kinematics applied to the Morison equation with the convective acceleration terms. In addition, a correction term presented by Manners and Rainey [30] is added to account for the fact that the cylinder is not slender in its axial direction.

The third model uses the same fully non-linear wave kinematics, and the force model developed by Kristiansen and Faltinsen [2], hereafter referred to as KF model. The point force of the KF model requires the kinematics at the mean water level. This is not trivial because when a wave trough passes the cylinder, the area around the mean water level is dry and no kinematics are available. A solution using Taylor expansion is suggested here.

The last model uses the same fully non-linear wave kinematics, and the so-called Rainey force model which is derived from energy balance arguments. When used with a circular cylinder, the model reduces to the Morison force model plus two additional terms. The first additional term is the above mentioned axial divergence term [30]. The second one is a point force at the surface which accounts for the change of kinetic energy in the fluid associated with the time variation of the wet portion of the cylinder [1].

For longcrested waves, the Rainey and KF models are identical apart from the point force terms that act at the free surface elevation (Rainey) and at the mean water level (KF). This difference between these models is analysed in detail in Section 6.

The aim of the present paper is to compare the predicted responses in strong sea states at intermediate depths for the four models with experimental data. Special focus is given to first- and second-mode response, and the role of slamming.

The paper is organised as follows: Section 2 presents the experimental set up used by DHI, and section 3 analyses the experimental data. In Section 4, we describe the numerical models in detail and some of the limitations in the way we apply them. Section 5 compares the responses obtained with the numerical models to those measured during the experimental campaign, and Section 6 analyses the differences between the Rainey model and the KF model. Conclusions are drawn in section 7.

2 Experiments

2.1 Experimental set-up

The experiments analysed in this paper were carried out at DHI Denmark in collaboration with the Technical University of Denmark (DTU) in the Wave Loads project [29]. A more detailed description of the experiments is given in the report of the Wave Loads Project [29] and in the work by Bredmose et al. [9], only the most relevant points are given here. The experiments were designed at a scale 1:80 following Froude scaling. All dimensions are given at full scale with the model scale in parenthesis and italic font, unless otherwise specified. The model was a circular cylinder of constant diameter and constant thickness of 6 m (*0.075 m*) and 0.144 m (*1.8 mm*), respectively, placed on a 1:25 slope. Three water depths were tested, 20.9 m, 31 m and 40.8 m (*0.26 m, 0.39 m* and *0.51 m*).

Two point masses of 937 t and 936 t (*1.786 kg* and *1.784 kg*) were placed 128.6 m and 87.0 m (*160.75 cm* and *108.75 cm*) above the sea bed, respectively, thus matching the first two eigenfrequencies of the support structure of the NREL 5 MW wind turbine [31], at $f_1 = 0.28$ Hz and $f_2 = 2.0$ Hz (*2.5 Hz* and *18 Hz*), as shown in Table 1. Figure 2 shows the dimensions of the experimental set up. The axis $(x, y) = (0,0)$ corresponds to the axis of the cylinder, and the height $z = 0$ corresponds to the still water level.

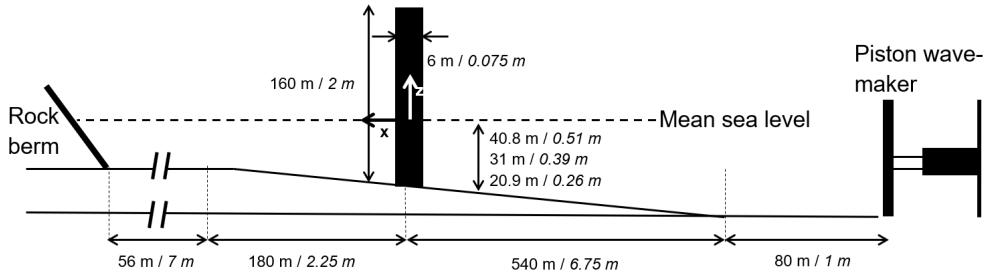

Figure 2. Experimental set-up (not to scale). Model scale dimensions are shown in italic font.

The wave conditions correspond to situations where the turbine is expected to be idling, therefore, no aerodynamics were modelled. Wet decay tests were carried out and the damping for the first and second mode was found to be 1.7% and 2.7% of the critical damping, see Table 1. For the first mode, this corresponds to a lower limit of damping ratios measured on similar idling full-scale wind turbines (1.7%-2.8% depending on the wind speed, [32]–[34]). Previous research suggests that the damping is more important for the decay than for maximum values [35].

Table 1. Eigenfrequencies and damping ratios of the first two modes of the model

	First mode	Second mode
Eigenfrequency [Hz]	0.28	2.0
Damping ratio [-]	0.017	0.027

Several wave gauges were placed in the wave basin at the centreline of the wave maker and towards the structure, and additional gauges were placed around the structure. A three-component force transducer at the bottom of the structure and five accelerometers distributed along the cylinder measured the response of the structure. One of the accelerometers was placed at the level of the highest point mass and is used in Section 5.1. All data was sampled at 200 Hz (model scale) giving a time step of 0.005 s (0.045 s in full scale).

2.2 Environmental conditions

Two different irregular sea states based on the JONSWAP spectrum [36] were considered. Combined with the three tested water depths, this gives six wave conditions, which are referred hereafter as load cases (Table 2). Some of these load cases have been used by Bredmose et al. [9] and Robertson et al. [37]. Each load case is defined by its targeted (as opposed to measured) significant wave height H_S, targeted spectral peak period T_p and water depth h, and named based on the depth and H_S. All sea states have a target spectral peakedness factor of $\gamma = 3.3$. Each load case is named with a letter corresponding to the depth (S-shallowest, M-medium and D-deepest) and a number corresponding to H_S. Note that the shallowest case does not correspond to shallow water waves [38] but rather to intermediate water waves.

For each sea state, we define an average steepness s_P based on the definition given in DNV-RP-C205 [21]. Instead of using the linear dispersion relationship, as is the case in DNV-RP-C205 [21], we calculate the average wave number k_p from the second-order dispersion relationship (eq (1) by Kirby and Dalrymple [39]). The average steepness is defined as

$$s_P = \frac{k_p H_S}{2\pi} \qquad 1$$

Full-scale measurements show that sea states above a certain average wave steepness are not realistic. All load cases are below the limiting value of s_P provided in DNV-RP-C205 [21].

For each sea condition, we also calculate an irregular Ursell parameter using the method suggested by Stansberg [40]:

$$U_r = \frac{k_p H_s}{2(k_p h)^3} \qquad 2$$

The Ursell parameter is typically defined for regular waves, and it has been showed that for $U_r > 0.33$, second-order wave theory is not valid to represent the regular wave kinematics [41]. Stansberg [40] extended the analysis to irregular waves and showed that this limit is also applicable. As shown in Table 2, load cases S8.3 and S11, which correspond to the shallowest water depth, are above this limit.

Table 2. Characteristics of the analysed load cases. The load cases are named after the depth (S – shallow, M - medium or D - deep) and the significant wave height (8.3 m, 11 m)

Name	Target H_s $[m]$	Measured H_s $[m]$	Target T_p $[s]$	Measured T_p $[s]$	h $[m]$	s_P $[-]$	U_r $[-]$
D8.3	8.3	7.88	12.6	11.95	40.8	0.2457	0.0697
M8.3	8.3	7.97	12.6	11.93	31	0.2664	0.1353
S8.3	8.3	8.32	12.6	11.99	20.9	0.2991	0.3500
D11	11	10.53	14	13.23	40.8	0.2795	0.1254
M11	11	10.55	14	13.42	31	0.3031	0.2431
S11	11	10.38	14	13.60	20.9	0.3301	0.6691

3 Analysis of the Measured Data

In this section, we analyse the data obtained during the experimental campaign. An analysis of the measured shear force at the seabed and acceleration at the highest point mass has also been performed by Bredmose et al [9]. A positive shear force corresponds to an external load in the direction of the waves (i.e. positive x-direction). For the design of wind turbine substructures, it is the amplitude of the shear force rather than its direction that is relevant. We therefore study the absolute value of the shear force and refer to 'maximum' or 'largest' shear force even when the forces are negative.

3.1 Statistical analysis

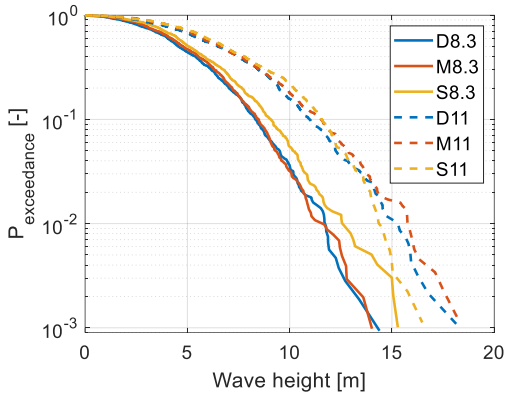

Figure 3. Exceedance probabilities for the measured wave heights

Figure 3 shows the exceedance probability plots for the measured wave heights for all six load cases. The wave height is measured between two zero-downcrossing values of the wave elevation time series. As expected, the load cases with $H_s = 8.3$ m show lower wave heights than the one with $H_s = 11$ m. For the $H_s = 8.3$ m load cases, non-linear shoaling effects induce an increase in wave heights for decreasing water depth. For the $H_s = 11$ m load cases, this effect occurs for the main part of the population. For the most extreme events however, the shallowest water case (S11) produces lower wave heights than the other two cases. This is due to wave breaking, which occurs more frequently in shallow waters.

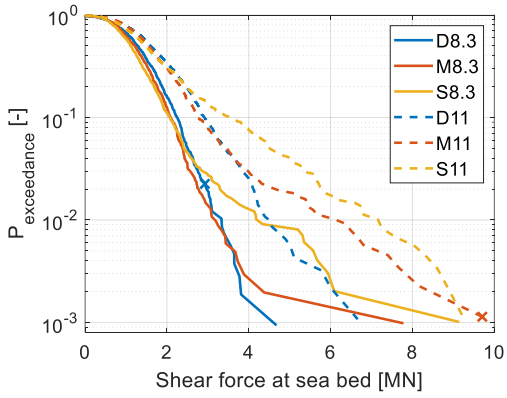

Figure 4. Exceedance probabilities for the measured shear force. The two events analysed in section 5.2 are marked with an X

Figure 4 shows the exceedance probability plots for the seabed shear force. To obtain Figure 4, two consecutive zero-downcrossings in the wave elevation signal are found, and the maximum absolute value in the force for each wave is identified. This procedure is applied throughout the paper for all exceedance probability plots. The measured shear force was filtered to remove frequencies above 4 Hz (full scale) by applying a Butterworth filter. This removes the contribution of the higher modes of the structure, as they were not tuned to fit any full-scale turbine. The third eigenfrequency of the structure lies at 5.6 Hz [29].

As for the wave heights, larger H_s implies larger shear forces for all three depths. Considering the $H_s = 11$ m cases, for 80% of the population ($P_{exceedance} > 0.2$), larger water depth implies larger shear forces. This is due to i) a larger water column acting on the structure and ii) a larger mode shape displacement further away from the sea bed. For deeper water, a load at the surface will induce higher modal loads than the same load at the surface for a shallower case. At $P_{exceedance} \approx 0.2$, the shear force in S11 becomes larger than that of D11 and M11. The shallower water depth produces more non-linear (steeper) waves which then have the necessary frequency content to excite the first mode of the structure. At $P_{exceedance} \approx 0.03$, the same phenomenon happens for M11, which then shows larger shear forces than D11. Similar trends can be observed when comparing load cases corresponding to $H_s = 8.3$ m.

3.2 Spectral analysis

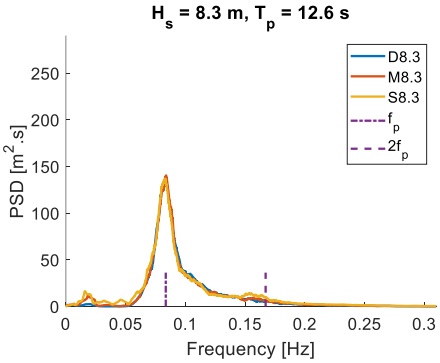

Figure 5. PSD of the wave elevation for the $H_s = 8.3$ m cases.

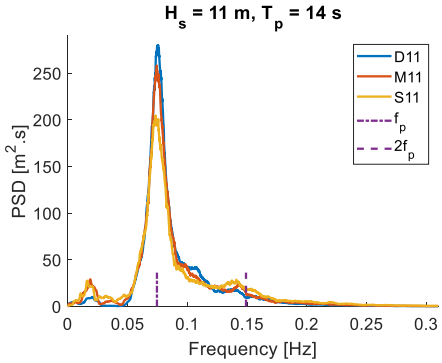

Figure 6 PSD of the wave elevation for the $H_s = 11$ m cases

Figure 5 and Figure 6 show the power spectral density of the wave elevation for $(H_S, T_P) = (8.3\text{ m}, 11.6\text{ s})$ and $(11\text{ m}, 14\text{ s})$, respectively. For the milder sea state of $H_s = 8.3$ m shown in Figure 5, the energy content around the peak frequency f_p is very similar for all three load cases. Differences appear in the difference-frequency region (between 0 and 0.05 Hz) and the sum- frequency region (around 0.16 Hz), where the load cases with shallower water have higher energy content. This is consistent with the fact that waves in shallow waters are more non-linear than in deep waters.

For the extreme sea state of $H_s = 11$ m shown in Figure 6, load cases in shallower water contain less energy around f_p. This is due to wave breaking, which occurs more frequently in shallow water than in deep water, and to the migration of energy to sub- and super harmonics. As for the previous sea state, the shallower cases show more energy in the difference- and sum-frequency region.

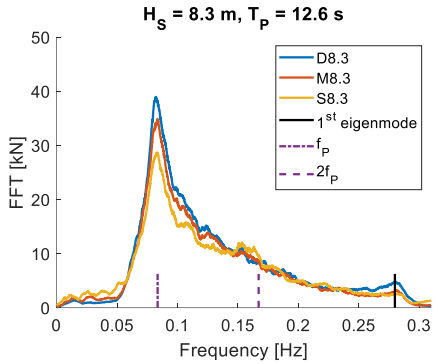

Figure 7. Discrete Fourier transform of the shear force for the $H_s = 8.3$ m cases

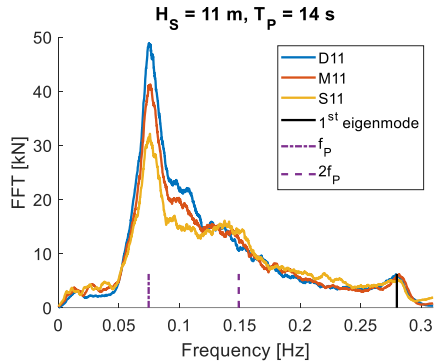

Figure 8. Discrete Fourier transform of the shear force for the $H_s = 11$ m cases

Figure 7 and Figure 8 show the Fourier components of the seabed shear force of the structure for $(H_S, T_P) = (8.3\text{ m}, 11.6\text{ s})$ and $(11\text{ m}, 14\text{ s})$, respectively. From these figures it appears that deeper waters induce larger shear forces around f_p. As explained in Section 3.1, this is due to a larger water column and to the loads acting at a level with a larger mode shape displacement. Around $2f_p$, the shear force in shallower waters becomes larger, due to the waves being more non-linear and therefore containing more energy at this frequency (as shown in Figure 5 and Figure 6).

The dynamic amplification of the first mode (0.28 Hz) is clearly visible in both Figure 7 and Figure 8. For the $H_s = 11$ m cases (Figure 8), the amplitude of the shear force around the first eigenfrequency is similar for all depths: the relative contribution of the response at the first natural frequency increases with decreasing water depth. This is consistent with Figure 6, as shallower depths induce steeper waves that contain energy at higher frequencies. This effect is not visible in Figure 7, where the amplitude of the shear force around the first eigenfrequency for the deepest case (D8.3) is larger than for the other cases. A possible explanation is that for the $H_s = 8.3$ m and $T_p = 12.6$ s cases, the sea state is milder and therefore produces less steep waves. For these cases, the effect of non-linearity of the waves is less important than for the stronger sea states of the $H_s = 11$ m and $T_p = 14$ s cases.

4 Presentation of the numerical models

In Section 5, we reproduce the measured shear forces with different numerical models. This is done in three steps: first the wave kinematics must be determined, then the hydrodynamic loads are computed and finally the shear force of the structure at the seabed is calculated.

The models used to perform these three steps are presented in this section.

4.1 Wave kinematics

In this study, we compare models using two different sets of wave kinematics.

The first set of wave kinematics includes components up to second order in terms of wave steepness. This set of kinematics is obtained by first linearizing the wave elevation measured on a wave gauge placed on the side of the cylinder, see Section 2.1 . The linearization is carried out by first removing the difference-frequency wave components, and then iteratively selecting the cut-off frequency of a low-pass filter such that the reconstructed wave spectrum (including first and second order terms) gives the best possible match to the spectrum measured on the wave gauge positioned on the side of the cylinder, see Section 2.1. Further details can be found in Bachynski et al. [6]. The reconstructed set of kinematics is hence referred to as 'second-order'.

The second set of wave kinematics is produced with the fully non-linear potential flow solver OceanWave3D, presented by Engsig-Karup et al. [42]. The code discretizes the domain by means of finite differences, and integrates the Laplace equation with fully nonlinear boundary conditions at the water surface. The Laplace problem is solved in a (x, y, σ) coordinate system, where

$$\sigma \equiv \frac{z+h(x,y)}{\eta(x,y,t)+h(x,y)} \quad 3$$

Here η is the wave elevation, h is the water depth and (x, y, z, t) are the spatial and time coordinates. Using the non-dimensional σ coordinate allows to solve for the Laplace equation in a time-invariant grid, increasing the accuracy and the speed of the solution. The kinematics in the physical coordinate system are then calculated from the potential $\Phi(x, y, \sigma)$ via a chain rule derivation. For example, the horizontal particle velocity for long crested waves is

$$u(x,z) = \frac{\partial \phi}{\partial x}(x,z) = \frac{\partial \phi}{\partial x}(x,\sigma) + \frac{\partial \sigma}{\partial x}\frac{\partial \phi}{\partial \sigma}(x,\sigma) \quad 4$$

The physical domain of the experiments from the wave maker to a position behind the cylinder was set up in the numerical domain. A linear representation of the incident waves was obtained by analysis of four wave gauges in the deeper part of the domain, by applying a variant of the reflection analysis of Goda and Suzuki [43], presented by Bredmose et al. [44]. This linear wave field was next imposed at the offshore boundary in a relaxation zone to the left of the wave maker. The approach is similar to the one used in Bredmose et al [9] and other OceanWave3D studies. In the relaxation zone, the numerical solution from the wave model is in each time step replaced by a weighted average of the numerical solution and the prescribed wave field. The weighting function undergoes a smooth transition from the prescribed wave field to the numerical wave field through the relaxation zone. Beyond the relaxation zone, only the internally- calculated potential is retained. The waves are then allowed to propagate through the shoaling numerical domain fulfilling the Laplace equation for the velocity potential and the fully non-linear kinematic and dynamic free surface boundary conditions. To represent the effect of wave breaking, which is beyond the physics of a potential-flow model, an ad-hoc dissipative filter was applied in each time step, whenever the downward local vertical particle acceleration exceeded 0.3 times gravity. This value was has provided good results in earlier studies, e.g. Schløer et al. [45].

The kinematics are then sampled in pre-defined positions in space and time and saved to memory. The fully non-linear kinematics are referred to as 'FNL' in the following.

Figure 9 shows the exceedance probability plots of the wave heights. For each load case, the exceedance probability is computed for the measured and modelled waves. The FNL kinematics generally agree with the measured wave elevation. S11 is the case with the shallowest water and the largest average steepness, and consequently produces the most non-linear waves. For S11, the results of the FNL model overestimate the most extreme wave heights by about 30%. Applying a stricter wave-breaking filter could enable a closer match but was not attempted here. It is therefore expected that the responses calculated with the FNL kinematics for S11 will be significantly larger than the measurements. As expected, although the second-order wave field is produced from a wave gauge at the same position as the structure, the kinematics from the second-order model produced wave heights slightly lower than those from the FNL model. As noted in Table 2, S8.3 and S11 have an Ursell number higher than 0.33 and therefore exceed the limit of validity of second-order theory. In addition, the second-order kinematics are obtained assuming a flat bottom, which is not consistent with the test conditions.

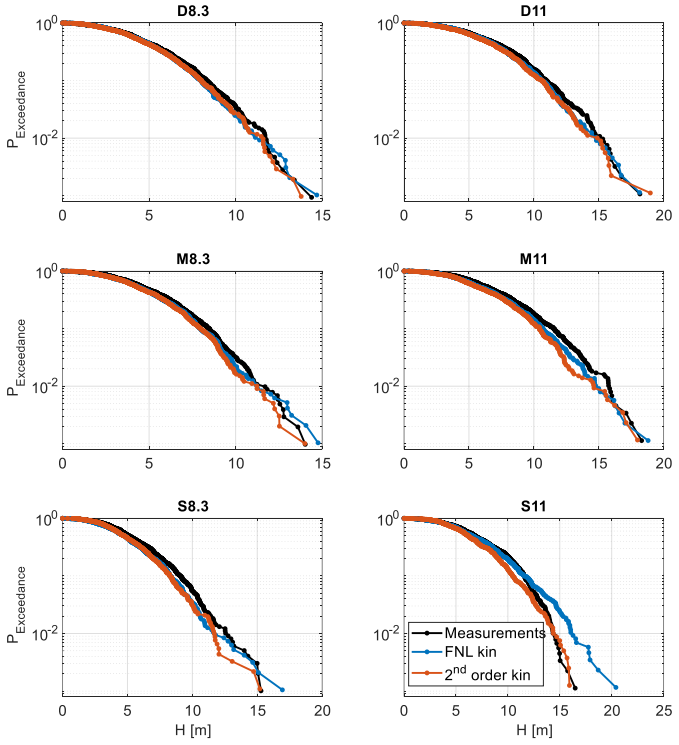

Figure 9. Exceedance probability plots for the wave height for all load cases. Comparison between the measured wave elevation and the wave elevations obtained with the FNL and second-order kinematics models

4.2 Load models

Four load models are used to compute the hydrodynamic loads on the structure: i) the Morison equation presented by Morison [23] with second-order wave kinematics, hereafter 'Morison second-order', ii) the Morison equation with FNL kinematics, hereafter 'Morison FNL', iii) the model proposed by Kristiansen and Faltinsen [2], with FNL kinematics, hereafter 'KF' and iv) the model proposed by Rainey [46], with FNL kinematics, hereafter 'Rainey'.

Note that the motion of the structure was not taken into consideration for any of the models. It is assumed that the displacement of the structure is not significant compared to other sources of uncertainty. This assumption was verified by modelling all load cases with and without the motion of the structure, where differences of less than 1% were found. The main damping of the response was found to be due to structural damping.

4.2.1 Morison second-order

The first model is based on the well-known Morison equation [23], often used due to its simplicity. The difficulty of using the Morison equation resides in the selection of the wave kinematics. As mentioned in the introduction, the simplest solution of applying linear wave kinematics does not produce accurate results in steep waves. At the other end, some advanced kinematic models such as those obtained by using a fully non-linear high-order boundary-element solver [14] are able to produce both first and second mode response of the structure. The Morison equation is composed of a drag term and an inertia term

$$F_{Morison} = F_D + F_I \quad 5$$

with

$$F_D = \int_{-h}^{\eta} \rho C_D a u|u|\, dz \quad 6$$

and

$$F_I = \int_{-h}^{\eta} C_M \rho \pi a^2 \frac{du}{dt} dz \quad 7$$

where η is the incident wave elevation, ρ is the water density, a is the cylinder radius, u is the horizontal wave particle velocity and C_D and C_M are the drag and inertia coefficients, respectively. In the present analysis, the values of C_D and C_M are obtained by calculating an irregular version of the KC and Reynolds numbers [47] based on the measured T_P and the standard deviation of the particle velocity from the FNL kinematics. Table 4.11 in Sumer and Fredsøe [48] is then used to determine C_D and C_M. In the present study, for all load cases, $C_D = 1.1$ and $C_M = 2$.

The derivative of the particle velocity is taken as the Langrangian derivative in 2D:

$$\frac{du}{dt} = \frac{\partial u}{\partial t} + u\frac{\partial u}{\partial x} + w\frac{\partial u}{\partial z} \quad 3$$

where w is the vertical particle velocity. The total load can thus be expressed as

$$F_{Morison\ 2^{nd}\ order} = \int_{-h}^{\eta} \left(\mathrm{C_M} \rho \pi a^2 \left(\frac{\partial u}{\partial t} + u\frac{\partial u}{\partial x} + w\frac{\partial u}{\partial z} \right) + \rho C_D a u|u| \right) dz \quad 4$$

In this model we use the second-order kinematics to compute the loads. The loads are thus integrated to second-order wave elevation.

4.2.2 Morison FNL

The Morison FNL model is the same as the Morison second-order model, except that 1) the FNL kinematics are used and, 2) to account for the fact that the cylinder is not slender in its axial direction, the term $\rho \pi a^2 u\, \partial w/\partial z$ is added [30]. As in the previous model, the Lagrangian acceleration is applied. For the present 2D incident waves, conservation of mass implies that $\frac{\partial u}{\partial x} = -\frac{\partial w}{\partial z}$, so the total load can then be expressed as:

$$F_{Morison\ FNL} = \int_{-h}^{\eta} \left(\mathrm{C_M} \rho \pi a^2 \left(\frac{\partial u}{\partial t} + w\frac{\partial u}{\partial z} \right) + (\mathrm{C_M} - 1) u \frac{\partial u}{\partial x} + \rho C_D a u|u| \right) dz \quad 5$$

As for the Morison second-order model, values of $C_D = 1.1$ and $C_M = 2$ are used.

4.2.3 KF model

The first version of the so-called FNV model was developed by Faltinsen et al. [11] in order to predict ringing responses of oil and gas platforms observed on model tests in the 90s [5]. This model was initially developed for deep water regular waves based on perturbation theory and includes the effect of long wave diffraction and the waves scattered by the cylinder. It is consistent up to third order in terms of wave steepness. Krokstad et al. [49] presented a validation of the model in deep water, and Paulsen et al. [50] showed that the third-order load matched calculations computed with CFD. This model was further extended to irregular waves by Newman [51] and eventually to finite water depth by Kristiansen and Faltinsen [2]. The latter implementation, referred to as KF model, is the one used in the present analysis, and the load is calculated as follows

$$F_{KF} = \int_{-h}^{\eta} F'(z,t) dz + F^{\psi} \quad 6$$

$F'(z,t)$ is a distributed load given by

$$F'(z,t) = \rho\pi a^2\left(\frac{\partial u}{\partial t} + u\frac{\partial u}{\partial x} + w\frac{\partial u}{\partial z}\right) + m_a\left(\frac{\partial u}{\partial t} + w\frac{\partial u}{\partial z}\right) \quad 7$$

where $m_a = \rho\pi a^2$ is the added mass in surge. F^{ψ} is the force due to the scattered potential and is applied at $z = 0$.

$$F^{\psi} = \rho\pi a^2 \frac{4}{g} u^2 \frac{\partial u}{\partial t} \quad 8$$

where g is the acceleration due to gravity. In the original paper from Kristiansen and Faltinsen the kinematics used to calculate F^{ψ} are to be taken at $z = 0$ [2]. However, in the current analysis, no FNL kinematics are available in the dry parts of the structure: whenever a trough passes the structure, there are no kinematics at $z = 0$. Therefore, the kinematics at $z = \eta$ are Taylor expanded to $z = 0$. This approach is assessed in section 4.4.1.

In the present implementation, we add a drag term based on the Morison equation with $C_D = 1.1$. The total force calculated with the KF model is then

$$F_{fFNV} = \int_{-h}^{\eta}\left(2\rho\pi a^2\left(\frac{\partial u}{\partial t} + w\frac{\partial u}{\partial z}\right) + \rho\pi a^2 u\frac{\partial u}{\partial x} + \rho C_D a u|u|\right)dz + F^{\psi} \quad 9$$

where F_D is defined as in subsection 4.2.1.

In the present analysis we use the FNL kinematics to compute the KF loads. To be consistent to third order, contributions higher than third order should be removed from the hydrodynamic loads thus calculated. This is not trivial and was not carried out in this analysis. This implies, for example, that loads of fourth order are obtained due to the multiplication of contributions of second-order kinematics in the convective acceleration, whereas fourth order terms due to the scattered potential will be missing since the scattered potential is consistent to third order only. The effects of this shortcoming are analysed in section 4.4.2.

4.2.4 Rainey model

The Rainey model is derived from energy balance arguments. When applied to circular cylinders, it reduces to the Morison equation as presented in section 4.2.1 with two additions. The first one accounts for the fact that the cylinder is not slender in its axial direction by adding the term $m_a u\frac{\partial w}{\partial z}$ [30]. The second one corresponds to a point force at the free surface to account for the change in fluid kinetic energy due to the variation in time of the submerged portion of the cylinder (equation 7.4 in the original paper [1]). This force is given by

$$F^{\eta} = -\frac{1}{2} m_a u^2 \frac{\partial \eta}{\partial x} \quad 10$$

where η is the instantaneous free surface elevation. By noting that conservation of mass for the present 2D waves gives $\frac{\partial u}{\partial x} = -\frac{\partial w}{\partial z}$, we can rewrite the force given by the Rainey model as

$$F_{Rainey} = \int_{-h}^{\eta}\left(2\rho\pi a^2\left(\frac{\partial u}{\partial t} + w\frac{\partial u}{\partial z}\right) + u\frac{\partial u}{\partial x} + \rho C_D a u|u|\right)dz + F^{\eta} \quad 11$$

with $C_D = 1.1$. In the present implementation, the FNL kinematics are used for the Rainey model. It should be noted that the integrated force of the Rainey model and the KF model in the present implementation are the same and equal to the force computed in the Morison with FNL kinematics model. The only difference between the Rainey and KF models lies in the point force and is further explored in section 6.

Table 3 is a summary of the four load models implemented in this analysis.

Table 3. Summary of the load models. 'X' means that the term is included in the model, '-' means that it is not

	Morison second-order	Morison FNL	KF	Rainey
Drag and inertia term	X	X	X	X
Lagrangian acceleration	X	X	X	X
Non-slender in axial direction	-	X	X	X
Point force	-	-	F^{ψ}	F^{η}
Wave kinematics	second-order	FNL	FNL	FNL

4.3 Structural model

The hydrodynamic loads calculated in the previous section are used as input to a finite element representation of the cylinder described in section 2.1 with 160 elements. The finite element software applied here is Ashes, which uses the Newmark-Beta integration method to solve for the deflections of the structure [52]. The added mass coefficient used is $C_a = 1$, and the first and second eigenfrequencies obtained with the finite element model match perfectly those given in section 2.1. The damping applied is Rayleigh damping, with the damping ratio tuned to match that of the first mode of the physical model. This implies that the damping of the second mode is larger on the numerical model than on the physical model.

Figure 10 shows the mode shapes of the structure obtained with Ashes. The mode shapes and the eigenfrequencies show slight variations depending on the water depth. These variations are accounted for in the numerical simulations.

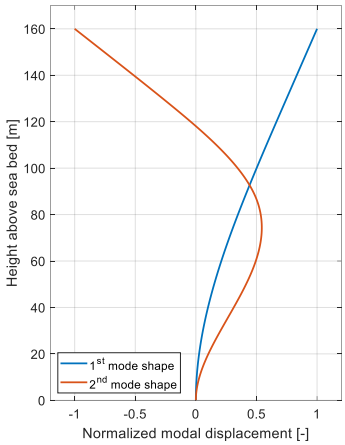

Figure 10. Mode shapes of the structure, obtained with Ashes ($h = 31$ m)

4.4 Limitations of the current method to compute the F^{ψ} term

4.4.1 Selection of the kinematics

As explained in section 4.2.3, the theory developed by Kristiansen and Faltinsen implies that F^{ψ} must be computed with kinematics at $z = 0$ and applied at $z = 0$ [2]. In the current work, since no FNL kinematics are available at $z = 0$ when the cylinder is in a wave trough, the kinematics at $z = 0$ are obtained through first order Taylor expansion:

$$u(z,t)|_{z=0} = u(z,t)|_{z=\eta} - \eta \left.\frac{\partial u(z,t)}{\partial z}\right|_{z=\eta} \quad 12$$

$$\left.\frac{\partial u(z,t)}{\partial t}\right|_{z=0} = \left.\frac{\partial u(z,t)}{\partial t}\right|_{z=\eta} - \eta \left.\frac{\partial^2 u(z,t)}{\partial z \partial t}\right|_{z=\eta} \quad 13$$

In the present study, $\partial^2 u/\partial z \partial t$ is not output by the fully non-linear solver, so it is calculated by numerical differentiation using the available grid points.

To assess the impact of this method for calculating F^{ψ}, the shear force of the structure is modelled in regular waves with kinematics calculated with the stream function wave theory, following the method presented by Rienecher and Fenton [24], which solves for a velocity potential in the whole domain and therefore provides kinematics in the dry parts of the domain also. Three procedures are studied, described hereafter.

- $z = 0$ based F^{ψ}: the kinematics are taken at $z = 0$, as proposed in the original method
- Taylor expansion based F^{ψ}: the kinematics are obtained from first order Taylor expansion (equations (17) and (18)).
- $z = \eta$ based F^{ψ}: the kinematics are taken at $z = \eta$ and the force is applied at $z = \eta$

To assess the difference between these formulations, the trough-to-trough characteristics of the wave that produced the largest shear force over the whole experimental campaign are selected: height $H = 13.7$ m, period $T = 17$ s and depth $h = 20.8$ m. As recommended in the standard IEC-61400-3 [22] for a wave of these characteristics, the order of the stream function is taken as $N = 9$. Figure 11 shows the shear force of the structure to the KF model where F^{ψ} has been calculated with the three procedures proposed above. The approach with the kinematics taken at $z = \eta$ produces an overestimation of the response of about 25% and will therefore not be used. Using the Taylor expansion approach produces an underestimation of the shear force of 3%. This procedure is kept in the rest of the analysis.

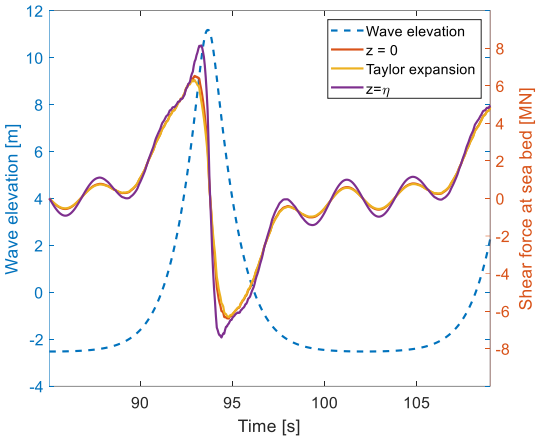

Figure 11. Shear force of the structure in regular waves with the KF model. $F^{\psi}$is computed following two different procedures

Adding more terms to the Taylor expansion produced good results in the simulations with the regular waves but gave clearly unphysical loads when applied to irregular waves. Therefore, analyses with more terms are not shown.

4.4.2 Contributions of higher than third order

Another limitation in the way the KF model is implemented in the present work is that we consider all orders in the incoming wave kinematics, as explained in section 4.2.3. To assess this limitation, the incoming kinematics must be separated into contributions to different orders. Since it is not straightforward to perform such a separation on a stream function wave, a Stokes fifth order wave is used instead, implemented following the work by Fenton [53]. The Stokes expansion does not converge for the regular wave previously analysed in section 4.4.1, therefore a less steep wave is chosen, with a height $H = 10.5$ m, a period $T = 16$ s in a depth $h = 31$ m. Two procedures are analysed here:

- KF3: only kinematics that produce loads up to third order are kept, both for the integrated load and for the F^{ψ} term, as proposed in the original method.
- KF5: all kinematics are kept. The integrated load is integrated to the instantaneous fifth order free surface.

Figure 12 shows the shear force of the structure for these two procedures. The KF5 procedure produces a maximum shear force about 15% lower than the KF3 procedure. Investigating the kinematics, it is found that higher order kinematics reduce the excitation load at lower harmonics. For instance, the fourth order kinematics reduce the second harmonic of the load, and the fifth order kinematics have a similar effect on the third harmonic of the load. As a consequence, the excitation load obtained with the KF5 procedure is lower than that obtained with the KF3 procedure. This is consistent with the work of Kristiansen and Faltinsen, who showed that the KF5 procedure generally produces lower loads than the KF3 procedure at the first, second and third harmonic of the force [2]. They also point out that the KF3 procedure tends to overestimate the excitation loads when compared to measurements. They finally show that using the KF5 procedure, while still overpredicting with respect to the measurements, gives a closer match [2].

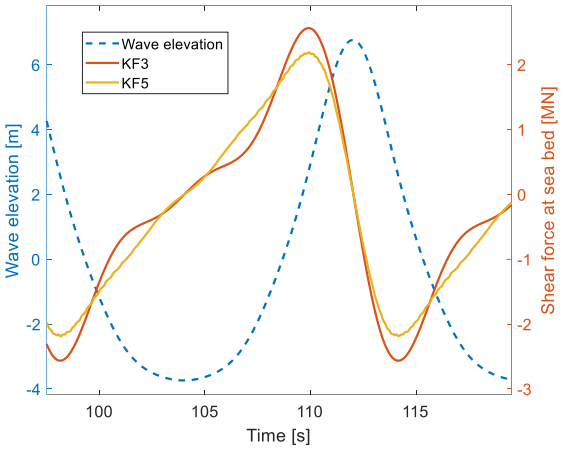

Figure 12. Shear force for a fifth order Stokes waves with H = 10.5 m, T =16 s in h = 31 m depth

In the case of fully nonlinear kinematics, it is most natural to apply the full kinematics with no attempt of decomposition into orders. While the above analysis is restricted to regular waves and fifth order, the results support that this approach is applicable. This will be further tested in section 5 where comparisons with measurements are presented.

5 Numerical responses

In this section, we assess how the different numerical models perform by comparing them to the measurements. As pointed out in section 4.1, for S8.3 and S11, the Ursell parameter shown in Table 2 is above the classical limit of 0.33, above which second-order theory is not sufficient to predict the wave kinematics [40]. The shear forces produced by the Morison second-order model were therefore largely underpredicting the measurements and are not shown in this section.

5.1 Statistical analysis

Figure 13 shows the exceedance probability plots for the shear force at the sea bed for the six load cases and four numerical models. The numerical results are compared against the experimental data.

Below shear forces of about 4 MN, all models compare well with the measurements, except the Morison second-order model, that shows a slight overprediction for D8.3 and M8.3. For shear forces above 4 MN, deviations from the measurements are observed. Generally, the Morison second-order model produces the smallest forces, followed by the Morison FNL model, the Rainey model and then the KF model.

In D11, the extreme force peaks are best predicted by the Rainey model, while they are overpredicted by the KF model. In M11, the largest force calculated with the KF and the Rainey model are 3.5 and 7.5% lower than the largest measured force, respectively. For load cases D-M-S8.3 and D-M11, and with the exception of the second largest force predicted by the KF model in D11, the forces calculated by the KF and the Rainey model lie within 12% of the measured forces. However, none of these two models can be said to generally over- or underpredict the results. For S11, all models using the FNL kinematics give larger results than the measurements due to the overprediction of the wave heights by the FNL model shown in Figure 9.

The Morison FNL model is equivalent to the Rainey and KF models without their respective point forces. It can be seen in Figure 13 that this model underpredicts most of the extreme events, which shows the importance of the point loads. The KF model has been shown to overpredict the third harmonic loads for steep waves [2]. The steepness for the waves producing the largest shear forces is calculated with the following formula:

$$s = kH/2\pi \qquad 14$$

where k is the wave number calculated from the second-order dispersion relationship (eq (1) given by Kirby and Dalrymple [39]) based on the downcrossing period and H is the crest-to-trough height. The steepnesses thus calculated are well above the $1/40$ limit for which Kristiansen and Faltinsen showed that the third harmonic load is overpredicted by the KF model [2]. Despite this overprediction, the

modelled extreme forces agree reasonably well with the measurements. This is explored further in this section by decomposing the acceleration at the highest point mass into first and second structural mode contributions.

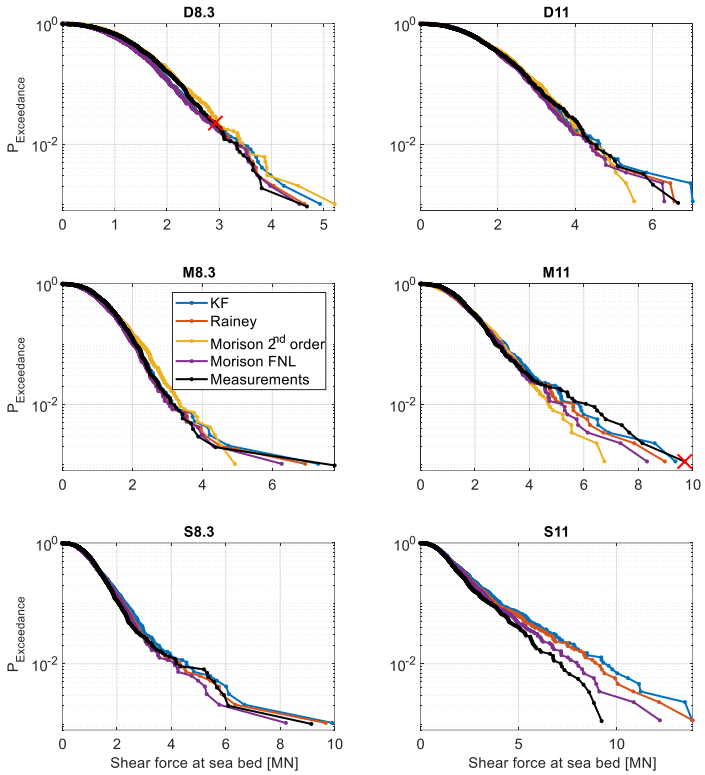

Figure 13. Exceedance probability plots for the shear force. The two individual events analysed in section 5.2 (one in D8.3 and the other in M11) are marked with a red asterisk.

To examine the dynamic load effects in detail, the structural accelerations are now analysed. Figure 14 shows the exceedance probability plots for the acceleration at the highest point mass of the structure. For the measured acceleration, Bredmose et al. found that increasing

depth led to an increased acceleration level due to the larger moment arm. Extreme accelerations, though, were strongest at the smallest depths due to the impulsive loads from very steep and breaking waves [9].

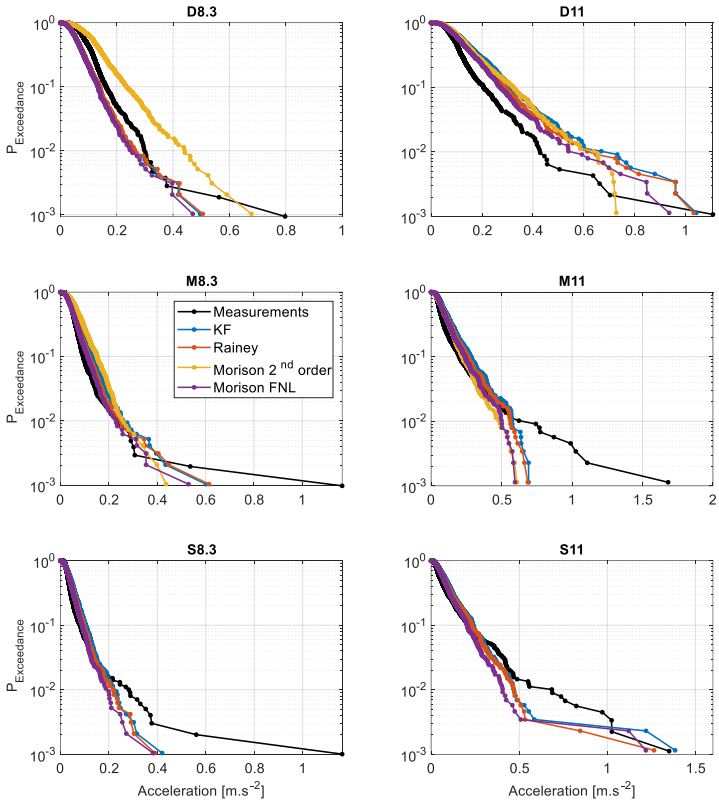

Figure 14. Exceedance probability plots for the total acceleration at the highest point mass

For S11, the numerical models largely overpredict the measurements due to the inaccurate wave heights resulting from the FNL kinematics visible in Figure 3. S11 is not analysed in further detail. In general, the models using the FNL kinematics show the same order obtained in the analysis of the shear forces: Morison FNL produces the lowest accelerations, followed by the Rainey model and then the KF model.

With the exception of D11 and the Morison second-order model in D8.3, all models match the main part of the population reasonably well. The extreme events however are consistently underestimated by all models in all load cases, and an increasing Ursell number leads to an increasing number of extreme events being underestimated.

To understand this effect, the accelerations are decomposed around the first and second eigenfrequencies of the structure. The decomposition is performed by applying a Butterworth band-pass filter. For the first mode, the filter was of ninth order and a frequency band of $f_1 \pm 0.022$ Hz was used. For the second mode, the filter was of sixth order and a frequency band of $f_2 \pm 0.2$ Hz was used. Different frequency bands and filter orders were tested. Although the amplitude of the filtered acceleration shows a slight sensitivity to those parameters, the qualitative results did not exhibit significant variations. Note that the accelerations that do not occur around the first or second eigenfrequency are not considered in this analysis. Figure 15 shows such a decomposition for the largest measured acceleration of M8.3.

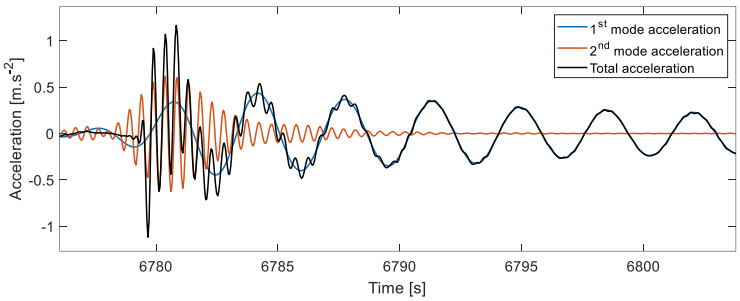

Figure 15. Decomposition of the measured acceleration at the nacelle for the largest acceleration during M8.3

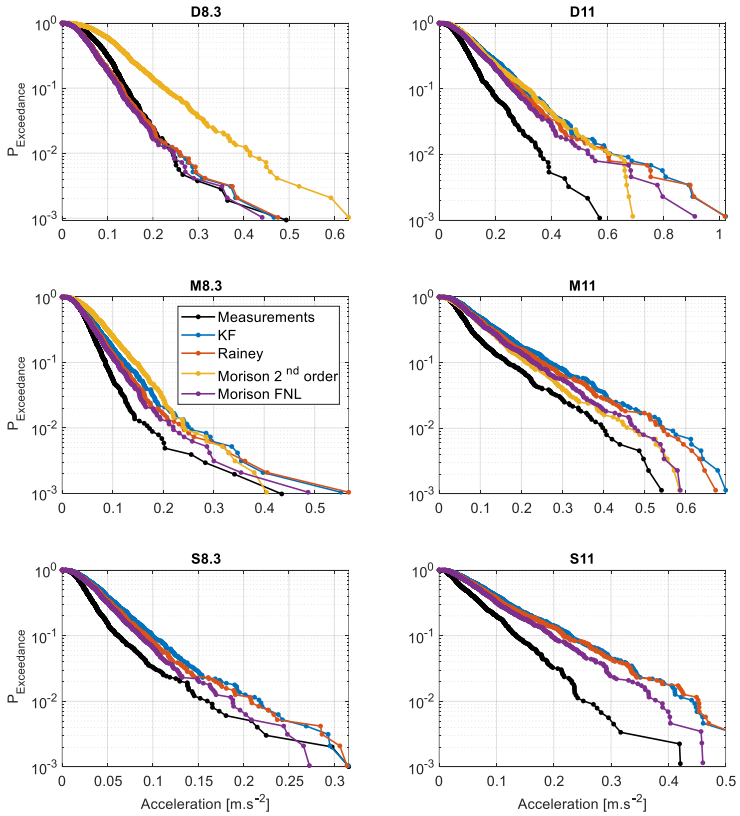

Figure 16. Exceedance probability plots for the acceleration at the first eigenfrequency

Figure 16 shows the exceedance probability plots for the structural acceleration filtered around the first eigenfrequency. Note that the number and order of the events shown in this figure might be different than that of the unfiltered acceleration shown in Figure 14, as the largest unfiltered acceleration does not necessarily exhibit the largest first mode acceleration.

For the main population of events, the results follow a similar trend as the unfiltered acceleration shown in Figure 14. This is consistent since non-extreme events are mainly the results of first mode forcing. For most extreme events however, all models overestimate the

measurements. As for the unfiltered accelerations, among the models using the FNL kinematics, the Morison FNL model produces the lowest results, followed by the Rainey model and the KF model.

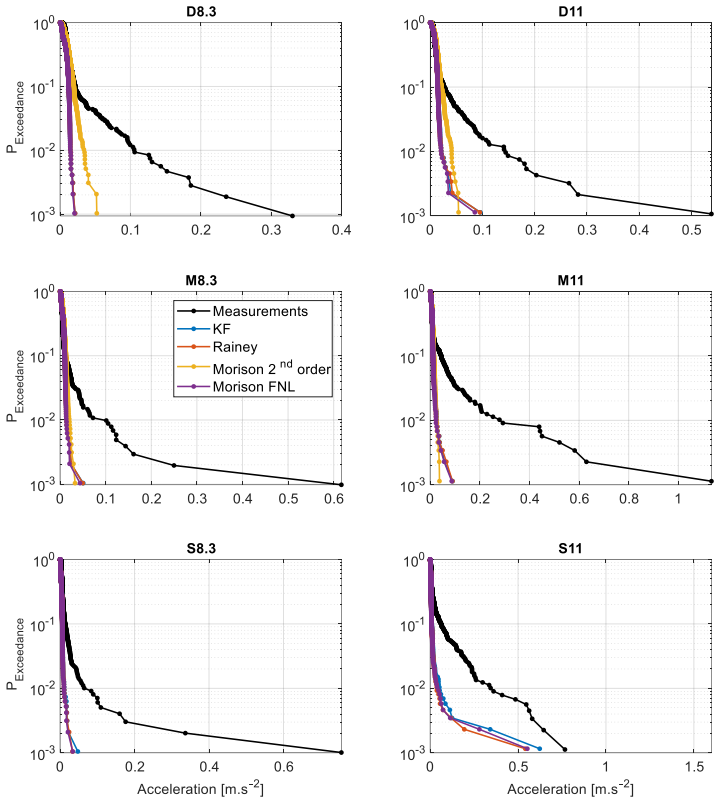

Figure 17. Exceedance probability plots for the acceleration at the second eigenfrequency

Figure 17 shows the acceleration around the second mode of the structure. For all load cases, the models follow the main part of the population reasonably well but largely underpredict extreme events. This is due to the absence of a slamming model in the numerical models: large events are produced by large waves which are generally breaking and thus will excite the second mode of the structure [19]. de Ridder et al. [7] showed based on similar experimental data that triggering the second mode of the structure has a large influence on the acceleration at the top. Suja-Thauvin et al. [28] compared different numerical models to calculate loads on offshore wind turbines and demonstrated that slamming models were required to produce impulse loads with a duration short enough to trigger second mode response. Since none of the models analysed in this study include a slamming model, it is expected that they underestimate the second mode acceleration.

The decomposition of the acceleration around the first and second eigenfrequencies of the structure shows that the models tend to overpredict the response around the first mode but underpredict the response around the second mode.

5.2 Single event analysis

In this section, we analyse two characteristic events of the experimental campaign, marked with an 'X' in Figure 4 and Figure 13. For each event, four time series are shown comparing the measurements and the numerical models:

- The wave elevation. Note that the KF, the Rainey and the Morison FNL models use the same kinematics and therefore show the same wave elevation.
- The modal excitation, computed with the mode shape of the first mode following the equation

$F_{m1} = \int_{-h}^{\eta} F_{ex}(z)\psi_1(z)dz$

where F_{ex} is the hydrodynamic load calculated with the models described in section 4.2 and ψ_1 is the first mode shape. Note that no measurement of the excitation load is available.

- The shear force at the seabed.
- The acceleration at the highest point mass.

Figure 18 illustrates an event where a mild shear force was recorded. No dynamic amplification appears in the measured or modelled shear forces. The lowest plot shows significant acceleration around the first mode and a lower acceleration at the second mode. . Thisplot also shows that the Morison second-order model produces higher acceleration at the first natural frequency than the other models, which is consistent with Figure 16. This is due to the different kinematics: the upper graph of Figure 18 shows that the wave obtained with the second-order kinematics is steeper than the one obtained with the fully nonlinear kinematics. This produces a larger amount of high frequency content in the load, which excites the first mode of the structure. The phasing between the wave elevation and therefore the shear force response is also better for the Morison second-order model than the KF and Rainey models. This is because the second-order kinematics are obtained from a linearization of the wave measured at the cylinder, while the FNL kinematics are produced from a linearization of the measured wave elevation that is allowed to propagate from the wave maker.

It can also be noted that the KF, the Rainey and the Morison FNL models produce very similar excitation loads and therefore very similar shear forces. As the waves composing the studied event have low steepness, the particle velocities and acceleration are also low. The F^{ψ} and F^{η} terms are of third order in terms of wave steepness, so these point forces become small compared to the F_I of the Morison equation defined in equation (5). Therefore, the excitation loads from the KF and the Rainey models are mainly due to the integrated load, which, as shown in section 4.2, is equal to the Morison FNL model.

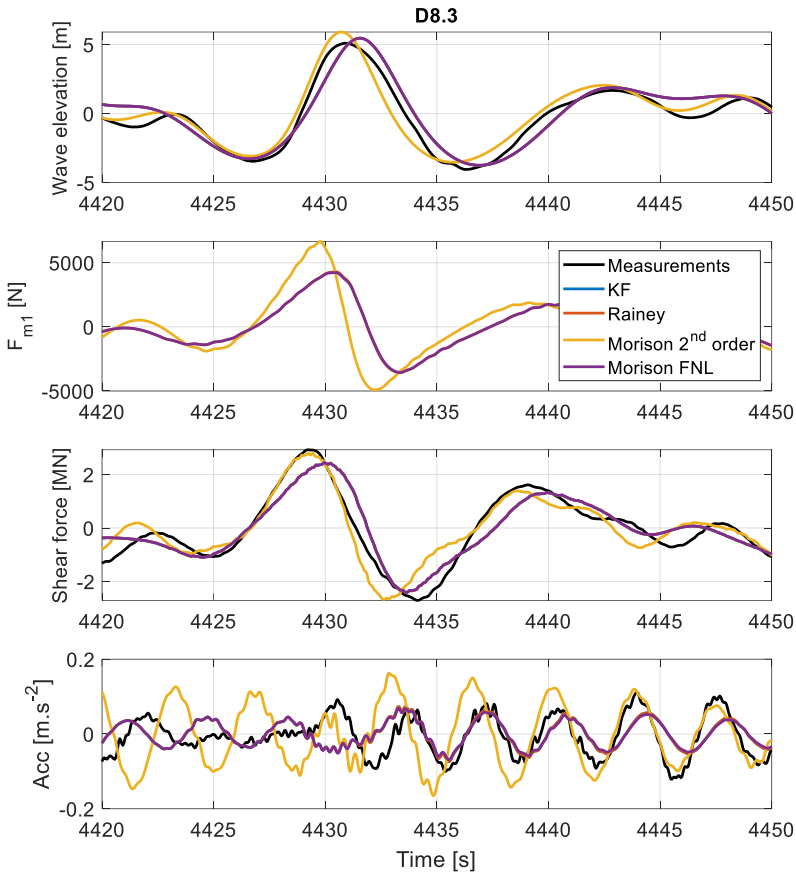

Figure 18. From top to bottom: wave elevation, modal excitation, shear force and acceleration for an event recorded during D8.3. In the second subplot, the differences in modal force F_{m1} for the Morison FNL, the Rainey and the KF models are indistinguishable.

As seen in Section 5.1, only the models that use the FNL kinematics can correctly predict the most extreme events. To understand this, the event that produced the largest measured response of M11 is now analysed individually. Figure 19 shows the same results as in the previous example for this event. The upper plot shows that the wave modelled using the second-order kinematics model is less steep than the measured one. Combined with the absence of a point load, the lower steepness produces lower excitation loads than the other models and the Morison second-order model therefore underpredicts both the shear force and the acceleration, consistent with the statistical analysis of section 5.1.

The steepness of the measured wave and the large second mode energy observed both in the measured shear force and acceleration indicate that the wave is breaking. The wave resulting from the FNL kinematics is significantly steeper than the one resulting from the second-order kinematics but less steep than the measured one. The shear force graph shows that the models using the FNL kinematics produce first mode response but fail to trigger the second mode. This is also the case for the acceleration. This suggests that the excitation forces calculated with these models do not have the required frequency content to significantly excite the second mode of the structure.

The KF model and the Rainey model give similar shear forces, as observed in Figure 13. However, the KF model produces a high frequency variation of the modal force around the maximum, which translates into slightly larger shear force and acceleration. This is consistent with the findings of section 5.1 where it was found that the KF model generally produces larger responses than the Rainey model.

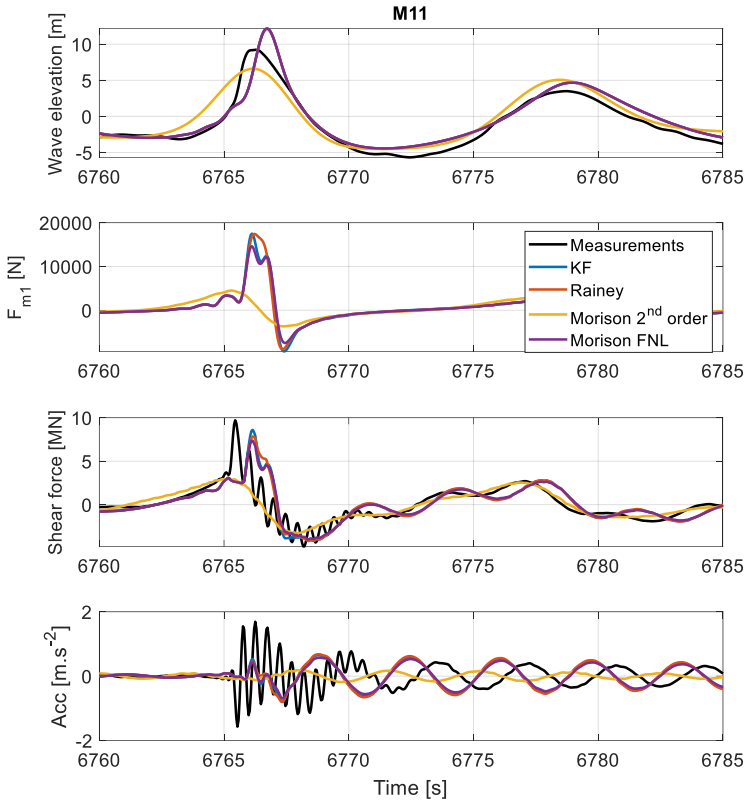

Figure 19. From top to bottom: wave elevation, modal excitation, shear force and acceleration for the event that produced the largest shear force in M11

6 Comparison between the F^{ψ} and the F^{η} terms

As shown in section 4.2.4, the Rainey model and the KF model in the Taylor expanded version only differ from the Morison FNL model by their respective point forces F^{η} and F^{ψ}, which contribution is visible in Figure 13. This figure also shows that the Rainey model and the KF model produce similar results. However, it is known that $F^{\psi} = 8F^{\eta}$ in the small amplitude limit [10], [11], [54]. To understand how the two models can produce similar results despite this apparent eightfold ratio, the point forces are analysed in detail in this section.

In the present context, the kinematics for F^{η} are taken at $z = \eta$ and the kinematics for F^{ψ} are taken at $z = 0$. In addition, the kinematics are fully nonlinear and the contributions of different orders are not isolated. In the following paragraph, a comparison between F^{ψ} and F^{η} is performed for regular waves. The waves analysed are shown in Figure 20: the three water depths studied in this work ($h = 20.9$ m, $h = 31$ m and $h = 40.8$ m) are tested, a period $T = 16$ s is chosen for all waves and the wave height H is varied to go from small steepness waves up to the breaking limit. As in section 4.4.2, the stream function theory is used to model the kinematics of the waves. The order of the stream function is chosen according to Figure 20. Note that the algorithm did not converge for steepness larger than the steepest ones shown in Figure 20.

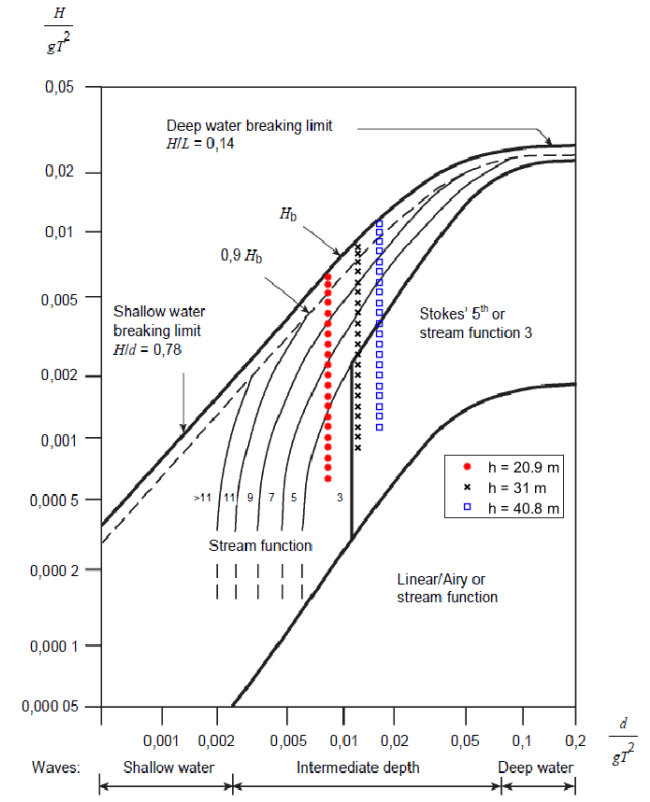

Figure 20. Selected waves for the comparison between F^{ψ} and F^{η} (taken from the IEC-61400-3 standard [22])

The analysis in this section focuses on the third harmonic of the F^{ψ} and the F^{η} forces. The third harmonic is extracted by band-pass filtering the time series for the two forces. Figure 21 shows the amplitude of the third harmonic of the two point forces for the waves shown in Figure 20. In this figure, for low wave height, the amplitude of the third harmonic predicted by the F^{ψ} term is about eight times larger than that of the F^{η} term. Note that this ratio is not visible in the total force (for example in Figure 13) because the contribution of both point forces is not significant compared to the integrated load for low wave heights.

As the wave height increases, the ratios between amplitudes of the third harmonic decrease until, for the largest wave heights, the third harmonic of both point forces becomes similar.

The result at small amplitudes is consistent with the previous research mentioned above [10], [11], [54]: the present analysis considers all orders, but at small amplitudes the non-linear kinematics are not significant compared to the linear ones and $F^{\psi} \approx 8F^{\eta}$. For larger amplitudes however, the higher orders play an important role in the estimation of the excitation loads. In particular, the difference between the kinematics at $z = \eta$ (taken as input for F^{η}) and $z = 0$ (taken as input for F^{ψ}) is significant and partially accounts for the eightfold difference in the small amplitude limit. This can be seen in Figure 22, which presents the ratio of the third harmonic of the term $u^2\, du/dt$ taken at $z = 0$ and taken at $z = \eta$. For large waves, the kinematics at $z = \eta$ are significantly larger than at $z = 0$.

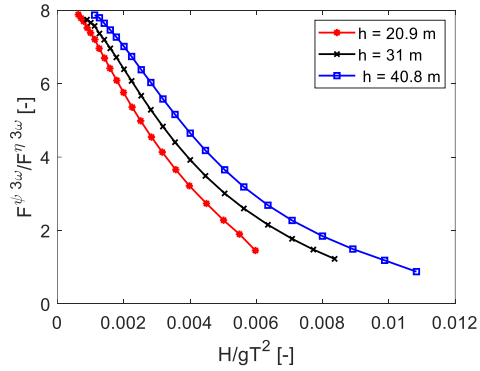

Figure 21. Amplitude of the third harmonic of the F^{ψ} and F^{η} forces at different depths

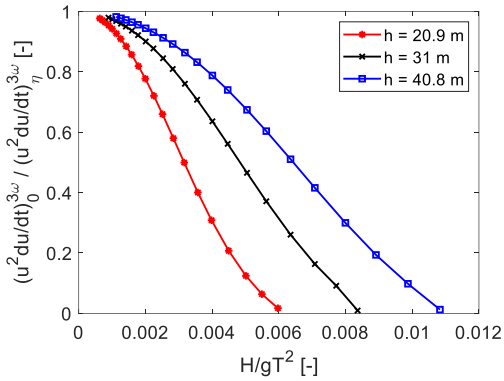

Figure 22. Comparison between the terms $u^2\,du/dt$ taken at $z = 0$ and $z = \eta$.

For small amplitude waves, Rainey [54] shows that the eightfold difference between F^{ψ} and F^{η} comes from neglecting the diffraction of the waves by the cylinder and suggests the addition of a so-called 'surface distortion' force to compensate for the difference. This force is given by

$$F_{dist} = \frac{7}{2g}\rho\pi a^2 u^2 \frac{\partial u}{\partial t}\Big|_{z=\eta} \quad 20$$

With this addition, the point force in the Rainey model produces similar loads to the F^{ψ} point force in the small amplitude limit. However, the derivation of the surface distortion force F_{dist} assumes that the Froude number $Fr = c/\sqrt{ag}$, where c is the wave celerity, is small [54]. This is not the case for waves producing large responses of the structure.

The analysis performed in this section indicates that the eightfold difference between F^{ψ} and F^{η} present in the small amplitude limit disappears for large waves because the difference between the wave kinematics taken at $z = 0$ for F^{ψ} and at $z = \eta$ for F^{η} becomes significant. This also justifies the procedure of Taylor expanding the kinematics from $z = \eta$ around 0 to apply them to the KF model.

7 Conclusions

Experimental data of an idling bottom-fixed offshore wind turbine under extreme irregular wave conditions have been analysed. The scaled model was fully flexible and its first and second modes fit those of the NREL 5 MW turbine mounted on a monopile [31], [55]. Three water depths (20.9 m, 31 m and 40.8 m) and two JONSWAP spectra ($H_s = 8.4$ m, $T_p = 12.6$ s and $H_s = 11$ m, $T_p = 14$ s) were considered, for a total of six load cases. The shear force at the seabed was measured and it was found that for the main population of events, the largest shear forces correspond to the deeper water cases. This is due to a larger water column acting on the cylinder and the loads acting

at a point with a larger modal displacement. For the largest events however, the trend was inverted, with the largest shear forces occurring for the shallower depths. In shallower water, the waves are more non-linear and carry energy at frequencies close to the eigenfrequencies of the structure. Excitation of the first mode and of the second mode therefore produced large shear forces.

In the second part of the paper, four numerical models were compared against the experimental results: the classical Morison equation with second-order wave kinematics, the Morison equation with fully non-linear kinematics, the Rainey model presented by Rainey [1] and the KF method presented by Kristiansen and Faltinsen [2]. The last three models use fully non-linear wave kinematics as input. Exceedance probability plots showed that the wave heights obtained with this kinematic model are in good agreement with the measurements for five of the six load cases tested in this paper. For the most extreme case (i.e. shallowest water and highest sea state), the wave heights produced with the fully non-linear kinematic model largely overpredicted the largest measured wave heights, undermining the possibility of a meaningful comparison. This case was therefore not examined in detail. Also note that the KF model requires using kinematics at $z = 0$, which were not available for the FNL kinematics when a trough passes the cylinder. Instead, the kinematics at $z = \eta$ are Taylor expanded to $z = 0$.

The Morison equation with second-order kinematics matched the main population of events well but underestimated the largest measured shear forces. There are two reasons for this underprediction: first, second-order kinematics miss some higher harmonics in the loads that are necessary to excite the eigenmodes of the structure. Second, this model did not include a point force load.

The models using fully non-linear kinematics predicted the most extreme shear forces reasonably well, but they were not in general conservative. The KF model and Rainey model underpredicted the largest measured shear force in two and four out of five load cases, respectively. To understand where the inaccuracies of these models come from, the acceleration at the highest point mass close to the top of the structure was decomposed into contributions around its first and the second mode. It was found that the models generally overpredicted the first mode acceleration but underpredicted the second mode acceleration for large response events. This was confirmed by the analysis of the time series for two characteristic events, where it was seen that these two models could produce ringing responses but did not produce significant response at the second mode.

The underprediction of the second mode shear force by the numerical models was expected since no slamming load model is implemented in the current analysis. As shown by Suja-Thauvin et al. [17], second mode response is triggered by the impulse load produced by waves breaking at the structure. Recommended future work is to include a slamming model consistent with the numerical models presented in this paper.

In the last part of this paper, the excitation from the point forces of the Rainey model, F^{η} and of the KF model, F^{ψ} were compared for regular waves of different steepnesses. In the small amplitude limit, F^{ψ} is eight times larger that F^{η}. This difference reduced to unity for large waves, mainly because the difference in the wave kinematics (taken at $z = 0$ for F^{ψ} and at $z = \eta$ for F^{ψ}), which is negligible in the small amplitude limit, becomes significant.

Several limitations to this work should be pointed out: the analysis was based on data obtained through an experimental campaign at a 1:80 scale, with all the limitations and uncertainties inherent to this type of testing. The study also dealt with only one pair of values for first and second eigenfrequencies, corresponding to a 5 MW wind turbine in idling conditions. Current wind turbines have exceeded this rated power, and it is expected that the second eigenfrequency of larger turbines will be lower than in this study. This will change the relative contribution of the first and second modes in the response and could allow for mechanisms other than wave breaking to trigger second mode response. In addition, no slamming load model was used in the current paper, thus missing a critical load component from breaking waves. Finally, this analysis did not include responses at frequencies higher than the second eigenfrequency. The influence of such higher frequencies could have a relevant impact on the overall response of the turbine.

It should also be noted that the inputs to these models were kinematics based on measured wave elevation time series. The difficulties inherent in producing accurate kinematics play a role in how well the modelled responses match the measured ones. However, for designing substructures for offshore wind turbines in the industry, the common workflow implies generating random sea states rather than using measurements. This removes the need for kinematics that accurately fit measurements and demands that the models perform well on a statistical rather than a deterministic level. Therefore, the models based on fully non-linear wave kinematics analysed in this paper have the potential to be used in the design of bottom-fixed offshore wind turbines, and can be further improved by adding a consistent slamming model. Finally, to be relevant for the industry, a remaining challenge will be to reduce the computational cost of producing fully non-linear wave kinematics. A database of fully non-linear kinematics is under production within the DeRisk project [56].

8 Acknowledgments

This study has partly been financed by Statkraft and the Norwegian Research Council, project number 237192. Funding from the DeRisk project (Innovation Fund Denmark, grant 4106-00038B) during the writing of the paper is acknowledged. The authors are grateful to DHI for providing the experimental data analyzed in this paper. The authors also want to thank Prof. Trygve Kristiansen for relevant input and interesting discussions.

[1] R. C. T. Rainey, “A new equation for calculating wave loads on offshore structures,” *Journal of Fluid Mechanics*, vol. 204, pp. 295–324, 1989.
[2] T. Kristiansen and O. M. Faltinsen, “Higher harmonic wave loads on a vertical cylinder in finite water depth,” *Journal of Fluid Mechanics*, vol. 833, pp. 773–805, Dec. 2017.
[3] GWEC, “Global Wind Report,” Global Wind Energy Council, 2017.
[4] WindEurope, “Offshore Wind in Europe, Key trends and statistics 2017,” WindEurope, Feb. 2018.
[5] B. J. Natvig and P. Teigen, “Review Of Hydrodynamic Challenges In Tlp Design,” *International Journal of Offshore and Polar Engineering*, vol. 3, no. 04, Dec. 1993.
[6] E. E. Bachynski, T. Kristiansen, and M. Thys, “Experimental and numerical investigations of monopile ringing in irregular finite-depth water waves,” *Applied Ocean Research*, vol. 68, pp. 154–170, Oct. 2017.
[7] E. J. de Ridder, P. Aalberts, J. van den Berg, B. Buchner, and J. Peeringa, “The Dynamic Response of an Offshore Wind Turbine With Realistic Flexibility to Breaking Wave Impact,” *Proceedings of the ASME 2011 30th International Conference on Ocean, Offshore and Arctic Engineering*, pp. 543–552, Jan. 2011.
[8] L. Suja-Thauvin, J. R. Krokstad, and J. Frimann-Dahl, “Maximum loads on a one degree of freedom model-scale offshore wind turbine,” *Energy Procedia*, vol. 94, pp. 329–338, 2016.
[9] H. Bredmose, P. Slabiak, L. Sahlberg-Nielsen, and F. Schlütter, “Dynamic Excitation of Monopiles by Steep and Breaking Waves: Experimental and Numerical Study,” *Proceedings of the ASME 2013 32nd International Conference on Ocean, Offshore and Arctic Engineering*, p. V008T09A062, Jun. 2013.
[10] J. R. Chaplin, R. C. T. Rainey, and R. W. Yemm, “Ringing of a vertical cylinder in waves,” *Journal of Fluid Mechanics*, vol. 350, pp. 119–147, 1997.
[11] O. M. Faltinsen, J. N. Newman, and T. Vinje, “Nonlinear wave loads on a slender vertical cylinder,” *Journal of Fluid Mechanics*, vol. 289, pp. 179–198, 1995.
[12] Š. Malenica and B. Molin, “Third-harmonic wave diffraction by a vertical cylinder,” *Journal of Fluid Mechanics*, vol. 302, pp. 203–229, 1995.
[13] H. Bredmose, S. Schløer, and B. T. Paulsen, “Higher-Harmonic Response of a Slender Cantilever Beam to Fully Nonlinear Regular Wave Forcing,” pp. 469–478, Jul. 2012.
[14] E. Marino, C. Lugni, and C. Borri, “A novel numerical strategy for the simulation of irregular nonlinear waves and their effects on the dynamic response of offshore wind turbines,” *Computer Methods in Applied Mechanics and Engineering*, vol. 255, pp. 275–288, Mar. 2013.
[15] B. T. Paulsen, H. Bredmose, H. B. Bingham, and S. Schløer, “Steep Wave Loads From Irregular Waves on an Offshore Wind Turbine Foundation: Computation and Experiment,” *Proceedings of the ASME 2013 32nd International Conference on Ocean, Offshore and Arctic Engineering*, p. V009T12A028, Jun. 2013.
[16] S. Schløer, H. Bredmose, and H. B. Bingham, “The influence of fully nonlinear wave forces on aero-hydro-elastic calculations of monopile wind turbines,” *Marine Structures*, vol. 50, pp. 162–188, Nov. 2016.
[17] L. Suja-Thauvin, J. R. Krokstad, E. E. Bachynski, and E.-J. de Ridder, “Experimental results of a multimode monopile offshore wind turbine support structure subjected to steep and breaking irregular waves,” *Ocean Engineering*, vol. 146, pp. 339–351, Dec. 2017.
[18] O. M. Faltinsen, *Sea loads on ships and offshore structures*. Cambridge, 1990.
[19] S. Hallowell, A. T. Myers, and S. R. Arwade, “Variability of breaking wave characteristics and impact loads on offshore wind turbines supported by monopiles,” *Wind Energ.*, p. n/a-n/a, Feb. 2015.
[20] DNV-OS-J101, “DNV-OS-J101 Design of offshore wind turbine structures,” DNV, May 2014.
[21] DNV-RP-C205, “DNV-RP-C205 Environmental Conditions and Environmental Loads,” DNV, Aug. 2017.
[22] IEC-61400-3, “IEC 61400-3: Wind Turbines–Part 3: Design Requirements for Offshore Wind Turbines,” *International Electrotechnical Commission, Geneva*, Feb. 2009.
[23] J. R. Morison, J. W. Johnson, and S. A. Schaaf, “The Force Exerted by Surface Waves on Piles,” *Journal of Petroleum Technology*, vol. 2, no. 05, pp. 149–154, May 1950.
[24] M. M. Rienecker and J. D. Fenton, “A Fourier approximation method for steady water waves,” *Journal of Fluid Mechanics*, vol. 104, pp. 119–137, Mar. 1981.
[25] J. Wienke and H. Oumeraci, “Breaking wave impact force on a vertical and inclined slender pile—theoretical and large-scale model investigations,” *Coastal Engineering*, vol. 52, no. 5, pp. 435–462, May 2005.
[26] A. Nestegård, A. J. Kalleklev, K. Hagatun, Y. L. Wu, S. Haver, and E. Lehn, “Resonant Vibrations of Riser Guide Tubes Due to Wave Impact,” pp. 987–994, Jan. 2004.
[27] C. J. Galvin, “Breaker type classification on three laboratory beaches,” *J. Geophys. Res.*, vol. 73, no. 12, pp. 3651–3659, Jun. 1968.
[28] L. Suja-Thauvin, J. R. Krokstad, and E. E. Bachynski, “Critical assessment of non-linear hydrodynamic load models for a fully flexible monopile offshore wind turbine,” *Ocean Engineering*, vol. 164, pp. 87–104, Sep. 2018.
[29] H. Bredmose, B. Jensen, S. Schløer, T. J. Larsen, T. Kim, and A. M. Hansen, “The Wave Loads Project,” DTU Vindenergi, Dec. 2013.
[30] W. Manners and R. C. T. Rainey, “Hydrodynamic Forces on Fixed Submerged Cylinders,” *Proc. R. Soc. Lond. A*, vol. 436, no. 1896, pp. 13–32, Jan. 1992.
[31] J. M. Jonkman, S. Butterfield, W. Musial, and G. Scott, “Definition of a 5-MW Reference Wind Turbine for Offshore System Development.” NREL, Feb-2009.
[32] M. Damgaard, L. B. Ibsen, L. V. Andersen, and J. K. F. Andersen, “Cross-wind modal properties of offshore wind turbines identified by full scale testing,” *Journal of Wind Engineering and Industrial Aerodynamics*, vol. 116, pp. 94–108, May 2013.
[33] M. Damgaard and J. K. F. Andersen, “Natural Frequency And Damping Estimation of an Offshore Wind Turbine Structure,” in *Proceedings of the Twenty-second (2012) International Offshore and Polar Engineering Conference*, 2012.
[34] R. Shirzadeh, W. Weijtjens, P. Guillaume, and C. Devriendt, “The dynamics of an offshore wind turbine in parked conditions: a comparison between simulations and measurements,” *Wind Energ.*, vol. 18, no. 10, pp. 1685–1702, Oct. 2015.
[35] E. E. Bachynski and T. Moan, “Ringing loads on tension leg platform wind turbines,” *Ocean Engineering*, vol. 84, pp. 237–248, Jul. 2014.

[36] K. Hasselmann *et al.*, “Measurements of wind-wave growth and swell decay during the Joint North Sea Wave Project (JONSWAP).” Deutches Hydrographisches Institut, 01-Jan-1973.
[37] A. Robertson *et al.*, “OC5 Project Phase I: Validation of Hydrodynamic Loading on a Fixed Cylinder,” 2015.
[38] T. Sarpkaya, *Wave forces on offshore structures*. Cambridge University Press, 2010.
[39] J. T. Kirby and R. A. Dalrymple, “An approximate model for nonlinear dispersion in monochromatic wave propagation models,” *Coastal Engineering*, vol. 9, no. 6, pp. 545–561, Mar. 1986.
[40] C. T. Stansberg, “Characteristics of Steep Second-Order Random Waves in Finite and Shallow Water,” *Proceedings of the ASME 2011 30th International Conference on Ocean, Offshore and Arctic Engineering*, pp. 859–869, Jan. 2011.
[41] R. A. Dalrymple and R. G. Dean, *Water wave mechanics for engineers and scientists*. Prentice-Hall, 1991.
[42] A. P. Engsig-Karup, H. B. Bingham, and O. Lindberg, “An efficient flexible-order model for 3D nonlinear water waves,” *Journal of Computational Physics*, vol. 228, no. 6, pp. 2100–2118, Apr. 2009.
[43] Y. Goda and T. Suzuki, “ESTIMATION OF INCIDENT AND REFLECTED WAVES IN RANDOM WAVE EXPERIMENTS,” *Coastal Engineering Proceedings*, vol. 1, no. 15, 1976.
[44] H. Bredmose, A. Hunt-Raby, R. Jayaratne, and G. N. Bullock, “The ideal flip-through impact: experimental and numerical investigation,” *J Eng Math*, vol. 67, no. 1–2, pp. 115–136, Nov. 2009.
[45] S. Schløer, H. Bredmose, and A. Ghadirian, “Experimental and Numerical Statistics of Storm Wave Forces on a Monopile in Uni- and Multidirectional Seas,” p. V010T09A073, Jun. 2017.
[46] R. C. T. Rainey, “Slender-Body Expressions for the Wave Load on Offshore Structures,” *Proc. R. Soc. Lond. A*, vol. 450, no. 1939, pp. 391–416, Aug. 1995.
[47] R. G. Longoria, J. J. Beaman, and R. W. Miksad, “An Experimental Investigation of Forces Induced on Cylinders by Random Oscillatory Flow,” *J. Offshore Mech. Arct. Eng*, vol. 113, no. 4, pp. 275–285, Nov. 1991.
[48] B. M. Sumer and J. Fredsøe, *Hydrodynamics Around Cylindrical Structures*, Revised., vol. 26. WORLD SCIENTIFIC, 2006.
[49] J. R. Krokstad, C. T. Stansberg, A. Nestegård, and T. Marthinsen, “A New Nonslender Ringing Load Approach Verified Against Experiments,” *J. Offshore Mech. Arct. Eng.*, vol. 120, no. 1, pp. 20–29, Feb. 1998.
[50] B. T. Paulsen, H. Bredmose, H. B. Bingham, and N. G. Jacobsen, “Forcing of a bottom-mounted circular cylinder by steep regular water waves at finite depth,” *Journal of Fluid Mechanics*, vol. 755, pp. 1–34, 2014.
[51] J. N. Newman, “Nonlinear Scattering of Long Waves by a Vertical Cylinder,” in *Waves and Nonlinear Processes in Hydrodynamics*, J. Grue, B. Gjevik, and J. E. Weber, Eds. Springer Netherlands, 1996, pp. 91–102.
[52] P. I. Bruheim, “Development and validation of a finite element software facilitating large-displacement aeroelastic analysis of wind turbines,” *83*, 2012.
[53] Fenton John D., “A Fifth-Order Stokes Theory for Steady Waves,” *Journal of Waterway, Port, Coastal, and Ocean Engineering*, vol. 111, no. 2, pp. 216–234, Mar. 1985.
[54] R. C. T. Rainey, “The hydrodynamic load at the intersection of a cylinder with the water surface,” in *Proceedings of 10th International Workshop on Water Waves and Floating Bodies*, 1995, pp. 207–210.
[55] J. M. Jonkman and W. Musial, *Offshore Code Comparison Collaboration (OC3) for IEA Task 23 offshore wind technology and deployment*. Golden, Colo. : National Renewable Energy Laboratory, 2010.
[56] H. Bredmose *et al.*, “DeRisk — Accurate Prediction of ULS Wave Loads. Outlook and First Results,” *Energy Procedia*, vol. 94, pp. 379–387, Sep. 2016.

Appendix B

Verification and validation of the numerical models

B.1 Structural models

B.1.1 Single degree of freedom

The matlab 1 degree of freedom equation is used to model the experiments carried out in the wave flume at NTNU. The model is a stiff cylinder mounted on a rotational spring. Assuming that the flexibility of the cylinder is negligible, the structure can be represented by:

$$M_{hydro} = (I_P + I_A)\ddot{\theta} + B\dot{\theta} + C\theta \tag{B.1}$$

with	M_{hydro}	excitation loads
	I_P	moment of inertia of the pile
	I_A	moment of inertia due to the added mass
	B	damping coefficient
	C	rotational stiffness of the spring
	θ	angular displacement of the structure

The dot over a variable means differentiation. The moment of inertia was calculated using a 2D added mass coefficient of $C_a = 1$. The rotational stiffness was calculated based on the material and geometrical properties of the spring and tuned to fit the eigenperiod of the structure. The damping coefficient was estimated from the logarithmic decrement

of decay tests. Figure B.1 shows the overturning moment measured at the base of the cylinder during the wet decay test and the simulation with the fitted parameters. The numerical results based on the implementation of equation B.1 in Matlab show a very good agreement with the experimental results.

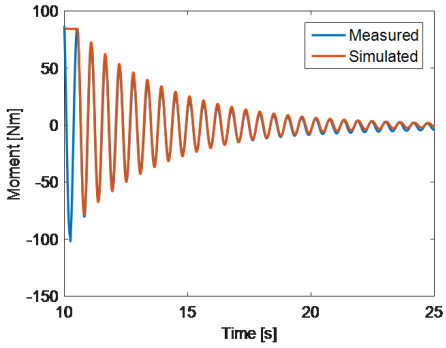

Figure B.1: Decay test, experimental and numerical response bending moment

B.1.2 Matlab mode shape solver

To simulate the experiments from the WiFi project, a simple mode shape solver was implemented in Matlab (see for example Gans 2015). The response bending moment of the structure is calculated with the Euler-Bernoulli beam equation assuming a slender structure in the vertical direction z:

$$M(z,t) = EI\frac{\partial \Psi^2(z,t)}{\partial z^2} \tag{B.2}$$

with M the response bending moment
E the Young's modulus
I the area moment of inertia of the cross section
Ψ the horizontal deflection of the system

The deflection is assumed to be the sum of the deflections of each individual mode:

$$\Psi(z,t) = \sum_{n=1}^{N} \psi_n(z)\xi_n(t) \tag{B.3}$$

with ψ_n the mode shape of the nth mode
ξ_n the modal displacement of the nth mode

The modal displacement for each mode is determined solving the simple one degree of freedom equation with Matlab:

$$f_n = m_n\ddot{\xi}_n + b_n\dot{\xi}_n + c_n\xi_n \tag{B.4}$$

with f_n the modal excitation for the nth mode
m_n the modal mass (including added mass) for the nth mode
b_n the modal damping for the nth mode
c_n the modal stiffness for the nth mode

The modal mass, damping and stiffness were provided by Bunnik et al. (2015). The modal excitation for each mode is obtained by integrating the product of the excitation force times the mode shape over the instantaneous wetted surface.

$$f_n = \int_h^{z_0} F(z)\psi_n(z)dz \tag{B.5}$$

with F the distributed hydrodynamic load
z_0 the instantaneous wave elevation
h the water depth

No decay tests were provided for this model, only static load cases and hammer tests. Figure B.2 shows the mode shapes of the experimental model, obtained from de Ridder (2015) and the mode shapes used in the present mode shape solver for the numerical simulations, provided by Bunnik et al. (2015).

The eigenfrequencies of the physical model were obtained during the experimental campaign through hammer tests. The modal masses and stiffnesses were provided by Bunnik et al. (2015) and were used to calculate the eigenfrequencies of the numerical model. The eigenfrequencies are shown in full scale in Table B.1.

eigenfrequency	de Ridder (2015)	Bunnik et al. (2015)	Present solver
1st mode (Hz)	0.29	0.29	0.29
2nd mode (Hz)	1.19	1.21	1.21
3rd mode (Hz)	3.11	3.11	3.11

Table B.1: Eigenfrequencies reported during the experimental hammer test (see de Ridder 2015), reported by Bunnik et al. (2015) and obtained through the numerical hammer test

The damping ratios used in the present solver were also provided by Bunnik et al. (2015). In de Ridder (2015), only damping ratios for the first 2 eigenmodes are given. To verify the

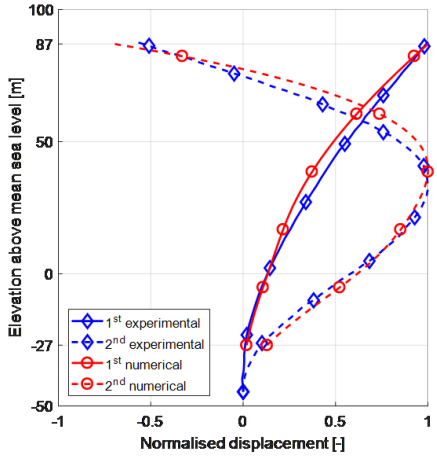

Figure B.2: Mode shapes obtained from the experiments and used for the numerical simulations

damping values of the present solver, decay tests were run numerically, and the damping ratio was computed based on the logarithmic decrement. The results are shown in Table B.2.

Damping ratio	de Ridder (2015)	Bunnik et al. (2015)	Present solver
1st mode (%)	1.09	1.10	1.07
2nd mode (%)	1.10	1.10	1.06

Table B.2: Damping ratios reported during the experimental hammer test (see de Ridder 2015), reported by Bunnik et al. (2015) and obtained through the numerical decay tests

During the static load cases, the structure was loaded by pulling with a known force at the sea level, and the response was measured at the sea bottom. The measured responses showed in Table B.3 are taken from de Ridder (2015). Next to the measured response, we show the response simulated with the mode shape solver under the same load conditions. The simulated results lie within 1.5% from the measured ones.

Applied load (kN)	Measured response (MNm)	Simulated response (MNm)	Simulated/measured
2870	84.616	84.313	99.6%
5740	170.593	168.627	98.8%
7175	212.195	210.783	99.3%

Table B.3: Measured and simulated responses during static load cases

B.1.3 Finite element software

To simulate the response obtained during the DHI experiments we use Ashes, which is a finite element solver for aeroelastic simulation of wind turbines. Ashes uses the Newmark-Beta integration method to solve for the deflections of the structure (see Bruheim 2012). This software was used to model the structure from the experimental campaign of the OC5 project Phase Ib, presented in Robertson et al. (2016).

The Ashes model is first verified against the model presented by MARINTEK in the OC5 project Phase Ib. The MARINTEK model is implemented using the finite element software Riflex. The eigenfrequencies obtained with Riflex and reported by Robertson et al. (2016) are shown in Table B.4.

Eigenfrequency	Robertson et al. (2016)	Riflex	Ashes
1st mode (Hz)	0.28	0.28	0.28
2nd mode (Hz)	2.0	2.0	2.0

Table B.4: Eigenfrequencies in full scale presented in Robertson et al. (2016), obtained with Riflex and with Ashes.

The mode shapes output by Ashes and by Riflex are plotted in Figure B.3 and show an excellent match.

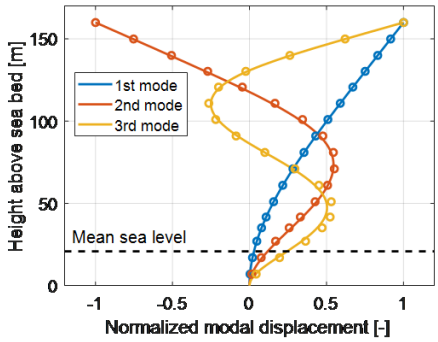

Figure B.3: Comparison between the mode shapes from Ashes and Riflex. The solid lines correspond to Ashes and the dotted lines correspond to Riflex

Figure B.4 shows a comparison between decay tests run with Riflex and with Ashes and indicates an excellent match between the two.

In addition to the decay tests, the response of the Ashes structural model with the Morison load equation with linear wave kinematics is compared with the results presented in Robertson et al. (2016) in Figure B.5. Here we compare the response in irregular waves

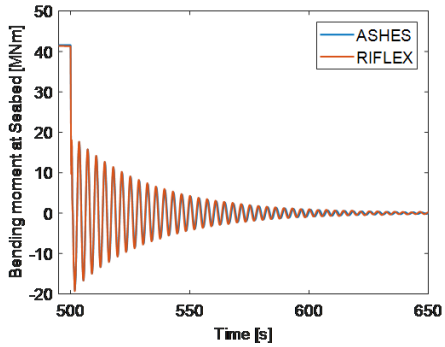

Figure B.4: Decay test comparison between Ashes and Riflex

with H_S = 0.104 m, T_P = 1.4 s in 0.51 m water depth (model scale values). This corresponds to H_S = 8.32 m, T_P = 12.5 s in 40.8 m water depth in full scale. The results from Ashes lie within the results from other codes. For large responses, the results from Ashes are significantly lower than the measured response (noted EXPERIMENT in the figure) because non-linearities in the wave kinematics are not included.

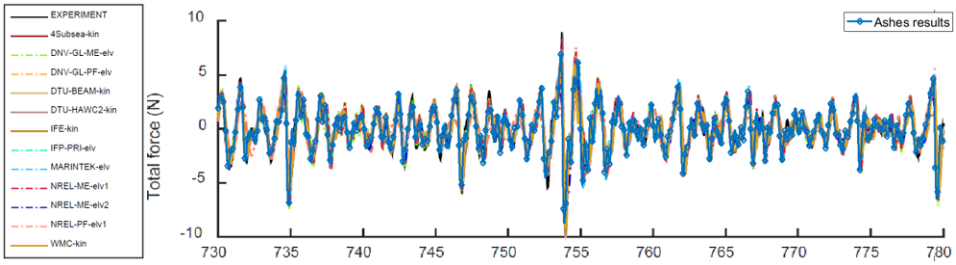

Figure B.5: Verification of simulated force against measurements for irregular waves with H_S = 0.104 m, T_P = 1.4 s in 0.56 m depth (model scale value). The results from Ashes have been added to Figure 11 in Robertson et al. (2016).

B.2 Wave kinematics models

B.2.1 Stream function theory

The wave kinematics used in the models based on stream function wave theory were implemented based on the work by Rienecker and Fenton (1981). In Table 1 of their paper, they present values of kc^2/g obtained with their method, where k is the wave number, c is the wave celerity and g is the acceleration due to gravity. They present values for different wave heights H for a constant value of kQ/c, where Q denotes the volume rate of flow underneath the steady wave and $\exp(-kQ/c) = 0.5$ (which is equivalent to wavelength/depth ≈ 9). In Table B.5 we show the comparison of the value of kc^2/g

obtained by Rienecker and Fenton (1981) to the one obtained with the present implementation. The results for the present implementation were calculated with a water depth $h = 27$ m and a stream function order $N = 16$. The match is excellent up to wave heights of 18 m. This discrepancy was deemed unimportant since all the waves occurrences during the experiments are below that value.

Height (m)	Period (s)	kc^2/g (-) (Rienecker and Fenton 1981)	kc^2/g (-) present implementation	diff (%)
4.67	15.93	0.6150	0.6150	-0.0042
6.82	15.69	0.6311	0.6310	-0.0049
10.26	15.19	0.6665	0.6664	-0.0046
13.35	14.69	0.7064	0.7064	-0.0022
16.26	14.21	0.7482	0.7482	-0.0028
17.58	14.05	0.7644	0.7644	-0.0050
18.14	14.18	0.7677	0.7541	-1.7725

Table B.5: Comparison of kc^2/g obtained by Rienecker and Fenton (1981) and with the present method

The current implementation of the stream function wave theory was also verified against other sets of data, listed below:

- **Peeringa**: data published by Peeringa (2005)
- **Dalrymple**: data produced with the code implemented by Dalrymple (1996)
- **Fenton**: data produced with the code implemented by Fenton (2015)

Two cases, published in Peeringa (2005), were used in this verification process. In case 1 (corresponding to test 1 in Peeringa 2005), the wave height is $H = 10$ m, the wave period is T=10 s, the water depth is $h = 20$ m and the stream function order is $N = 12$.

The implementation is tested for 3 results: wave elevation, wave particle horizontal acceleration at free surface and wave particle horizontal velocity at free surface. The results are plotted in Figure B.6 show an excellent match for all 3 comparisons.

In case 2 (corresponding to test 4 in Peeringa 2005), the wave height is $H = 10$ m, the wave period is $T = 10$ s, the water depth is $h = 20$ m and the stream function order is $N = 7$. In this test, the wave particle horizontal velocity is computed below the crest and below the trough.

Both Figure B.7(a) and Figure B.7(b) show an excellent match between the present implementation and the results obtained with the codes implemented by Fenton (2015) and Dalrymple (1996). The results presented by Peeringa (2005) show discrepancies below the mean sea level. The reason for these discrepancies was not established.

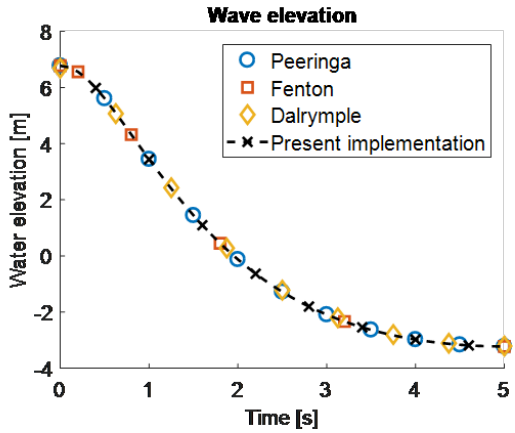

(a) Wave elevation

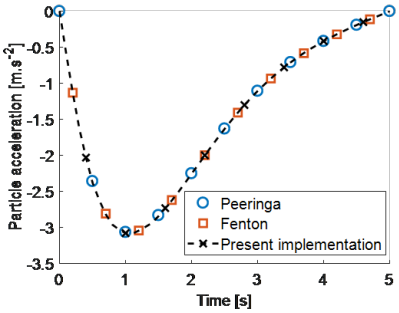

(b) Horizontal particle acceleration

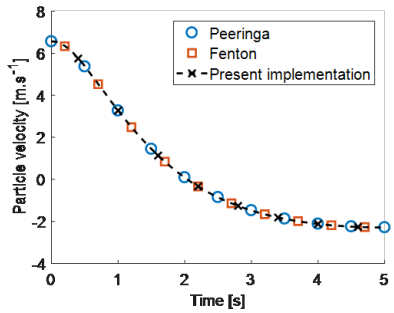

(c) Horizontal particle velocity

Figure B.6: Verification of the present implementation at the free surface

B.3 Hydrodynamic load models

B.3.1 Morison equation

In different models presented throughout this thesis, the Morison equation Morison et al. (1950) has been used to calculate hydrodynamic loads on vertical cylinders. In the presented work, the inertia term of the Morison equation is dominating. The inertia force on a section of the cylinder of length dz is given by

$$dF_I = \rho\pi R^2 C_M a(z) dz \tag{B.6}$$

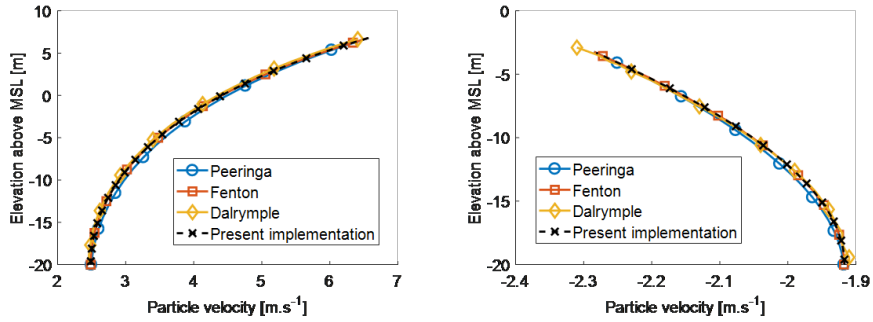

(a) Horizontal particle velocity under crest **(b)** Horizontal particle velocity under trough

Figure B.7: Verification of the present implementation under the crest and trough

with ρ the water density
R the cylinder radius
C_M the inertia coefficient
$a(z)$ the horizontal water particle acceleration at height (z)

At a water depth h, for a wave of amplitude A, frequency ω and wave number k, the amplitude of the horizontal acceleration is

$$a(z) = \omega^2 A \frac{\cosh[k(z+h)]}{\sinh(kh)} \tag{B.7}$$

So the amplitude of the inertia Morison load integrated from $z = -h$ to $z = 0$ is

$$F_I = \frac{\omega^2 A \rho \pi R^2 C_M}{k} \tag{B.8}$$

In order to determine the cylinder length dz required for accurate results, the integration of the load in equation B.6 is performed for different vertical discretizations of the cylinder and compared to the analytical result obtained through equation B.8.

2 regular wave cases were tested with R = 2.89 m, C_M = 1.8, ρ = 1000 kg.m^{-3} and h = 27 m. Table B.6 shows the ratio between the solution from the present implementation and the analytical solution. For each case, the current implementations was tested with the cylinder divided into 10, 20, 50 and 100 elements, respectively. For more than 50 elements, the present formulation matches the analytical solution within 5 significant digits.

	Analytical (MN)	10 el	20 el	50 el	100 el
H=5 m, T=7 s	1.1336	99.79 %	99.94 %	100 %	100 %
H=10 m, T=12 s	1.7585	99.94 %	99.99 %	100 %	100 %

Table B.6: Comparison of the amplitude of the inertia Morison load obtained from the analytical solution and with the present implementation

B.3.2 FNV model

The hydrodynamic loads as calculated by the FNV method are given in Newman (1996). In our implementation we modify the original equations by introducing the water depth h, and we obtain the following equation: $F_{FNV} = F_1 + F_2 + F_31 + F_{3\psi}$ with

$$F_1 = 2\pi\rho R^2 \int_{-h}^{0} u_t(z)dz \tag{B.9}$$

$$F_2 = 2\pi\rho R^2 u_t|_{z=0}\zeta^{(1)} + \pi\rho R^2 \int_{-h}^{0} \left(2w(z)w_x(z) + u(z)u_x(z)\right) dz \tag{B.10}$$

$$F_{31} = \pi\rho R^2 \left[\zeta^{(1)} \left(u_{tz}\zeta^{(1)} + 2ww_x + uu_x - \frac{2}{g}u_t w_t\right) - \left(\frac{u_t}{g}\right)(u^2 + v^2)|_{z=0}\right] \tag{B.11}$$

$$F_{3\psi} = \pi\rho\frac{R^2}{g}u^2 u_t|_{z=o}\beta\left(\frac{h}{R}\right) \tag{B.12}$$

with
- ρ the water density
- R the cylinder radius
- u, v the horizontal and vertical first order velocity components
- $\zeta^{(1)}$ the first order wave elevation
- h the water depth

Subscript indicates differentiation. β is given by

$$\beta\left(\frac{h}{R}\right) = \int_0^{h/R} \left(3\Psi_1(Z) + 4\Psi_2(Z)\right) dZ \tag{B.13}$$

with Ψ_1 and Ψ_2 defined in Newman (1996). Note that in deep water, $\beta = 4$.

Newman (1996) illustrated these equations with results obtained for an irregular sea state composed of 5 regular waves with different frequencies and amplitudes. Figure B.8 shows the comparison between the 1st and 2nd order free surface elevation presented in Newman (1996) and the present implementation. Correctly estimating the 1st order elevation does not pose any difficulties, but the 2nd order elevation requires a correct calculation of the particle velocities and vertical acceleration. Figure B.8 shows that the 2nd order free surface elevation matches the published work.

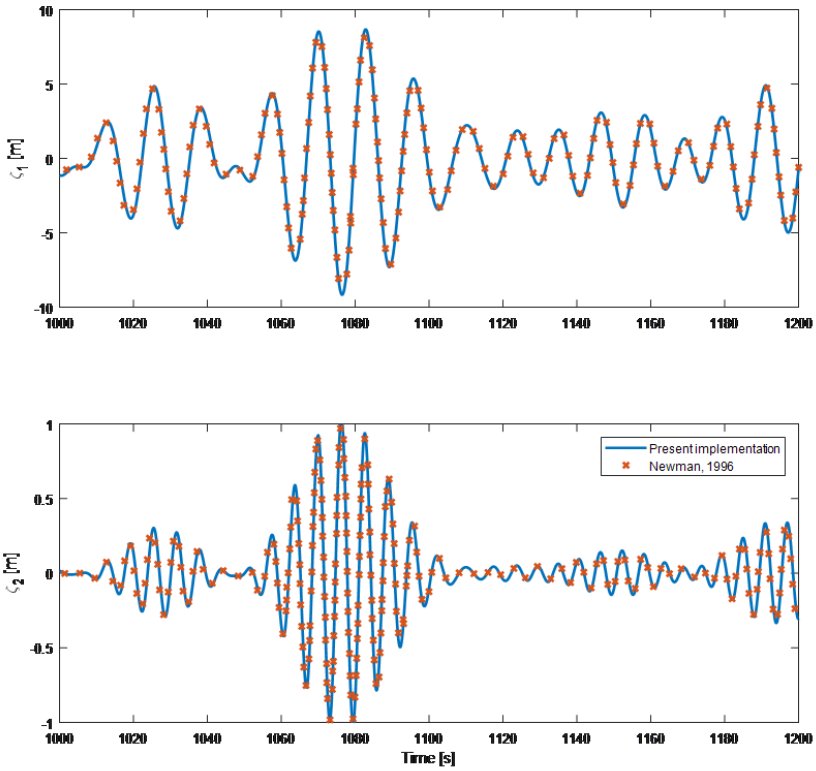

Figure B.8: 1st order free surface elevation and corresponding 2nd order elevation

The next step is to verify the FNV equations. To remove the influence of the water depth in the present implementation, a depth h = 500 m is used.

For this verification, it is not possible to superimpose the results presented by Newman (1996) to the results of the present implementation because the quality of the digital version of their paper does not allow it. Instead, the results are presented in two separate figures, namely Figure B.9 and Figure B.10. These figures show that the hydrodynamic forces from the present implementation match those from Newman (1996).

B.3.3 KF model

Kristiansen and Faltinsen (2017) generalized the model of Faltinsen et al. (1995) to finite water depth. Their model is hereafter referred to as KF. In their model, the hydrodynamic excitation load is calculated as

$$\int_{-h}^{\zeta} F'(z,t)dz + F^{\psi} \tag{B.14}$$

$F'(z,t)$ is a distributed load given by

$$F'(z,t) = \rho\pi R^2 \left(\frac{\partial u}{\partial t} + u\frac{\partial u}{\partial x} + w\frac{\partial u}{\partial v}\right) + m_a \left(\frac{\partial u}{\partial t} + w\frac{\partial u}{\partial z}\right) \tag{B.15}$$

with $m_a = C_a\rho\pi a^2$ the added mass in surge and $C_a = 1$. F^{ψ} is the force due to the scattered potential and is applied at $z = 0$. As shown by Kristiansen and Faltinsen (2017), F^{ψ} is no different than in deep water and is given by

$$F^{\psi} = \rho\pi R^2 \frac{4}{g} u^2 \frac{\partial u}{\partial v}|_{z=0} \tag{B.16}$$

In order to verify our implementation of the KF model, the excitation loads thus obtained are compared to those shown in Figure 14 of Kristiansen and Faltinsen (2017). A regular wave with a height H = 8.25 m and a period T = 13.98 s, in a water depth h = 27 m and for a cylinder radius R = 3.45 m is selected. The wave kinematics are computed following the Stokes 5$^{\text{th}}$ order theory presented by Fenton John D. (1985). Consistently with the results presented in Kristiansen and Faltinsen (2017), the terms in the integral are evaluated up to the 5$^{\text{th}}$ order wave elevation. Figure B.11 shows a comparison between the excitation loads obtained with the present implementation and shown in Kristiansen and Faltinsen (2017). The excitation loads are decomposed around the 1$^{\text{st}}$, 2$^{\text{nd}}$ and 3$^{\text{rd}}$ harmonic of the wave. The results show a perfect match.

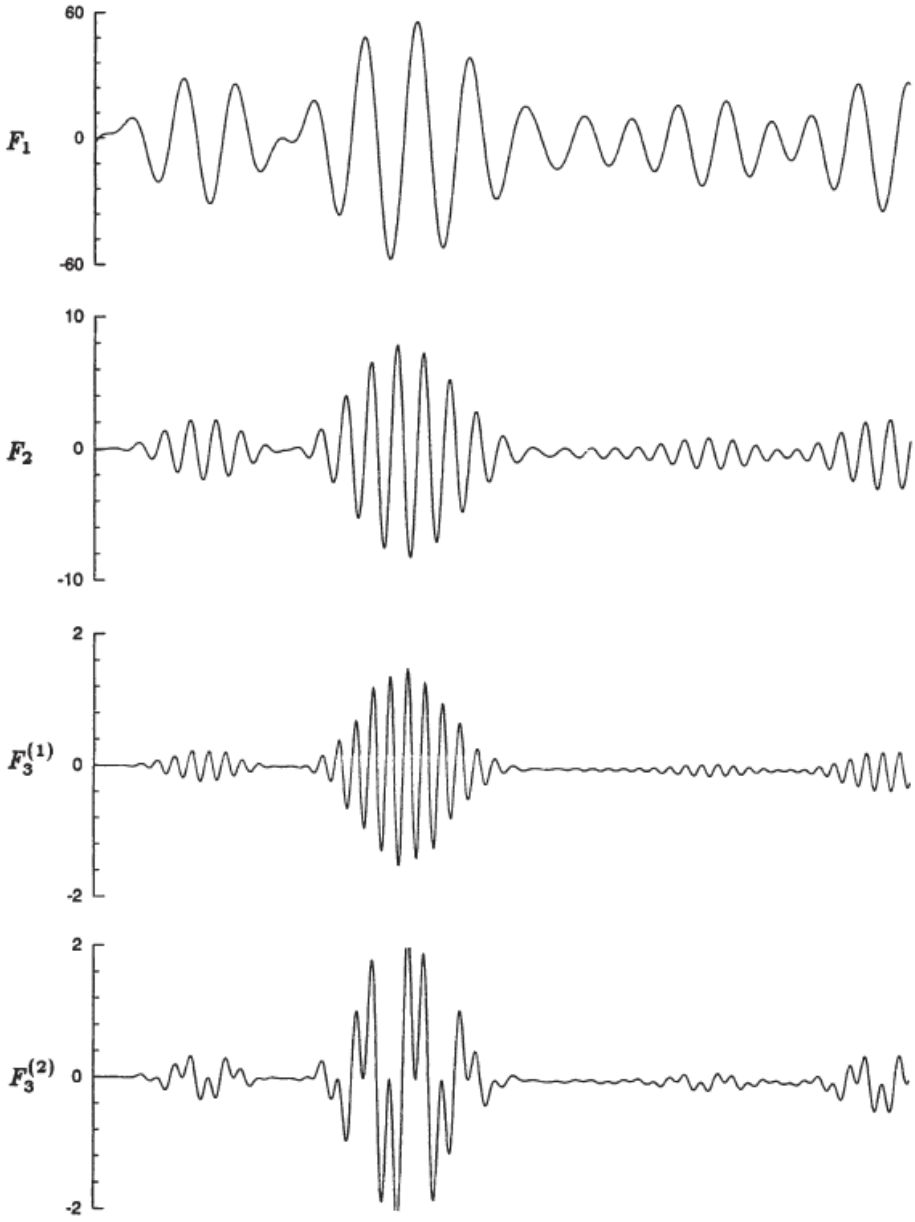

Figure B.9: Components of the force acting on the cylinder for the same times as shown in Figure B.8. All forces are normalized by the factor $\rho g R^2$, and the results are in units of meters. Taken from Newman (1996)

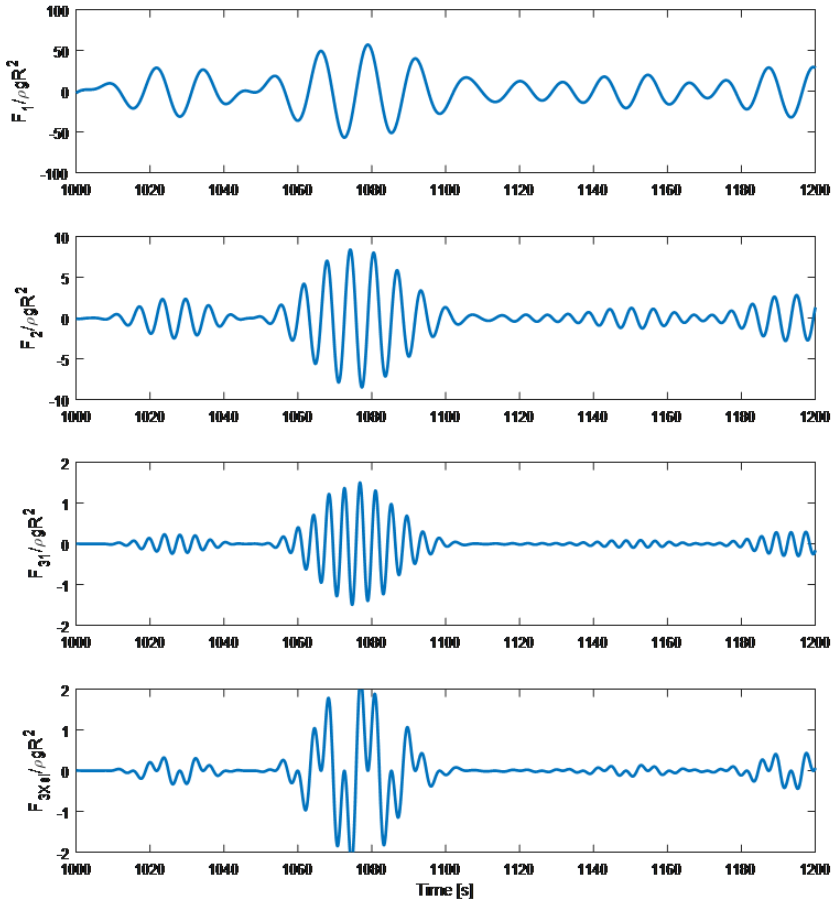

Figure B.10: Components of the force acting on the cylinder from the present implementation

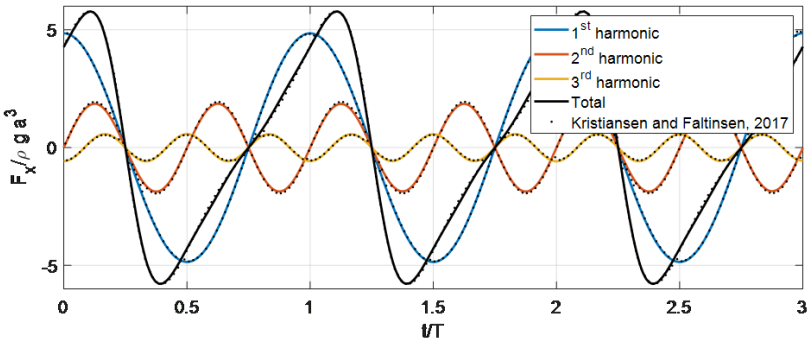

Figure B.11: Comparison between the excitation loads obtained by Kristiansen and Faltinsen (2017) and those obtained with the present implementation

Previous PhD theses published at the Department of Marine Technology
(earlier: Faculty of Marine Technology)
NORWEGIAN UNIVERSITY OF SCIENCE AND TECHNOLOGY

Report No.	Author	Title
	Kavlie, Dag	Optimization of Plane Elastic Grillages, 1967
	Hansen, Hans R.	Man-Machine Communication and Data-Storage Methods in Ship Structural Design, 1971
	Gisvold, Kaare M.	A Method for non-linear mixed -integer programming and its Application to Design Problems, 1971
	Lund, Sverre	Tanker Frame Optimalization by means of SUMT-Transformation and Behaviour Models, 1971
	Vinje, Tor	On Vibration of Spherical Shells Interacting with Fluid, 1972
	Lorentz, Jan D.	Tank Arrangement for Crude Oil Carriers in Accordance with the new Anti-Pollution Regulations, 1975
	Carlsen, Carl A.	Computer-Aided Design of Tanker Structures, 1975
	Larsen, Carl M.	Static and Dynamic Analysis of Offshore Pipelines during Installation, 1976
UR-79-01	Brigt Hatlestad, MK	The finite element method used in a fatigue evaluation of fixed offshore platforms. (Dr.Ing. Thesis)
UR-79-02	Erik Pettersen, MK	Analysis and design of cellular structures. (Dr.Ing. Thesis)
UR-79-03	Sverre Valsgård, MK	Finite difference and finite element methods applied to nonlinear analysis of plated structures. (Dr.Ing. Thesis)
UR-79-04	Nils T. Nordsve, MK	Finite element collapse analysis of structural members considering imperfections and stresses due to fabrication. (Dr.Ing. Thesis)
UR-79-05	Ivar J. Fylling, MK	Analysis of towline forces in ocean towing systems. (Dr.Ing. Thesis)
UR-80-06	Nils Sandsmark, MM	Analysis of Stationary and Transient Heat Conduction by the Use of the Finite Element Method. (Dr.Ing. Thesis)
UR-80-09	Sverre Haver, MK	Analysis of uncertainties related to the stochastic modeling of ocean waves. (Dr.Ing. Thesis)
UR-81-15	Odland, Jonas	On the Strength of welded Ring stiffened cylindrical Shells primarily subjected to axial Compression
UR-82-17	Engesvik, Knut	Analysis of Uncertainties in the fatigue Capacity of Welded Joints
UR-82-18	Rye, Henrik	Ocean wave groups
UR-83-30	Eide, Oddvar Inge	On Cumulative Fatigue Damage in Steel Welded Joints
UR-83-33	Mo, Olav	Stochastic Time Domain Analysis of Slender Offshore Structures

UR-83-34	Amdahl, Jørgen	Energy absorption in Ship-platform impacts
UR-84-37	Mørch, Morten	Motions and mooring forces of semi submersibles as determined by full-scale measurements and theoretical analysis
UR-84-38	Soares, C. Guedes	Probabilistic models for load effects in ship structures
UR-84-39	Aarsnes, Jan V.	Current forces on ships
UR-84-40	Czujko, Jerzy	Collapse Analysis of Plates subjected to Biaxial Compression and Lateral Load
UR-85-46	Alf G. Engseth, MK	Finite element collapse analysis of tubular steel offshore structures. (Dr.Ing. Thesis)
UR-86-47	Dengody Sheshappa, MP	A Computer Design Model for Optimizing Fishing Vessel Designs Based on Techno-Economic Analysis. (Dr.Ing. Thesis)
UR-86-48	Vidar Aanesland, MH	A Theoretical and Numerical Study of Ship Wave Resistance. (Dr.Ing. Thesis)
UR-86-49	Heinz-Joachim Wessel, MK	Fracture Mechanics Analysis of Crack Growth in Plate Girders. (Dr.Ing. Thesis)
UR-86-50	Jon Taby, MK	Ultimate and Post-ultimate Strength of Dented Tubular Members. (Dr.Ing. Thesis)
UR-86-51	Walter Lian, MH	A Numerical Study of Two-Dimensional Separated Flow Past Bluff Bodies at Moderate KC-Numbers. (Dr.Ing. Thesis)
UR-86-52	Bjørn Sortland, MH	Force Measurements in Oscillating Flow on Ship Sections and Circular Cylinders in a U-Tube Water Tank. (Dr.Ing. Thesis)
UR-86-53	Kurt Strand, MM	A System Dynamic Approach to One-dimensional Fluid Flow. (Dr.Ing. Thesis)
UR-86-54	Arne Edvin Løken, MH	Three Dimensional Second Order Hydrodynamic Effects on Ocean Structures in Waves. (Dr.Ing. Thesis)
UR-86-55	Sigurd Falch, MH	A Numerical Study of Slamming of Two-Dimensional Bodies. (Dr.Ing. Thesis)
UR-87-56	Arne Braathen, MH	Application of a Vortex Tracking Method to the Prediction of Roll Damping of a Two-Dimension Floating Body. (Dr.Ing. Thesis)
UR-87-57	Bernt Leira, MK	Gaussian Vector Processes for Reliability Analysis involving Wave-Induced Load Effects. (Dr.Ing. Thesis)
UR-87-58	Magnus Småvik, MM	Thermal Load and Process Characteristics in a Two-Stroke Diesel Engine with Thermal Barriers (in Norwegian). (Dr.Ing. Thesis)
MTA-88-59	Bernt Arild Bremdal, MP	An Investigation of Marine Installation Processes – A Knowledge - Based Planning Approach. (Dr.Ing. Thesis)
MTA-88-60	Xu Jun, MK	Non-linear Dynamic Analysis of Space-framed Offshore Structures. (Dr.Ing. Thesis)
MTA-89-61	Gang Miao, MH	Hydrodynamic Forces and Dynamic Responses of Circular Cylinders in Wave Zones. (Dr.Ing. Thesis)
MTA-89-62	Martin Greenhow, MH	Linear and Non-Linear Studies of Waves and Floating Bodies. Part I and Part II. (Dr.Techn. Thesis)
MTA-89-63	Chang Li, MH	Force Coefficients of Spheres and Cubes in Oscillatory Flow with and without Current. (Dr.Ing. Thesis
MTA-89-64	Hu Ying, MP	A Study of Marketing and Design in Development of Marine Transport Systems. (Dr.Ing. Thesis)
MTA-89-65	Arild Jæger, MH	Seakeeping, Dynamic Stability and Performance of a Wedge Shaped Planing Hull. (Dr.Ing. Thesis)
MTA-89-66	Chan Siu Hung, MM	The dynamic characteristics of tilting-pad bearings

MTA-89-67	Kim Wikstrøm, MP	Analysis av projekteringen for ett offshore projekt. (Licenciat-avhandling)
MTA-89-68	Jiao Guoyang, MK	Reliability Analysis of Crack Growth under Random Loading, considering Model Updating. (Dr.Ing. Thesis)
MTA-89-69	Arnt Olufsen, MK	Uncertainty and Reliability Analysis of Fixed Offshore Structures. (Dr.Ing. Thesis)
MTA-89-70	Wu Yu-Lin, MR	System Reliability Analyses of Offshore Structures using improved Truss and Beam Models. (Dr.Ing. Thesis)
MTA-90-71	Jan Roger Hoff, MH	Three-dimensional Green function of a vessel with forward speed in waves. (Dr.Ing. Thesis)
MTA-90-72	Rong Zhao, MH	Slow-Drift Motions of a Moored Two-Dimensional Body in Irregular Waves. (Dr.Ing. Thesis)
MTA-90-73	Atle Minsaas, MP	Economical Risk Analysis. (Dr.Ing. Thesis)
MTA-90-74	Knut-Aril Farnes, MK	Long-term Statistics of Response in Non-linear Marine Structures. (Dr.Ing. Thesis)
MTA-90-75	Torbjørn Sotberg, MK	Application of Reliability Methods for Safety Assessment of Submarine Pipelines. (Dr.Ing. Thesis)
MTA-90-76	Zeuthen, Steffen, MP	SEAMAID. A computational model of the design process in a constraint-based logic programming environment. An example from the offshore domain. (Dr.Ing. Thesis)
MTA-91-77	Haagensen, Sven, MM	Fuel Dependant Cyclic Variability in a Spark Ignition Engine - An Optical Approach. (Dr.Ing. Thesis)
MTA-91-78	Løland, Geir, MH	Current forces on and flow through fish farms. (Dr.Ing. Thesis)
MTA-91-79	Hoen, Christopher, MK	System Identification of Structures Excited by Stochastic Load Processes. (Dr.Ing. Thesis)
MTA-91-80	Haugen, Stein, MK	Probabilistic Evaluation of Frequency of Collision between Ships and Offshore Platforms. (Dr.Ing. Thesis)
MTA-91-81	Sødahl, Nils, MK	Methods for Design and Analysis of Flexible Risers. (Dr.Ing. Thesis)
MTA-91-82	Ormberg, Harald, MK	Non-linear Response Analysis of Floating Fish Farm Systems. (Dr.Ing. Thesis)
MTA-91-83	Marley, Mark J., MK	Time Variant Reliability under Fatigue Degradation. (Dr.Ing. Thesis)
MTA-91-84	Krokstad, Jørgen R., MH	Second-order Loads in Multidirectional Seas. (Dr.Ing. Thesis)
MTA-91-85	Molteberg, Gunnar A., MM	The Application of System Identification Techniques to Performance Monitoring of Four Stroke Turbocharged Diesel Engines. (Dr.Ing. Thesis)
MTA-92-86	Mørch, Hans Jørgen Bjelke, MH	Aspects of Hydrofoil Design: with Emphasis on Hydrofoil Interaction in Calm Water. (Dr.Ing. Thesis)
MTA-92-87	Chan Siu Hung, MM	Nonlinear Analysis of Rotordynamic Instabilities in Highspeed Turbomachinery. (Dr.Ing. Thesis)
MTA-92-88	Bessason, Bjarni, MK	Assessment of Earthquake Loading and Response of Seismically Isolated Bridges. (Dr.Ing. Thesis)
MTA-92-89	Langli, Geir, MP	Improving Operational Safety through exploitation of Design Knowledge - an investigation of offshore platform safety. (Dr.Ing. Thesis)
MTA-92-90	Sævik, Svein, MK	On Stresses and Fatigue in Flexible Pipes. (Dr.Ing. Thesis)
MTA-92-91	Ask, Tor Ø., MM	Ignition and Flame Growth in Lean Gas-Air Mixtures. An Experimental Study with a Schlieren System. (Dr.Ing. Thesis)
MTA-86-92	Hessen, Gunnar, MK	Fracture Mechanics Analysis of Stiffened Tubular Members. (Dr.Ing. Thesis)

MTA-93-93	Steinebach, Christian, MM	Knowledge Based Systems for Diagnosis of Rotating Machinery. (Dr.Ing. Thesis)
MTA-93-94	Dalane, Jan Inge, MK	System Reliability in Design and Maintenance of Fixed Offshore Structures. (Dr.Ing. Thesis)
MTA-93-95	Steen, Sverre, MH	Cobblestone Effect on SES. (Dr.Ing. Thesis)
MTA-93-96	Karunakaran, Daniel, MK	Nonlinear Dynamic Response and Reliability Analysis of Drag-dominated Offshore Platforms. (Dr.Ing. Thesis)
MTA-93-97	Hagen, Arnulf, MP	The Framework of a Design Process Language. (Dr.Ing. Thesis)
MTA-93-98	Nordrik, Rune, MM	Investigation of Spark Ignition and Autoignition in Methane and Air Using Computational Fluid Dynamics and Chemical Reaction Kinetics. A Numerical Study of Ignition Processes in Internal Combustion Engines. (Dr.Ing. Thesis)
MTA-94-99	Passano, Elizabeth, MK	Efficient Analysis of Nonlinear Slender Marine Structures. (Dr.Ing. Thesis)
MTA-94-100	Kvålsvold, Jan, MH	Hydroelastic Modelling of Wetdeck Slamming on Multihull Vessels. (Dr.Ing. Thesis)
MTA-94-102	Bech, Sidsel M., MK	Experimental and Numerical Determination of Stiffness and Strength of GRP/PVC Sandwich Structures. (Dr.Ing. Thesis)
MTA-95-103	Paulsen, Hallvard, MM	A Study of Transient Jet and Spray using a Schlieren Method and Digital Image Processing. (Dr.Ing. Thesis)
MTA-95-104	Hovde, Geir Olav, MK	Fatigue and Overload Reliability of Offshore Structural Systems, Considering the Effect of Inspection and Repair. (Dr.Ing. Thesis)
MTA-95-105	Wang, Xiaozhi, MK	Reliability Analysis of Production Ships with Emphasis on Load Combination and Ultimate Strength. (Dr.Ing. Thesis)
MTA-95-106	Ulstein, Tore, MH	Nonlinear Effects of a Flexible Stern Seal Bag on Cobblestone Oscillations of an SES. (Dr.Ing. Thesis)
MTA-95-107	Solaas, Frøydis, MH	Analytical and Numerical Studies of Sloshing in Tanks. (Dr.Ing. Thesis)
MTA-95-108	Hellan, Øyvind, MK	Nonlinear Pushover and Cyclic Analyses in Ultimate Limit State Design and Reassessment of Tubular Steel Offshore Structures. (Dr.Ing. Thesis)
MTA-95-109	Hermundstad, Ole A., MK	Theoretical and Experimental Hydroelastic Analysis of High Speed Vessels. (Dr.Ing. Thesis)
MTA-96-110	Bratland, Anne K., MH	Wave-Current Interaction Effects on Large-Volume Bodies in Water of Finite Depth. (Dr.Ing. Thesis)
MTA-96-111	Herfjord, Kjell, MH	A Study of Two-dimensional Separated Flow by a Combination of the Finite Element Method and Navier-Stokes Equations. (Dr.Ing. Thesis)
MTA-96-112	Æsøy, Vilmar, MM	Hot Surface Assisted Compression Ignition in a Direct Injection Natural Gas Engine. (Dr.Ing. Thesis)
MTA-96-113	Eknes, Monika L., MK	Escalation Scenarios Initiated by Gas Explosions on Offshore Installations. (Dr.Ing. Thesis)
MTA-96-114	Erikstad, Stein O., MP	A Decision Support Model for Preliminary Ship Design. (Dr.Ing. Thesis)
MTA-96-115	Pedersen, Egil, MH	A Nautical Study of Towed Marine Seismic Streamer Cable Configurations. (Dr.Ing. Thesis)
MTA-97-116	Moksnes, Paul O., MM	Modelling Two-Phase Thermo-Fluid Systems Using Bond Graphs. (Dr.Ing. Thesis)
MTA-97-117	Halse, Karl H., MK	On Vortex Shedding and Prediction of Vortex-Induced Vibrations of Circular Cylinders. (Dr.Ing. Thesis)
MTA-97-118	Igland, Ragnar T., MK	Reliability Analysis of Pipelines during Laying, considering Ultimate Strength under Combined Loads. (Dr.Ing. Thesis)

MTA-97-119	Pedersen, Hans-P., MP	Levendefiskteknologi for fiskefartøy. (Dr.Ing. Thesis)
MTA-98-120	Vikestad, Kyrre, MK	Multi-Frequency Response of a Cylinder Subjected to Vortex Shedding and Support Motions. (Dr.Ing. Thesis)
MTA-98-121	Azadi, Mohammad R. E., MK	Analysis of Static and Dynamic Pile-Soil-Jacket Behaviour. (Dr.Ing. Thesis)
MTA-98-122	Ulltang, Terje, MP	A Communication Model for Product Information. (Dr.Ing. Thesis)
MTA-98-123	Torbergsen, Erik, MM	Impeller/Diffuser Interaction Forces in Centrifugal Pumps. (Dr.Ing. Thesis)
MTA-98-124	Hansen, Edmond, MH	A Discrete Element Model to Study Marginal Ice Zone Dynamics and the Behaviour of Vessels Moored in Broken Ice. (Dr.Ing. Thesis)
MTA-98-125	Videiro, Paulo M., MK	Reliability Based Design of Marine Structures. (Dr.Ing. Thesis)
MTA-99-126	Mainçon, Philippe, MK	Fatigue Reliability of Long Welds Application to Titanium Risers. (Dr.Ing. Thesis)
MTA-99-127	Haugen, Elin M., MH	Hydroelastic Analysis of Slamming on Stiffened Plates with Application to Catamaran Wetdecks. (Dr.Ing. Thesis)
MTA-99-128	Langhelle, Nina K., MK	Experimental Validation and Calibration of Nonlinear Finite Element Models for Use in Design of Aluminium Structures Exposed to Fire. (Dr.Ing. Thesis)
MTA-99-129	Berstad, Are J., MK	Calculation of Fatigue Damage in Ship Structures. (Dr.Ing. Thesis)
MTA-99-130	Andersen, Trond M., MM	Short Term Maintenance Planning. (Dr.Ing. Thesis)
MTA-99-131	Tveiten, Bård Wathne, MK	Fatigue Assessment of Welded Aluminium Ship Details. (Dr.Ing. Thesis)
MTA-99-132	Søreide, Fredrik, MP	Applications of underwater technology in deep water archaeology. Principles and practice. (Dr.Ing. Thesis)
MTA-99-133	Tønnessen, Rune, MH	A Finite Element Method Applied to Unsteady Viscous Flow Around 2D Blunt Bodies With Sharp Corners. (Dr.Ing. Thesis)
MTA-99-134	Elvekrok, Dag R., MP	Engineering Integration in Field Development Projects in the Norwegian Oil and Gas Industry. The Supplier Management of Norne. (Dr.Ing. Thesis)
MTA-99-135	Fagerholt, Kjetil, MP	Optimeringsbaserte Metoder for Ruteplanlegging innen skipsfart. (Dr.Ing. Thesis)
MTA-99-136	Bysveen, Marie, MM	Visualization in Two Directions on a Dynamic Combustion Rig for Studies of Fuel Quality. (Dr.Ing. Thesis)
MTA-2000-137	Storteig, Eskild, MM	Dynamic characteristics and leakage performance of liquid annular seals in centrifugal pumps. (Dr.Ing. Thesis)
MTA-2000-138	Sagli, Gro, MK	Model uncertainty and simplified estimates of long term extremes of hull girder loads in ships. (Dr.Ing. Thesis)
MTA-2000-139	Tronstad, Harald, MK	Nonlinear analysis and design of cable net structures like fishing gear based on the finite element method. (Dr.Ing. Thesis)
MTA-2000-140	Kroneberg, André, MP	Innovation in shipping by using scenarios. (Dr.Ing. Thesis)
MTA-2000-141	Haslum, Herbjørn Alf, MH	Simplified methods applied to nonlinear motion of spar platforms. (Dr.Ing. Thesis)
MTA-2001-142	Samdal, Ole Johan, MM	Modelling of Degradation Mechanisms and Stressor Interaction on Static Mechanical Equipment Residual Lifetime. (Dr.Ing. Thesis)
MTA-2001-143	Baarholm, Rolf Jarle, MH	Theoretical and experimental studies of wave impact underneath decks of offshore platforms. (Dr.Ing. Thesis)
MTA-2001-144	Wang, Lihua, MK	Probabilistic Analysis of Nonlinear Wave-induced Loads on Ships. (Dr.Ing. Thesis)
MTA-2001-145	Kristensen, Odd H. Holt, MK	Ultimate Capacity of Aluminium Plates under Multiple Loads, Considering HAZ

		Properties. (Dr.Ing. Thesis)
MTA-2001-146	Greco, Marilena, MH	A Two-Dimensional Study of Green-Water Loading. (Dr.Ing. Thesis)
MTA-2001-147	Heggelund, Svein E., MK	Calculation of Global Design Loads and Load Effects in Large High Speed Catamarans. (Dr.Ing. Thesis)
MTA-2001-148	Babalola, Olusegun T., MK	Fatigue Strength of Titanium Risers – Defect Sensitivity. (Dr.Ing. Thesis)
MTA-2001-149	Mohammed, Abuu K., MK	Nonlinear Shell Finite Elements for Ultimate Strength and Collapse Analysis of Ship Structures. (Dr.Ing. Thesis)
MTA-2002-150	Holmedal, Lars E., MH	Wave-current interactions in the vicinity of the sea bed. (Dr.Ing. Thesis)
MTA-2002-151	Rognebakke, Olav F., MH	Sloshing in rectangular tanks and interaction with ship motions. (Dr.Ing. Thesis)
MTA-2002-152	Lader, Pål Furset, MH	Geometry and Kinematics of Breaking Waves. (Dr.Ing. Thesis)
MTA-2002-153	Yang, Qinzheng, MH	Wash and wave resistance of ships in finite water depth. (Dr.Ing. Thesis)
MTA-2002-154	Melhus, Øyvin, MM	Utilization of VOC in Diesel Engines. Ignition and combustion of VOC released by crude oil tankers. (Dr.Ing. Thesis)
MTA-2002-155	Ronæss, Marit, MH	Wave Induced Motions of Two Ships Advancing on Parallel Course. (Dr.Ing. Thesis)
MTA-2002-156	Økland, Ole D., MK	Numerical and experimental investigation of whipping in twin hull vessels exposed to severe wet deck slamming. (Dr.Ing. Thesis)
MTA-2002-157	Ge, Chunhua, MK	Global Hydroelastic Response of Catamarans due to Wet Deck Slamming. (Dr.Ing. Thesis)
MTA-2002-158	Byklum, Eirik, MK	Nonlinear Shell Finite Elements for Ultimate Strength and Collapse Analysis of Ship Structures. (Dr.Ing. Thesis)
IMT-2003-1	Chen, Haibo, MK	Probabilistic Evaluation of FPSO-Tanker Collision in Tandem Offloading Operation. (Dr.Ing. Thesis)
IMT-2003-2	Skaugset, Kjetil Bjørn, MK	On the Suppression of Vortex Induced Vibrations of Circular Cylinders by Radial Water Jets. (Dr.Ing. Thesis)
IMT-2003-3	Chezhian, Muthu	Three-Dimensional Analysis of Slamming. (Dr.Ing. Thesis)
IMT-2003-4	Buhaug, Øyvind	Deposit Formation on Cylinder Liner Surfaces in Medium Speed Engines. (Dr.Ing. Thesis)
IMT-2003-5	Tregde, Vidar	Aspects of Ship Design: Optimization of Aft Hull with Inverse Geometry Design. (Dr.Ing. Thesis)
IMT-2003-6	Wist, Hanne Therese	Statistical Properties of Successive Ocean Wave Parameters. (Dr.Ing. Thesis)
IMT-2004-7	Ransau, Samuel	Numerical Methods for Flows with Evolving Interfaces. (Dr.Ing. Thesis)
IMT-2004-8	Soma, Torkel	Blue-Chip or Sub-Standard. A data interrogation approach of identity safety characteristics of shipping organization. (Dr.Ing. Thesis)
IMT-2004-9	Ersdal, Svein	An experimental study of hydrodynamic forces on cylinders and cables in near axial flow. (Dr.Ing. Thesis)
IMT-2005-10	Brodtkorb, Per Andreas	The Probability of Occurrence of Dangerous Wave Situations at Sea. (Dr.Ing. Thesis)
IMT-2005-11	Yttervik, Rune	Ocean current variability in relation to offshore engineering. (Dr.Ing. Thesis)
IMT-2005-12	Fredheim, Arne	Current Forces on Net-Structures. (Dr.Ing. Thesis)

IMT-2005-13	Heggernes, Kjetil	Flow around marine structures. (Dr.Ing. Thesis
IMT-2005-14	Fouques, Sebastien	Lagrangian Modelling of Ocean Surface Waves and Synthetic Aperture Radar Wave Measurements. (Dr.Ing. Thesis)
IMT-2006-15	Holm, Håvard	Numerical calculation of viscous free surface flow around marine structures. (Dr.Ing. Thesis)
IMT-2006-16	Bjørheim, Lars G.	Failure Assessment of Long Through Thickness Fatigue Cracks in Ship Hulls. (Dr.Ing. Thesis)
IMT-2006-17	Hansson, Lisbeth	Safety Management for Prevention of Occupational Accidents. (Dr.Ing. Thesis)
IMT-2006-18	Zhu, Xinying	Application of the CIP Method to Strongly Nonlinear Wave-Body Interaction Problems. (Dr.Ing. Thesis)
IMT-2006-19	Reite, Karl Johan	Modelling and Control of Trawl Systems. (Dr.Ing. Thesis)
IMT-2006-20	Smogeli, Øyvind Notland	Control of Marine Propellers. From Normal to Extreme Conditions. (Dr.Ing. Thesis)
IMT-2007-21	Storhaug, Gaute	Experimental Investigation of Wave Induced Vibrations and Their Effect on the Fatigue Loading of Ships. (Dr.Ing. Thesis)
IMT-2007-22	Sun, Hui	A Boundary Element Method Applied to Strongly Nonlinear Wave-Body Interaction Problems. (PhD Thesis, CeSOS)
IMT-2007-23	Rustad, Anne Marthine	Modelling and Control of Top Tensioned Risers. (PhD Thesis, CeSOS)
IMT-2007-24	Johansen, Vegar	Modelling flexible slender system for real-time simulations and control applications
IMT-2007-25	Wroldsen, Anders Sunde	Modelling and control of tensegrity structures. (PhD Thesis, CeSOS)
IMT-2007-26	Aronsen, Kristoffer Høye	An experimental investigation of in-line and combined inline and cross flow vortex induced vibrations. (Dr. avhandling, IMT)
IMT-2007-27	Gao, Zhen	Stochastic Response Analysis of Mooring Systems with Emphasis on Frequency-domain Analysis of Fatigue due to Wide-band Response Processes (PhD Thesis, CeSOS)
IMT-2007-28	Thorstensen, Tom Anders	Lifetime Profit Modelling of Ageing Systems Utilizing Information about Technical Condition. (Dr.ing. thesis, IMT)
IMT-2008-29	Refsnes, Jon Erling Gorset	Nonlinear Model-Based Control of Slender Body AUVs (PhD Thesis, IMT)
IMT-2008-30	Berntsen, Per Ivar B.	Structural Reliability Based Position Mooring. (PhD-Thesis, IMT)
IMT-2008-31	Ye, Naiquan	Fatigue Assessment of Aluminium Welded Box-stiffener Joints in Ships (Dr.ing. thesis, IMT)
IMT-2008-32	Radan, Damir	Integrated Control of Marine Electrical Power Systems. (PhD-Thesis, IMT)
IMT-2008-33	Thomassen, Paul	Methods for Dynamic Response Analysis and Fatigue Life Estimation of Floating Fish Cages. (Dr.ing. thesis, IMT)
IMT-2008-34	Pákozdi, Csaba	A Smoothed Particle Hydrodynamics Study of Two-dimensional Nonlinear Sloshing in Rectangular Tanks. (Dr.ing.thesis, IMT/ CeSOS)
IMT-2007-35	Grytøyr, Guttorm	A Higher-Order Boundary Element Method and Applications to Marine Hydrodynamics. (Dr.ing.thesis, IMT)
IMT-2008-36	Drummen, Ingo	Experimental and Numerical Investigation of Nonlinear Wave-Induced Load Effects in Containerships considering Hydroelasticity. (PhD thesis, CeSOS)
IMT-2008-37	Skejic, Renato	Maneuvering and Seakeeping of a Singel Ship and of Two Ships in Interaction. (PhD-Thesis, CeSOS)
IMT-2008-38	Harlem, Alf	An Age-Based Replacement Model for Repairable Systems with Attention to High-

		Speed Marine Diesel Engines. (PhD-Thesis, IMT)
IMT-2008-39	Alsos, Hagbart S.	Ship Grounding. Analysis of Ductile Fracture, Bottom Damage and Hull Girder Response. (PhD-thesis, IMT)
IMT-2008-40	Graczyk, Mateusz	Experimental Investigation of Sloshing Loading and Load Effects in Membrane LNG Tanks Subjected to Random Excitation. (PhD-thesis, CeSOS)
IMT-2008-41	Taghipour, Reza	Efficient Prediction of Dynamic Response for Flexible amd Multi-body Marine Structures. (PhD-thesis, CeSOS)
IMT-2008-42	Ruth, Eivind	Propulsion control and thrust allocation on marine vessels. (PhD thesis, CeSOS)
IMT-2008-43	Nystad, Bent Helge	Technical Condition Indexes and Remaining Useful Life of Aggregated Systems. PhD thesis, IMT
IMT-2008-44	Soni, Prashant Kumar	Hydrodynamic Coefficients for Vortex Induced Vibrations of Flexible Beams, PhD thesis, CeSOS
IMT-2009-45	Amlashi, Hadi K.K.	Ultimate Strength and Reliability-based Design of Ship Hulls with Emphasis on Combined Global and Local Loads. PhD Thesis, IMT
IMT-2009-46	Pedersen, Tom Arne	Bond Graph Modelling of Marine Power Systems. PhD Thesis, IMT
IMT-2009-47	Kristiansen, Trygve	Two-Dimensional Numerical and Experimental Studies of Piston-Mode Resonance. PhD-Thesis, CeSOS
IMT-2009-48	Ong, Muk Chen	Applications of a Standard High Reynolds Number Model and a Stochastic Scour Prediction Model for Marine Structures. PhD-thesis, IMT
IMT-2009-49	Hong, Lin	Simplified Analysis and Design of Ships subjected to Collision and Grounding. PhD-thesis, IMT
IMT-2009-50	Koushan, Kamran	Vortex Induced Vibrations of Free Span Pipelines, PhD thesis, IMT
IMT-2009-51	Korsvik, Jarl Eirik	Heuristic Methods for Ship Routing and Scheduling. PhD-thesis, IMT
IMT-2009-52	Lee, Jihoon	Experimental Investigation and Numerical in Analyzing the Ocean Current Displacement of Longlines. Ph.d.-Thesis, IMT.
IMT-2009-53	Vestbøstad, Tone Gran	A Numerical Study of Wave-in-Deck Impact usin a Two-Dimensional Constrained Interpolation Profile Method, Ph.d.thesis, CeSOS.
IMT-2009-54	Bruun, Kristine	Bond Graph Modelling of Fuel Cells for Marine Power Plants. Ph.d.-thesis, IMT
IMT 2009-55	Holstad, Anders	Numerical Investigation of Turbulence in a Sekwed Three-Dimensional Channel Flow, Ph.d.-thesis, IMT.
IMT 2009-56	Ayala-Uraga, Efren	Reliability-Based Assessment of Deteriorating Ship-shaped Offshore Structures, Ph.d.-thesis, IMT
IMT 2009-57	Kong, Xiangjun	A Numerical Study of a Damaged Ship in Beam Sea Waves. Ph.d.-thesis, IMT/CeSOS.

IMT 2010-58	Kristiansen, David	Wave Induced Effects on Floaters of Aquaculture Plants, Ph.d.-thesis, CeSOS.
IMT 2010-59	Ludvigsen, Martin	An ROV-Toolbox for Optical and Acoustic Scientific Seabed Investigation. Ph.d.-thesis IMT.
IMT 2010-60	Hals, Jørgen	Modelling and Phase Control of Wave-Energy Converters. Ph.d.thesis, CeSOS.
IMT 2010- 61	Shu, Zhi	Uncertainty Assessment of Wave Loads and Ultimate Strength of Tankers and Bulk Carriers in a Reliability Framework. Ph.d. Thesis, IMT/ CeSOS
IMT 2010-62	Shao, Yanlin	Numerical Potential-Flow Studies on Weakly-Nonlinear Wave-Body Interactions with/without Small Forward Speed, Ph.d.thesis,CeSOS.
IMT 2010-63	Califano, Andrea	Dynamic Loads on Marine Propellers due to Intermittent Ventilation. Ph.d.thesis, IMT.
IMT 2010-64	El Khoury, George	Numerical Simulations of Massively Separated Turbulent Flows, Ph.d.-thesis, IMT
IMT 2010-65	Seim, Knut Sponheim	Mixing Process in Dense Overflows with Emphasis on the Faroe Bank Channel Overflow. Ph.d.thesis, IMT
IMT 2010-66	Jia, Huirong	Structural Analysis of Intect and Damaged Ships in a Collission Risk Analysis Perspective. Ph.d.thesis CeSoS.
IMT 2010-67	Jiao, Linlin	Wave-Induced Effects on a Pontoon-type Very Large Floating Structures (VLFS). Ph.D.-thesis, CeSOS.
IMT 2010-68	Abrahamsen, Bjørn Christian	Sloshing Induced Tank Roof with Entrapped Air Pocket. Ph.d.thesis, CeSOS.
IMT 2011-69	Karimirad, Madjid	Stochastic Dynamic Response Analysis of Spar-Type Wind Turbines with Catenary or Taut Mooring Systems. Ph.d.-thesis, CeSOS.
IMT - 2011-70	Erlend Meland	Condition Monitoring of Safety Critical Valves. Ph.d.-thesis, IMT.
IMT – 2011-71	Yang, Limin	Stochastic Dynamic System Analysis of Wave Energy Converter with Hydraulic Power Take-Off, with Particular Reference to Wear Damage Analysis, Ph.d. Thesis, CeSOS.
IMT – 2011-72	Visscher, Jan	Application of Particla Image Velocimetry on Turbulent Marine Flows, Ph.d.Thesis, IMT.
IMT – 2011-73	Su, Biao	Numerical Predictions of Global and Local Ice Loads on Ships. Ph.d.Thesis, CeSOS.
IMT – 2011-74	Liu, Zhenhui	Analytical and Numerical Analysis of Iceberg Collision with Ship Structures. Ph.d.Thesis, IMT.
IMT – 2011-75	Aarsæther, Karl Gunnar	Modeling and Analysis of Ship Traffic by Observation and Numerical Simulation. Ph.d.Thesis, IMT.
Imt – 2011-76	Wu, Jie	Hydrodynamic Force Identification from Stochastic Vortex Induced Vibration Experiments with Slender Beams. Ph.d.Thesis, IMT.

Imt – 2011-77	Amini, Hamid	Azimuth Propulsors in Off-design Conditions. Ph.d.Thesis, IMT.
IMT – 2011-78	Nguyen, Tan-Hoi	Toward a System of Real-Time Prediction and Monitoring of Bottom Damage Conditions During Ship Grounding. Ph.d.thesis, IMT.
IMT- 2011-79	Tavakoli, Mohammad T.	Assessment of Oil Spill in Ship Collision and Grounding, Ph.d.thesis, IMT.
IMT- 2011-80	Guo, Bingjie	Numerical and Experimental Investigation of Added Resistance in Waves. Ph.d.Thesis, IMT.
IMT- 2011-81	Chen, Qiaofeng	Ultimate Strength of Aluminium Panels, considering HAZ Effects, IMT
IMT- 2012-82	Kota, Ravikiran S.	Wave Loads on Decks of Offshore Structures in Random Seas, CeSOS.
IMT- 2012-83	Sten, Ronny	Dynamic Simulation of Deep Water Drilling Risers with Heave Compensating System, IMT.
IMT- 2012-84	Berle, Øyvind	Risk and resilience in global maritime supply chains, IMT.
IMT- 2012-85	Fang, Shaoji	Fault Tolerant Position Mooring Control Based on Structural Reliability, CeSOS.
IMT- 2012-86	You, Jikun	Numerical studies on wave forces and moored ship motions in intermediate and shallow water, CeSOS.
IMT- 2012-87	Xiang ,Xu	Maneuvering of two interacting ships in waves, CeSOS
IMT- 2012-88	Dong, Wenbin	Time-domain fatigue response and reliability analysis of offshore wind turbines with emphasis on welded tubular joints and gear components, CeSOS
IMT- 2012-89	Zhu, Suji	Investigation of Wave-Induced Nonlinear Load Effects in Open Ships considering Hull Girder Vibrations in Bending and Torsion, CeSOS
IMT- 2012-90	Zhou, Li	Numerical and Experimental Investigation of Station-keeping in Level Ice, CeSOS
IMT- 2012-91	Ushakov, Sergey	Particulate matter emission characteristics from diesel enignes operating on conventional and alternative marine fuels, IMT
IMT- 2013-1	Yin, Decao	Experimental and Numerical Analysis of Combined In-line and Cross-flow Vortex Induced Vibrations, CeSOS
IMT- 2013-2	Kurniawan, Adi	Modelling and geometry optimisation of wave energy converters, CeSOS
IMT- 2013-3	Al Ryati, Nabil	Technical condition indexes doe auxiliary marine diesel engines, IMT
IMT- 2013-4	Firoozkoohi, Reza	Experimental, numerical and analytical investigation of the effect of screens on sloshing, CeSOS

IMT-2013-5	Ommani, Babak	Potential-Flow Predictions of a Semi-Displacement Vessel Including Applications to Calm Water Broaching, CeSOS
IMT-2013-6	Xing, Yihan	Modelling and analysis of the gearbox in a floating spar-type wind turbine, CeSOS
IMT-7-2013	Balland, Océane	Optimization models for reducing air emissions from ships, IMT
IMT-8-2013	Yang, Dan	Transitional wake flow behind an inclined flat plate-----Computation and analysis, IMT
IMT-9-2013	Abdillah, Suyuthi	Prediction of Extreme Loads and Fatigue Damage for a Ship Hull due to Ice Action, IMT
IMT-10-2013	Ramìrez, Pedro Agustìn Pèrez	Ageing management and life extension of technical systems-Concepts and methods applied to oil and gas facilities, IMT
IMT-11-2013	Chuang, Zhenju	Experimental and Numerical Investigation of Speed Loss due to Seakeeping and Maneuvering. IMT
IMT-12-2013	Etemaddar, Mahmoud	Load and Response Analysis of Wind Turbines under Atmospheric Icing and Controller System Faults with Emphasis on Spar Type Floating Wind Turbines, IMT
IMT-13-2013	Lindstad, Haakon	Strategies and measures for reducing maritime CO2 emissons, IMT
IMT-14-2013	Haris, Sabril	Damage interaction analysis of ship collisions, IMT
IMT-15-2013	Shainee, Mohamed	Conceptual Design, Numerical and Experimental Investigation of a SPM Cage Concept for Offshore Mariculture, IMT
IMT-16-2013	Gansel, Lars	Flow past porous cylinders and effects of biofouling and fish behavior on the flow in and around Atlantic salmon net cages, IMT
IMT-17-2013	Gaspar, Henrique	Handling Aspects of Complexity in Conceptual Ship Design, IMT
IMT-18-2013	Thys, Maxime	Theoretical and Experimental Investigation of a Free Running Fishing Vessel at Small Frequency of Encounter, CeSOS
IMT-19-2013	Aglen, Ida	VIV in Free Spanning Pipelines, CeSOS
IMT-1-2014	Song, An	Theoretical and experimental studies of wave diffraction and radiation loads on a horizontally submerged perforated plate, CeSOS
IMT-2-2014	Rogne, Øyvind Ygre	Numerical and Experimental Investigation of a Hinged 5-body Wave Energy Converter, CeSOS
IMT-3-2014	Dai, Lijuan	Safe and efficient operation and maintenance of offshore wind farms ,IMT
IMT-4-2014	Bachynski, Erin Elizabeth	Design and Dynamic Analysis of Tension Leg Platform Wind Turbines, CeSOS
IMT-5-2014	Wang, Jingbo	Water Entry of Freefall Wedged – Wedge motions and Cavity Dynamics, CeSOS

IMT-6-2014	Kim, Ekaterina	Experimental and numerical studies related to the coupled behavior of ice mass and steel structures during accidental collisions, IMT
IMT-7-2014	Tan, Xiang	Numerical investigation of ship's continuous- mode icebreaking in leverl ice, CeSOS
IMT-8-2014	Muliawan, Made Jaya	Design and Analysis of Combined Floating Wave and Wind Power Facilities, with Emphasis on Extreme Load Effects of the Mooring System, CeSOS
IMT-9-2014	Jiang, Zhiyu	Long-term response analysis of wind turbines with an emphasis on fault and shutdown conditions, IMT
IMT-10-2014	Dukan, Fredrik	ROV Motion Control Systems, IMT
IMT-11-2014	Grimsmo, Nils I.	Dynamic simulations of hydraulic cylinder for heave compensation of deep water drilling risers, IMT
IMT-12-2014	Kvittem, Marit I.	Modelling and response analysis for fatigue design of a semisubmersible wind turbine, CeSOS
IMT-13-2014	Akhtar, Juned	The Effects of Human Fatigue on Risk at Sea, IMT
IMT-14-2014	Syahroni, Nur	Fatigue Assessment of Welded Joints Taking into Account Effects of Residual Stress, IMT
IMT-1-2015	Bøckmann, Eirik	Wave Propulsion of ships, IMT
IMT-2-2015	Wang, Kai	Modelling and dynamic analysis of a semi-submersible floating vertical axis wind turbine, CeSOS
IMT-3-2015	Fredriksen, Arnt Gunvald	A numerical and experimental study of a two-dimensional body with moonpool in waves and current, CeSOS
IMT-4-2015	Jose Patricio Gallardo Canabes	Numerical studies of viscous flow around bluff bodies, IMT
IMT-5-2015	Vegard Longva	Formulation and application of finite element techniques for slender marine structures subjected to contact interactions, IMT
IMT-6-2015	Jacobus De Vaal	Aerodynamic modelling of floating wind turbines, CeSOS
IMT-7-2015	Fachri Nasution	Fatigue Performance of Copper Power Conductors, IMT
IMT-8-2015	Oleh I Karpa	Development of bivariate extreme value distributions for applications in marine technology,CeSOS
IMT-9-2015	Daniel de Almeida Fernandes	An output feedback motion control system for ROVs, AMOS
IMT-10-2015	Bo Zhao	Particle Filter for Fault Diagnosis: Application to Dynamic Positioning Vessel and Underwater Robotics, CeSOS
IMT-11-2015	Wenting Zhu	Impact of emission allocation in maritime transportation, IMT

IMT-12-2015	Amir Rasekhi Nejad	Dynamic Analysis and Design of Gearboxes in Offshore Wind Turbines in a Structural Reliability Perspective, CeSOS
IMT-13-2015	Arturo Jesùs Ortega Malca	Dynamic Response of Flexibles Risers due to Unsteady Slug Flow, CeSOS
IMT-14-2015	Dagfinn Husjord	Guidance and decision-support system for safe navigation of ships operating in close proximity, IMT
IMT-15-2015	Anirban Bhattacharyya	Ducted Propellers: Behaviour in Waves and Scale Effects, IMT
IMT-16-2015	Qin Zhang	Image Processing for Ice Parameter Identification in Ice Management, IMT
IMT-1-2016	Vincentius Rumawas	Human Factors in Ship Design and Operation: An Experiential Learning, IMT
IMT-2-2016	Martin Storheim	Structural response in ship-platform and ship-ice collisions, IMT
IMT-3-2016	Mia Abrahamsen Prsic	Numerical Simulations of the Flow around single and Tandem Circular Cylinders Close to a Plane Wall, IMT
IMT-4-2016	Tufan Arslan	Large-eddy simulations of cross-flow around ship sections, IMT
IMT-5-2016	Pierre Yves-Henry	Parametrisation of aquatic vegetation in hydraulic and coastal research,IMT
IMT-6-2016	Lin Li	Dynamic Analysis of the Instalation of Monopiles for Offshore Wind Turbines, CeSOS
IMT-7-2016	Øivind Kåre Kjerstad	Dynamic Positioning of Marine Vessels in Ice, IMT
IMT-8-2016	Xiaopeng Wu	Numerical Analysis of Anchor Handling and Fish Trawling Operations in a Safety Perspective, CeSOS
IMT-9-2016	Zhengshun Cheng	Integrated Dynamic Analysis of Floating Vertical Axis Wind Turbines, CeSOS
IMT-10-2016	Ling Wan	Experimental and Numerical Study of a Combined Offshore Wind and Wave Energy Converter Concept
IMT-11-2016	Wei Chai	Stochastic dynamic analysis and reliability evaluation of the roll motion for ships in random seas, CeSOS
IMT-12-2016	Øyvind Selnes Patricksson	Decision support for conceptual ship design with focus on a changing life cycle and future uncertainty, IMT
IMT-13-2016	Mats Jørgen Thorsen	Time domain analysis of vortex-induced vibrations, IMT
IMT-14-2016	Edgar McGuinness	Safety in the Norwegian Fishing Fleet – Analysis and measures for improvement, IMT
IMT-15-2016	Sepideh Jafarzadeh	Energy effiency and emission abatement in the fishing fleet, IMT

IMT-16-2016	Wilson Ivan Guachamin Acero	Assessment of marine operations for offshore wind turbine installation with emphasis on response-based operational limits, IMT
IMT-17-2016	Mauro Candeloro	Tools and Methods for Autonomous Operations on Seabed and Water Coumn using Underwater Vehicles, IMT
IMT-18-2016	Valentin Chabaud	Real-Time Hybrid Model Testing of Floating Wind Tubines, IMT
IMT-1-2017	Mohammad Saud Afzal	Three-dimensional streaming in a sea bed boundary layer
IMT-2-2017	Peng Li	A Theoretical and Experimental Study of Wave-induced Hydroelastic Response of a Circular Floating Collar
IMT-3-2017	Martin Bergström	A simulation-based design method for arctic maritime transport systems
IMT-4-2017	Bhushan Taskar	The effect of waves on marine propellers and propulsion
IMT-5-2017	Mohsen Bardestani	A two-dimensional numerical and experimental study of a floater with net and sinker tube in waves and current
IMT-6-2017	Fatemeh Hoseini Dadmarzi	Direct Numerical Simualtion of turbulent wakes behind different plate configurations
IMT-7-2017	Michel R. Miyazaki	Modeling and control of hybrid marine power plants
IMT-8-2017	Giri Rajasekhar Gunnu	Safety and effiency enhancement of anchor handling operations with particular emphasis on the stability of anchor handling vessels
IMT-9-2017	Kevin Koosup Yum	Transient Performance and Emissions of a Turbocharged Diesel Engine for Marine Power Plants
IMT-10-2017	Zhaolong Yu	Hydrodynamic and structural aspects of ship collisions
IMT-11-2017	Martin Hassel	Risk Analysis and Modelling of Allisions between Passing Vessels and Offshore Installations
IMT-12-2017	Astrid H. Brodtkorb	Hybrid Control of Marine Vessels – Dynamic Positioning in Varying Conditions
IMT-13-2017	Kjersti Bruserud	Simultaneous stochastic model of waves and current for prediction of structural design loads
IMT-14-2017	Finn-Idar Grøtta Giske	Long-Term Extreme Response Analysis of Marine Structures Using Inverse Reliability Methods
IMT-15-2017	Stian Skjong	Modeling and Simulation of Maritime Systems and Operations for Virtual Prototyping using co-Simulations
IMT-1-2018	Yingguang Chu	Virtual Prototyping for Marine Crane Design and Operations
IMT-2-2018	Sergey Gavrilin	Validation of ship manoeuvring simulation models

IMT-3-2018	Jeevith Hegde	Tools and methods to manage risk in autonomous subsea inspection,maintenance and repair operations
IMT-4-2018	Ida M. Strand	Sea Loads on Closed Flexible Fish Cages
IMT-5-2018	Erlend Kvinge Jørgensen	Navigation and Control of Underwater Robotic Vehicles
IMT-6-2018	Bård Stovner	Aided Intertial Navigation of Underwater Vehicles
IMT-7-2018	Erlend Liavåg Grotle	Thermodynamic Response Enhanced by Sloshing in Marine LNG Fuel Tanks
IMT-8-2018	Børge Rokseth	Safety and Verification of Advanced Maritime Vessels
IMT-9-2018	Jan Vidar Ulveseter	Advances in Semi-Empirical Time Domain Modelling of Vortex-Induced Vibrations
IMT-10-2018	Chenyu Luan	Design and analysis for a steel braceless semi-submersible hull for supporting a 5-MW horizontal axis wind turbine
IMT-11-2018	Carl Fredrik Rehn	Ship Design under Uncertainty
IMT-12-2018	Øyvind Ødegård	Towards Autonomous Operations and Systems in Marine Archaeology
IMT-13-2018	Stein Melvær Nornes	Guidance and Control of Marine Robotics for Ocean Mapping and Monitoring
IMT-14-2018	Petter Norgren	Autonomous Underwater Vehicles in Arctic Marine Operations: Arctic marine research and ice monitoring
IMT-15-2018	Minjoo Choi	Modular Adaptable Ship Design for Handling Uncertainty in the Future Operating Context
MT-16-2018	Ole Alexander Eidsvik	Dynamics of Remotely Operated Underwater Vehicle Systems
IMT-17-2018	Mahdi Ghane	Fault Diagnosis of Floating Wind Turbine Drivetrain- Methodologies and Applications
IMT-18-2018	Christoph Alexander Thieme	Risk Analysis and Modelling of Autonomous Marine Systems
IMT-19-2018	Yugao Shen	Operational limits for floating-collar fish farms in waves and current, without and with well-boat presence
IMT-20-2018	Tianjiao Dai	Investigations of Shear Interaction and Stresses in Flexible Pipes and Umbilicals
IMT-21-2018	Sigurd Solheim Pettersen	Resilience by Latent Capabilities in Marine Systems
IMT-22-2018	Thomas Sauder	Fidelity of Cyber-physical Empirical Methods. Application to the Active Truncation of Slender Marine Structures

IMT-23-2018	Jan-Tore Horn	Statistical and Modelling Uncertainties in the Design of Offshore Wind Turbines
IMT-24-2018	Anna Swider	Data Mining Methods for the Analysis of Power Systems of Vessels
IMT-1-2019	Zhao He	Hydrodynamic study of a moored fish farming cage with fish influence
IMT-2-2019	Isar Ghamari	Numerical and Experimental Study on the Ship Parametric Roll Resonance and the Effect of Anti-Roll Tank
IMT-3-2019	Håkon Strandenes	Turbulent Flow Simulations at Higher Reynolds Numbers
IMT-4-2019	Siri Mariane Holen	Safety in Norwegian Fish Farming – Concepts and Methods for Improvement
IMT-5-2019	Ping Fu	Reliability Analysis of Wake-Induced Riser Collision
IMT-6-2019	Vladimir Krivopolianskii	Experimental Investigation of Injection and Combustion Processes in Marine Gas Engines using Constant Volume Rig
IMT-7-2019	Anna Maria Kozlowska	Hydrodynamic Loads on Marine Propellers Subject to Ventilation and out of Water Condition.
IMT-8-2019	Hans-Martin Heyn	Motion Sensing on Vessels Operating in Sea Ice: A Local Ice Monitoring System for Transit and Stationkeeping Operations under the Influence of Sea Ice
IMT-9-2019|	Stefan Vilsen	Method for Real-Time Hybrid Model Testing of Ocean Structures – Case on Slender Marine Systems
IMT-10-2019	Finn-Christian W. Hanssen	Non-Linear Wave-Body Interaction in Severe Waves
IMT-11-2019	Trygve Olav Fossum	Adaptive Sampling for Marine Robotics
IMT-12-2019	Jørgen Bremnes Nielsen	Modeling and Simulation for Design Evaluation
IMT-13-2019	Yuna Zhao	Numerical modelling and dyncamic analysis of offshore wind turbine blade installation
IMT-14-2019	Zhengru Ren	Advanced control algorithms to support automated offshore wind turbine installation
IMT-15-2019	Drazen Polic	Ice-propeller impact analysis using an inverse propulsion machinery simulation approach
IMT-16-2019	Endre Sandvik	Sea passage scenario simulation for ship system performance evaluation
IMT-17-2019	Loup Suja-Thauvin	Response of Monopile Wind Turbines to Higher Order Wave Loads

ISBN 978-82-326-4112-3 (printed version)
ISBN 978-82-326-4113-0 (electronic version)
ISSN 1503-8181

Doctoral theses at NTNU, 2019:258

Loup Suja-Thauvin

Response of Monopile Wind Turbines to Higher Order Wave Loads

NTNU
Norwegian University of
Science and Technology
Faculty of Engineering
Department of MarineTechnology

NTNU
Norwegian University of
Science and Technology

Doctoral theses at NTNU, 2019:258

NTNU

NTNU
Norwegian University of
Science and Technology